Design, modeling, and characterization of innovative terahertz detectors

Duy Thong Nguyen

UNIVERSITÉ DE GRENOBLE

THÈSE

Pour obtenir le grade de

DOCTEUR DE L'UNIVERSITÉ DE GRENOBLE

Spécialité : **Optique et Radiofréquences**

Arrêté ministériel : 7 août 2006

Présentée par

Duy Thong NGUYEN

Thèse dirigée par **Jean-Louis COUTAZ** et
codirigée par **François SIMOENS**

préparée au sein du **Laboratoire CEA-Léti**
dans **l'École Doctorale EEATS**

Conception, modélisation et caractérisation de détecteurs térahertz innovants

Thèse soutenue publiquement le **12 novembre 2012**
devant le jury composé de :

Pr. Jean-Louis COUTAZ
Professeur, IMEP-LAHC, Université de Savoie, directeur de thèse
Dr. Gian Piero GALLERANO
Chef du Laboratoire des Sources de Rayonnement, ENEA, Frascati (Italie), rapporteur
Pr. Ronan SAULEAU
Professeur, IETR, Université de Rennes, rapporteur
Dr. François SIMOENS
Responsable du programme stratégique "Imageurs", CEA-LETI Grenoble, encadrant de thèse
Pr. Carlo SIRTORI
Professeur, LMPQ, Université de Paris 7 Diderot, Président

UNIVERSITY OF GRENOBLE

Number attributed by library
|_|_|_|_|_|_|_|_|_|_|

PhD Thesis

in partial fulfillment to obtain the degree of

DOCTEUR OF PHYSICS

Doctoral Course : Optics & Radiofrequencies

Doctoral School : EEATS (Electronique, Electrotechnique, automatique, Télécommunications, Signal)

Design, modeling, and characterization of innovative terahertz detectors

Prepared by

NGUYEN Duy Thong
under the direction of Pr. Jean-Louis COUTAZ
at CEA, Leti, Department of Optoelectronics, MINATEC Campus

To be defended on 12 November, 2012 in front of the following examining committee

JURY

Gian Piero GALLERANO	PhD, ENA, Italy	Referee
Ronan SAULEAU	Professor, IETR , France	Referee
Carlo SIRTORI	Professor, University of Paris 7, France	Examiner
François SIMOENS	PhD, CEA-Leti, France	Supervisor
Jean-Louis COUTAZ	Professor, University of Grenoble	PhD Supervisor

Abstract

Design, modeling, and characterization of innovative terahertz detectors

This PhD thesis aims to establish an electromagnetic modeling of the bolometer at terahertz (THz) range that can facilitate the design of the detector from the uncooled infrared bolometer technology. The envisaged application for the detectors lies in active THz imaging at room temperature. We have studied the optical coupling of a THz antenna-coupled bolometer operating in the range 1 – 5 THz. Simulations in receiving and transmitting modes have been performed to study the optical characteristics of the bolometer. The combination of these two simulation types leads to a powerful toolset to design terahertz bolometers. For the experimental aspect, measurements have been performed by using Fourier-transform technique to study experimentally the electromagnetic behavior of the bolometer. They are measurement of reflectivity of the focal plane array's surface and spectral response measurement. The results of measurement were found to be in good agreement with the simulation. The understanding from the study in this PhD helps us make improvement to the actual detector. Also the design of bolometer for low frequency (850 GHz) has been proposed. This leads to a perspective of using bolometer for terahertz imaging at the frequency where many characteristic of the terahertz radiation are favorable for imaging application.

Key words: Terahertz, antenna-coupled bolometer, electromagnetic simulation, Fourier-transform spectroscopy, spectral response, terahertz imaging.

Résumé

Conception, modélisation et caractérisation de détecteurs térahertz innovants

Le but de cette thèse est d'établir une modélisation électromagnétique du détecteur bolométrique térahertz (THz). Ce travail aide à faciliter la conception de bolomètre THz dont la structure est basée sur celle de bolomètre infrarouge à température ambiante. Le contexte de la thèse est l'imagerie THz active. Nous avons étudié le comportement électromagnétique d'un bolomètre à antenne de bande spectrale 1 – 5 THz. Deux modes de simulation ont été réalisées : l'une est en mode de réception et l'autre est d'émission. La combinaison de ces modes de simulation constitue un outil important pour concevoir le bolomètre THz. La technique de spectroscopie par transformée de Fourier a été utilisée pour caractériser expérimentalement le comportement électromagnétique du détecteur. Nous avons mesuré la réflectivité de la surface du plan focal de détecteur ainsi que la réponse spectrale du détecteur. Les deux sont confrontées avec la simulation et elles se trouvent en bon accord. Avec les connaissances obtenues des résultats théorique et mesuré, la recherche aide à améliorer des performances du détecteur actuel. Nous avons aussi proposé un design pour le bolomètre de faible fréquence (850 GHz). Ce dernier ouvre la perspective d'emmener la technologie de bolomètre d'infrarouge vers la bande sous-térahertz où l'imagerie est beaucoup plus favorable.

Mots clés : Térahertz, bolomètre à antenne, simulation électromagnétique, spectroscopie par transformée de Fourier, réponse spectrale, imagerie térahertz

TABLE OF CONTENTS

Abstract ..... **i**

Acknowledgements ..... **iv**

Chapter 1 Introduction to THz science & technologies **1**

1.1 Terahertz domain 1
1.1.1 Technological development of THz components and systems 1
1.1.2 Features of THz domain 2
1.1.3 Applications of THz waves 5
1.2 Imaging in the THz domain 7
1.2.1 Common specifications of imaging systems 7
1.2.2 Other important features of terahertz imaging 10
1.2.3 Passive imaging vs active imaging 13
1.2.4 Context of the PhD work: THz imaging with room-temperature bolometer array 17
1.3 Summary 19
References 20

Chapter 2 Bolometric detectors **23**

2.1 Principle of bolometer 23
2.1.1 Bolometer overview 23
2.1.2 Electro-thermal model 25
2.1.3 Noise in bolometers 29
2.1.4 Figures of merit 32
2.2 Summary 34
References 35

Chapter 3 IR-THz transformation for uncooled bolometer **36**

3.1 Cryogenic terahertz bolometer 36
3.1.1 Antenna-coupled bolometer 36
3.1.2 Distributed absorbing element bolometer 37
3.2 Uncooled IR Bolometer 39
3.2.1 Structure 39
3.2.2 Optical coupling 41
3.2.3 Thermal insulation 41
3.2.4 Heat capacity and thermometer volume 45
3.2.5 Response time 47
3.3 IR-THz transformation 48
3.3.1 Absorbing film design 48
3.3.2 Antenna coupled bolometer design 50
3.4 Summary 52
References 53

Chapter 4 Bolometer stack for THz frequency **55**

4.1 Absorption of metallic thin film structure 55
4.1.1 Infinite size film 55
4.1.2 Finite size films 59
4.2 Bolometer stack for THz wavelength 64
4.2.1 Infrared stack 64
4.2.2 Optical coupling at THz frequency range 67
4.2.3 THz bolometer stack 69
4.3 Summary 71
References 72

Chapter 5 THz bolometer modeling **73**

5.1 Absorbing film bolometer (AFB design) 73

5.1.1 Structure ... 73
5.1.2 Figures of merit ... 75
5.2 Antenna-coupled bolometers (THEDEX design) ... 80
5.2.1 Structure ... 80
5.2.2 Figures of merit ... 82
5.2.3 Impedance matching for antenna-coupled bolometer ... 86
5.3 Improved design (Bambolo) ... 92
5.3.1 Structure ... 92
5.3.2 Optimization of optical coupling ... 94
5.3.3 Figures of merit ... 103
5.4 Perspective design for low frequency ... 106
5.4.1 Frequency selective surface ... 106
5.4.2 Implementation in bolometer structure ... 108
5.5 Summary ... 112
References ... 114

Chapter 6 Detector characterization results ... 116

6.1 Optical coupling measurement ... 116
6.1.1 Characterization with a Fourier-transform spectrometer ... 116
6.1.2 Reflectivity ... 119
6.1.3 Spectral response ... 127
6.2 Result of optical coupling measurement ... 135
6.2.1 Reflectivity ... 135
6.2.2 Spectral response ... 143
6.3 Other figures of merit ... 147
6.3.1 Thermal conductance and response time ... 147
6.3.2 Responsivity and sensitivity measurement ... 148
6.4 Examples of THz active imaging with the antenna-coupled bolometer FPA ... 150
6.4.1 Raster scanning imaging ... 150
6.4.2 Real-time imaging with 320×240 pixel array ... 151
6.5 Summary ... 152
References ... 154

Chapter 7 General conclusion ... 155

7.1 General summary ... 155
7.2 Perspectives ... 157

Vita ... 159

Publications of the author ... 160

List of figures ... 162

Acknowledgements

This work was only possible with the help of many nice people, to whom I am indebted.

First and foremost, I would like to express my gratefulness to Professor Jean-Louis Coutaz for doing a great job on supervising my research. Thank you for your support throughout my thesis, from the fruitful discussions on physics at the beginning to the correction during the writing phase.

I am also grateful to Dr. François Simoens who is the co-supervisor of the thesis. Thank you for taking me aboard and providing me the opportunity to work in a very professional and innovative environment as at CEA-LETI. Thank you also for your continuing advice, encouragement and patience.

A special thanks is for Dr. Jean-Louis Ouvrier-Buffet, my colleague at LIR laboratory, for sharing his expertise on the bolometer technology. Also, I would like to take this opportunity to thank all other colleagues at DOPT department: Jérôme Meilhan, Valérie Goudon, Claire Vialle, Lasfargues Gilles, Hamelin Antoine, Lalanne-Dera Jérémy, Gravrand Olivier…, for their support during three years of thesis.

Last but not least, I would like to express my appreciation to those people outside the academic environment, especially to my family, my friends who supported and encouraged me all throughout these years.

Chapter 1 Introduction to THz science & technologies

The aim of this chapter is to introduce step by step the context of this PhD work. We start by presenting the background of the THz domain: its historical development, its features and the related applications. Then we go into imaging, which is one important sector of the applications of the THz waves. We present the principles of imaging as well as some specific characteristics related to the THz range. Some THz imaging systems in literature, both passive and active, are mentioned in order to demonstrate the perspective of THz imaging in real-life. Finally, we present the concrete context of this PhD thesis, which is the development of detectors for THz active imaging.

1.1 Terahertz domain

The study of electromagnetic waves constitutes a key science in the 20th century. From the radio waves to gamma rays, the whole spectrum has been explored and is nowadays employed for a multitude of applications in everyday life. However, there still exists a spectral range that is poorly explored, that is the terahertz (THz) band. It lies between the infrared and microwave domains. This section presents briefly a history of this science, its characteristic features and perspectives.

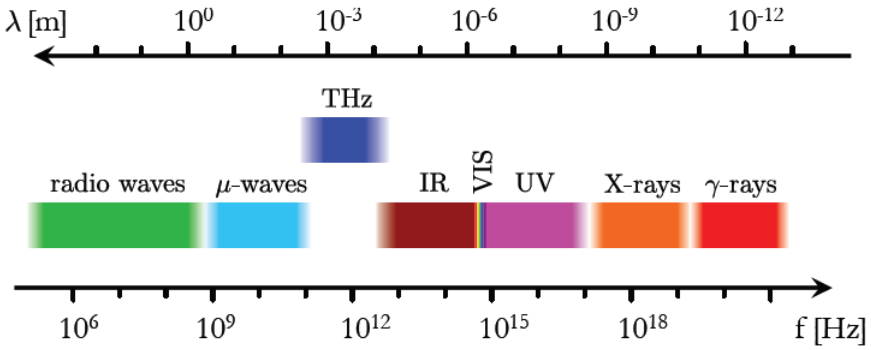

Fig. 1.1: Terahertz region is between infrared and microwave domains

1.1.1 Technological development of THz components and systems

The term "TeraHertz" first appeared in the early 1970s with the description of "whisker" diodes [1] and of Michelson interferometer [2]. One can see (Fig. 1.1) that this term is used to describe the upper limit of the radiofrequency (RF) domain or the lower limit of the optical domain.

Technological developments have been hindered because of this intermediate position between the electronic and optical ranges, and still now no devices meet the requirements of mass volume applications.

Since 1970, for decades, the sole niche for THz technology has been high-resolution spectroscopy and remote sensing areas where heterodyne and Fourier transform techniques have allowed astronomers, chemists, Earth, planetary, and space scientists to measure, catalogue, and map thermal emission lines for a wide variety of lightweight molecules [3]. Half of the radiance in our universe is at THz frequencies, and the astronomy science is based on the observation of electromagnetic radiation emitted by the stars, galaxies. Hence observation at THz frequencies plays an important role in astronomy physics and drives the development of detectors whose performances can approach the quantum limit. These include

Schottky barrier diodes, hot electron bolometers (HEBs), superconductor-insulator-superconductor bolometer, etc. Most of them operate at cryogenic temperature.

At the end of the 1980s, THz time domain spectroscopy (THz – TDS) emerged thanks to the availability of femtosecond lasers. The possibility of recording THz images with this system open the way to the so-called T-ray imaging. Many general public applications using T-ray imaging technique, such as medical imaging or especially security screening, bring THz science from the academic and laboratory level period to the public for the first time.

The THz spectrum is seen not as a new domain that brings fundamental physics law or phenomenon, but rather an unexploited region whose characteristic features may constitute interesting applications. Therefore, one of the tendencies of THz technologies is low cost, less bulky and complicated, more application oriented. For the source side, some components that have many (but not all) of these assets are the THz quantum cascade laser (QCL) or solid-state frequency multipliers driven by conventional microwave sources. For detectors side, some uncooled detectors such as Schottky diode, field effect transistor (FET) or uncooled bolometer are being developed. Of course, depending on applications, other components are also developed to fulfil the diversifying needs in the emerging domain.

Today, though few THz (or strictly speaking sub-THz) technologies are being commercialized for applications as screening remote inspection at airport checkpoints, the domain is far from being mastered. On the source side, the lack of high power, compact, low cost sources is still present. Concerning detectors, besides the cryogenic detectors for astronomy that ensure truly high performances but also are very costly and complex, the THz community is still searching low-cost technologies suitable for general public applications. The story of THz does still continue.

1.1.2 Features of THz domain

1.1.2.1 Spectrum

THz technologies have been independently developed by researchers from several different disciplines. In fact, “THz gap” became a common term to describe the gap between microwave and far-infrared spectrum. Still now, THz band does not have any industrial standard definition. In this thesis, we consider the universal definition suggested by [4] in which THz band spans from 0.1 THz to 10 THz. One can see that this band overlaps neighboring spectral regions such as millimeter-wave, the submillimeter-wave, and the far-infrared (FIR) listed in table 1.1. These bands can also be distinguished with respect to technologies. Millimeter wave emitters and sensors are derived from microwave solid-state devices whereas, traditionally, far-IR applications rely on optical and thermal devices.

Frequency Band	Frequency	Wavelength
Millimeter wave	30 – 300 GHz	1 – 10 mm
Sub-millimeter wave	0.3 – 3 THz	0.1 – 1 mm
Far-infrared	≈ 1.2 – ≈ 10 THz	35 – 300 μm
Terahertz	0.1 – 10 THz	30 μm – 3 mm

Table 1.1: Frequency band definitions of terahertz domain.

Let us take the frequency of 1 THz to see its conversions:

- Frequency: $\nu = 1$ THz = 1000 GHz,
- Period: $\tau = 1/\nu = 1$ ps,
- Wavelength: $\lambda = c/\nu = 0.3$ mm = 300 μm,
- Wavenumber: $k = 1/\lambda = 33.3$ cm^{-1},
- Photon energy: $h\nu = 4.14$ meV,
- Temperature: $T = h\nu/k_B = 48$ K,

where c is the speed of light in vacuum, h is Plank's constant, and k_B is Boltzmann's constant.

1.1.2.2 Properties of terahertz radiation

The most fabulous characteristic of THz radiation is the capability of THz wave to go through non-polar and non-metallic materials such as paper, plastic, cloth, dry wood and ceramics that are usually opaque at optical wavelengths. This property comes from specific interactions between THz radiation and matter. The THz photon energy is low and as a consequence, the THz radiation can only excite low energy resonances in matter. Typically, THz resonances in matter are related to roto-vibrational modes of gas molecules, to collective oscillations (phonons), to alignment of dipole in polar molecule liquid, or to the excitation of free charge in metal and doped semiconductor. Phonon resonances in dielectrics are generally above a few THz, thus most of dielectrics do not exhibit these resonance modes in the lower part of the THz range; therefore dielectrics do not absorb much THz radiation.

For metals, the THz wave behaves just like any electromagnetic waves below the plasma frequency of the metal. They can excite free electrons and thus create a high-frequency current, since THz radiation, though higher in frequency than microwave, is still so small as compared to the plasma frequency (which is at the range of UV-ray). More concretely, wavelength that corresponds to the plasma frequency is in the range 100 ~ 300 nm when compared to the typical wavelength of 300 μm of THz band. The skin depth in a good metal, like copper, is about 90 nm at 1 THz. Therefore common metals such as copper, aluminum, iron, behave as perfect conductors for THz radiation, thus THz radiation is reflected almost completely on metal.

One should also point out that since the water molecules are polar, water absorbs strongly THz radiation. As a consequence, since atmosphere contains water vapor, its transmission shows strong absorption lines and consequently atmosphere is poorly transparent in the upper part of the THz range when compared to infrared or visible light [5]. On the other hand, the only advantage of THz wave related to free-space propagation is that the THz wave is less scattered by dust or fog (because the THz wavelength is much larger than infrared or visible wavelength).

A last critical feature of THz radiation stands in its low level of photon energy that makes them non-ionizing. Until today, there is no harm reported by using THz on biological molecules or cells. However, still some additional studies are being led to verify the inoffensive effects of THz radiation on human cells.

1.1.2.3 Terahertz gap and devices

The THz region is the last exploited spectrum and exhibits a gap of technology between microwave and optical domains. For microwave and also radio frequency – RF –regions, the devices are basically electronic devices. Their operation is based on the generation, transmission and processing of a high-frequency current. The electronic devices have started

with low frequency, in the range of MHz (RF domain), and have extended to higher frequency, in the range of GHz (microwave). At higher frequency, i.e. in the THz range, the performance of these devices degrades dramatically, thus very little devices are able to function at these frequencies. One of the reasons is that the attenuation of the signal is very high at THz range due to the propagation loss of propagation of the signal. Another reason originates in the effect of parasitic elements such as capacitance or inductance, which increases strongly at THz range. Thus we can say that the THz range is beyond the upper limits of today microwave and RF industry.

For optical or optronic devices such as lasers or photodiodes, the THz frequency range stands at the lower spectral boundary. The corresponding photon energy of THz wave is very low, of the order of meVs. This energy level is small when compared to the band gap energy of semiconductor materials, which takes a value ~ 100 – 1000 times bigger (~ eV). This makes the interband photon-electron interaction in semi-conductor less efficient or even impossible. Besides, the thermal excitation at room-temperature has the same level of energy as the photon energy, and hence it dominates the photo-conduction processes; this phenomenon implies that the thermal noise in optical devices in the THz regime is a big issue. The devices need to be cooled to low (even cryogenic) temperatures.

These limitations explain the origin of this so-called THz gap. Recently, on both electronic and optical sides, technologies are emerging and this gap is being progressively fulfilled. Though there are still big technical challenges, some interesting applications in THz domain are beginning to be demonstrated. Some available techniques and devices for the generation and detection of the terahertz wave are presented as following.

Sources

- Thermal source (blackbody): the radiation is large band and incoherent, and the power in terahertz range is very weak. The typical power range is pW at 0.1 THz and μW at 10 THz.
- Narrow band and coherent source: multiplier frequency source such as Schottky diode or laser such as quantum cascade laser (QCL). Today, many Schottky-diode based multiplier sources work in the range of 0.2–1.9 THz that produce a THz power of about 50 mW at 200 GHz and still 10 μW at 1.9 THz [6]. Above 2 THz, the QCL source is very promising since it delivers a high power, in the range of mW [7]. The cooling requirement and the weak tenability of this source are the main drawback.
- Other kinds of source: some photoconductive switching techniques can generate terahertz pulse that is used broadly in time domain spectroscopy (TDS) system.
- BWO, molecular lasers, optical rectification…

Detector

- Bolometers: The superconducting bolometer such as superconductor-insulator-superconductor (SIS) or hot-electron bolometer (HEB) can perform both direct and heterodyne detection. These detectors are extremely sensitive. However they require cryogenic operation and are very costly.
- Schottky diode, HEMT transistor: these devices can operate at room temperature and perform heterodyne detection thus highly sensitive. The electronics equipped with these detectors require expensive low noise amplification. These devices bandwidth is limited to the sub-THz region.
- Field effect transistor (FET) and uncooled bolometer: they operate at room temperature with direct detection. The sensitivity is less than Schottky diode or HEMT transistor, however they are relatively cheap.

- Electro-optics, pyroelectrics, photoconduction…

1.1.3 Applications of THz waves

The applications in terahertz domain are quite various: they began from the astronomy and earth science and today they spread to the general public applications. Some prospective sectors include medical imaging, wireless communication, security screening and non-destructive testing.

Astronomy and earth science

In astronomy, terahertz spectroscopy is used to study the structure and forming as well as the nature of universe. Results from the NASA Cosmic Background Explorer (COBE) Diffuse Infrared Background Experiment (DIRBE) and examination of the spectral energy distributions in observable galaxies, indicate that approximately one-half of the total luminosity and 98% of the photons emitted since the Big Bang fall into the submillimeter and far-IR. Thus submillimeter (and therefore teraherz) detectors are true probes into the early universe [3].

THz technology is also now important in the environmental monitoring of Earth. The major objectives are to obtain information about the upper atmosphere (stratosphere, ionosphere, troposphere…) physico-chemistry to better understand global warming, to quantify aspects of how the atmospheric composition affects climate and to study aspects of pollution in the upper troposphere [8]. For example, THz technology may help at detecting and mapping ozone in the atmosphere.

Medical Imaging

Due to their low photon energies and non-ionizing character, THz waves are promising candidate for applications in the medical field. They are not expected to damage DNA or tissue molecules as X-rays can do. Even though THz waves cannot penetrate the entire body, many applications are possible. For instance, the detection of skin cancers (in-vivo), breast cancer (ex-vivo), skin burns, or osteoarthritis in knee joints has been demonstrated with reflection imaging techniques [9], [10]. THz time-domain spectroscopy (THz-TDS) could ultimately be used for in-vivo DNA analysis due to rotational and vibrational resonances of this molecule.

Communication

As a rule of thumb, due to the demand for ever increasing data rates, the wireless communication tends to operate at higher frequency. The wireless communications above 100 GHz are under development and therefore, in a mid-term future, THz communications would be in use, especially as HEMT transistors and other ultrafast electronics components are now able to operate at up to 500 GHz or beyond.

Two constraints that can cause limitations to terahertz wireless communication are atmospheric attenuation and propagation characteristics of terahertz wave. The first one restricts terahertz communication to short distance or inter-satellite communication while the propagation of terahertz wave, especially the scattering property leads to the line-of-sight communication. The line-of-sight problem is more serious when operating at higher frequency. Communication at infrared or visible range also exhibits line-of-sight concern. However, since these technologies do not suffer atmospheric attenuation, they may be more attractive than terahertz. In the near future, perhaps communication at 110 – 120 GHz, i.e. the low frequency part of terahertz band is commercialized. A wireless link of a few hundred meters at 120 GHz of 10 Gb/s data transmission is already reported in [11].

Two constraints that can cause limitations to THz wireless communication are atmospheric attenuation and propagation characteristics of THz wave. The first one restricts THz communication to short distance (in-building) or inter-satellite communication while the propagation of THz wave, especially the scattering property leads to the line-of-sight communication. The line-of-sight problem is more serious when operating at higher frequency. Communication at infrared or visible range also exhibits line-of-sight concern. However, since these technologies do not suffer atmospheric attenuation, they may be more attractive than THz. However, commercial 100-GHz wireless links are expected soon and researches are performed at 300-GHz carrier frequency [12].

Security screening

Security screening is one prominent application of the THz domain. The high transmission of THz wave in fabric material helps, through THz imaging, detecting metallic weapons concealed under clothes [13]. The active THz imaging has an advantage over X-ray technique (backscatter X-ray system) in the sense that THz wave, unlike X-ray, is not a ionizing radiation. The passive THz imaging is completely safe. Although some THz cameras for security screening are available on the market (Thruvision, Qinetiq), the research is still carried on in laboratories to find a cost-effective imaging system to bring the technology not only to airport but also in another high transportation places, such as train and metro stations.

Spectroscopy to detect drugs or explosives can also be used in combination with imaging in a security screening system. Some common explosives (RDX, TNT, HMX…) show strong absorption peaks in THz range that can be used as fingerprints to identify the material. Originally, TDS or Fourier-transform infrared (FT-IR) spectroscopy are used to characterize the materials in transmission mode [14]. Since then, many efforts are devoted to bring this explosive identification technique to a simpler and more realistic level. In [15], the specular reflection scheme is used in a FTIR spectroscopic system to identify the explosive and also to image the explosive. Diffuse reflection spectroscopy of explosives is also studied and has a potential for standoff detection and identification of explosives concealed in packages or under clothing [16]. A very good review of THz spectroscopy and imaging for defense and security applications can be found in [17].

Non-destructive testing

The identification of defects in the Columbia space shuttle foam insulation led to understand why this shuttle was destroyed during re-entry in the Earth atmosphere and thus constitutes a prominent example of using THz technology for non-destructive testing. It is difficult to locate defects in low-density, low-absorption medium using other nondestructive inspection techniques such as X-rays or ultrasound. In this case, the THz technique can be useful because THz time-of-flight tomography is sensitive in detecting small changes in optical properties of media such as the refractive index and absorption coefficient [18]. In addition, THz analysis can be employed for low molecular weight materials, which is not the case of X-ray techniques.

Non-destructive testing may find applications in pharmacy or semiconductor industry as a technique for quality control. Reference [19] gives an example in which THz imaging is used to detect damaged MOSFETs transistors, showing potential applications for fault analysis in large-scale-integration (LSI) circuit. Moreover, historical artwork or fine art analysis is also a promising application for THz non-destructive testing. THz tomographic imaging helps analyzing the structure of sealed pottery [20]. Also, historical paintings reveal a lot of information by using THz imaging and spectroscopy [21], [22].

1.2 Imaging in the THz domain

Imaging is a prominent application of the THz domain thanks to the unique characteristics of THz radiation, in particular the transparency through clothing and plastic packaging. In this PhD work, we study THz uncooled bolometers for active imaging, thus we are only interested on the detector side. Nevertheless some characteristics of the detector are related strongly to the specification of the imaging system. Thus we present here the principle of (geometrical) imaging that determines some specifications of detector, such as the elementary detector size or the size of an array of detectors. Also other characteristics related to the THz range are presented. They also may affect the detector specifications, mostly its working frequency.

1.2.1 Common specifications of imaging systems

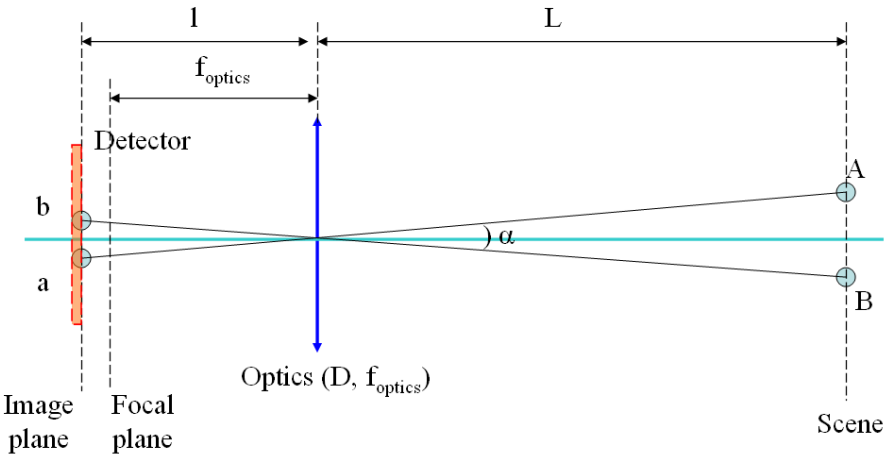

Fig. 1.2: Simple scheme of imaging system

Common imaging systems consist of an optical system (lens, mirror, etc.) and an imager, usually an array of detectors, set at the focal plane. The optical system has a diameter D and a focal length f_{optics}. The scene is at a distance L far from the optics. The optics forms the image ab at the image plane of an object AB in the scene. If L is large enough when compared to f_{optics}, the image plane is very close to the focal plane, i.e. $l \approx f_{optics}$.

1.2.1.1 Resolution

We desire to distinguish 2 points A and B of the object, separated by AB. As A and B are far from the optical system, the difference of incoming angle, for rays emitted respectively by A and B, is

$$\alpha \approx \frac{AB}{L}. \qquad (1.1)$$

The Rayleigh's criterion states that there exists a minimum angle beyond which the image is hardly resolved due to the diffraction that occurs at the entrance of the optics. This minimum angle is angular resolution of the imaging system, which is related to the wavelength λ and parameter of optics by:

$$\alpha_{\min} = \frac{1.22\lambda}{D}. \quad \textbf{(1.2)}$$

At the detector, assuming the scene is far from the optics, the size of the image is $ab \approx \alpha \times f_{optics}$. Thus the minimum distance between two resolved image points a and b is:

$$ab_{\min} = \frac{1.22\lambda}{D} f_{optics}. \quad \textbf{(1.3)}$$

This spatial resolution has some impacts on detector pitch and detector size. Detector pitch is the distance between two pixels in an array of detectors. One can see that this distance should be at least equal to the spatial resolution because even if it is smaller, the resolution of the image obtained by the detector is not better than this limit. The detector size should be at least equal to the spatial resolution because it can receive more incoming flux. The diameter and focal length of the optical system is related to its f-number (F_{no}) by the expression:

$$F_{no} = \frac{f_{optics}}{D}. \quad \textbf{(1.4)}$$

Thus the spatial resolution can be rewritten as:

$$ab_{\min} = 1.22\lambda \times F_{no}. \quad \textbf{(1.5)}$$

The typical minimum value, limited by technology, of f-number is 1; below this value some other phenomena such as aberration will degrade the quality of the image. Thus one can see that, in the best case (F_{no}=1) the typical spatial resolution is 122 μm at 3 THz (λ = 100 μm), 366 μm at 1 THz (λ = 300 μm), and becomes 1.220 mm at 300 GHz (λ = 1 mm).

At the scene side, the angular resolution also sets a limit for the spatial resolution of the scene. This limit is:

$$AB_{\min} \approx \alpha_{\min} L = \frac{1.22\lambda}{D} L. \quad \textbf{(1.6)}$$

In visible or infrared imaging, the scene resolution is high enough so that the image is easy to be understood (interpreted). In millimeter-wave or terahertz imaging, since the wavelength is much longer, the scene resolution is very important to the capability of precise interpretation of the image. From the equation 2.6, one can see that the desired scene resolution imposes a constraint to the diameter of the optics of the imaging system:

$$D = 1.22\lambda \frac{L}{AB_{\min}}. \quad \textbf{(1.7)}$$

We give an simple example in which the imaging range (the distance L) is 2 m, the desired scene resolution is 1 cm. From the above equation, we can deduce easily that the diameter of the optical system must be at least 2.44 cm if the imaging system operates at 3 THz. The value becomes to 7.32 cm if the frequency is 1 THz and 24.4 cm if the system works at 300 GHz. If the scene is at 10 m, all these values must be multiplied by 5. Thus at 300 GHz, we end up with a large and heavy optics of about 75 cm of diameter.

1.2.1.2 Angle of view and field of view

The angle of view is also a very important parameter of the imaging system. It describes the angular extent of a given scene that is imaged by the array of detector. In Fig. 1.3, we see that when the array of detector is located at the image plane, the part of the image that is outside of the area of the detector is not detected. Thus the size of array of detectors $l_{detector}$ imposes a maximum angle of view, which is

$$\alpha_{max} = 2\arctan\left(\frac{l_{detector}}{2\,f_{optics}}\right). \quad \textbf{(1.8)}$$

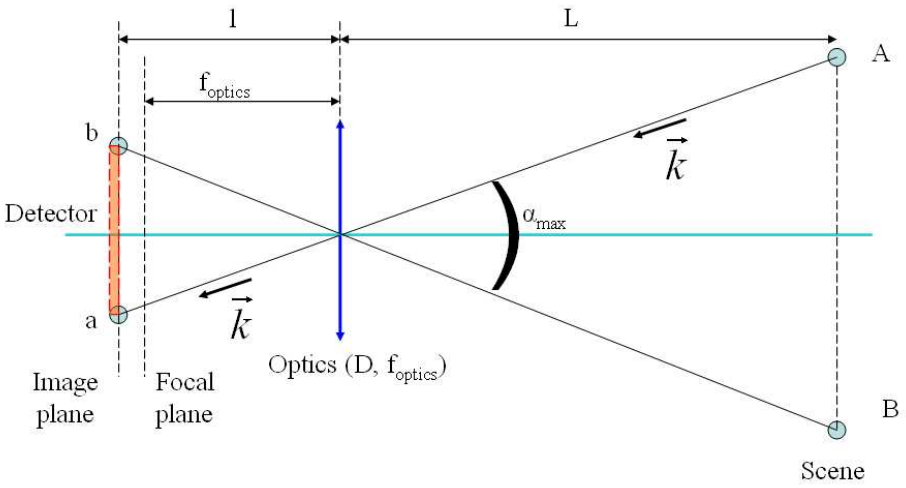

Fig. 1.3: Angle of view is determined by optics and size of array of detectors

The field of view (FOV) is the size of the scene whose image has the size of the detector array. For moderate values of α_{max}, the FOV obeys the simple following expression:

$$FOV = L\tan\alpha_{max} = \frac{L \times l_{detector}}{f_{optics}}. \quad \textbf{(1.9)}$$

In the THz domain, there are not many detectors whose total size is so large. We will take the size of the array of detectors studied in this PhD work as an example. The detector has a length of 16 mm and will operate at 3 THz. We consider the case f-number = 1 so that the image quality is not degraded much by aberration. If the desired resolution of the scene is 1 cm at 2 m range, the diameter of optics is 2.44 cm as calculated previously. Since f-number = 1, we deduce that the focal length is also equal to 2.44 cm. The angle of view in this case is 36^o and the FOV, at 2 m, is 1.33 m. The same reasoning leads to 12^o if the same detector operates at 1 THz, and thus FOV = 44 cm only.

1.2.1.3 Incident angle

The incident angle of the rays reaching the array of detectors is not the same for the pixels at the center or at the border of the array. Let us consider rays coming from the center of the scene, located on the optical axis. On the optical axis, the incident angle is zero, but it increases to its maximum value at the edge position, which is equal to half of the angle of view.

$$\alpha_{\text{incident\_max}} = \frac{1}{2}\alpha_{\max} . \quad \textbf{(1.10)}$$

Due to the effect of the incident angle, the detected signal of the pixel at center is in general higher than at the edge. However, this effect can be corrected by image processing to obtain the "homogeneous" image, as long as the signal to noise ratio is good enough.

1.2.2 Other important features of terahertz imaging

1.2.2.1 Atmospheric transmission

The atmospheric transmission is one of the biggest concerns for THz imaging. We can see clearly in Fig. 1.4 that the atmospheric attenuation of THz domain is much more severe than in the other spectral regions, such as millimeter, infrared, and visible regions. This imposes that THz imaging must be short-range when compared to imaging in the other domains. In the visible range, light is still strong enough to be detected without difficulty after propagating 70~80 km. Thus infrared imaging can attain a range of several tens of kilometers. Imaging in the range of kilometer is very challenging, if not impossible at THz range.

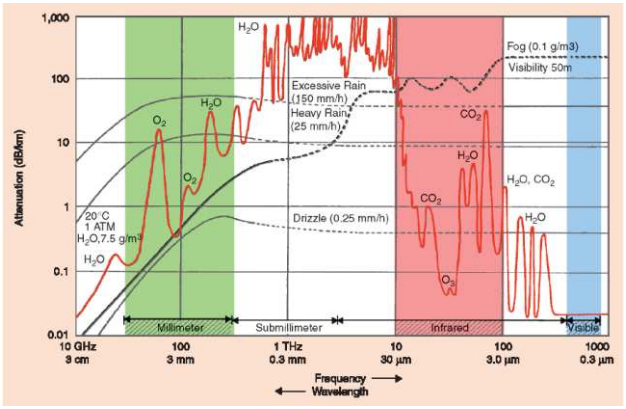

Fig. 1.4: Atmospheric attenuation from millimeter to visible range [5]

The attenuation of THz radiation depends strongly on the density of the vapor in atmosphere. Thus the humidity has a high impact on the atmospheric transmission. The measurement in humid condition weather (summer) shows a large difference when compared to dry weather (winter).

We should examine more concretely the problem to find out which transmission windows should be used in THz imaging. Fig. 1.5 depicts the atmospheric attenuation (dB/km) from 10 GHz to 10 THz, taken from [23]. The curve above exhibits sharp peaks (mostly water vapor absorption lines) and valleys between these peaks. These valleys define the transmission windows of the atmosphere, which should be used in imaging system to mitigate the loss due to propagation of THz wave. The attenuation increases by two orders of magnitude from 100 GHz to 1 THz. From 1 to 10 THz, the attenuation continues to increase with roughly one order of magnitude. Thus, the THz imaging is more favorable at low frequency than at high frequency in respect to the loss of signal due to the atmospheric attenuation.

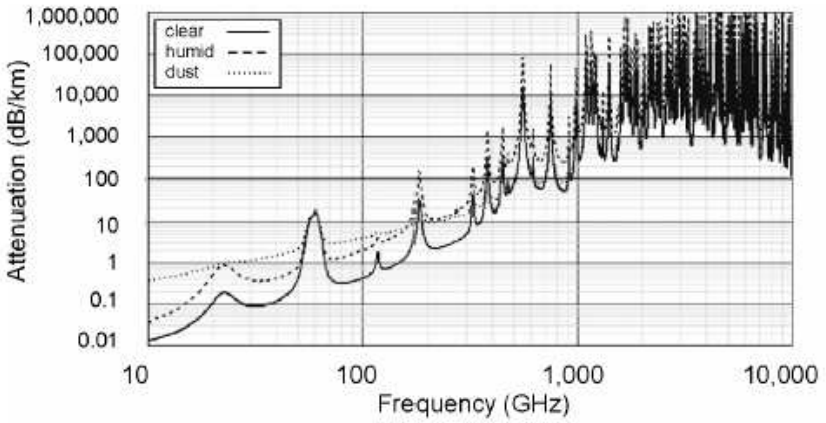

Fig. 1.5: Atmospheric attenuation (dB/km) from 10 GHz to 10 THz

Several transmission windows can be defined in the range 0.2 – 1 THz. Reference [24] suggests 6 transmission windows within this range. It should be noted that the value of atmospheric attenuation given here is related to the experimental condition during measurement. The experiment has been performed in laboratory, with a reported humidity of 51 %. At other weather condition, the absolute value may change but the tendency of atmospheric attenuation for different frequency still remains.

Window	#1	#2	#3	#4	#5	#6
Frequency (THz)	0.21	0.35	0.41	0.68	0.85	0.93
Power attenuation (dB/km)	7	21	28	72	92	148

Table 1.2: Transmission window in the range 0.2 – 1 THz as suggested by [24].

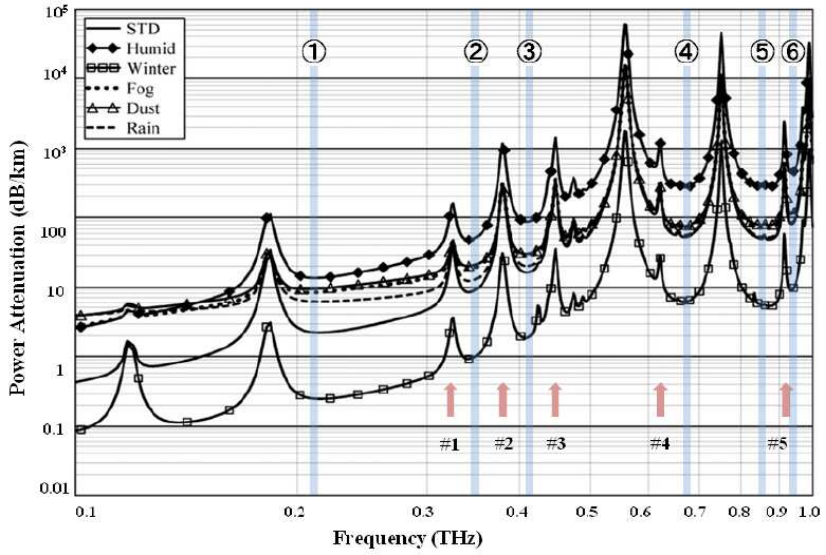

Fig. 1.6: Atmospheric attenuation (dB/km) at different weather conditions from 0.1 to 1 THz

Thermal detectors as pyro-electric or Golay cells can access the whole THz range. In principle, the bolometer is also able to detect the whole THz range. However, the performance of each type of bolometers varies strongly with the spectral range. Other kinds of detectors, such as monolithic microwave integrated circuit (MMIC) detector, Schottky diode or field effect transistor (FET), have a much more limited bandwidth. MMIC detectors operate at 35

and 94 GHz, thus almost outside the THz band. FET can operate below 1 THz. Their performance degrades dramatically at higher frequencies.

1.2.2.2 Transmission through clothing

Transmission through clothing is a critical feature of THz imaging. Reference [25] gives the transmission in the THz range for several common cloth materials, such as wool, linen, leather, silk, nylon, etc. All samples are transparent at millimeter-wave frequencies (up to 300 GHz) based on a 3 dB criterion, but became progressively opaque at higher frequencies in a highly sample-dependent manner. In general, the transmission of thin sheet of cloth in THz range is quite high, which allows imaging through clothing to detect concealed weapons.

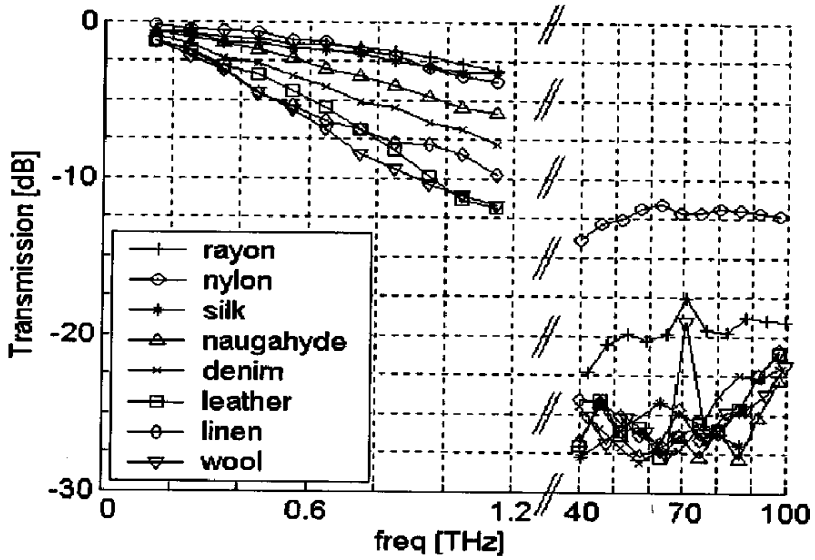

Fig. 1.7: Transmission through some common clothing materials [25].

The attenuation when propagating through clothing depends on the cloth materials, but also on the geometry of the textile. Thus the attenuation varies strongly with each type of clothing, making the phenomenon difficult to be generalized. However, in general, we can say that the attenuation through clothing such as nylon, silk, cotton is less than other materials, such as linen, leather, and denim. The table below presents the detailed properties of the clothing materials, which is reproduced from the data in [25].

Material	Thickness (mm)	Density (kg/m^3)	-3dB frequency (THz)	Attenuation at 1 THz (dB)
Wool	2.2	214	0.35	11.0
Linen	1.1	509	0.35	8.0
Leather	0.75	813	0.40	10.0
Denim	0.96	490	0.50	6.5
Naugahyde	0.65	800	0.70	5.5
Silk	0.36	256	1.0	3.0
Nylon	0.19	379	1.0	3.0

Rayon	0.15	733	>1	2.5

Table 1.3: Properties of some common clothing materials

The attenuation due to the propagation through the clothing exhibits a roughly similar tendency as the atmospheric attenuation in a sense that it increases with frequency. Propagation through the clothing is the most important attenuation mechanism in the close-remote THz imaging system. In terms of power budget, the THz imaging is more favorable at low frequency than at high frequency.

1.2.3 Passive imaging vs active imaging

THz imaging exists in both passive and active types. Each type exhibits advantages as well as disadvantages, which depends strongly on the desired application. Although some THz systems (both passive and active) have been commercialized, the research in the field is still extending to find a more attractive trade-off between cost and performance.

1.2.3.1 Passive imaging

In passive imaging, detector receives the optical flux that is radiated naturally from the scene. The natural radiation of the scene is the thermal radiation and shares many characteristics with the radiation of a blackbody whose radiance is described by the Planck's law:

$$L_{bb,\nu}(\nu,T) = \frac{2hc}{(e^{\frac{h\nu}{k_B T}} - 1)} \left(\frac{\nu}{c}\right)^3 . \quad \textbf{(1.11)}$$

where ν is the optical frequency, k_B the Boltzmann constant, c the light velocity in vacuum and T the temperature of the blackbody. At room temperature and in the THz range, the above expression tends towards the Rayleigh-Jeans law:

$$L_{bb,\nu}(\nu,T) \approx 2k_B T \left(\frac{\nu}{c}\right)^2 . \quad \textbf{(1.12)}$$

Thus in the THz range the luminance varies linearly with temperature. We employ a simple calculation to evaluate the power of optical flux in this range.

Supposing that the optics of the THz imaging system is characterized by a f-number F_{no}. The detector operate at central frequency ν_{center} (wavelength: λ_{center}) and has a bandwidth BW. In the diffraction-limited case, the detector has the size of the Airy-disk whose radius follows the Rayleigh's criterion:

$$r_{Airy} = \frac{1}{2}\frac{1.22\lambda_{center}}{D} f_{optics} = 0.61\lambda_{center} F_{no} . \quad \textbf{(1.13)}$$

Thus, the area of the detector is:

$$A_{detector} = \pi \times r_{Airy}^2 = \pi \times 0.61^2 \lambda_{center}^2 F_{no}^2 . \quad \textbf{(1.14)}$$

The expression for optical power absorbed within the detector with area $A_{detector}$ and absorption rate η due to a distant blackbody target with radiance L_{bb} can be found in some textbook, such as [26]:

$$Q = \frac{A_{detector}\pi}{1+4F_{no}^2}\int_{BW}\eta(\nu)L_{bb,\nu}d\nu . \quad \textbf{(1.15)}$$

The quantity $\int_{BW}\eta(\nu)L_{bb,\nu}d\nu$ represents the radiance absorbed by detector, which depends on the performance of source and detector. For a narrow band system, this quantity can be approximated as:

$$\int_{BW}\eta(\nu)L_{bb,\nu}d\nu \approx \eta L_{bb,\nu}(\nu_{center})BW . \quad \textbf{(1.16)}$$

By replacing (1.12) into (1.16), we obtain:

$$\int_{BW}\eta(\nu)L_{bb,\nu}d\nu \approx \eta 2k_BT\left(\frac{\nu_{center}}{c}\right)^2 BW . \quad \textbf{(1.17)}$$

Thus, the optical power in (1.15) becomes:

$$Q = \frac{A_{detector}\pi}{1+4F_{no}^2}\eta 2k_BT\left(\frac{\nu_{center}}{c}\right)^2 BW . \quad \textbf{(1.18)}$$

Finally, be replacing $A_{detector}$ by (1.14) in the above equation, we have:

$$Q = \frac{\pi\times 0.61^2\lambda_{center}^2 F_{no}^2\pi}{1+4F_{no}^2}\eta 2k_BT\left(\frac{\nu_{center}}{c}\right)^2 BW . \quad \textbf{(1.19)}$$

Since the wavelength λ_{center} and the frequency ν_{center} is related by the equation:

$$\lambda_{center} = \frac{c}{\nu_{center}} . \quad \textbf{(1.20)}$$

The expression in (1.19) can be reduced to

$$Q = \frac{\pi^2\times 0.61^2 F_{no}^2}{1+4F_{no}^2}\times\eta\times 2k_BT\times BW . \quad \textbf{(1.21)}$$

In the best practical case, f-number of optics is equal to 1. Supposing also that the detector assures a high absorption rate 80 %, the numerical calculation of the above expression gives:

$$Q = 1.2\times k_BT\times BW \approx k_BT\times BW . \quad \textbf{(1.22)}$$

We can see the order of magnitude of the absorbed power at THz range at room temperature is $k_B T \times BW$. For a 100 GHz bandwidth detection system watching an object at room temperature, the power absorbed by a pixel is ~ 400 pW. However, the image is formed by the power difference between pixels (contrast of the scene), not by the absolute power. The power difference between an object at T and another one at $T + \Delta T$ is:

$$\Delta Q = k_B \Delta T \times BW . \quad \textbf{(1.23)}$$

This power contrast for an object at 300 K and another one at 300 K + 0.1 K is ~ 0.14 pW.

This range of power is the biggest challenge of THz imaging because it requires a highly sensitive detector. To detect this level of power, in general heterodyne detection is employed. In the case of direct detection, the detector usually operates at a low temperature. However, for such system, complexity or high-cost are the inherent disadvantages.

Fig. 1.8: Passive imaging at 94 GHz from QinetiQ [13]

Some prominent examples of terahertz passive imaging can be mentioned. The image in Fig. 1.8 is from the company QinetiQ and shows a man hiding a knife in a newspaper [13]. QinetiQ does not disclose details of the used imaging system, but it is likely that Schottky diode based detectors operating at microwave frequencies (f = 94 GHz) have been applied.

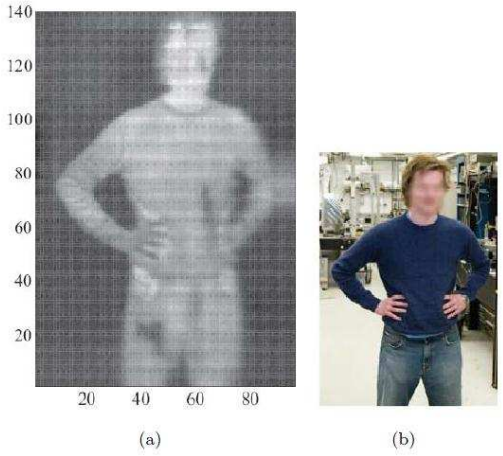

Fig. 1.9: Passive imaging with superconducting bolometer at NIST & VTT

Passive imaging can also be performed with superconducting bolometer that operates at cryogenic temperature. Fig. 1.9 is a raw passive image of a person carrying concealed weapons (ceramic knife on the chest and handgun on bottom) taken by raster-scanning a module of 8 pixels. Grossman (NIST, USA) and Luukanen (VTT, Finland) have dedicated a lot of works to bring the superconducting bolometer technology to the general public

application, which is, in this case, security screening [27], [28]. The detector in use is a superconducting bolometer that has spectral range of 0.1 – 1.2 THz and operates at ~ 4 K. A recent improvement includes the development of a linear array of 64 pixels [29].

This result seems prospective for security screening high-end application: the scene scenario is realistic and the image quality is good enough to detect the concealed weapon. The drawback of the system is in the cryogenic requirement.

Institute Ipht-Jena (Germany) also develops a passive THz imaging system based on superconducting bolometer [30]. The system uses an array of 20 superconducting transition-edge sensors operated at a temperature of 450 to 650 mK, and a closed-cycle cryorefrigerator. The main figures of the system include: a frequency band of 350±40 GHz, an object distance of 7 to 10 m, a circular field of view of 1.05 m diameter, and a spatial resolution in the image center of 2 cm at 8.5 m distance, a noise equivalent temperature difference of 0.1 to 0.4 K, and a maximum frame rate of 10 Hz. Like imaging system at NIST & VTT, this system requires cryogenic operation. The closed-cycle cryorefrigerator seems the most favorable cooling system for such case thanks to its compactness.

1.2.3.2 Active imaging

Active imaging refers to the technique of illuminating the target with a source of radiation, and then measuring the reflected (scattered) or transmitted radiation. The technique has both advantages and disadvantages when compared to the passive imaging.

In an active imaging scenario, strong scene illumination can overcome the low power contrast of passive detection. Also, the frequency of the radiation can be chosen to match with the system requirements. For example, high frequency should be used where spatial resolution is the main requirement. Therefore, the imaging system is more flexible.

Penetration through thick clothing can be also accomplished by increasing the transmitting power. Unlike passive detectors, active transceivers will confront no fundamental detection sensitivity limit determined by a scene thermal background radiation; a very high signal-to-noise ratio (SNR) can be achieved given a strong enough illumination source. In reality, compact solid-state sources can typically only generate about ~1 mW up to ~1 THz giving an upper limit to the radiation penetrating ability.

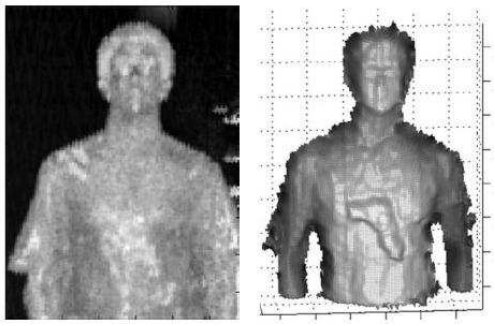

Fig. 1.10: 2D image and 3D image obtained by heterodyne detection at JPL [31]

One of the biggest disadvantages of the active imaging is that the obtained image has large signal clutter and speckle caused by a scene with a diversity of angles of incidence, surface roughness, and layers of concealing clothing. This is particularly true for active THz through-clothes imagers that rely on coherent illumination and detection [32]. We can say the image is less “natural” than with the passive imaging. Some techniques such as frequency modulated continuous wave (FMCW) radar techniques employed at the JPL (Jet Propulsion

Laboratory, NASA) can solve the issue. However, this approach also increases the complexity of the imaging system.

Another problem for active imaging is perhaps the health concern related to illumination. As mentioned earlier, until now, there is no harm reported by using THz on biological molecules or cells. However, this problem should be studied more deeply before the use of active imaging in large-scale.

A prominent example of active imaging is high performance heterodyne detection system using Schottky diode as mixer developed at the JPL [31]. The system allows 3D imaging with sub-centimeter resolution at a stand-off distance of 4 to 25 m with the acquisition time of a few minutes. In Fig. 1.10, we can see that the 3D image is easier to interpret than the usual 2D image.

Fig. 1.11: a): Threat need to be detected; b) and c): Detection by terahertz active imaging

A recent development includes the second-generation 0.67 THz imaging radar capable of imaging a person torso (50×50 cm) in 5 seconds, with 1 cm-scale resolution, at a standoff range of 25 m [32]. This represents an improvement in imaging speed and standoff range by factors of about 30 and 6, respectively.

This system is certainly suited for high-end applications where stand-off detection is needed. It is however also very complex and expensive. Adding a few pixels is complicated and multiplies the system costs.

1.2.4 Context of the PhD work: THz imaging with room-temperature bolometer array

Bolometer is one type of thermal sensors that detect electromagnetic radiation through a photo-induced variation of the device temperature. In a bolometer, the temperature variation is sensed by a thermo-resistor, i.e. the resistance value changes in function of temperature.

The bolometer studied in this work derives from the uncooled infrared bolometer, which is employed in passive imaging at mid-infrared range [8 – 14 μm]. Although the spectral response of the detector is optimized for mid-infrared range, the detector can detect terahertz wave, provided that the radiation intensity is high enough.

The sub-pW power range involved passive imaging is well beyond the sensitivity of the present state-of-the-art uncooled bolometer. For example, reference [33] reported that the commercial uncooled infrared bolometer requires a minimum power of 320 pW at 4.3 THz. The prototype of uncooled terahertz bolometer [34], [35] requires the minimum power in the range ~ 50 pW. Thus the passive imaging with uncooled bolometer is not realistic.

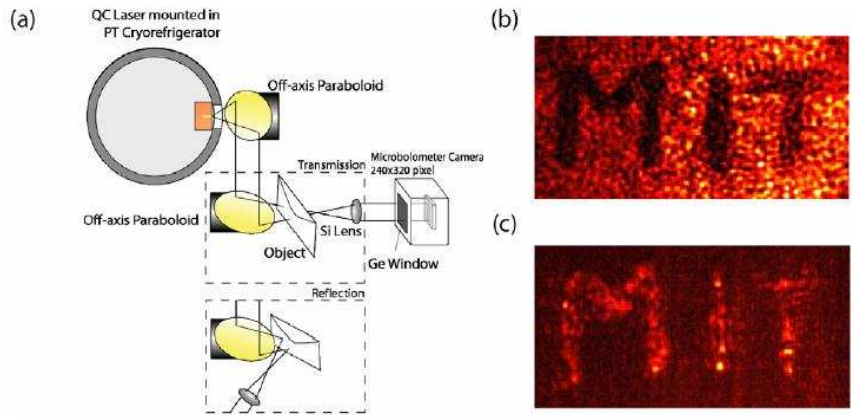

Fig. 1.12: Demonstration of terahertz imaging with uncooled bolometer [33]

The possibility of using bolometer as detector for active THz imaging was first demonstrated experimentally at MIT [36], [33]. In these works, QCL sources at 2.52 THz delivering 10 mW and at 4.3 THz (50 mW) have been employed. The detector is a commercial uncooled infrared bolometer for the mid-infrared range. The active THz imaging system can record video films at the rate of 20–60 frames/s with a signal to noise ratio in the range 13 ~ 25 dB.

The demonstration by the MIT group has encouraged many other institutes to develop uncooled THz bolometer based on the well-mastered infrared bolometer technology. These institutes include NEC from Japan [34] and CEA-Leti from France [37], [35]. The work presented in this PhD thesis is in the context of the development of uncooled THz bolometer at CEA-Leti.

The first part of the work was devoted to design, fabricate, and characterize a bolometer that has spectral response around ~3 THz. This work was performed in the framework of an active spectroscopy-imaging project named THEDEX. The project aims at two objectives:

- Active imaging for security screening: detection of concealed weapons, such as handgun or metallic knife,
- Spectroscopy: detection of explosives such as TNT, RDX, PETN.

The spectral range of the THEDEX bolometer sensitivity was choosen as 2 – 5 THz. This selection derives from the following reasons:

- Trade-off between imaging and spectroscopy: Although atmospheric transmission and transmission through clothing suggest that THz imaging should be performed at low frequency (f < 1 THz), this spectral range is less favorable for spectroscopic detection of explosives. Many common explosives TND, RDX, and PETN exhibit strong absorption lines over 1 THz [38], which facilitates the explosive identification in this range.
- Availability of high power source: the project makes use of QCL sources that can deliver a power in the mW range over 1.7 THz.
- Availability of detector: we have modified the design of the infrared bolometer to optimize their spectral response around ~3 THz. Presently, this technological optimization is easier than for the sub-THz range.
- High resolution: working at high frequency helps getting a good spatial resolution of the scene, which is important for interpreting the image.

However, the range 2 – 5 THz also undergoes many attenuation due to the propagation of THz wave though atmosphere and clothing. The whole frequency selection trade-off is

really challenging to characterize precisely each aspect. The development of the bolometer in a concrete project (THEDEX) helps us to evaluate the perspective of uncooled bolometers in THz imaging.

In the second part of my work, the knowledge and experience obtained from the development of the 3-THz bolometer will help us to optimize the design of a low frequency (sub-THz) bolometer, which is more adapted to imaging.

1.3 Summary

In the first section of this introductory chapter we gave a short historical overview of THz domain. THz science and technology has started from the niche spectroscopy and remote sensing application in astronomy and extends progressively to more general public application. Then THz spectrum is defined and some prominent properties of the THz radiation have been presented. They include: high transparency through dielectric material, good reflection on metal, high absorption in water, non-ionizing radiation. With its original features, the domain is very promising for plenty of application, such as imaging and sensing, communication, etc.

The general context of this PhD is terahertz imaging, which is one of the most attractive applications of THz waves. Principle of imaging has been presented, followed by the examination of some characteristic related to the THz domain. These characteristics are atmospheric attenuation and transmission through clothing. Some THz imaging systems in literature, both passive and active, were mentioned in order to demonstrate the perspective of THz imaging in real-life. Passive imaging requires highly sensitive detector. Such detectors generally make the imaging system quite complex and high-cost. Active imaging employs a combination between source and detector in which the detector performance can be less demanding by using a powerful source. Finally, we present the concrete context of this PhD, which is the development of uncooled bolometer for THz active imaging.

References

[1] A. J. Kerecman, “The Tungsten - P Type Silicon Point Contact Diode,” in Microwave Symposium, 1973 IEEE G-MTT International, 1973, pp. 30 –34.

[2] J. W. Fleming, “High-Resolution Submillimeter-Wave Fourier-Transform Spectrometry of Gases,” Microwave Theory and Techniques, IEEE Transactions on, vol. 22, no. 12, pp. 1023 – 1025, Dec. 1974.

[3] P. H. Siegel, “Terahertz technology,” Microwave Theory and Techniques, IEEE Transactions on, vol. 50, no. 3, pp. 910 –928, Mar. 2002.

[4] Y.-S. Lee, Principles of Terahertz Science and Technology. Springer, 2008.

[5] L. Yujiri, M. Shoucri, and P. Moffa, “Passive millimeter wave imaging,” Microwave Magazine, IEEE, vol. 4, no. 3, pp. 39 – 50, Sep. 2003.

[6] G. Chattopadhyay, “Technology, Capabilities, and Performance of Low Power Terahertz Sources,” Terahertz Science and Technology, IEEE Transactions on, vol. 1, no. 1, pp. 33 –53, Sep. 2011.

[7] J. R. Gao, J. N. Hovenier, Z. Q. Yang, J. J. A. Baselmans, A. Baryshev, M. Hajenius, T. M. Klapwijk, A. J. L. Adam, T. O. Klaassen, B. S. Williams, S. Kumar, Q. Hu, and J. L. Reno, “Terahertz heterodyne receiver based on a quantum cascade laser and a superconducting bolometer,” Applied Physics Letters, vol. 86, no. 24, pp. 244104–244104–3, Jun. 2005.

[8] M. Tonouchi, “Cutting-edge terahertz technology,” Nature Photonics, vol. 1, no. 2, pp. 97–105, Feb. 2007.

[9] W.-C. Kan, W.-S. Lee, W.-H. Cheung, V. P. Wallace, and E. Pickwell-MacPherson, “Terahertz pulsed imaging of knee cartilage,” Biomed. Opt. Express, vol. 1, no. 3, pp. 967–974, Oct. 2010.

[10] Z. D. Taylor, R. S. Singh, M. O. Culjat, J. Y. Suen, W. S. Grundfest, H. Lee, and E. R. Brown, “Reflective terahertz imaging of porcine skin burns,” Opt. Lett., vol. 33, no. 11, pp. 1258–1260, Jun. 2008.

[11] A. Hirata, T. Kosugi, H. Takahashi, R. Yamaguchi, F. Nakajima, T. Furuta, H. Ito, H. Sugahara, Y. Sato, and T. Nagatsuma, “120-GHz-band millimeter-wave photonic wireless link for 10-Gb/s data transmission,” Microwave Theory and Techniques, IEEE Transactions on, vol. 54, no. 5, pp. 1937 – 1944, May 2006.

[12] H.-J. Song, K. Ajito, Y. Muramoto, A. Wakatsuki, T. Nagatsuma, and N. Kukutsu, “24 Gbit/s data transmission in 300 GHz band for future terahertz communications,” Electronics Letters, vol. 48, no. 15, pp. 953 –954, 2012.

[13] R. Appleby and H. B. Wallace, “Standoff Detection of Weapons and Contraband in the 100 GHz to 1 THz Region,” Antennas and Propagation, IEEE Transactions on, vol. 55, no. 11, pp. 2944 –2956, Nov. 2007.

[14] F. Huang, B. Schulkin, H. Altan, J. F. Federici, D. Gary, R. Barat, D. Zimdars, M. Chen, and D. B. Tanner, “Terahertz study of 1,3,5-trinitro-s-triazine by time-domain and Fourier transform infrared spectroscopy,” Applied Physics Letters, vol. 85, no. 23, pp. 5535–5537, Dec. 2004.

[15] Y. C. Shen, T. Lo, P. F. Taday, B. E. Cole, W. R. Tribe, and M. C. Kemp, “Detection and identification of explosives using terahertz pulsed spectroscopic imaging,” Applied Physics Letters, vol. 86, no. 24, pp. 241116–241116–3, Jun. 2005.

[16] H.-B. Liu, Y. Chen, G. J. Bastiaans, and X.-C. Zhang, “Detection and identification of explosive RDX by THz diffuse reflection spectroscopy,” Opt. Express, vol. 14, no. 1, pp. 415–423, Jan. 2006.

[17] H.-B. Liu, H. Zhong, N. Karpowicz, Y. Chen, and X.-C. Zhang, “Terahertz Spectroscopy and Imaging for Defense and Security Applications,” Proceedings of the IEEE, vol. 95, no. 8, pp. 1514 –1527, Aug. 2007.

[18] H. Zhong, J. Xu, X. Xie, T. Yuan, R. Reightler, E. Madaras, and X.-C. Zhang, “Nondestructive defect identification with terahertz time-of-flight tomography,” Sensors Journal, IEEE, vol. 5, no. 2, pp. 203 – 208, Apr. 2005.

[19] M. Yamashita, C. Otani, T. Matsumoto, Y. Midoh, K. Miura, K. Nakamae, K. Nikawa, S. Kim, H. Murakami, and M. Tonouchi, “THz emission characteristics from p/n junctions with metal lines under non-bias conditions for LSI failure analysis,” Opt. Express, vol. 19, no. 11, pp. 10864–10873, May 2011.

[20] J.-P. Caumes, A. Younus, S. Salort, B. Chassagne, B. Recur, A. Zi□gl□, A. Dautant, and E. Abraham, “Terahertz tomographic imaging of XVIIIth Dynasty Egyptian sealed pottery,” Appl. Opt., vol. 50, no. 20, pp. 3604–3608, Jul. 2011.

[21] I. Hosako, N. Sekine, M. Patrashin, S. Saito, K. Fukunaga, Y. Kasai, P. Baron, T. Seta, J. Mendrok, S. Ochiai, and H. Yasuda, “At the Dawn of a New Era in Terahertz Technology,” Proceedings of the IEEE, vol. 95, no. 8, pp. 1611 –1623, Aug. 2007.

[22] K. Fukunaga, I. Hosako, Y. Ogawa, and S. Hayashi, “THz spectroscopy for art conservation science,” in Infrared and Millimeter Waves, 2007 and the 2007 15th International Conference on Terahertz Electronics. IRMMW-THz. Joint 32nd International Conference on, 2007, pp. 678 –679.

[23] Committee on Assessment of Security Technologies for Transportation, National Research Council, Assessment of Millimeter-Wave and Terahertz Technology for Detection and Identification of Concealed Explosives and Weapons. Washington, D.C.: The National Academies Press, 2007.

[24] Y. Yang, A. Shutler, and D. Grischkowsky, “Measurement of the transmission of the atmosphere from 0.2 to 2 THz,” Opt Express, vol. 19, no. 9, pp. 8830–8838, Apr. 2011.

[25] J. E. Bjarnason, T. L. J. Chan, A. W. M. Lee, M. A. Celis, and E. R. Brown, “Millimeter-wave, terahertz, and mid-infrared transmission through common clothing,” Applied Physics Letters, vol. 85, no. 4, pp. 519–521, Jul. 2004.

[26] P. W. Kruse, Uncooled Infrared Imaging Arrays and Systems. Academic Press, 1997.

[27] E. N. Grossman, C. R. Dietlein, M. Leivo, A. Rautiainen, and A. Luukanen, “Multispectral terahertz camera,” in Electromagnetics in Advanced Applications, 2009. *ICEAA ’09. International Conference on*, 2009, pp. 1002 –1005.

[28] A. Luukanen, M. Gronholm, P. Lappalainen, M. Leivo, A. Rautiainen, A. Tamminen, J. Ala-Laurinaho, A. Raisanen, C. R. Dietlein, and E. N. Grossman, “Passive real-time submillimetre-wave imaging system utilizing antenna-coupled microbolometers for stand-off security screening applications,” in Antenna Technology (iWAT), 2010 International Workshop on, 2010, pp. 1 –4.

[29] E. N. Grossman, C. R. Dietlein, M. Leivo, A. Rautiainen, and A. Luukanen, "A passive, real-time, terahertz camera for security screening, using superconducting microbolometers," in Microwave Symposium Digest, 2009. MTT *'09. IEEE MTT*-S International, 2009, pp. 1453 –1456.

[30] E. Heinz, T. May, D. Born, G. Zieger, G. Thorwirth, S. Anders, V. Zakosarenko, T. Krause, A. Krüger, M. Schulz, H.-G. Meyer, M. Schubert, and M. Starkloff, "Toward high-sensitivity and high-resolution submillimeter-wave video imaging," Opt. Eng, vol. 50, no. 11, pp. 113204–113204, Nov. 2011.

[31] K. B. Cooper, R. J. Dengler, N. Llombart, T. Bryllert, G. Chattopadhyay, E. Schlecht, J. Gill, C. Lee, A. Skalare, I. Mehdi, and P. H. Siegel, "Penetrating 3-D Imaging at 4- and 25-m Range Using a Submillimeter-Wave Radar," Microwave Theory and Techniques, IEEE Transactions on, vol. 56, no. 12, pp. 2771 –2778, Dec. 2008.

[32] K. B. Cooper, R. J. Dengler, N. Llombart, A. Talukder, A. V. Panangadan, C. S. Peay, I. Mehdi, and P. H. Siegel, "Fast high-resolution terahertz radar imaging at 25 meters," 2010, p. 76710Y–76710Y–8.

[33] A. Lee, S. Kumar, B. S. Williams, Q. Hu, and J. L. Reno, "Real-time imaging using a 4.3-THz quantum cascade laser and a 240x320 element focal-plane array," in Lasers and Electro-Optics, 2006 and 2006 Quantum Electronics and Laser Science Conference. CLEO/QELS 2006. Conference on, 2006, pp. 1 –2.

[34] N. Oda, "Uncooled bolometer-type Terahertz focal plane array and camera for real-time imaging," Comptes Rendus Physique, vol. 11, no. 7–8, pp. 496–509, Aug. 2010.

[35] J. Meilhan, B. Dupont, V. Goudon, G. Lasfargues, J. Lalanne Dera, D. T. Nguyen, J. L. Ouvrier-Buffet, S. Pocas, T. Maillou, O. Cathabard, S. Barbieri, and F. Simoens, "Active THz imaging and explosive detection with uncooled antenna-coupled microbolometer arrays," Proceedings of SPIE, vol. 8023, no. 1, p. 80230E–80230E–13, May 2011.

[36] A. W. Lee and Q. Hu, "Real-time, continuous-wave terahertz imaging by use of a microbolometer focal-plane array," Opt. Lett., vol. 30, no. 19, pp. 2563–2565, Oct. 2005.

[37] F. Simoens, T. Durand, J. Meilhan, P. Gellie, W. Maineult, C. Sirtori, S. Barbieri, H. Beere, and D. Ritchie, "Terahertz imaging with a quantum cascade laser and amorphous-silicon microbolometer array," 2009, p. 74850M–74850M–10.

[38] M. Leahy-Hoppa, M. Fitch, and R. Osiander, "Terahertz spectroscopy techniques for explosives detection," Analytical and Bioanalytical Chemistry, vol. 395, no. 2, pp. 247–257, 2009.

Chapter 2 Bolometric detectors

The basic principle of bolometers is presented in this chapter. A very simple model gives the key factors that determine the performance of a bolometric detector without going too far into the details that the reader can find in cited references.

2.1 Principle of bolometer

2.1.1 Bolometer overview

Bolometer is one type of thermal sensor that detects electromagnetic radiation through a photo-induced variation of the device temperature. In a bolometer (here we use this term to speak about a resistive bolometer), the temperature of the device is sensed by a thermo-resistor, i.e. the resistance value changes in function of temperature.

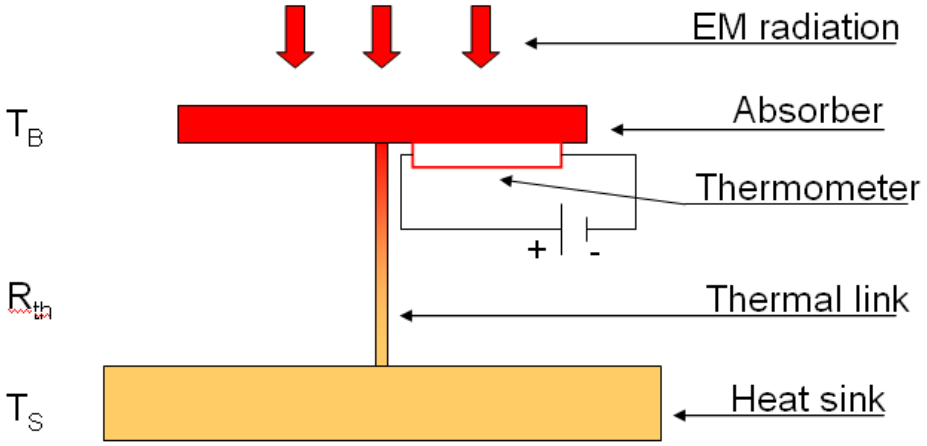

Fig. 2.1: Bolometer principle

The general structure of a bolometer consists of a sensitive element connected to a heat sink by a thermal link. The sensitive element itself combines two important elements that are an absorber to collect the incident radiation or particles striking the sensor and a temperature transducer (thermometer). The thermal link prevents heat losses but also provides its mechanical support and electrical contacts between the bolometer and the read-out circuit in an actual bolometer.

The thermometer converts the resulting temperature variation into parameters that are measured electrically by the read-out circuit. So as illustrated by Fig. 2.1, thermal sensors detection makes use of cascaded functions: electro-magnetic absorber, thermometer, thermal link and read-out circuit. Some functions can be ensured by a common device. There is a case where thermometer also plays the role of absorber. However, in order to optimize absorption efficiency of detector and its electrical characteristics, the absorber is generally a separate element.

Like many other thermal detectors, bolometers are incoherent sensors, meaning they detect only the radiation intensity, not its phase. On the other side, since the thermal conversion is independent to the spectrum of the incident wave, bolometers can be very broadband detectors. Their bandwidth is in fact limited by the spectral response of the absorber. Some superconducting bolometers, such as HEBs, can perform heterodyne

detection: the incident wave beats with a local oscillation wave to produce an intermediate frequency signal. In this case, the phase of a coherent impinging radiation can be measured.

Another characteristic should be mentioned: the bolometers invoke a thermal phenomenon which is a slow process (when compared with electric process), therefore bolometers are slow detectors. The fastest response time of bolometers is in the range of nanosecond, which is the case of HEBs.

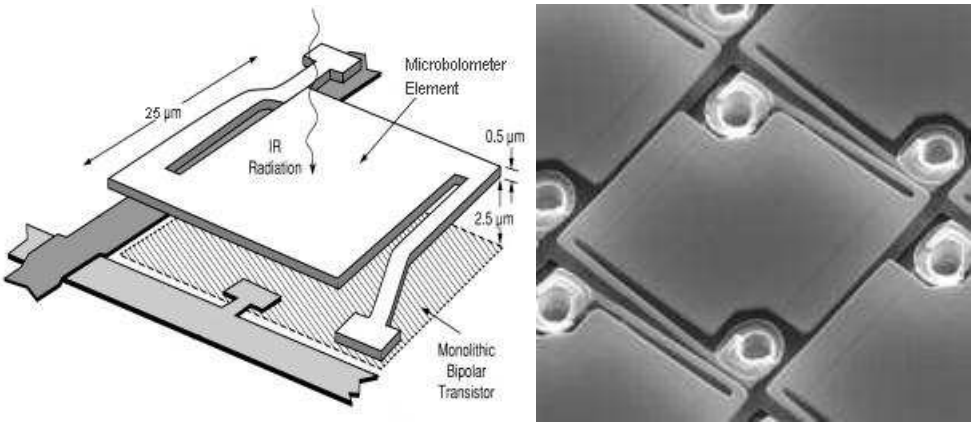

Fig. 2.2: Example of bolometer

The material of the thermometric element plays a key role in determining the performance of bolometers. This material should give a large temperature dependence of resistivity while keeping the noise, especially excess noise, as low as possible. The parameter used to quantify the dependence of bolometer resistance on temperature is the temperature coefficient of resistance (TCR), defined as:

$$\alpha = \frac{1}{R}\frac{dR}{dT}. \qquad \textbf{(2.1)}$$

Metals show little change in free-carrier density with temperature, but the mobility of the free carriers decreases with temperature, producing a positive α, typically about +0.002 K^{-1}. This value usually varies weakly with temperature. Meanwhile, semiconductor materials have mobile carrier densities that increase with increasing temperature, also their carrier mobilities change with temperature, producing a higher negative α that is generally temperature-dependent. A typical $R(T)$ behavior for a semiconductor, whose mobile carrier density is controlled by thermal excitation across a bandgap, is:

$$R(T) = R_0 \exp\left(\frac{\Delta E}{kT}\right) \qquad \textbf{(2.2)}$$

where ΔE is the activation energy, equal to half the bandgap E_g, and R_0 is a reference resistance, k is the Boltzmann constant. This dependence of the resistance of semiconductor on temperature leads to the value of TCR:

$$\alpha = \frac{1}{R}\frac{dR}{dT} = -\frac{\Delta E}{kT^2}. \qquad \textbf{(2.3)}$$

For amorphous silicon material, this value is about -0.02 K^{-1} at $T = 300\,K$.

2.1.2 Electro-thermal model

The operation of bolometer is based on an electro-thermal model that has been well formulated in some text books. The model presented here is derived from [Kruse]. We simplify it to treat the case of the bolometers studied in this PhD work. In order to establish this electro-thermal model for bolometer, some phenomena are simplified. We will consider the whole suspended structure (which consists of several layers, such as absorber or thermometer) as a single element with a homogeneous temperature.

As depicted in Fig. 2.1, the main physical parameters are:

- η is absorption efficiency of the bolometer,
- T and C_{th} are respectively the temperature and the thermal capacity of the suspended element,
- g is the thermal conductance between the suspended element and the heat sink,
- T_S is the temperature of the heat sink, it could be constant or at least varies very slowly when compared to T.
- (I, V) is the current and voltage of the external circuit that biases the thermometer.

The microbolometer's temperature T depends on the energy exchange with its heat sink at temperature T_S, on the IR radiation power; and on the power P_{bias} produced by the bias current through Joule effect in the thermometer. The heat balance equation for a microbolometer at temperature T is

$$C_{th}\frac{dT}{dt} = IV + Q - g(T - T_S). \qquad \textbf{(2.4)}$$

Q is the net absorbed radiation power from the radiative energy exchange between the suspended element and its surrounding. In general, Q can be expressed as

$$Q = \eta P_t + \eta P_S - 2A\eta\sigma T^4. \qquad \textbf{(2.5)}$$

P_t and P_S are the radiation powers from the target (the scene) and the heat sink, respectively. The last term is Stefan law contribution in which we have modeled the suspended element as a grey body of surface A and a constant emissivity $\varepsilon = \eta$ (Kirchhoff law of thermal radiation). In equation 2.4, we see that the Joule power and the net absorbed radiation power help increasing the temperature of the suspended element. However, the energy loss by thermal conduction between this suspended element and the heat sink tends to balance this temperature increasing. By solving the heat equation 2.4, we can understand better the way the bolometer interacts with the surrounding (heat sink in particular) (1) and the bias supply (2).

2.1.2.1 Heat balance with no applied bias

Without the Joule power, the heat equation is rewritten:

$$C_{th}\frac{dT}{dt} = Q - g(T - T_S). \qquad \textbf{(2.6)}$$

In the simple case Q is step function, the solution of the above equation is:

$$T(t) = T_S + \frac{Q}{g}(1 - e^{-t/\tau_{th}}) \quad \textbf{(2.7)}$$

with $\tau_{th} = C_{th}/g$ is the thermal time constant. As, for $t < 0$, Q is zero, then the thermal conduction makes the suspended element having the same temperature as the heat sink. For $t \geq 0$, by absorbing the radiation power Q, the temperature of bolometer increases exponentially. After a period of much longer τ, the bolometer temperature approaches the steady-state value

$$T(t >> \tau_{th}) = T_S + \frac{Q}{g}. \quad \textbf{(2.8)}$$

From this equation, we also see that a small change in the absorbed radiation power induces a change in temperature

$$\delta T = \frac{\delta Q}{g}. \quad \textbf{(2.9)}$$

With the same amount of absorbed radiation power, a smaller thermal conductance g leads to a larger temperature elevation.

If the radiation power Q is not a constant but an alternative signal (by using a chopper to modulate the incident beam, for example) $Q = Q_0(1 + e^{j\omega t})$, then the temperature T is also modulated at frequency ω:

$$\Delta T(\omega) = \frac{Q_0 e^{j\omega t}}{g(1 + j\omega\tau_{th})}. \quad \textbf{(2.10)}$$

The amplitude of this signal therefore varies as $1/\sqrt{1 + \omega^2\tau_{th}^2}$, and its 3 dB cut-off frequency is $f_c = 1/2\pi\tau_{th}$. For example, if τ_{th} = 10 ms, then $f_c = 1/2\pi\tau_{th} \approx 16$ Hz is the cut-off frequency of the bolometer, meaning if the optical beam is modulated at much higher frequency than 16 Hz, the temperature variation is degraded a lot due to the slow thermal relaxation of the suspended element.

2.1.2.2 Heat balance with applied bias

In order to convert the variation of bolometer temperature into an electric signal, we must apply a bias to the bolometer. For bolometer of positive TCR, usually a constant current bias is applied and for bolometer of negative TCR (semiconductor), a constant voltage bias takes place. The main reason is to enhance the sensitivity of bolometer by making use of the electrothermal effect that will be presented in the following section. We focus on the case of semiconductor bolometer biased by constant voltage, which is the one being studied in this thesis.

The biased bolometer is heated by a total power $W = Q + P = Q + IV$, where Q is the net absorbed radiation power and $P = IV$ is the Joule power from the applied bias. Normally, $P >> Q$, so that W may be replaced by P whenever the differentiation of W is not involved. When bolometer absorbs the radiation power dQ, the heat changes its temperature,

causing a change in the bolometer resistance. If no bias is applied, the temperature elevation should be $dT = dQ/g$ as expected from equation 2.9. However, when a bias is applied, the Joule power $P = \frac{V^2}{R}$ is changed due to the variation of the bolometer resistance. The heat from this power will play the role of feedback and affects the bolometer temperature. This results in a different net temperature change from the previous value in equation 2.9. The phenomenon is stated as electrothermal effect.

To quantify the electrothermal effect, we use the circuit (Fig. 2.3) in which the voltage bias source V_b is applied to the bolometer. It should be noted that since the Joule power of the bias modifies the bolometer temperature and changes its resistance value, therefore the I-V characteristic of bolometer is not a straight line, but a curve as shown in Fig. 2.3. The operating point of the bolometer (V, I) is given by the intersection of the load line $V = V_b$ with the bolometer V-I curve. We can see that at the same constant bias voltage V_b, as the radiation power $Q + dQ$ makes the bolometer hotter (than radiation power Q), the resistance of bolometer decreases, thus the current circulating through bolometer increases by an amount dI.

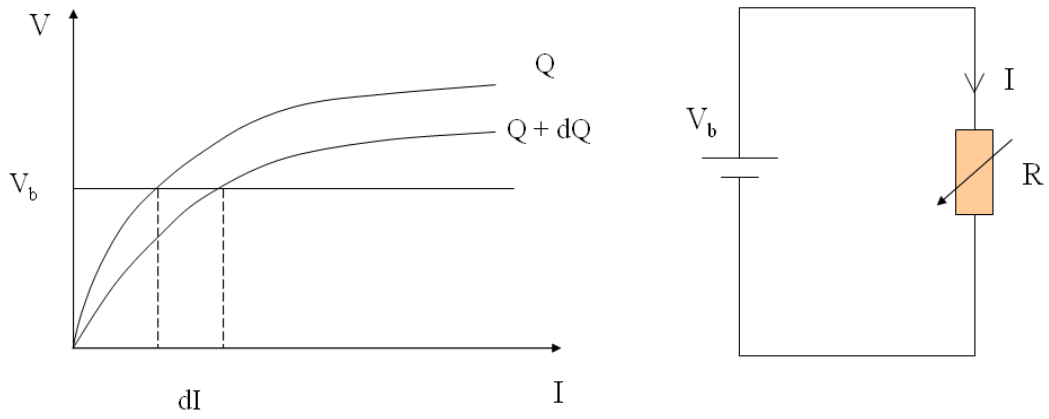

Fig. 2.3: I-V characteristic of bolometer under constant voltage bias

The responsivity of bolometer is a key factor that characterizes its performance. It is defined as

$$\Re_I = \frac{dI}{dQ}. \qquad \textbf{(2.11)}$$

We will formulate this expression to see how the characteristics of bolometer affect its responsivity. First, we develop dI as function of R

$$dI = d\left(\frac{V_b}{R}\right) = -\frac{V_b}{R^2}dR. \qquad \textbf{(2.12)}$$

Then, we rewrite the heat balance equation 2.4 under steady state condition

$$C_{th}\frac{dT}{dt} = IV_b + Q - g(T - T_S) = 0. \quad \textbf{(2.13)}$$

We deduce:

$$Q = -IV_b + g(T - T_S) = -\frac{V_b^2}{R} + gT - gT_S. \quad \textbf{(2.14)}$$

Thus:

$$dQ = \frac{V_b^2}{R^2}dR + gdT. \quad \textbf{(2.15)}$$

From equations 2.12 and 2.15, we obtain:

$$\Re_I = \frac{dI}{dQ} = \frac{-\frac{V_b}{R^2}dR}{\frac{V_b^2}{R^2}dR + gdT} = \frac{\frac{-V_b}{R}\frac{dR}{RdT}}{\frac{V_b^2}{R}\frac{dR}{RdT} + g} = \frac{\frac{-V_b}{R}\alpha}{\frac{V_b^2}{R}\alpha + g} = \frac{-I\alpha}{g + IV_b\alpha} = \frac{-I\alpha}{g_{eff}} \quad \textbf{(2.16)}$$

where:

$$g_{eff} = g + IV_b\alpha. \quad \textbf{(2.17)}$$

In the case of semiconductor, the TCR is negative, so the responsivity is written as

$$\Re_I = \frac{I|\alpha|}{g_{eff}}. \quad \textbf{(2.18)}$$

In equation 2.14, as we have mentioned earlier, the radiation power term Q is usually negligible when compared to the Joule power IV_b supplied by the bias source, so the temperature elevation $\Delta T = T - T_S$ is in fact mostly caused by the Joule power, i.e.:

$$IV_b \approx g(T - T_S) = g\Delta T. \quad \textbf{(2.19)}$$

Then equation 2.17 can be approximated as:

$$g_{eff} = g + IV_b\alpha \approx g(1 + \alpha\Delta T). \quad \textbf{(2.20)}$$

Since the thermal capacity of bolometer is unchanged by the applied bias, the effective g value results in an “effective” thermal time constant for changes in Q, given by:

$$\tau_{eff} = C_{th}/g_{eff} \approx \tau\frac{1}{(1 + \alpha\Delta T)}. \quad \textbf{(2.21)}$$

In the case of semiconductor bolometers, since α is negative value, $g_{eff} < g$ and $\tau_{eff} > \tau$. This means that due to the electrothermal effect, the responsivity of bolometer increases but

the detector responses more slowly. While increasing the bolometer responsivity and thus its sensitivity, the electrothermal effect also presents a risk of operation instability. In Fig. 2.3, each I-V curve of a bolometer, corresponding to a given absorbed radiation power, has a limit V_{lim} at which the current passing the bolometer increases to infinite. Of course, in reality, the heat produced by this current will damage the detector when the current is high enough. Let us consider the case we bias the bolometer near this value V_{lim} (I-V curve corresponding to Q). If this bias voltage is higher than the V_{lim} value of the I-V curve corresponding to $Q + dQ$, the thermal runaway will destroy the bolometer.

In equation 2.16, we see that the bolometer responsivity is proportional to both the current passing bolometer and its TCR. The current can be augmented by increasing the bias voltage. The bias voltage is usually limited by a practical reason: monolithic read-out electronics may reach a maximum voltage (about 2 V for today CMOS). This value is several times larger than the V_{lim} of bolometer at room temperature. However, at higher bias voltage, the excess noise (that proportional to the applied voltage) increases and dominates other noise sources. Therefore the sensitivity has an optimum point regarding the bias voltage.

In order to enhance the bolometer responsivity without having risk of instability, most CMOS read-out circuit use today pulsed voltage bias. The maximum voltage 2 V delivers a maximum current to the bolometer in a time short enough to ensure that the damage by heating does not happen.

2.1.3 Noise in bolometers

Various types of noise may contribute to the total noise, degrading the bolometer performance, in particular the sensitivity. The total noise includes the noise generated by the read-out circuit, which contains a stage of amplification. For the up-to-date uncooled semiconductor bolometer technology, if the read-out integrated circuit (ROIC) of bolometer is properly designed, the contribution of ROIC noise is small when compared to the noise generated by the bolometer. In this section, we only consider the noise of bolometer, not the ROIC.

Since the bolometer operation is based on the conversion from radiation into thermal energy and then into an electric signal, the noise in the detector originates from all these sources. The contribution of each type of noise in superconductor bolometers is different from the uncooled bolometers, mostly because of the difference in the operation temperature. The noise that can affect the sensitivity of uncooled bolometer usually is the electronic noise, in particular the Johnson noise and the 1/f noise.

2.1.3.1 Johnson noise

This noise originates from the fluctuation of voltage across the terminal of a resistance R at temperature T due to the thermal agitation of the charge carriers that move forward but also backward. The power spectral density of this noise is independent of frequency for frequencies $f << kT/h$, which is much greater than the bandwidth of detector. Therefore, this electrical noise can be considered as a "white" noise in the modeling. For a given bandwidth, this noise is quantified by the fluctuation in voltage V from the average value $\overline{V}$ (variance) per Hertz of bandwidth as:

$$\overline{\Delta V^2} = \overline{(V - \overline{V})^2} = 4k_B TR. \qquad \textbf{(2.22)}$$

As an example, a 1-KΩ resistor at room temperature of 300 K has a root mean square (rms) Johnson noise of 4 nV/√Hz. This noise exists even at zero bias but can be decreased dramatically by cryogenic cooling (in the case of superconductor bolometer for example). In terms of current, the Johnson noise is given by:

$$\overline{\Delta I^2} = \frac{4k_B T}{R}. \qquad \textbf{(2.23)}$$

2.1.3.2 1/f noise

The thermometer of a bolometer usually shows some degree of fluctuation in resistance, with a variance $\overline{\Delta R^2}$. If a bias I flows through the resistor, this resistance fluctuation produces a voltage noise $I\sqrt{\overline{\Delta R^2}}$ in addition to the Johnson noise. This noise is referred as the excess noise. The 1/f noise is one type of excess noise and has a power per unit bandwidth that varies approximately as 1/f (there comes the term 1/f noise). The 1/f noise appears in all thin-film components and seems resulting from the imperfections in the resistor material structure and electrical contacts. Despite many researches in the domain, there is no theory that explains completely this phenomenon. In a general manner, the resistance fluctuation results from the fluctuation of electrical conductivity of material, which depends on the free carrier density and on the mobility of these carriers. The carrier density and mobility are then two factors that appear to characterize the 1/f noise. The power spectral density of 1/f noise in bolometer is usually:

$$\overline{\Delta V^2} = V^2 \frac{k_f}{f}. \qquad \textbf{(2.24)}$$

Where k_f is called the 1/f noise parameter. This parameter depends strongly on each particular resistor, i.e. on its material, deposition technique, dimensions, and electrical contacts, etc., and can be expressed as:

$$k_f = \alpha_H / nV_{volume}. \qquad \textbf{(2.25)}$$

where n is the mobile charge carrier density and V_{volume} is the volume of the resistor material. In terms of current, the 1/f noise is:

$$\overline{\Delta I^2} = I^2 \frac{k_f}{f}. \qquad \textbf{(2.26)}$$

It should be noted that the above formula, established by Hooge [2], is the accepted model to characterize the 1/f noise of a resistor. It does not, however, explain completely the origin of the 1/f noise.

The 1/f noise is quite common for electronic devices, not only for bolometers. Its influence can be reduced a lot by performing a lock-in measurement. This technique is quite useful for characterizing a single bolometer but it is really challenging for a 2D array of detectors equipped with multiplexing scheme in ROIC. The 1/f noise plays an important role in the design of bolometer itself (material, technique of deposition, electrical contact), and also in the operation of read-out circuit since this noise depends on the bias level.

2.1.3.3 Other sources of noise

Thermal noise

Thermal noise -or phonon noise- arises from the random exchange of energy between the bolometer and the heat sink. The temperature of bolometer (the suspended element) in thermal equilibrium has a fluctuation that depends on temperature itself and the capacity of the element

$$\overline{\Delta T^2} = k_B T^2 / C_{th} . \quad \textbf{(2.27)}$$

Also the thermal conductance g of the arm between suspended element and heat sink exhibits some fluctuation due to the thermal aspect. The temperature of heat sink is stabilized by an external thermal regulator to minimize the temperature variation that could add more noise to the bolometer. The thermal noise is intrinsic and can be decreased by cooling. In practice, this noise is negligible when compared to electronic noise of the resistance of bolometer.

Radiation noise

Photons radiated from the detector and those impinging on it also carry energy. Radiative exchange of energy takes place with the environment of the detector, e.g. the walls of the enclosure. The fluctuation in this radiative exchange gives a noise, but this noise source can be decreased if the surroundings of the detector are sufficiently cooled. In the case of superconductor bolometer, in particular SIS bolometer, the sensitivity of the detector is limited by this noise which is fundamental and is a theorical limit (background limited or BLIP) in quantum physics. In the case of uncooled bolometers, this noise is usually negligible.

2.1.3.4 Calculation of total noise of bolometer

For uncooled bolometers, the electrical noise of the resistance of bolometer dominates and is characterized by the sum of Johnson noise and the 1/f noise. In a measurement bandwidth extending from frequency f_1 to f_2 , these two noises combine to produce a total bolometer voltage noise (mean square value):

$$\overline{\Delta V^2} = 4k_B TR(f_2 - f_1) + V^2 k_f \ln(f_2 / f_1) . \quad \textbf{(2.28)}$$

In terms of current, the noise writes:

$$\overline{\Delta I^2} = \frac{4k_B T}{R}(f_2 - f_1) + I^2 k_f \ln(f_2 / f_1) . \quad \textbf{(2.29)}$$

Usually, for a bolometer equipped with ROIC, the detector is biased in pulse mode during a time Δt_{int} and the bolometer signal (current) is integrated during this period. Therefore the upper frequency f_2 is

$$f_2 = \frac{1}{2\Delta t_{int}} . \quad \textbf{(2.30)}$$

The lower limit f_1 is related to the frame rate of the camera, therefore the staring time T_{stare} by the relation:

$$f_1 \approx \frac{1}{4T_{stare}}. \quad \textbf{(2.31)}$$

In practice, a frequency of 1 Hz usually is chosen.

2.1.4 Figures of merit

Bolometers are widely used in different domains of applications (X-ray, infrared, millimeter-wave) in both passive and active imagings. Several figures of merit are used to characterize the performances of detector, in terms of spectral response, sensitivity, and response time.

2.1.4.1 Spectral response

The bolometer opearation is based on the conversion radiation energy → thermal energy → electrical signal. The spectral response of bolometer depends only on the conversion from incident radiation energy to thermal energy in absorber. In the case of uncooled infrared bolometers, the absorber is usually a thin film of metal. Since electrons in metal do not have prohibited band as the case of semiconductor, the interaction between the electrons in the absorber and the incident radiation can extend up to plasma frequency. Thus, the absortion efficiency of the detector depends mainly in the 3D electromagnetic design. Below is the typical spectral absorption of an uncooled bolometer working in the 8-14 μm range. As we can see, the spectral response of a typical bolometer is very large. In general, thermal detectors are always classified as large band detectors.

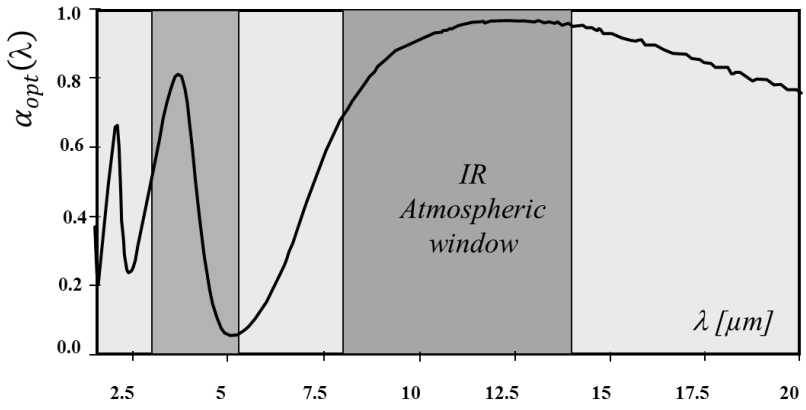

Fig. 2.4: Typical spectral response of uncooled mid-infrared bolometer

The absorption efficiency of this detector at long wavelength range (beyond the limit 20 μm of the above figure) decreases since the 3D electromagnetic design is not optimum. However, there is no strict limit in the absorption: the absorption can be low but the detector can still absorb the electromagnetic wave. Some institutes have successfully demonstrated the detection of long wavelength (f = 3 THz, λ = 100 μm) [3], [4] by uncooled bolometers.

The absorption efficiency is very challenging to evaluate, even by simulation. Therefore, the responsivity as a function of wavelength is used instead to characterize the spectral aspect of the detector response.

2.1.4.2 Sensitivity

The sensitivity relates directly to the noise level of the detector. Noise equivalent power (NEP) and noise equivalent temperature difference (NETD) are two common parameters that quantify the sensitivity of bolometers.

Noise equivalent power (NEP)

NEP is defined as the incident or absorbed power change that produces a signal equal to the total root mean square noise. The NEP defined with incident power change contains the absorption efficiency and characterizes the sensitivity of detector in a practical manner, therefore usually employed to compare detectors. The NEP is expressed in terms of the noise i_n and responsivity $\Re_I$ (or: v_n and $\Re_V$ for voltage noise and signal)

$$NEP = \frac{i_n}{\Re_I} = \frac{v_n}{\Re_V}. \qquad \textbf{(2.32)}$$

The NEP of a bolometer, in which the dominant noise sources are the Johnson and 1/f noises, is deduced from equations 2.18 and 2.29:

$$NEP = \frac{i_n}{\Re_I} = \frac{\sqrt{\frac{4k_B T}{R}(f_2 - f_1) + I^2 k_f \ln(f_2/f_1)}}{\frac{I|\alpha|}{g_{eff}}}. \qquad \textbf{(2.33)}$$

Since the read-out scheme is different for each read-out circuit, the NEP per unit bandwidth is used instead of NEP to represent better the sensitivity of the detector itself, without the influence of the read-out circuit. The NEP per unit bandwidth is simply the NEP divided by square root of bandwidth of the read-out circuit.

Noise equivalent temperature difference (NETD)

One useful and practical parameter to evaluate the sensitivity of a bolometer in passive imaging is NETD, defined as the temperature change at the target that produces a signal in the bolometer equal to the total (rms) noise. The relation between NETD and NEP therefore depends on how a temperature change at the target results a radiation power arriving on the bolometer:

$$NEP = \frac{dQ}{dT_{target}} NETD. \qquad \textbf{(2.34)}$$

Assuming that a bolometer has a front area A and absorption efficiency η, the radiation power Q absorbed by the bolometer due to a distant blackbody target with radiance L is

$$Q = \frac{A\eta\pi}{4F_{no}^2} L \qquad \textbf{(2.35)}$$

where F_{no} is the F-number of the optics. Therefore, the NETD is:

$$NETD = \frac{4F_{no}^{2}}{A\eta\pi(dL/dT_{target})} NEP \quad \textbf{(2.36)}$$

NETD is one of the most important performance parameters for infrared imaging systems because it specifies the performance of a detector in a very simple manner regarding the requirement of application. This parameter is directly characterized by exposing the bolometer in front of a blackbody source and varying its temperature. The NETD of state-of-the-art uncooled bolometers is about 50 – 100 mK.

2.1.4.3 Response time

Without the electrothermal effect, the response time of a bolometer depends only on the thermal capacity C_{th} and the thermal conductance g :

$$\tau_{th} = \frac{C_{th}}{g} \quad \textbf{(2.37)}$$

A typical uncooled 35-µm-pitch bolometer with a thermal capacity of 250 – 300 nJ/K, and a thermal conductance of 25 nW/K, presents a response time of 10 ms. This typical response time of thermal detector is of course very low when compared to photo diodes, but still fast enough to perform real-time rate video. The electrothermal effect can modify a little bit the response time as shown in equation 2.21.

2.2 Summary

In this chapter, the principle of uncooled bolometer is presented. We have introduced the structure of an uncooled bolometer, starting by a schematic structure of any kind of bolometer whether cooled or not, followed by the actual structure of an uncooled bolometer today. Then, the electric-thermal modeling of the bolometer is presented, providing a basic formulation about operation of bolometers. Different types of noise are mentioned, concentrating on Johnson noise and 1/f noise. Finally, some important figures of merit of detector are given. These bolometer parameters will be used in the next chapters.

References

[1] P. W. Kruse, Uncooled Infrared Imaging Arrays and Systems. Academic Press, 1997.

[2] F. N. Hooge, “Discussion of recent experiments on $1/f$ noise,” Physica, vol. 60, no. 1, pp. 130–144, Jul. 1972.

[3] A. W. M. Lee, B. S. Williams, S. Kumar, Q. Hu, and J. L. Reno, “Real-time imaging using a 4.3-THz quantum cascade laser and a 320 x 240 microbolometer focal-plane array,” IEEE Photonics Technology Letters, vol. 18, no. 13, pp. 1415 –1417, Jul. 2006.

[4] F. Simoens, T. Durand, J. Meilhan, P. Gellie, W. Maineult, C. Sirtori, S. Barbieri, H. Beere, and D. Ritchie, “Terahertz imaging with a quantum cascade laser and amorphous-silicon microbolometer array,” 2009, p. 74850M–74850M–10.

Chapter 3 IR-THz transformation for uncooled bolometer

The aim of this chapter is to present the necessary changes in the uncooled bolometer design to go from the infrared (IR) commercial device to the new THz prototype that is studied in this PhD thesis. In the first section, different designs of cryogenic millimeter-wave bolometers are examined. Of course, the structure of these detectors is specific for cryogenic operation. However, the study of these "historical" detector structures gives us some guidelines in designing our own bolometer. The second section is devoted to present in details the uncooled IR bolometer produced by CEA-Leti. This detector is the starting point for the development of uncooled THz bolometer, which is the subject of this thesis. In the last section, we present the present tendency, as published in the literature, of transformation of IR bolometer to obtain THz bolometers. The design of these "THz bolometers" is examined carefully in order to get a better solution for our own bolometer design, which will be presented in the next chapters.

3.1 Cryogenic terahertz bolometer

3.1.1 Antenna-coupled bolometer

The bolometer developed simultaneously at NIST-Boulder and at VTT-Helsinki by Grossman and Luukanen [1], [2], is a typical example showing the advantage of coupling the incident signal to the bolometer with an antenna. The device operates at 4.2 K and shows an amplifier-limited electrical NEP of 1.4×10^{-14} W/√Hz. In antenna-coupled devices, the thermal sensing element can be made much smaller than the detected wavelength, resulting in a much smaller heat capacity C_{th}, thus allowing for smaller thermal conductance g and better NEP, and also for a smaller time constant τ_{th}.

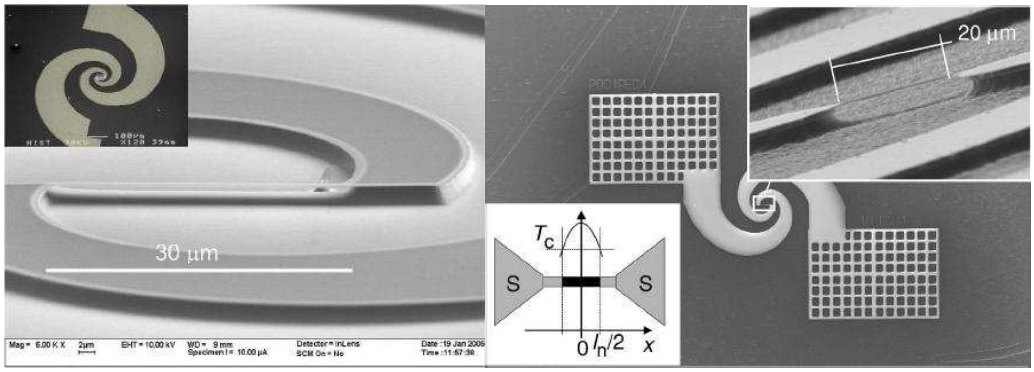

Fig. 3.1: Structure of a superconducting antenna-coupled bolometer

In this design, the sensitive element has the form of a long strip made of superconducting material and plays also the role of resistive load for the antenna made of normal metal. The strip has dimensions of 20 μm × 1 μm × 100 nm in a form of a microbridge structure, obtained by etching the underneath substrate. The antenna is logarithmic spiral-type with a dimension of inter and outer radii of the spiral of 200 and 20 μm, respectively. The antenna is deposited on a silicon substrate, which has a permittivity of $\varepsilon_r = 11.7$. With this configuration, the antenna is supposed to be very large band, from 455 GHz to 2 THz, at least as simulated. The measurement of the antenna bandwidth at THz frequencies is really challenging. The spectral response of the whole detector is measured instead, and it shows a much narrower bandwidth [1].

In terms of optical coupling, the use of lithographic antenna is a good way to obtain a high coupling efficiency of the impinging THz wave. The impedance of the spiral antenna is about 75 Ω while the resistance of the superconducting strip is 130 Ω. Taking in account the resistance and the 10-pH self inductance of the bridge, the impedance mismatch between the antenna and the bridge is estimated to reflect less than 20% of the optical power.

In terms of thermal characteristics, the antenna is considered as heat sink with a temperature maintained near below the superconducting transition temperature. The small heat-sensitive element receives the Joule power from the RF current and conducts the heat to the inner ends of antenna. The thermal conductance then is determined by the dimension and the thermal conductivity of the superconducting strip itself. The thermal conductivity of the superconducting strip is calculated being equal to $\kappa_{th} = 0.54\,\mathrm{W/Km}$ and the thermal conductance is about 2 nW/K. As seen earlier in chapter 2, decreasing the thermal conductance results in a better sensitivity but also increases the response time. In the case of this detector, the response time is in the range of μs, which is much faster than the frame rate in imaging. Thus, the thermal conductance is not much limited by the response time. It is actually limited by the impedance matching with the antenna. A better thermal conductance implies that the length of the superconducting strip is longer or the cross section of the strip is smaller. This will increase the electric resistance of the superconducting strip beyond 130 Ω and thus the impedance mismatch.

3.1.2 Distributed absorbing element bolometer

The spider-web design has became very popular for millimeter-wave superconducting bolometers since the work of [Mauskopf 03] .

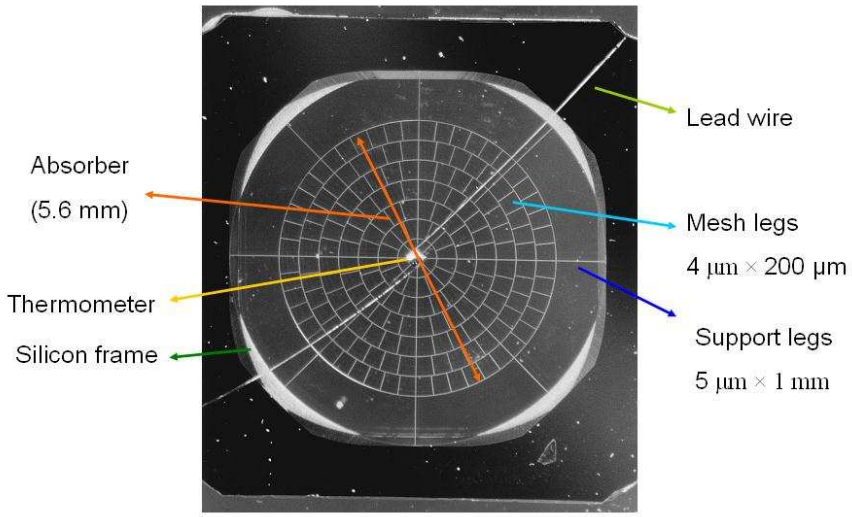

Fig. 3.2: Spider-web design

In this design, the absorber consists of a 1 μm – thick Si_3N_4 mesh metalized by 25 nm – thick metal and has a "spider web" form. The absorber is connected to a solid silicon frame that plays the role of heat sink by 8 radial support legs. The thermometer is placed in the center of the spider-web absorber and read out by two lead wires.

In terms of optical coupling, this absorber corresponds to a distributed absorbing configuration. Since the basic element of the spider-web is a leg of 1 μm × 4 μm × 200 μm of Si3N4 coated (metalized) by a thin metal (25 nm), it acts as a lossy conductor. The lossy grid is configured in a way that it is equivalent to a 189 Ω/square resistance sheet to optimize the optical absorption. According to the electromagnetic theory, if the infinitely large sheet has

this resistance value, it absorbs 50% the radiation passing through it (single pass), independently of frequency. In the case of lossy grid, the result is valid for $\lambda >> l_{grid}$, where λ is the wavelength and l_{grid} is the grid spacing (denoted as the mesh leg of 200 μm length in the previous figure) [Ulrich 03]. It should be noted that, in order to satisfy the single pass condition (the incident pass though the absorber grid once), the detector does not employ a reflector beneath it. This also means that the read out integrated circuit (ROIC), which consists of several layers of dense metallic wires and thus can act as a reflector, should not be placed underneath the absorber layer. This does not cause a problem for most of superconducting bolometers since the number of detectors in the array is small, thus a simpler read-out scheme can be used instead of ROIC.

In terms of thermal characteristics, the lightweight absorber design minimizes the heat capacity and facilitates thinner support legs while keeping a good optical absorption at long wavelength up to 5 mm. With this design, the heat capacity is dominated by the thermometer and the absorber heat capacity is no longer a constraint on the bolometer size. The thermal conductance between the thermometer and heat sink (the silicon frame in previous figure) is the sum of conduction by support legs (2×10^{-11} W/K) and by lead wire (2×10^{-11} W/K), thus it has a value of 4×10^{-11} W/K.

Recently, the spider-web design was combined with horn antenna [5]. The reason is certainly to engineer more precisely the frequency range of detector and also to enhance its optical efficiency.

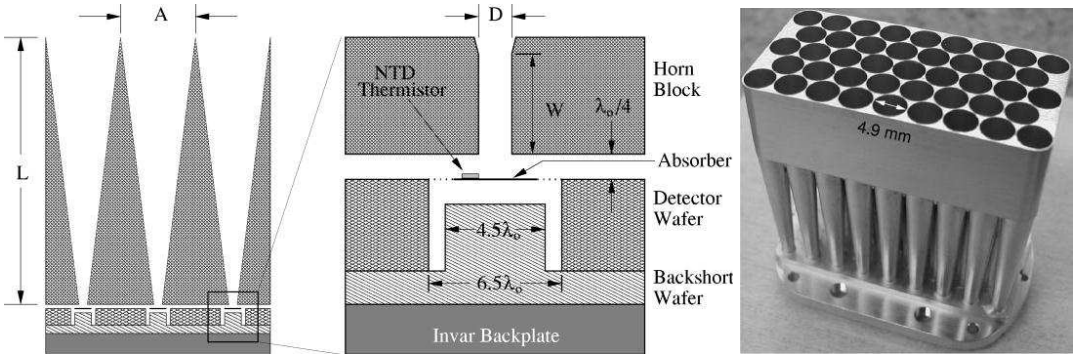

Fig. 3.3: Horn antenna coupled bolometer

This design uses a monolithic array of horn antennas. Each antenna couples the free space wave and guides it to the bolometer. The detector wafer includes spider-web bolometers on a 350μm-thick silicon substrate. The detector wafer is mounted on a second metalized silicon wafer, which has been etched to form tuned backshorts. The detector wafer and backshort wafer combination is fixed to an invar backplate. The feed horn block is mounted on the invar backplate so that it is suspended over the detector wafer and maintains a safe vacuum gap between them. The lower half of the feed horn block, referred as the "frontshort," and the backshort along with the detector form the integrating cavity. The dimension of this integrating cavity is determined so that the electric field is maximized at the position of absorber, thus facilitating the absorption efficiency.

The horn antenna-coupled bolometer has several different characteristics when compared to the bolometer alone:

- The bolometer can be made smaller: the wavelength depends on the horn diameter; the horn guides the wave to a smaller area where its energy is dissipated in the absorber of the bolometer.

- The horn antenna supports several modes whose frequency is well defined and can be tuned by resizing the horn parameter.
- The horn antenna is highly directive.
- By configuring the horn, the detector can by polarization sensitive.

Each of these characteristics can be exploited depending on the foreseen application.

3.2 Uncooled IR Bolometer

In this section, the main characteristics of uncooled IR bolometer of CEA-Leti are presented. This IR bolometer is considered as the starting-point for the development of uncooled THz bolometers. The aim of this section is not to cover all the aspects of the IR bolometer technology, which is quite large and out of the scope of this thesis. Here, we emphasize on the aspects that should be considered in respect to the IR-THz transformation. Although these features are from our specific bolometer, they can be used to refer to the state-of-the-art of uncooled IR bolometer because the main difference between bolometers today is within the thermometric material, not in the design.

3.2.1 Structure

The structure of each pixel can be adjusted a little to fulfill the specifications of each targeted application, i.e. to get the best trade-off between thermal insulation, time constant, and electrical noise. The basic design can be illustrated as in the following figure.

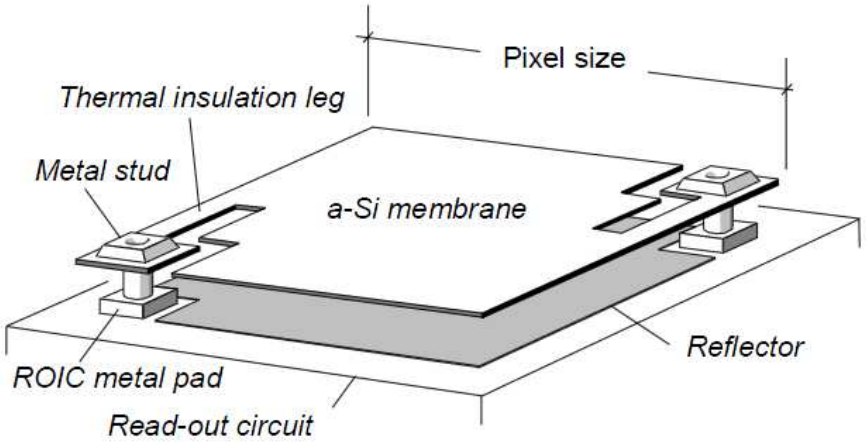

Fig. 3.4: Schematic view of bolometer

The bolometer has a micro-bridge structure, which is very common nowadays for uncooled bolometers. The suspended membrane consists of a thin metal (titanium nitride, TiN) layer playing the role of absorber and the thermometer layer made of amorphous silicon. They are insulated electrically by a dielectric thin film (usually silicon nitride, SiN). This membrane is held by thermal legs, which are a strip of three-layer thin film (see Fig. 3.8 and 3.9) obtained by etching. The dimension and the material composition of this strip determine how good the thermal conduction between the membrane and the metal stud is. The metal stud is considered to be isothermal with the underneath substrate, which plays the role of heat sink. It should be noted that this metal stud can be referred by many technical terms. It is the electrical contact between the thermometer and read-out circuit in substrate underneath. It also is a mechanical strut that supports the membrane suspending in air. And last, since it is obtained by via etching technique, it is sometimes referred as via.

In terms of electrical aspects, the bolometer has two electrodes on the suspended membrane. These electrodes connect the thermometer without being in contact with the absorber to avoid short-circuit, because the electric conductivity of the metal absorber is much higher than the semiconductor thermometer. In addition to the thermal insulation function, the thermal leg also supplies an electrical link between the metal stud and the electrode.

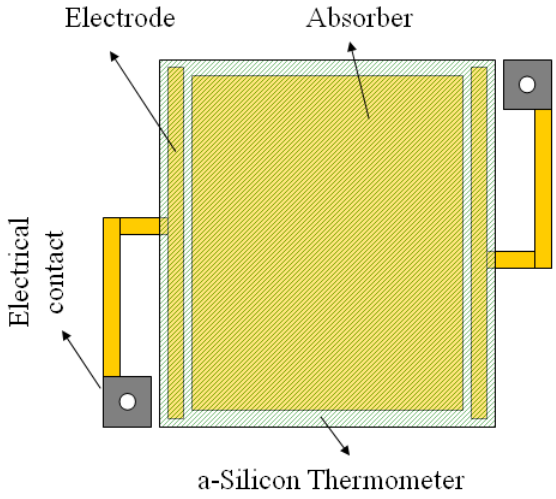

Fig. 3.5: Schematic view of the bolometer

The device is fabricated by using deposition and etching techniques. The figure below is a cross section cut showing the different layers of the stack. The whole structure description can be found with more details in several patents [6], [7].

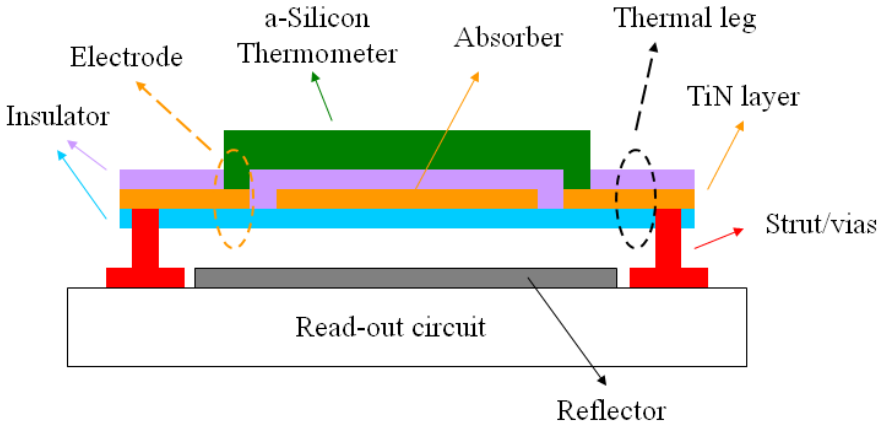

Fig. 3.6: Schematic view of bolometer

From Fig. 3.5 and 3.6, it can be seen that the absorber, the thermal leg, the electrodes and the electrical contact share the same TiN layer. The bottom insulator layer usually is made from SiN and has a thickness in the range 10 – 25 nm. The TiN layer is 8 nm-thick. Another insulator layer of 10 – 25 nm made from the same material is deposited on the TiN layer. Finally, a thick (100 nm or more, depending on each detector design) amorphous silicon is deposited on the top insulator layer. The size and thickness of each layer are chosen to ensure an assembly of proper characteristics in terms of mechanical strength, thermal isolation, heat capacity, optical absorption, and electric properties of thermometer.

In this arrangement, the thermometer layer is above the other insulator layer. The arrangement can be inversed, meaning the thermometer layer is beneath the insulator layer.

The silicon material exhibits very low absorption in long-wavelength infrared (LWIR) range. Thus the order of the arrangement does not change much the absorption of the bolometer. However, since the thermometer layer is thick, this layer should be deposited last to facilitate the forming of the thin insulator layers.

The whole membrane above is suspended in air over a metallic reflector. The air gap between the reflector and the suspended membrane is about 2 μm. This creates a quarter-wavelength cavity so that the absorption of the bolometer is optimized.

The bolometer design is usually classified by pixel pitch. Over the last ten years, the pixel pitch scales down from the initial 45 μm pitch (in year 2000), to 35 μm (2003), 25 μm (2005), 17 μm (2008) and perhaps 12 μm for the next generation.

3.2.2 Optical coupling

The optical coupling of IR bolometer is performed by the thin TiN layer. This layer is made very thin so that the sheet resistance of the layer is about 377 Ω/□. With a cavity of ~ 2 μm, the structure can exhibit a very good absorption [8]. Fig. 3.7 presents the typical absorption of a bolometer which exhibits high absorption rate in the LWIR range [8 – 14 μm].

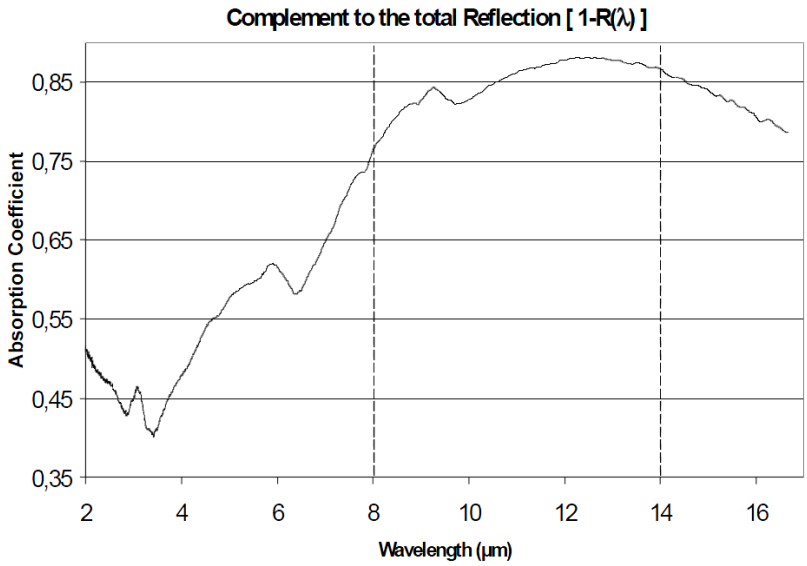

Fig. 3.7: Spectral range of bolometer for several cavity heights (Ref [9]).

Since the size of absorber of an actual bolometer is finite, the fill factor, which is the ratio of the area of absorber to the area of a pixel, becomes quite important in the bolometer design. In general, a higher fill factor means that the absorption efficiency of the pixel is better. The fill factor of our bolometer varies in the range of 50 – 70 %, depending on pixel pitch. For pixel pitch of 25 or 35 μm, the fill factor is about 60 – 70 %. For 12 or 17 μm pitch pixel, it is about 50 – 60 %. However, one should not confuse the fill factor with the absorption: they do not share the same value and the increase of absorption as function of fill factor is not linear, especially when the pixel size gets close to the wavelength. For example, a 17 μm-pitch pixel can get absorption of 80 % over the [8 – 14 μm] spectral range although the fill factor is just about 55 %.

3.2.3 Thermal insulation

Thermal insulation plays a critical role in the bolometer design because the sensitivity depends mainly on the thermal conductance g_{th}. When the size of the pixel is reduced, the optical absorption decreases and the electrical noise of the bolometer increases. The thermal

insulation is the only way to compromise on these degradation effects. Therefore, the golden rule and the most important effort in technology are to improve more and more the thermal insulation.

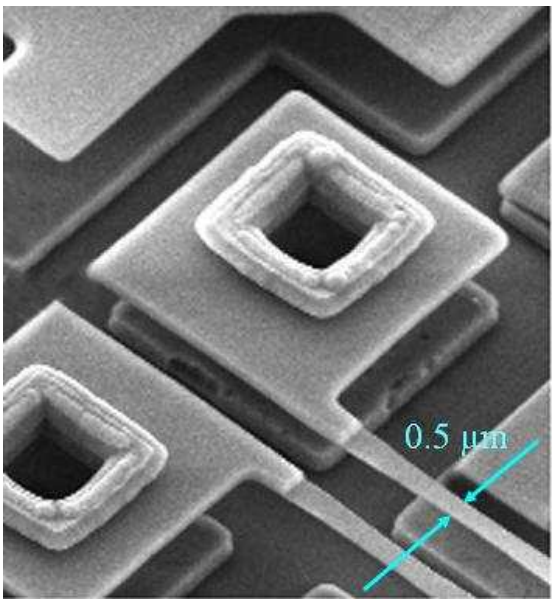

Fig. 3.8: SEM image of 17-µm pitch bolometer shows contact and thermal leg [10].

There are two mechanisms contributing to the heat exchange between the suspended membrane and the ambient: heat conduction by the thermal legs and radiation exchange. Normally, for uncooled IR bolometer, the heat conduction of thermal legs is the main contribution of heat exchange.

Thermal leg consists of a thin TiN strip sandwiched between two insulator layers of SiN. Thus, the thermal conductance depends on the composition SiN/TiN/SiN and also the geometry of the leg. While the sandwich composition is remained, the thermal insulation gets better mostly by reducing the width of the thermal leg. The table below shows the tendency of reducing thermal leg for each pixel pitch [11].

Pixel pitch	Thermal leg width	Thermal conductance
45 µm	1.5 µm	71 nW/K
35 µm	1.2 µm	31 nW/K
25 µm	0.8 µm	18 nW/K
17 µm	0.5 µm	9 nW/K

Table 3.1: Thermal leg's performance for each pixel pitch

Fig. 3.8 shows the electrical contact and thermal leg with 0.5-µm width for the 17- µm pitch CEA-Leti bolometer. The hole at the center of the contact is formed during the deposition processes (one should remember that the contact is also a via).

The geometry of the thermal leg may be more complicated than a long linear strip. Some geometries give a good mechanical strength while maintaining a small thermal conduction. In general, it consists of a combination of basic leg elements, which are rectangular strips as shown in Fig. 3.9. The thermal conduction along the length of the leg

element consists of contributions from the insulator layer and the TiN layer. Since the thickness of theses layers (in the range of nm) is very small as compared to the leg length (in the range of µm), we suppose that the temperature in these layers are the same and varies along the leg length.

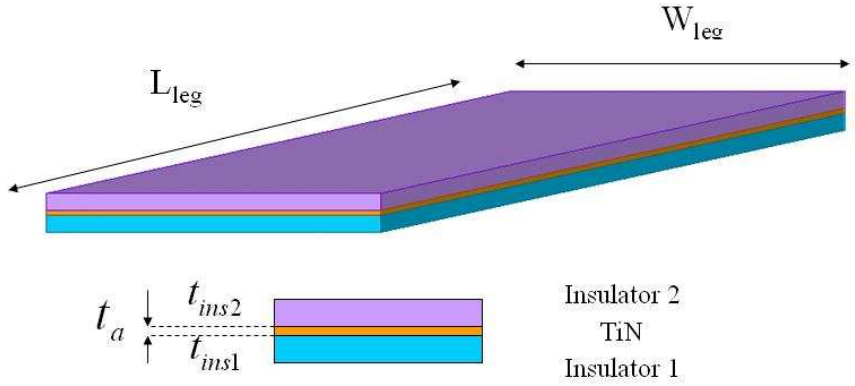

Fig. 3.9: Composition of an elementary leg

The actual geometry of thermal leg can by modeled simply by using the "effective length" concept. This is the length of a strip that has the same cross section and has a thermal conductance equivalent to that of an actual leg. Knowing the geometry of the leg and the thermal conductivity of each material, we can calculate the thermal conductance of the leg. The thermal conductance of the leg that has an effective length $L_{effective}$ is then calculated:

$$g_{leg} = k_{SiN}\frac{W_{leg}(t_{ins1}+t_{ins2})}{L_{eff}} + k_{TiN}\frac{W_{leg}t_a}{L_{eff}}. \qquad \textbf{(3.1)}$$

where k_i is the thermal conductivity of the layer i. Usually, the two insulator layers are made of the same material and have the same thickness, therefore the above formula can be simplified as:

$$g_{leg} = k_{SiN}\frac{W_{leg}2t_{ins}}{L_{eff}} + k_{TiN}\frac{W_{leg}t_a}{L_{eff}} = \frac{W_{leg}}{L_{eff}}(2t_{ins}k_{SiN} + t_a k_{TiN}). \qquad \textbf{(3.2)}$$

From the above equation, we can deduce the contribution percentage of the TiN layer and of the insulator layers to the thermal conductance of the leg:

$$\eta_{TiN} = \frac{W_{leg}t_a k_{TiN}}{L_{eff}} \Big/ g_{leg} = \frac{t_a k_{TiN}}{2t_{ins}k_{SiN} + t_a k_{TiN}} \qquad \textbf{(3.3)}$$

and

$$\eta_{SiN} = \frac{W_{leg}2t_{ins}k_{SiN}}{L_{eff}} \Big/ g_{leg} = \frac{2t_{ins}k_{SiN}}{2t_{ins}k_{SiN} + t_a k_{TiN}} \qquad \textbf{(3.4)}$$

We perform a simple calculation to show the contribution of each element in the leg. The thickness as well as the thermal conductivity of each layer employed in our calculation are presented in the table below.

Element	Material	Thermal conductivity	Thickness
Insulator 1	Si-N	1.3 μW/(μm.K)	t_{ins1} ~ 10 – 25 nm
Absorber	TiN	5 μW/(μm.K)	t_a = 8 nm
Insulator 2	Si-N	1.3 μW/(μm.K)	t_{ins2} ~ 10 – 25 nm

Table 3.2: Element's material and its specific heat

The thermal conductivity of material in a form of thin film is different from the bulk value and depends considerably on the characteristics of thin film (grain size, thickness, etc.) [12]. The values of thermal conductivity presented above are empirical data deduced from the measurement in our laboratory of the thermal conductance of the bolometer. For TiN thermal conductivity, the value is roughly consistent with [13], which reports a thermal conductivity of about 3 μW/(μm.K) for 10 – 20 nm thickness TiN thin film. For Si-N thermal conductivity, the value is in between 0.5 μW/(μm.K) reported in [12] and 3 μW/(μm.K) reported in [14].

Let us apply this calculation for a 17 μm pitch-pixel. The pixel has four thermal legs; each leg has a meandering form to get a length of 13 μm. The leg width for 17 μm pitch-pixel is 0.5 μm and the thickness of insulator layer is 15 nm to ensure the good thermal isolation. By applying the above formulae, we estimate that the thermal conductance of each leg is:

$$g_{leg} = \frac{W_{leg}}{L_{eff}}(2t_{ins}k_{SiN} + t_a k_{TiN}) = \frac{0.5}{13}(2\times 0.015\times 1.3 + 0.008\times 5) \approx 3\,\text{nW/K}. \quad \textbf{(3.5)}$$

Since there are four legs, the total thermal conductance of legs is 12 nW/K. In this case (t_{ins} = 15 nm), the TiN layer contributes by:

$$P_{TiN} = \frac{t_a k_{TiN}}{2t_{ins}k_{SiN} + t_a k_{TiN}} = \frac{0.008\times 5}{2\times 0.015\times 1.3 + 0.008\times 5} \approx 51\ \% \quad \textbf{(3.6)}$$

to the leg thermal conductance. The remained part is due to the Si-N layers.

Another mechanism of heat exchange occurs through radiation exchange between the suspended membrane and the ambient medium. This heat exchange can be modeled as a radiation thermal conductance g_{rad} by using Stefan's law:

$$g_{rad} = \frac{d}{dT}\left(A\varepsilon\sigma T^4\right) = 4A\varepsilon\sigma T^3 \ [\text{W/K}]. \quad \textbf{(3.7)}$$

with A and ε are the area and the emissivity of the detector, respectively [15]. σ is Stefan's constant ($\sigma \approx 5.67\times 10^{-8}\ \text{Js}^{-1}\text{m}^{-2}\text{K}^{-4}$). The emissivity is equal to the absorption of the absorber material (Kirchhoff's law). The formula 3.7 considers the detector as a surface with an area equal to A, and an emissivity equal to absorption $\varepsilon = \eta$, emitting towards the half upper space.

Using the above formula with typical values ($\varepsilon = \eta = 0.8, T = 25^{\circ}C$), we obtain the value for the radiation thermal conductance corresponding with pixel pitch.

Pixel pitch	g_{rad} **(evaluated)**	Typical g_{total} **(measured)**	g_{rad}/g_{total}
45 μm	12.2 nW/K	71 nW/K	17 %
35 μm	7.4 nW/K	31 nW/K	24 %
25 μm	3.8 nW/K	18 nW/K	21 %
17 μm	1.8 nW/K	9 nW/K	20 %

Table 3.3: Radiation thermal conductance for each pixel pitch

As we can see on the above table, the radiation thermal conductance contributes by about 20 % the total thermal conductance of a bolometer. The thermal conductance problem will be examined with more details in chapter 5. Also, in this chapter 5, we will reconsider the calculation of radiation thermal conductance for the case of room temperature THz bolometers.

3.2.4 Heat capacity and thermometer volume

Heat capacity and thermometer volume are also important parameters of the bolometer response. They present a trade-off between the thermal performance and the electrical performance of a bolometer. As explained in chapter 2, with the same thermal conductance, a smaller heat capacity results a smaller time constant, meaning the bolometer responds faster. However, since the heat capacity of a bolometer originates mostly from the thermometer, a smaller heat capacity implies a smaller volume of thermometer. This will increase the 1/f noise of the thermometer. Therefore, the general design rule is that after the thermal conductance of a bolometer is determined, a maximum volume of thermometer that still satisfies the time constant constrain is employed to minimize the 1/f noise.

The heat capacity of bolometer is determined mainly by the heat capacity of the suspended membrane since the contribution of thermal leg is really small. The membrane can be treated as cascading rectangular blocks having the same width and length but with different thicknesses. This is illustrated in Fig. 3.10.

We will use a simple calculation to show that the thermometer contributes mainly to the overall heat capacity of the bolometer. The heat capacity calculation involves knowing the specific heat capacity of each material in the bolometer stack and the dimension of each block (see Fig. 3.10). These parameters are listed in table 3.3. It should be noted that the calculation just gives a rough estimation because of two reasons. The first one is related to the geometrical errors: while the area of each element of bolometer is known thanks to the lithography precision, their thickness is not easy to control. The second reason is that the specific heat of materials is taken from literature, which presents a little deviation when compared to our specific bolometer materials.

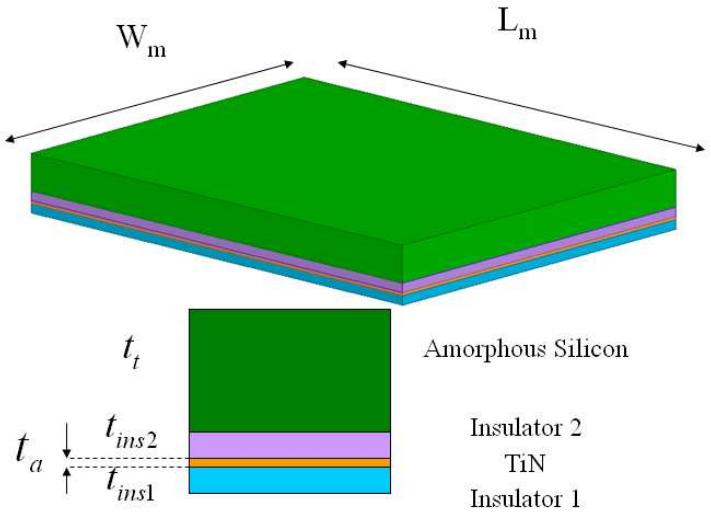

Fig. 3.10: Stack of IR bolometer at Leti

Element	Material	Specific Heat Capacity	Thickness
Insulator 1	Si-N	1.12 pJ/(μm^3.K)	t_{ins1} ~ 10 – 25 nm
Absorber	TiN	3.26 pJ/(μm^3.K)	t_a = 8 nm
Insulator 2	Si-N	1.12 pJ/(μm^3.K)	t_{ins2} ~ 10 – 25 nm
Thermometer	Amorphous Silicon	1.63 pJ/(μm^3.K)	t_t ~ 100 – 300 nm

Table 3.4: Bolometer materials and their specific heat

As we can see in the above table, while sharing the same area, the thickness of the thermometer is more than 5 times bigger than the insulator elements. The thickness of these elements may vary depending on the desired thermal and electric characteristics of each design. The thickness of TiN is fixed at 8 nm, which is a good compromise for the sheet resistance of the absorber and the thermal conductance of bolometer (we have seen earlier that the absorber and the thermal leg share the same TiN layer).

The volume specific heat of amorphous silicon is calculated from the literature. In [16], the specific heat of silicon at 298 K is reported as 0.168 Cal/g/K, a simple calorie-joule conversion gives the value of 0.70 J/g/K. With the mass density of silicon of 2.33 g/cm^3, the volume specific heat is 1.63 J/cm^3/K, i.e. 1.63 pJ/μm^3/K. This value is also used in [17] to simulate the thermal properties of a pyroelectric detector. The insulator layers are usually made of amorphous Si-N, the thickness of these layers vary in the range of 10 – 25 nm, depending on the desired mechanical strength of thermal leg. The specific heat capacity of Si-N is taken from literature. In [14], the authors report on the measurement of heat capacity of an amorphous Si-N membrane as function of temperature. The effective volume is 2.15×10^6 μm^3 and the heat capacity measured is about 2.4 μJ/K (value deduced from the figure in [14]) at 300 K. This gives a specific heat capacity of 1.12 pJ/μm^3/K). The specific heat of TiN is also taken from literature as 0.601 J/g/K at 298 K [18]. By considering a mass

density of 5.43 g/cm^3 [16], we calculate the volume heat capacity of TiN as 3.26 J/cm^3/K, i.e. 3.26 pJ/μm^3/K.

Let us take an example to see how the heat capacity of bolometer changes for each generation of detector. Assuming a typical case in which the thickness of insulator layers is 25 nm, the thickness of thermometer is 200 nm and the fill factor of pixel is 0.8. The following table shows the contributions of each element to the whole bolometer heat capacity. The calculation for the 45 μm-pitch pixel is not presented since the bolometric stack of this pixel is different.

Pixel pitch	Thermometer heat capacity (pJ/K)	Insulators heat capacity (pJ/K)	Absorber heat capacity (pJ/K)	Total heat capacity (pJ/K)
35 μm	319	55	26	400
25 μm	163	28	13	204
17 μm	75	13	6	94

Table 3.5: Heat capacity contribution in IR bolometer

From the table, we can see that the thermometer (with a thickness of 200 nm) contributes to 80 % of the total heat capacity, the insulator layers participates to about 14 % and the contribution of TiN is 6 %.

3.2.5 Response time

Heat capacitance and thermal conductance result in time constant as mentioned in chapter 2. We rewrite the expression to facilitate the presentation of this section:

$$\tau_{th} = \frac{C_{th}}{g} \qquad \textbf{(3.8)}$$

For each bolometer generation, both heat capacitance and thermal conductance have been established in Table 3.3 and 3.5. We deduce easily the time constant for each bolometer generation, which is presented in Table 3.6.

Pixel pitch	Heat capacity (pJ/K)	Thermal conductance (nW/K)	Time constant (ms)
35 μm	400	31	12.9
25 μm	204	18	11.3
17 μm	94	9	10.4

Table 3.6: Time constant for each IR bolometer generation

Usually, the frame rate of the array of IR bolometers is determined as:

$$f_{frame} = \frac{1}{3\tau_{th}}. \quad \textbf{(3.9)}$$

In such case, the read-out circuit waits a time of $3\tau_{th}$ before doing acquisition. Since bolometer's signal evolutes exponentially with time constant τ_{th}, the bolometer reaches 95 % of its established regime signal after a period of $3\tau_{th}$. The frame rate in equation 3.9 is chosen to gain a high signal while keeping the waiting time small enough for a fast imaging. This value can be considered roughly as the "optimum frame rate" regarding signal to noise ratio (SNR). One should note that the frame rate is not necessarily chosen as in equation 3.9. We can choose a higher frame rate (thus waiting time is smaller than $3\tau_{th}$) in the expense of getting a lower signal, thus smaller SNR.

The frame rate of real-time video is 25 Hz, thus the time constant of the bolometer should be inferior to:

$$\tau_{th} = \frac{1}{3 f_{frame}} = \frac{1}{3\times 25} = 13.3 \text{ ms} \quad \textbf{(3.10)}$$

in order to reach the maximum signal. Time constant of all bolometer generation in Table 3.6 satisfies this criterion.

3.3 IR-THz transformation

The designs of cryogenic cooling millimeter-wave bolometer presented previously may not be transferred easily to uncooled THz bolometers for two reasons: cost effectiveness and technical aspect. The development of uncooled THz bolometer from the well-mastered IR bolometer technology seems more feasible. The main issue of developing uncooled THz bolometers based on IR bolometer technology is the optical coupling of the detector to THz wave due to the mismatch between the long THz wavelength and the detector dimension. It should be noted that the dimension of the cryogenic cooled bolometers is at least 200 μm and can be even ~ 6 mm in the case of spider-web bolometer, which are in the range or several times bigger than wavelength of the radiation of interest. Meanwhile, for uncooled IR bolometer technology, the size of detector tends to decrease from 45 μm to 35 μm, then to 25 and to 17 μm. If we take 100 μm (f = 3 THz) as a reference, the IR detector size is therefore smaller than this THz wavelength. In this section, we will see how, in the literature, the IR bolometer structure is modified to be better coupled with the impinging THz radiation.

3.3.1 Absorbing film design

Naoki Oda from NEC, Japan, presented the first attempt of IR-THz adaptation of bolometer structure [19]. The detector is reported to show a NEP of 41 pW at 3.1 THz, which is a big improvement as compared to the results of Lee [20] (a NEP of 320 pW with commercial IR bolometer). This work maintains the thin-film absorber structure, while modifying the cavity dimension and the sheet resistance of the absorber layer. The schematic view of this design is presented in the figure below.

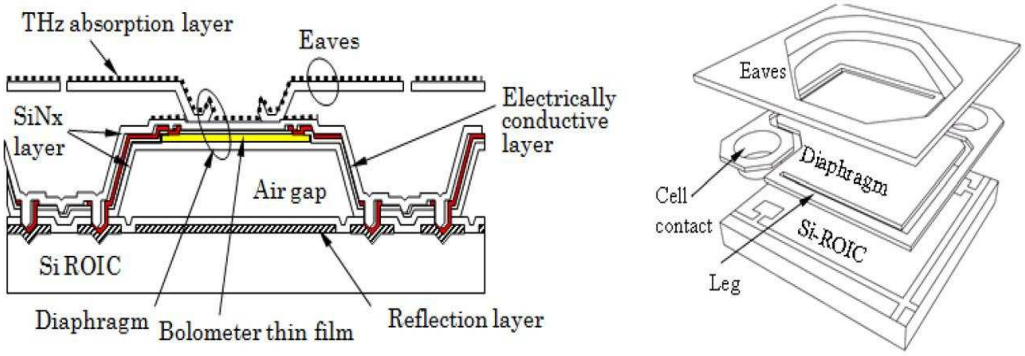

Fig. 3.11: THz bolometer (NEC, Japan) with "eaves"-like absorber to enhance coupling.

We can see in the left image of the figure above that an additional layer, called "eaves", is deposited on the IR bolometer structure. This creates a two-level structure for thin film absorber and seems to help increasing absorption at higher wavelength due to two reasons:

- The thickness of bolometer cavity increases from 1.5 μm to 3 μm.
- The fill factor increases (the area of absorber layer increases).

Naoki Oda argues that the total absorption of the detector consists of contribution from the bottom layer absorber (equipped with cavity 1.5 μm) and the top layer absorber (equipped with cavity 3 μm). Therefore, the formula to calculate the absorption of the thin film absorber is modified as:

$$\eta_{\text{total}} = \beta_1 \eta(\lambda, \mathrm{d}_1) + \beta_2 \eta(\lambda, \mathrm{d}_2)\,. \tag{3.11}$$

with β_1 and β_2 are area occupancy ratios corresponding to bottom and top layers, respectively. The modified structure of absorber from traditional IR bolometer is shown in the figure below with parameters (thickness of cavity, sheet resistance). Using the modified formula of absorption, the author calculated the total absorption versus the sheet resistance of absorber at several wavelength (70, 100, 150, 300 μm), which is shown in Fig. 3.13.

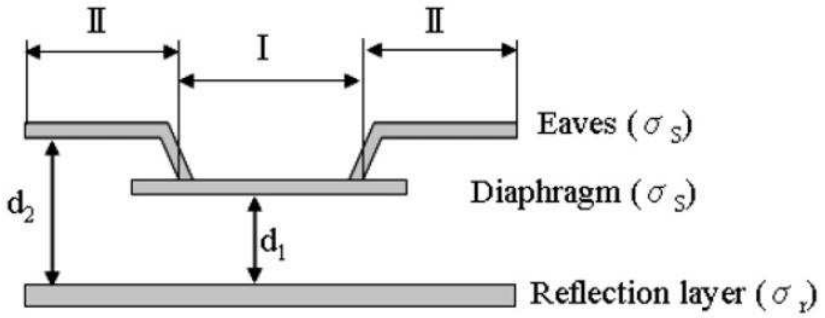

Fig. 3.12: Absorber structure with parameters

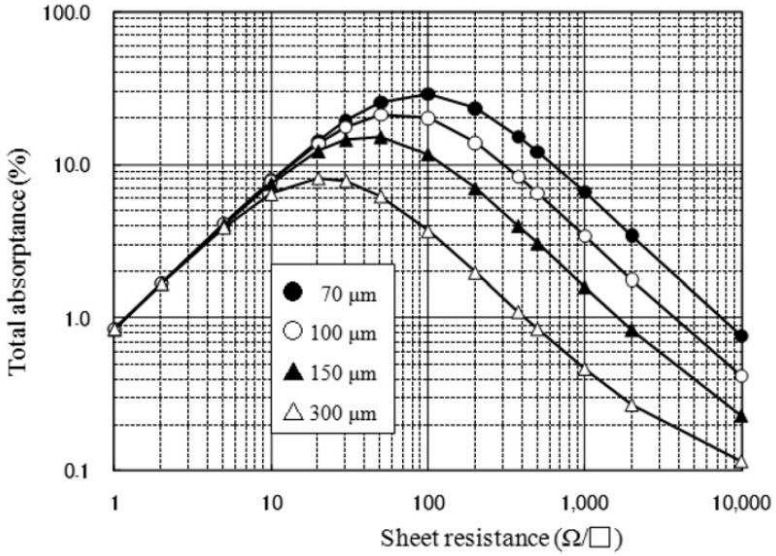

Fig. 3.13: Absorption as function of absorber sheet resistance at several wavelengths.

By observing the figure, we see that the absorption decreases at longer wavelengths, which is predictable since the cavity thickness is too small when compared to the wavelength. It is interesting to note that, at longer wavelength, the absorption is maximum for smaller values of the sheet resistance. The highest absorption obtained at wavelength 100 μm (f = 3 THz) is about 20 % with 50 – 100 Ω/□ sheet resistance. The author also claims a perspective absorption of about 80 % at the same wavelength by increasing the cavity thickness to 12 μm. In this case, the sheet resistance value should change to the range of 200 – 400 Ω/□.

Concerning the thermal aspect, the presence of additional eaves increases the heat capacity of the suspended membrane. Thus, it increases the response time of the detector. However, this effect is not a problem because the response time of detector is still good enough to perform 60 fps frame rate video. While increasing heat capacity, this design keeps the thermal conductance g_{th} of IR bolometer and it is reported to be as low as 30 nW/K.

The approach employed by Oda seems to be very good because there are not many modifications from the traditional IR bolometer structure and the absorption of 20 % is acceptable. This will keep the cost effective aspect of the THz bolometer development and also profits the high yield of matured IR bolometer technology to obtain a large FPA. However, as we will see in the chapter 4, the absorption calculation involved in this approach is too optimistic. In reality, the absorber size is limited, and its absorption is lower than this calculation for infinite absorber case. More importantly, the small modification presented by Oda does not help the design to operate at lower frequency, i.e. in the range below 1 THz. For example, the NEP measured at 1.1 THz of the NEC bolometer is degraded dramatically due to the low absorption at this frequency (2 nW as compared to 41 pW at 3.1 THz).

3.3.2 Antenna coupled bolometer design

Attaching an antenna to a bolometer has been proposed and employed quite largely for superconducting bolometers as described in the previous section. For the uncooled bolometer, due to the mismatch between the dimension of IR bolometer and the THz wavelength, the use of antenna is also a good approach to improve the coupling of the incident wave without changing too much the size of the bolometer. In [21], the authors propose a way to make use of antenna with a traditional IR bolometer.

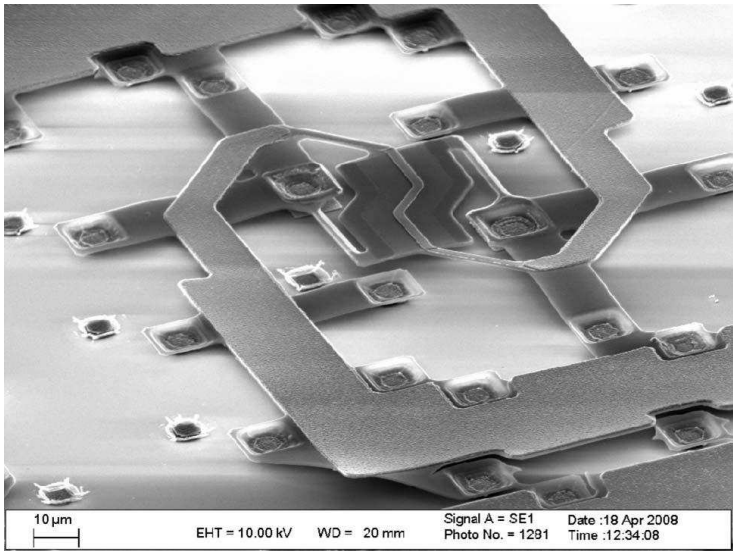

Fig. 3.14: IR bolometer structure associated with antenna to enhance optical coupling.

In Fig. 3.14, the IR bolometer (size: 30 × 30 µm) is associated with a much bigger antenna of 250 × 250 µm. The big antenna is suspended above the silicon substrate containing the readout circuit at a height of 2.5 µm by means of SiN struts. The antenna has a quasi-spiral type and thus is supposed to work at 1.2 THz (corresponding to 250 µm wavelength). If the effect of the silicon substrate, which has a permittivity of $\varepsilon_r = 11.7$, is taken into account, the frequency to be considered is 350 GHz. The presence of an antenna can affect the performance of IR bolometer in terms of optical coupling and also thermal properties. We will see how each aspect evolves due to this design modification.

The quasi-spiral antenna is loaded by a resistive metal strip that plays the role of absorber. The antenna is made from highly conductive metal while the strip is 70 µm long, 2 µm wide, and 200 nm thick, and its resistance is about 100 Ω. The central part of the long metal strip is deposited on the IR membrane (separated from the thermometer by a thin insulator layer). When the antenna couples with the incident THz wave, the induced current appears across the whole antenna but it gives a Joule heat only at the resistive load strip. This heat is easily conducted from the load strip to the suspended membrane, which supports the thermometer.

It should be noted that the antenna is also the heat sink. The big antenna has almost the same temperature as the silicon substrate underneath since the large SiN struts conduct thermally very well. The Joule heat at the load is conducted to the antenna and finally to the substrate level (both antenna and load are made from metal, with a high thermal conductivity). At this point, we can see that, in addition to the bolometer legs, the load strip also contributes to the thermal conduction link. The thermal isolation of this design thus is very bad, which may explain the very poor NEP (33 nW at 3.9 THz).

In antenna-type superconducting bolometers, the load for the antenna is itself a thermometer that has a resistance impedance-matched with the antenna, equal to 100 Ω in order of magnitude. The thermometer of uncooled bolometers based on semiconductor has a resistance of about 100 kΩ in order of magnitude. Therefore, it is not reasonable to use the thermometer as the load of the antenna. The employment of an additional metal strip separated electrically from the thermometer by a thin dielectric layer helps resolving the impedance matching. However, the additional thermal conductance presented by this metal strip is a severe penalty that degrades dramatically the total thermal conductance of bolometer, thus it decreases the detector sensitivity.

A simple calculation will help us having an idea on the thermal conductance presented by the load strip. In Fig. 3.14, the load strip can be considered as connected to the heat sink (antenna) by two parallel thermal links; each has a dimension of 20 × 2 × 0.2 μm. First, let us assume that the metal of load strip has a low thermal conductivity as the one of TiN (5 W/mK at room temperature). This value has been employed in the thermal conductance of our own bolometer for an 8 nm thick TiN film. The single link has then a thermal conductance of:

$$G_{link} = \frac{\kappa_{th} A}{L} = \frac{5 \times 2 \times 0.2 \times 10^{-6}}{20} = 0.1 \ \mu W/K. \quad \textbf{(3.12)}$$

Since there are two thermal links in parallel, the thermal conductance presented by the load strip is $2 \times 0.1 = 0.2$ μW/K, in addition to the thermal conductance of the legs themselves. This order of magnitude is a serious concern because the total thermal conductance of state-of the-art IR bolometers is about 30 nW/K or better.

One can note that this design of uncooled antenna-coupled bolometer is not far from the design of superconducting bolometers [2]. Both designs involve a big antenna loaded by a resistive thin long metal strip. The induced current on antenna gives rise to heat across the load strip while the antenna plays the role of a heat sink. The load strip of superconducting bolometer has 20 × 1 × 0.1 μm dimension compared to 70 × 2 × 0.2 μm dimension of uncooled bolometer. However, the thermal conductivity at 4.2 K temperature of the load strip of superconducting bolometer is very low, $\kappa_{th} = 0.54$ W/Km, and this helps keeping its thermal conductance very good, about 2 nW/K. The thermal conductance of uncooled bolometer, on the other side, is very poor.

3.4 Summary

The chapter has revealed the variety of designs of THz bolometers, either for cooled or uncooled operations. The development of uncooled THz bolometers requires a change in the structure to better couple to the long THz wavelength. This will affect the operation of the traditional IR bolometer. The characteristics of this starting point detector have been presented in detail. The calculations employed for thermal conductance and heat capacity will serve in the next chapter to evaluate the affect caused by design changes. Several tendencies of IR-THz transformation are presented. Some more detailed works in the next chapter will reveal the problems of these designs concerning the optical coupling.

References

[1] E. N. Grossman, C. R. Dietlein, M. Leivo, A. Rautiainen, and A. Luukanen, "A passive, real-time, terahertz camera for security screening, using superconducting microbolometers," in *Microwave Symposium Digest, 2009. MTT '09. IEEE MTT*-S International, 2009, pp. 1453 –1456.

[2] A. Luukanen and J. P. Pekola, "A superconducting antenna-coupled hot-spot microbolometer," Applied Physics Letters, vol. 82, no. 22, pp. 3970–3972, Jun. 2003.

[3] P. D. Mauskopf, J. J. Bock, H. Del Castillo, W. L. Holzapfel, and A. E. Lange, "Composite infrared bolometers with Si3N4 micromesh absorbers," Appl. Opt., vol. 36, no. 4, pp. 765–771, Feb. 1997.

[4] R. Ulrich, "Far-infrared properties of metallic mesh and its complementary structure," Infrared Physics, vol. 7, no. 1, pp. 37–55, Mar. 1967.

[5] G. Chattopadhyay, J. Glenn, J. J. Bock, B. K. Rownd, M. Caldwell, and M. J. Griffin, "Feed horn coupled bolometer arrays for SPIRE - design, simulations, and measurements," Microwave Theory and Techniques, IEEE Transactions on, vol. 51, no. 10, pp. 2139 – 2146, Oct. 2003.

[6] E. Peytavit and J.-L. Ouvrier-Buffet, "Patent US 2006/0231761," .

[7] J.-L. OUVRIER-BUFFET, "US 2010/0276597," .

[8] K. C. Liddiard, "Application of interferometric enhancement to self-absorbing thin film thermal IR detectors," Infrared Physics, vol. 34, no. 4, pp. 379–387, Aug. 1993.

[9] J. J. Yon, "First demonstration of 25 μm pitch uncooled amorphous silicon microbolometer IRFPA at LETI-LIR," 2005, vol. 5783, pp. 432–440.

[10] J.-L. Tissot, S. Tinnes, A. Durand, C. Minassian, P. Robert, M. Vilain, and J.-J. Yon, "High-performance uncooled amorphous silicon video graphics array and extended graphics array infrared focal plane arrays with 17-μm pixel pitch," Optical Engineering, vol. 50, no. 6, pp. 061006–061006–7, May 2011.

[11] J.-J. Yon, E. Mottin, and J.-L. Tissot, "Latest amorphous silicon microbolometer developments at LETI-LIR," 2008, vol. 6940, p. 69401W–69401W–8.

[12] S.-M. Lee and D. G. Cahill, "Heat transport in thin dielectric films," Journal of Applied Physics, vol. 81, no. 6, pp. 2590–2595, Mar. 1997.

[13] A. Albert Irudayaraj, R. Srinivasan, P. Kuppusami, E. Mohandas, S. Kalainathan, and K. Ramachandran, "Photoacoustic measurement of thermal properties of TiN thin films," Journal of Materials Science, vol. 43, no. 3, pp. 1114–1120, 2008.

[14] B. Revaz, B. L. Zink, and F. Hellman, "Si-N membrane-based microcalorimetry: Heat capacity and thermal conductivity of thin films," Thermochimica Acta, vol. 432, no. 2, pp. 158–168, Jul. 2005.

[15] D. W. Denlinger, E. N. Abarra, K. Allen, P. W. Rooney, M. T. Messer, S. K. Watson, and F. Hellman, "Thin film microcalorimeter for heat capacity measurements from 1.5 to 800 K," Review of Scientific Instruments, vol. 65, no. 4, pp. 946 –959, Apr. 1994.

[16] J. F. Shackelford and W. Alexander, Eds., CRC Materials Science and Engineering Handbook, Third Edition, 3rd ed. CRC Press, 2000.

[17] G. Teowee and D. R. Uhlmann, “Modeling of a thin film pyroelectric pixel: Steady state results,” Integrated Ferroelectrics, vol. 22, no. 1–4, pp. 411–419, 1998.

[18] M. W. J. Chase, Ed., NIST-JANAF Thermochemical Tables 2 Volume-Se, 4th ed. American Inst. of Physics, 1998.

[19] N. Oda, “Uncooled bolometer-type Terahertz focal plane array and camera for real-time imaging,” Comptes Rendus Physique, vol. 11, no. 7–8, pp. 496–509, Aug. 2010.

[20] A. Lee, S. Kumar, B. S. Williams, Q. Hu, and J. L. Reno, “Real-time imaging using a 4.3-THz quantum cascade laser and a 240x320 element focal-plane array,” in Lasers and Electro-Optics, 2006 and 2006 Quantum Electronics and Laser Science Conference. CLEO/QELS 2006. Conference on, 2006, pp. 1 –2.

[21] M. A. Dem’yanenko, D. G. Esaev, V. N. Ovsyuk, B. I. Fomin, A. L. Aseev, B. A. Knyazev, G. N. Kulipanov, and N. A. Vinokurov, “Microbolometer detector arrays for the infrared and terahertz ranges,” J. Opt. Technol., vol. 76, no. 12, pp. 739–743, Dec. 2009.

Chapter 4 Bolometer stack for THz frequency

In this chapter, we study the optical coupling of traditional infrared bolometers. By extending the theory of absorption of thin film absorber to the THz range and performing some electromagnetic simulations, we demonstrate and explain why the absorption at THz frequencies of uncooled infrared bolometer is low. Then a new bolometer stack optimized for the THz frequency range is presented.

4.1 Absorption of metallic thin film structure

4.1.1 Infinite size film

4.1.1.1 General theory of three-layer structure

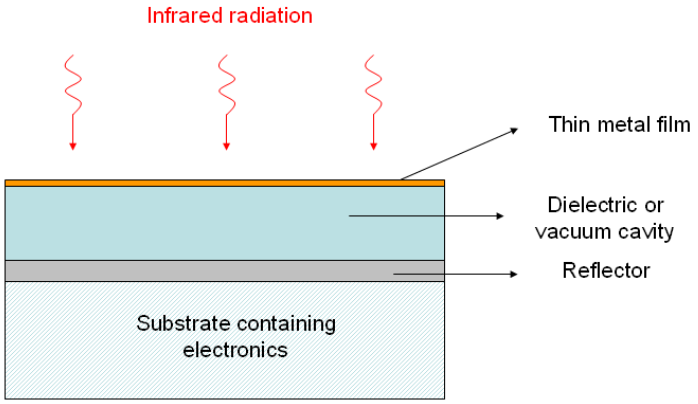

Fig. 4.1: General three-layers structure for uncooled infrared bolometers.

The popular absorber design of uncooled infrared bolometer uses the absorption principle of a three-layer structure depicted in Fig. 4.1 [1]. Assuming all the layers are infinitely large, the general expression for absorption η as function of wavelength λ for the three-layers structure is [2]:

$$\eta(\lambda, d) = 4\frac{(f_s(f_r+1)^2/n^2 + f_r)\sin^2\theta + (f_r + f_s)\cos^2\theta}{Dn^2}, \quad \textbf{(4.1)}$$

where

$$D = \left(\frac{(f_r+1)(f_s+1)}{n^2}+1\right)^2 \sin^2\theta + \frac{(f_r + f_s + 2)^2}{n^2}\cos^2\theta \quad \textbf{(4.2)}$$

and $f_r = 120\pi/R_r$, $f_s = 120\pi/R_s$, $\theta = 2\pi nd/\lambda$. R_r is the sheet resistance of the reflector metal film, R_s is the sheet resistance of the front surface metal film onto which the radiation is incident. The dimension of sheet resistance is Ohm per square (Ω/□). The dielectric layer has a thickness d and a refractive index n. The dielectric layer is assumed to be non-absorbing, which is valid for many dielectric materials and low conductivity semiconductors of interest.

If the reflector is perfect, meaning its conductivity is infinitely large or its sheet resistance is zero, we have:

$$R_r \to 0, \quad f_r \to \infty$$

$$\eta = \frac{4 f_s}{(1+ f_s)^2 + n^2 \cot^2 \theta} \tag{4.3}$$

This absorption reaches a maximum of unity when:

$$d = (2m+1)\lambda/4n, \; m = 0, 1, 2\ldots \tag{4.4}$$

$$\text{and} \quad f_s = 1. \tag{4.5}$$

$f_s = 1$ implies that $R_s = 120\pi \approx 377$ Ω/□. In an ideal case, a metallic thin film (infinitely large) of sheet resistance equal to the impedance of vacuum can absorb 100 % the incident wave if the film is placed at a distance of a quarter wavelength from an ideal reflector. This general theory can be applied for any wavelength, either in the infrared or in the millimeter-wave ranges. We examine now two cases of cavity thickness to demonstrate the absorption over a given spectral range. The first one is quarter wavelength for uncooled mid-infrared bolometers, i.e. in the 8 – 14 µm range. The second one is a THz quarter wavelength cavity. In this case, though the examined structure does not exist as a real device, it provides wealthy information about the absorption at THz range using the three-layers structure.

4.1.1.2 Infrared quarter wavelength structure

Usually, the dielectric cavity of infrared bolometers consists of vacuum, therefore n = 1. The dimension of the cavity between the thin film absorber and the reflector is chosen to be the smallest, i.e. $d = \lambda/4$. For λ = 10 µm, this equals to 2.5 µm. The quarter-wavelength dimension is chosen instead of a multiple of this value to facilitate the actual fabrication of the micro-bridge structure that will be presented in the next section.

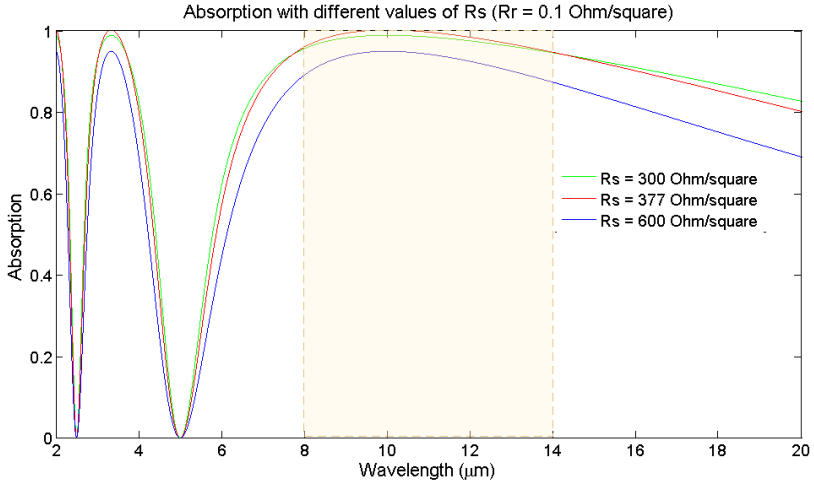

Fig. 4.2: Absorption of the three-layer structure with different values of absorber resistance R_s

Most commercial IR bolometers make use of this optical cavity design: a thin metal film of sheet resistance of 377 Ω/□ above a perfect reflector located at a distance equal to quarter-wavelength. This design provides very high optical absorption. It should be noted that the sheet resistance of the thin film absorber may not be well controlled during the fabrication process and moreover that the sheet resistance of reflector, of course, is not perfectly null in

practice. Therefore, it is worthwhile to assess how the absorption varies depending on the sheet resistance of the absorber and the reflector.

A simple Matlab® code is used to calculate the absorption of the three-layers structure for different values of R_s varying from 300 to 600 Ω/□ while keeping R_r constant at 0.1 Ω/□. We choose vacuum as the dielectric layer and a cavity thickness of 2.5 µm. As shown in Fig. 4.2, the absorption of infinitely large three-layer structure is very large band. It is better than 95 % in the LWIR window (8 – 14 µm) for R_s values ranging from 300 to 377 Ω/□. A very large variation in the sheet resistance of the absorber thin film (for example R_s = 600 Ω/□) degrades the absorption only by a factor of 10 % in the spectral range of interest.

The absorption curve exhibits some interference fringes at shorter wavelengths. This interference behavior was well studied in [3]. In this spectral range, the dimension of cavity (2.5 µm) becomes multiple of the quarter value of the wavelength, which leads to a phase-shift of 0 (in phase) or π (out of phase). Therefore the constructive and destructive interferences appear. For example, the constructive interference appears at wavelength of 10 µm, (10µm)/3, (10µm)/5 and so on. Meanwhile, the destructive interference appears at (10µm)/2, (10µm)/4 and so on.

The value R_s of the absorber may vary greatly, up to ± 100 Ω/□ around the optimum value of 377 Ω/□ because of bolometer manufacturing drifts. However, this does not affect significantly the absorption in Fig. 4.2. The value R_r is much easier to control, since it depends on the reflector conductivity rather than on its thickness. A typical aluminum layer of 300 nm can have a sheet resistance as low as 0.1 Ω/□.

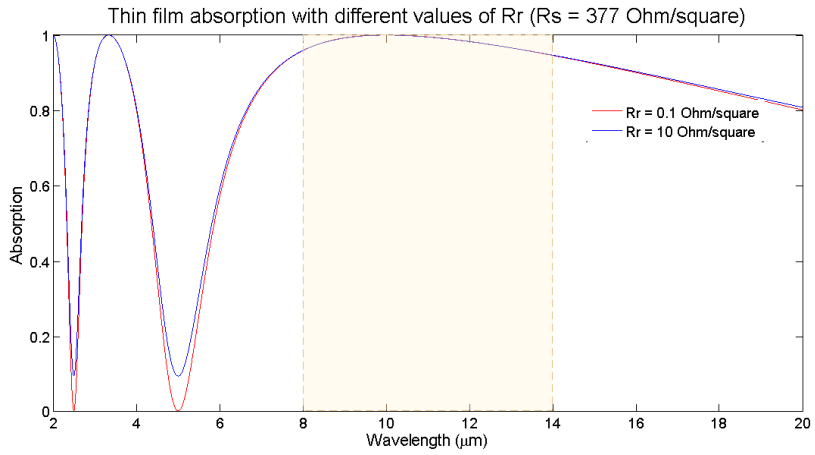

Fig. 4.3: Absorption of the three-layers structure with different values of reflector resistance R_r .

In Fig. 4.3, we plot the absorption of the absorber thin film for two values of the sheet resistance of the reflector, 0.1 Ω/□ and 10 Ω/□ respectively. There is almost no difference in the absorption in the 8-14 µm infrared range. This means that the variation of the sheet resistance of the reflector due to some fabrication defect does not affect greatly the absorption.

The absorption of this metallic thin film configuration can be evaluated in the THz range. Let us consider an infinite thin film of 300 Ω/□ sheet resistance placed at a distance of 2 µm from a good metallic reflector (0.1 Ω/□ sheet resistance). Its absorption in the range of 30–200 µm is plotted in the figure below. The absorption is pretty good at 30 µm (10 THz) with about 50 % of the incident wave power. It decreases monotonically to 7.5 % at 100 µm

(3 THz) and to 2 % at 200 µm (1.5 THz). By varying the sheet resistance of the thin film absorber, it is found that at 100 µm, the absorption gets maximum value (22 %) when R_s=50 Ω/□. This result is consistent with literature [4]. The absorption is still 9 % at 200 µm.

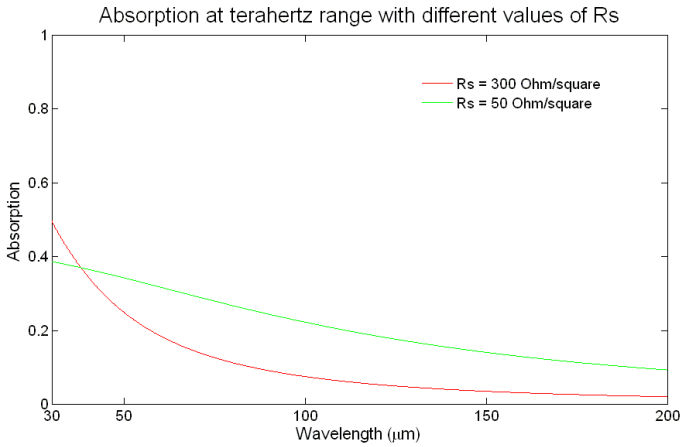

Fig. 4.4: Absorption of infinite size thin film absorber at THz range, air gap is 2µm

The order of magnitude of absorption about 9–20 % in the range 1.5–3 THz is not an unacceptable value, especially if the bolometer is used in active imaging. However, the above absorption calculation has employed an important condition: the films (absorber and reflector) must be infinite in size, or at least several times bigger than the wavelength. This is definitely not the case of infrared bolometers because their pixel pitch is in the range of 17–35 µm, smaller than the wavelength in the THz range. We will see later that the finite size film absorbs less than the infinite one.

4.1.1.3 THz quarter wavelength structure

According to the general theory three-layers structure, if the cavity height is equal to a quarter of wavelength in the THz range, the absorption is expected to be optimized similarly to the infrared case. The cavity must have a thickness

$$t_{cavity} = \frac{\lambda}{4n} \qquad \textbf{(4.6)}$$

where λ is the wavelength and n is the refractive index of the cavity. By considering λ = 100 µm (f = 3 THz), the height of an air cavity must equal 25 µm. This is a very unusual dimension in today semi-conductor microelectronics. Another more realistic solution is to fill the cavity with a high refractive index. This approach will be presented later. Right now, for sake of simplicity, we assume an air gap cavity of 25 µm and evaluate the absorption in the THz and infrared ranges.

The absorption of an infinite size thin film of 300 Ω/□ sheet resistance, placed 25 µm from a reflector (0.1 Ω/□ sheet resistance), is plotted in Fig. 4.5 for the range of 8–300 µm. The absorption reaches a maximum of nearly 99 % at 100 µm. It decreases at longer wavelengths but still attains 60 % at 300 µm. In the infrared region, the absorption curve shows interference fringes, similarly to the behavior of the 2.5 µm cavity structure at short wavelength. The average absorption in the mid-infrared region 8–14 µm is estimated at 66 %.

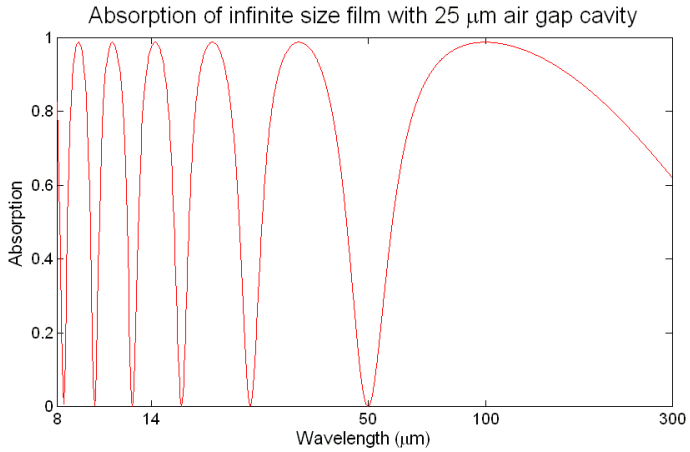

Fig. 4.5: Absorption of infinite size thin film absorber, air gap is 25μm, R_s = 300 Ω/□

At this point, we can see the similarity in the absorption of THz and infrared quarter wavelength structures. This similarity and the successful implementation of uncooled infrared bolometers lead to the idea of designing uncooled THz bolometers by simply making a bigger detector. This is quite true in principle. However, as we will see later on, several additional parameters will intervene in the actual design of uncooled THz bolometers.

4.1.2 Finite size films

The previous absorption study is based on solving the Maxwell equations for the three-layers structure assuming infinite planar dimensions. The assumption leads to consider the Maxwell equations in one dimension, meaning that the boundary conditions are related to only one dimension. As a consequence, the wavelength dependence of absorption curve is restricted to only one dimension: the relative ratio between the air gap and wavelength (the variable $\theta = 2\pi nd/\lambda$ in equation 4.2). In reality, the absorber film and the reflector have finite size. This adds boundary conditions in the two other dimensions. As a consequence, the absorption curve depends also on the width and length of the absorber film.

In this section, we simulate a film absorber of finite size, to investigate the impact of the absorber dimension on its absorption. The simulations have been performed with HFSS® (High Frequency Structural Simulator), which is a finite element method solver for electromagnetic structures.

4.1.2.1 Film with infinite reflector

The simulated structure is presented in Fig. 4.6. The absorber layer is made of metal square periodic patches that share a unique infinitely planar reflector. The reflector is 2-μm below the patch array. The interest of this simulation is to investigate the impact of the finite dimensions of the absorber on its absorption, particularly in the THz range.

The dimension L_p is chosen to be similar to the pitches of commercialized uncooled infrared bolometers, which are commonly 35, 25, and 17 μm. L_a is chosen to ensure a geometric fill factor close to 70 %. The absorber sheet resistance is 300 Ω/□, which is the typical value for infrared bolometers. Table 4.1 presents detailed dimensions of the simulated structure.

L_p	L_a	Absorber sheet resistance	Geometric fill factor
35 µm	29 µm	300 Ω/□	69 %
25 µm	21 µm		71 %
17 µm	14 µm		68 %

Table 4.1: Parameters of the periodic absorbing patch array.

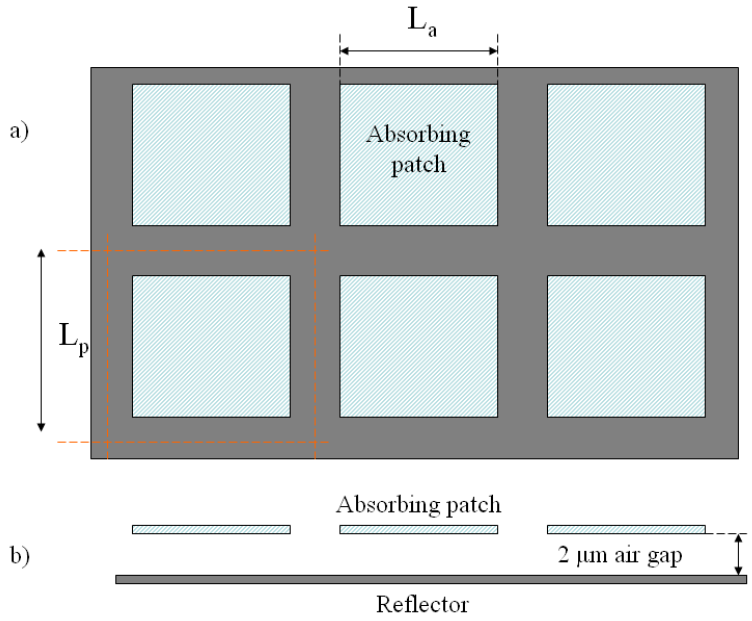

Fig. 4.6: Periodic metallic square patch with infinite reflector underneath:

a) top view, b) side view showing 2 µm air gap

THz absorption

Fig. 4.7 shows the simulated absorption in the THz range for different values of the pitch dimension. The absorption is found to be low. In general, the (transverse) THz electric field is very weak near the reflector surface because the reflector is a good conductor. The induced current on the absorber is therefore systematically small. There is not considerable variation in absorption between the different pitches. The absorption increases monotonically with frequency and attains about 4 % at 3 THz and 18 % at 6 THz.

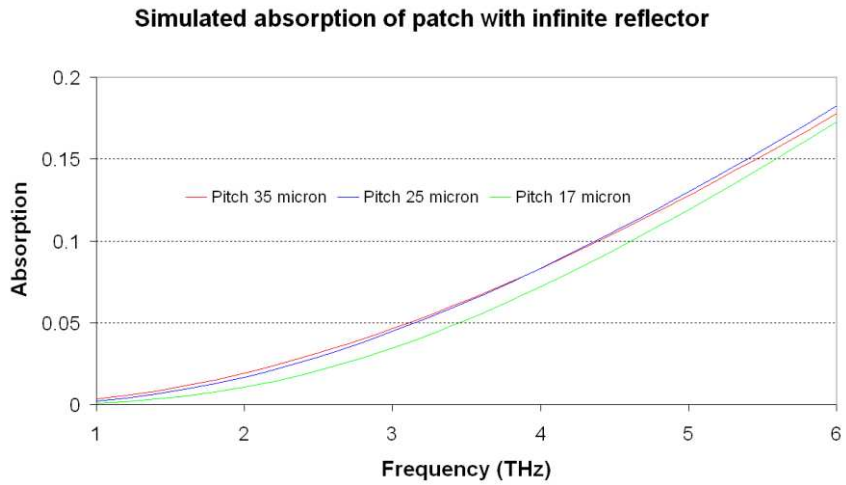

Fig. 4.7: Absorption of a patch standing 2 µm above an infinite reflector.

Infrared absorption

The following figure shows the simulated absorption in the 8–14 µm band. The overall absorption is found to be better than 80 % over the spectral range. The air gap of 2 µm is optimized for 8-µm wavelength, which explains it is very high. The absorption tends to decrease as the wavelength is longer mostly because of the mismatch of the air gap. Meanwhile, the pixel size does not have a strong impact on the absorption.

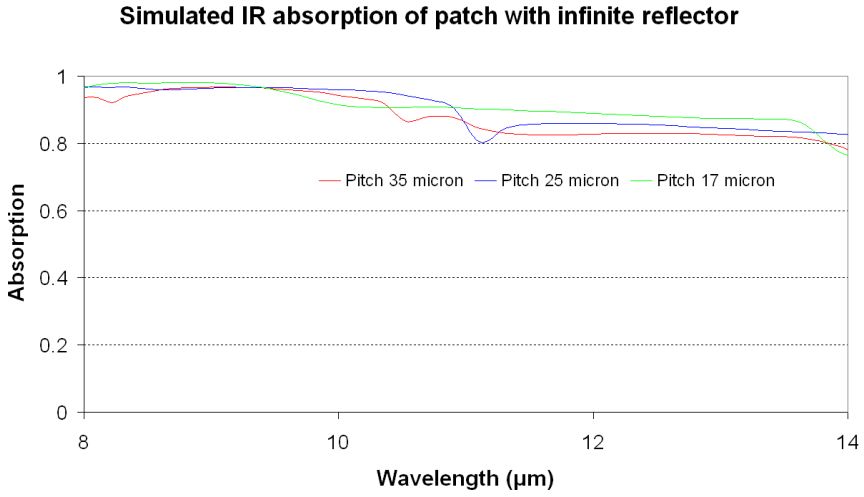

Fig. 4.8: Absorption at infrared range of a patch standing 2 µm over infinite reflector.

4.1.2.2 Film with finite reflector

In Fig. 4.9, the considered configuration is a periodic array that consists of finite patches (absorbing layer and reflector). Such an architecture is close to the real bolometer array structure. The metal patch is supposed to have a sheet resistance of 300 Ω/□ and to be 2 µm above a finite size reflector. The sheet resistance of the reflector is 0.1 Ω/□. The infinite reflector with this sheet resistance reflects almost all the incident wave independently of frequency. However, for finite reflectors arranged periodically, the reflection is better at short wavelength (infrared) than at long wavelength (THz). This common electromagnetic response has been mentioned in many electromagnetism textbook, such as [5]. We simulate the absorption in THz and infrared range to investigate the impact of the geometrical parameters of the finite reflector.

L_p	L_a	L_r	Sheet resistance	Geometric fill factor
35 µm	29 µm	34 µm	300 Ω/□	69 %
25 µm	21 µm	24 µm		71 %
17 µm	14 µm	16 µm		68 %

Table 4.2: Parameters of the periodic absorbing and reflector patch array.

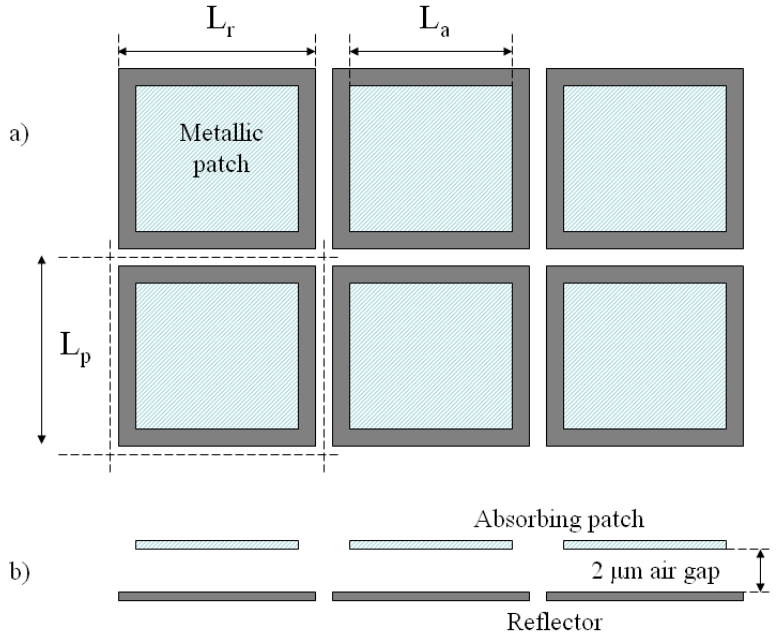

Fig. 4.9: Periodic metallic square patch with reflector underneath.

THz absorption

As in the case of an absorbing patch with an infinite reflector, the absorption with a limited reflector is found to be low in the THz range. As we will see later, the main cause of low optical coupling is that the absorber film placed too close to the good conducting surface. Thus the magnitude of the (transverse) electric field at the absorber is very small. The finite size of the reflector does not change greatly the situation when compared to the infinite size case; therefore the absorption is always low. There is, however, a difference: the absorption is not a monotonic function of frequency anymore. We can see some bumps in the absorption curve at low frequency.

An important characteristic of the patch with finite reflector is that low frequency wave can propagate through the array quite easily. The narrow space (1 µm) between reflectors and the high occupancy ratio of their area (nearly 89 % for the lowest case) give the impression that the transmission is very low. However as we can see in Fig. 4.11, the transmission is quite high, especially for lower frequency. We also observe that the smaller the pitch, the higher the transmission.

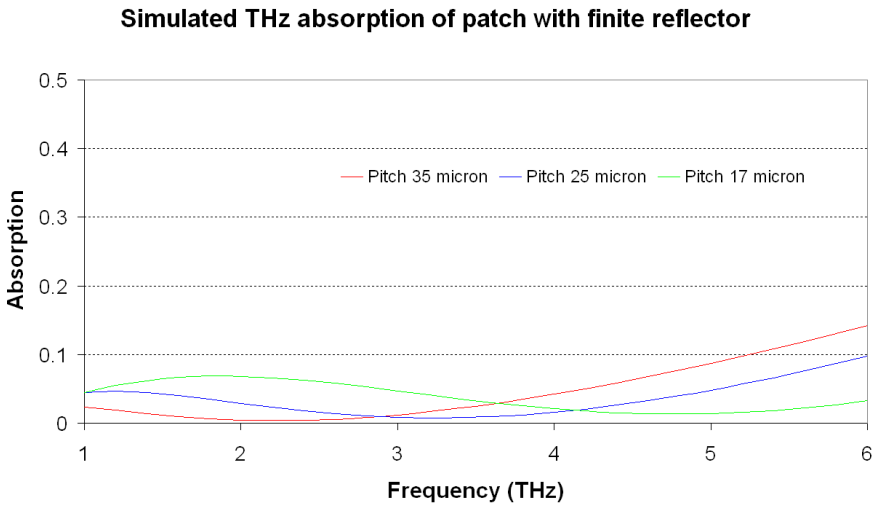

Fig. 4.10: Absorption of a patch standing 2 µm above a finite reflector.

The transmission of microwaves through the metallic array has been studied in [5]. At lower frequencies, the wavelength becomes much larger than the metallic patch. These waves do not induce a strong high frequency current on the surface of the metallic patch due to the mismatch between the patch size and the wavelength of the excitation. Hence, the interaction between the metallic patch and the electromagnetic wave is very weak. As a consequence, the wave then can pass through the array of metallic patch. The mismatch is more evident at lower frequency, or for smaller pitch. In such case, the interaction is weaker and the transmission gets higher.

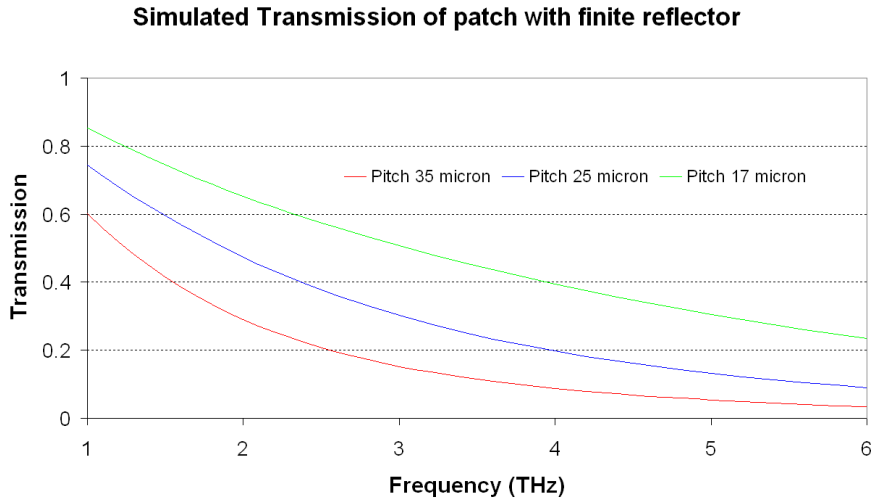

Fig. 4.11: Transmission through a patch standing 2 µm above a finite reflector.

The phenomenon of propagation through finite reflectors leads to many effects that should be considered carefully when designing THz bolometers. THz bolometers in this PhD work are derived from the infrared bolometers with a moderate increase of the pixel size. Thus, the THz wavelength is usually larger than the pixel size. The above simulation of transmission shows that the THz waves can propagate through the detector structure. However, as revealed later, there is read-out circuit structure below the reflector level. Thus the passing waves may interact with the read-out circuit. The interaction is complicated and will be highlighted in the next section.

Infrared absorption

In the THz range, the patterned reflector layer does not act as a good reflector and the THz wave can propagate through it. However, in the infrared range, since the wavelength is much shorter, the size of each reflector patch is large as compared to the wavelength. For example, the smallest pitch of 17 µm is still greater than the wavelength in the 8–14 µm band. The array of square reflectors acts as the case of infinite size reflector for which we have seen a good absorption in the 8–14 µm band. Indeed, the simulation in Fig. 4.12 shows that the absorption is similar to the previous case of an infinite reflector. The absorption is better than 80 % over the 8–14 µm band and tends to decrease at longer wavelength.

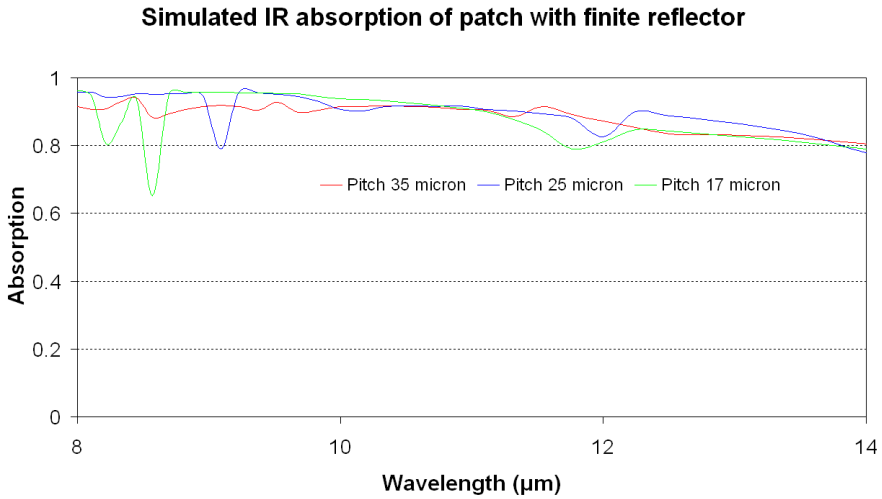

Fig. 4.12: Absorption in the infrared range of absorbing patches standing 2 µm above a finite reflector.

4.2 Bolometer stack for THz wavelength

4.2.1 Infrared stack

The most common, from the point of view of optical coupling, infrared bolometer stack is illustrated by Fig. 4.13. The suspended membrane contains a thin film absorber (for example a TiN layer) and a thermometer (made of amorphous silicon in the case of the CEA-LETI device).

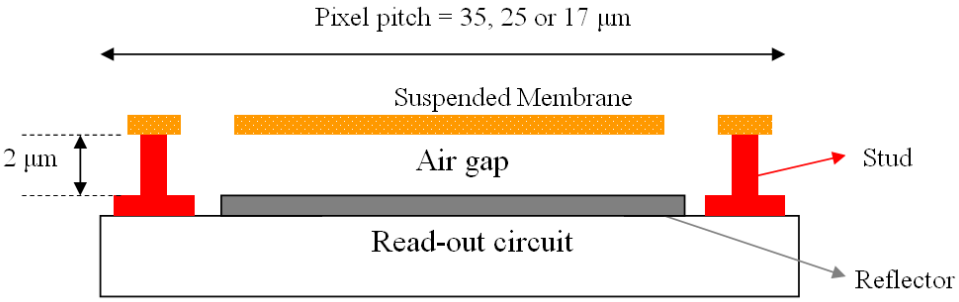

Fig. 4.13: CEA-LETI bolometer stack with 2 µm air gap.

The absorber size is 20 × 20 µm for the 25 µm pitch pixel. The size of the metallic reflector is also finite. Within each pixel, the reflector is separated from the metallic stud, which provides electrical contact for bolometer, by a margin of 0.5 µm. This margin should be large enough to ensure that the metallic studs do not touch the reflector. Such contact would induce short-circuit problem. The reflector of each pixel is separated from each other by a gap of 1 µm. This configuration (Fig. 4.11) ensures that even if a short circuit happens in

a pixel, this pixel is insulated from the rest of the array. Therefore, the array is able to continue functioning.

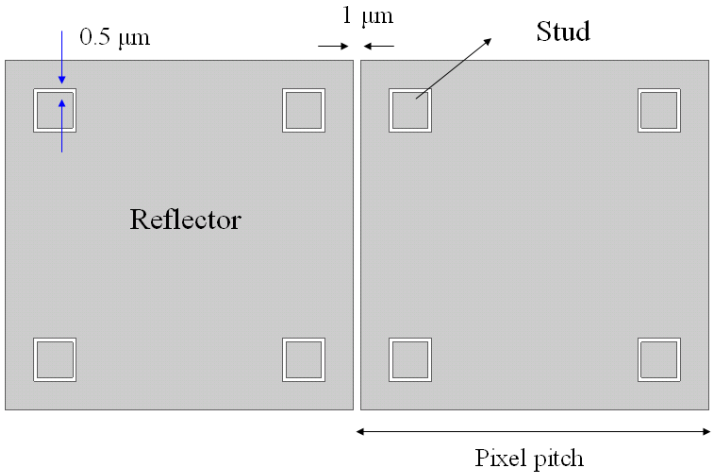

Fig. 4.14: Metallic reflector patterning.

One major characteristic of the infrared bolometer stack is that the array of bolometers is fabricated above the CMOS (Complementary metal–oxide–semiconductor) read-out integrated circuit (ROIC) with standard microelectronic process techniques. Intentionally, the CEA-LETI detector fabrication uses only silicon-compatible standard processes. This is one of the key factors that ensure a low cost fabrication.

The reflector layer is just above the CMOS ROIC layer. As mentioned in the last section, the THz wave may propagate through the patterned reflector layer. Interactions between the incident wave and the ROIC may happen. Therefore, it may be useful, for a whole modeling of the device, to know the ROIC structure.

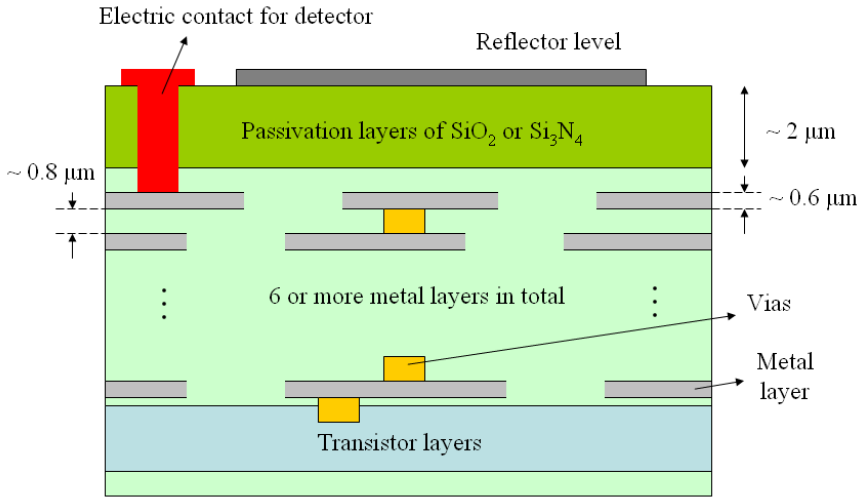

Fig. 4.15: Structure of CMOS read-out circuit at CEA-LETI contains 6 metallic layers.

The geometry of CMOS ROIC is extremely complex and varies for each circuit. In general, the ROIC has two main parts: the transistor layer and the addressing scheme. The addressing scheme consists of 4 (or more) metal layers; each being sandwiched between dielectric layers of SiO_2. The metal layers can be interconnected through vias that carry the electrical signal from the transistor layers to upper metal contacts.

Metal layers consist of very long aluminum strips with thickness of about 0.6 µm. Some strips may extend to the entire length of the detector chip, i.e. centimeters. The orientation of the metal strips may be crossed from one layer to the next. For example, the following figure shows the geometry of two neighboring metal layers in one pixel of size 50 µm × 50 µm. It should be note that, in an array of pixels, this geometry is repeated periodically and then generates long continuous strips.

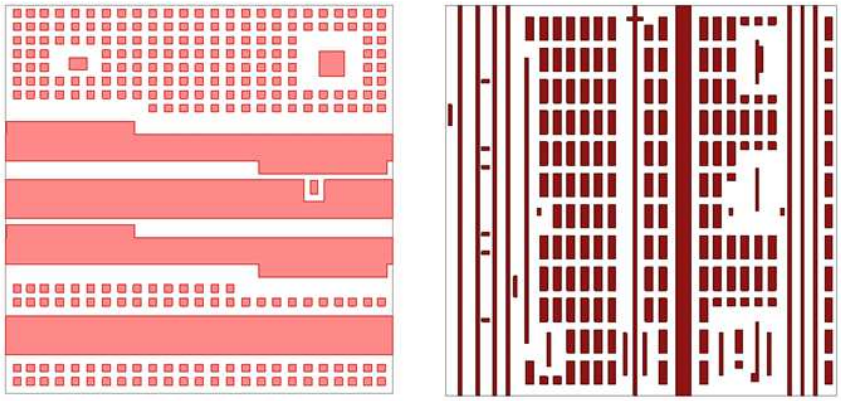

Fig. 4.16: Geometry of two different metallic layers

The thickness of 0.6 µm is large in comparison to the skin depth in aluminum at THz frequencies (about 50 nm at 3 THz). Therefore, long Al strips can be considered as good conductors. The typical strip length is of the order of one centimeter which is much longer than wavelength in the THz range (100 µm at 3 THz). Thus, strips act as infinitely long lines in this spectral domain. The general behavior of infinite long and good conductor strip in a dense arrangement is reflective and the reflection is better at lower frequency [5].

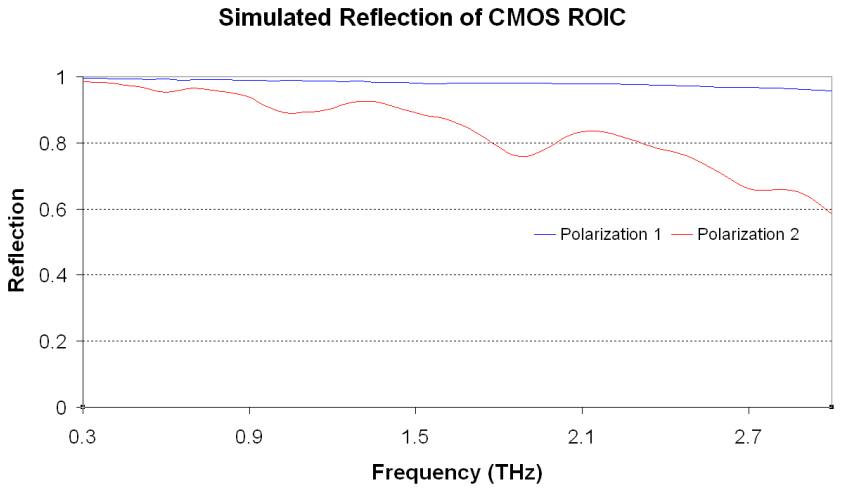

Fig. 4.17: Simulated reflection of the CMOS ROIC structure with many conductor strips

In order to investigate the reflection of the CMOS ROIC, we have performed a simulation of the reflection of this structure. It should be noted that the reflector is not counted into this simulated structure so that we can investigate the behavior of the ROIC only. To simplify the structure, we have omitted the transistor layer with the silicon wafer beneath and we have limited the domain of simulation to the last (lowest) metallic layer. Thus, in this simulation, the six metal layers with vias (the reflector level is not included) are embedded into the SiO_2 substrate. The dielectric constant and loss tangent of the substrate have been chosen to be 4.2 and 0.025 respectively. The simulation has been carried out with HFSS®.

The simulation shows in Fig. 4.17 a considerable difference in reflection for the two different polarizations. This is mainly due to the different arrangement of metal strip in each corresponding direction. More concretely, polarization 1 corresponds to the direction of long strips at left of Fig. 4.16. Polarization 2 is for other direction. However, the reflection is the characteristic of the whole structure of six metallic layers. Thus, one should not associate the difference in Fig. 4.17 to the geometry of these two metallic layers in Fig. 4.16. At lower frequencies, the wavelength becomes larger than the pixel pitch (50 μm in this case) and therefore the dense array of infinite long conductive strips acts as a good reflector.

As a general comment, this presence of CMOS ROIC under bolometer arrays is specific to uncooled infrared detectors. The consequences of this feature on the optical coupling are discussed in the next section and also in the chapter 6.

4.2.2 Optical coupling at THz frequency range

The THz radiation covers a wide range large, spanning from 300 GHz to 10 THz. It is really difficult -or even unrealistic- to design a detector that can sense the whole spectrum. This is even true for thermal detectors that are credited to be wideband sensors. Therefore it is more realistic to target appropriate designs for limited parts of the THz spectrum.

In the high frequency end of the THz spectrum, the standard infrared bolometer stack, with ~ 2-μm air gap, may still be employed because some modifications can assure a moderately good optical coupling. We have seen in section 4.1.1.2 that the absorption of infinite three-layer structure can reach 22 % at 3 THz if the sheet resistance of the absorber layer is modified from 300 to 50 Ω/□. The absorption increases at higher frequency and attains 35 % at 6 THz and nearly 40 % at 10 THz.

The sheet-resistance modification leads to a degradation of the thermal insulation of bolometers. We have mentioned in chapter 3 that the absorber and the thermal legs are made from the same TiN layer. This layer is patterned so that the central part is large (the absorber) and the edge part is narrow (thermal legs). The reduction of the sheet resistance from 300 to 50 Ω/□ leads to an increase of the thickness of the TiN layer by a factor of 6. This increases thermal conductance of the thermal legs and thus degrade the thermal insulation of bolometers. In order to investigate this effect, we have performed a simple calculation of thermal conductance by using the formulation established in chapter 3. The result shows that the thermal insulation of bolometers is degraded by a factor of ~ 3.5. This effect is not desirable because it decreases strongly the sensitivity of the bolometer.

At lower frequency, for example in the 1–3 THz range, the optical coupling of the absorber is poor (5–10 %), as we have seen in section 4.1.2.2. This low efficiency is primarily due to the mismatch between the 2-μm air gap and the THz quarter wavelength cavity condition as illustrated in Fig. 4.18.

Let us suppose that THz wave at 3 THz impinges on the metallic reflector at normal incidence. At the air-metal interface, the wave is almost totally reflected (the reflection of aluminum surface at THz frequency is around 99 %). The incident wave and the reflected wave combine to form a standing wave in the half space above the reflector. The electric field distribution of the interference follows the sine function

$$E = E_0 \sin(\frac{2\pi}{\lambda} d), \quad \textbf{(4.7)}$$

where d is the distance in respect to the air-metal interface, and λ is the wavelength. The air-metal interface is node position because according to electromagnetism, the good conducting characteristic of the reflector imposes the transverse electric field to be null at the reflector surface. An anti-node (maximum electric field magnitude) is located at quarter wavelength position (25 µm at 3 THz).

At the position of 2 µm above the reflector, the electric field magnitude is only 12.5 % of its maximum value. This low electric field induces a weak THz current on the absorber surface, which explains the low optical coupling of this configuration.

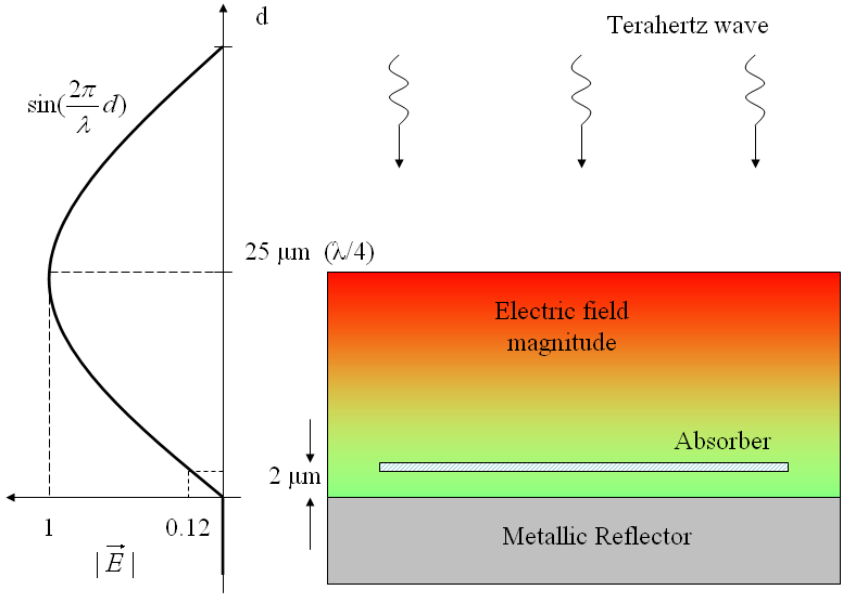

Fig. 4.18: Distribution of electric field on a conducting surface

In reality, the reflector is not infinite, and the presence of the absorber modifies the distribution of the electric field. However the good conducting characteristic of the reflector always imposes that the transverse electric field must be null on the surface. Therefore low optical coupling of the standard bolometer infrared stack in the THz range is an inherent characteristic.

To overcome this constraint, one possible option is to suppress the reflector. In fact, the spider-web design [6], which has been presented in chapter 3, does not employ any reflector because of this phenomenon. However, for uncooled bolometers, even if the reflector is suppressed, the CMOS ROIC is still present underneath the array. Thus optical radiation interacts with the underneath ROIC structure. We have seen that the ROIC structure mentioned in section 4.2.1 acts as a reflector. In such case, the problem of low optical coupling near reflector still remains.

In general, the interaction between optical radiation and the ROIC is very complicated and can lead to a modification of the response of the detector. One should remember that the ROIC structure is extremely complex and varies depending on each circuit design. Due to this complexity, modeling the electromagnetic response of such structure is generally inaccurate; sometimes the response is unpredictable.

The case may get even worse if the ROIC is obtained from a third-party; in such a case, the ROIC structure is unknown, thus it can not be simulated. Therefore, it looks more reasonable to keep the reflector layer and build a thicker cavity. This is the approach that

CEA-LETI has employed in its development of THz bolometer, which is presented in the next section.

4.2.3 THz bolometer stack

4.2.3.1 Structure

In order to solve the optical coupling issue, a specific bolometer stack has been designed at CEA-LETI. We have modified both the vertical cascading layers stack and the pixel pitch. The layers stack makes use of a quarter wavelength cavity tailored for THz frequencies while the pixel pitch is increased to match the absorber dimensions to the wavelength.

At $\lambda = 100$ µm ($f = 3$ THz), quarter-wavelength air-gap cavity has a thickness of 25 µm. This design requires 25-µm height stud for electric contact between the suspended membrane containing thermometer and the read-out circuit. Building 25 µm metallic vias through is considered as too complicated if only standard microelectronic processes are applied.

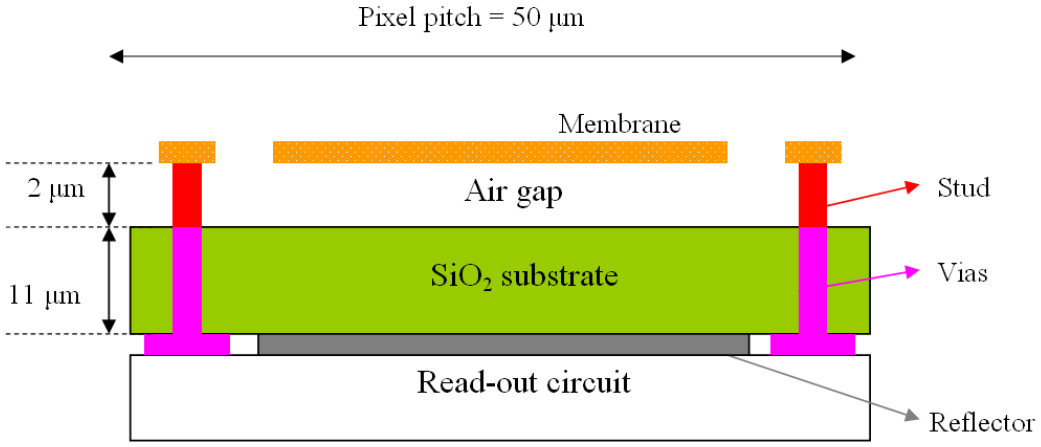

Fig. 4.19: Bolometer stack with 11 µm SiO_2 substrate

A possible way to reduce the cavity height is to fill it partly (see Fig. 4.19) with a substrate that has a high refractive index and a low absorption at THz frequencies. Thanks to the high refractive index, the physical length of the cavity and thus of the vias is reduced. The stack structure is easier to be processed.

Amorphous SiO_2 (fused quartz) is chosen as material for the substrate. The optical properties of fused quartz have been tabulated in some engineering handbooks (for example [7]) and also reviewed recently in paper [8]. It exhibits a nearly constant refractive index close to 2 over 40–500 µm. The refractive index is reported to decrease slightly from 2.1 at 40 µm to 1.955 at 500 µm (the corresponding frequency range is 7.5–0.6 THz). Meanwhile, the imaginary part of refractive index is reported to be low in this spectral range, ranging from 4.6×10^{-2} at 40 µm down to 7.96×10^{-3} at 500 µm.

A specific study has been devoted at CEA-LETI to the development of the technological process of 11 µm-thick SiO_2 cavity with metallic vias. This 11-µm layer and the 2-µm thick air gap (see Fig. 4.19) form together a quarter-wavelength cavity at the wavelength:

$$\lambda = 4(n_{SiO_2} t_{SiO_2} + h_{airgap}) = 4(2 \times 11 + 2) = 96 \ \mu m, \quad \textbf{(4.8)}$$

where the n_{SiO_2}, t_{SiO_2} are respectively the refractive index and thickness of the substrate; h_{airgap} is the air gap height. Clearly, this is a big leap forward to shift the spectral response from infrared (about 10 µm, i.e. 30 THz) to THz (approximately 100 µm, i.e. 3 THz).

The key difficulty of this new bolometer stack is the process of metallic vias ensuring electrical contacts through the cavity. In this case, 11-µm height vias go through the SiO_2 substrate, supplying an electric link between the "regular" bolometer microbridge stud and the read-out circuit. Based on the CEA-Leti experience in bolometer technology, 11-µm thick cavity has been considered as a compromise between electromagnetic optimization and fabrication feasibility and manufacturing yield. And indeed such technological stack has been successfully fabricated for large bolometer array as following chapters will show.

4.2.3.2 Optical coupling

In Fig. 4.20, a simplified structure has been simulated with HFSS of to assess the contribution of this SiO_2 layer on the optical coupling and also to evaluate the dielectric loss. It consists of an array of finite absorbing patches standing separated from the 11-µm SiO_2 layer by a 2-µm thick air gap. The pixel pitch and absorber size are selected to be 35 µm and 29 µm, respectively. This ensures a fill factor close to 70 %, which is a typical value for regular bolometer technology.

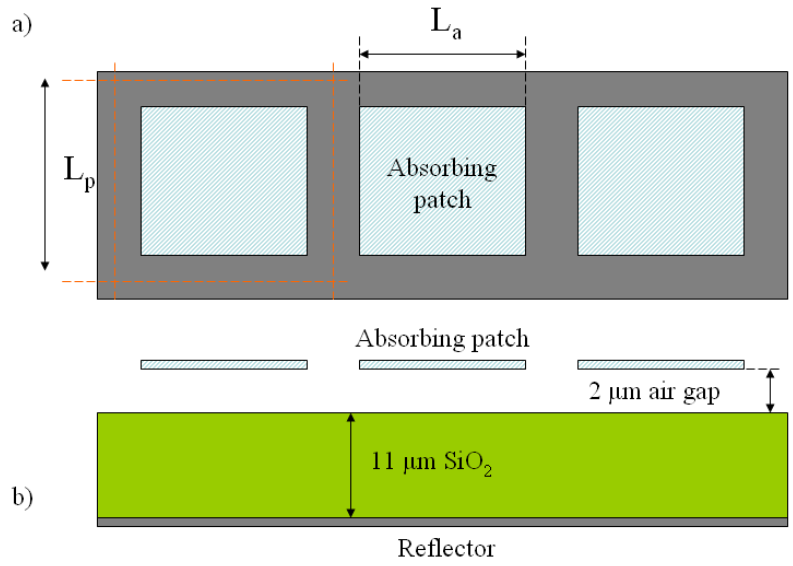

Fig. 4.20: Periodic metallic square patch with 11 µm SiO_2 substrate and reflector underneath

For this simulation, optical constants of SiO_2 gathered by [7] have been employed: the relative permittivity and the dielectric loss tangent at 3 THz are 3.869 and 0.0163, respectively.

In Fig. 4.21, the simulation shows a great improvement of absorption, especially in the vicinity of 3 THz thanks to the THz quarter wavelength configuration. The dielectric losses in the SiO_2 substrate are negligible. Providing its technological feasibility, this result demonstrates the potential of this bolometer stack for the development of uncooled THz bolometer. The actual CEA-Leti design will be presented in the next chapter.

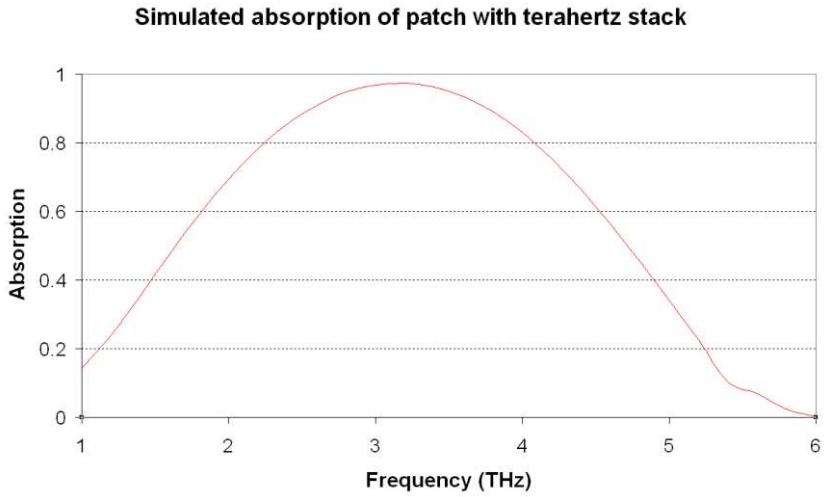

Fig. 4.21: Simulated absorption of the THz bolometer stack

4.3 Summary

In this chapter, we have examined the optical coupling of the infrared bolometer stack. In the first step, the absorption mechanism of the three-layer structure has been investigated in the infrared as well as in the THz range. Then, the electromagnetic simulation of 3D finite structure, which is closer to the real bolometer device, has been performed. This work leads to a conclusion that the infrared bolometer stack exhibits a low absorption at THz frequencies. This low efficiency is an inherent characteristic due to the mismatch between the cavity thickness and the long THz wavelength.

For a high optical coupling in the THz range, a new bolometer stack with quarter wavelength cavity tailored for THz frequencies is required. CEA-LETI has implemented a new THz bolometer stack by adding an 11-µm layer made from SiO_2. This is a big leap forward to shift the spectral response from infrared (about 10 µm, i.e. 30 THz) to THz (approximately 100 µm, i.e. 3 THz). A preliminary simulation shows that optical coupling of this stack is very promising at the vicinity of 3 THz. Optical coupling of actual CEA-Leti designs will be presented in the next chapter.

References

[1] K. C. Liddiard, “Application of interferometric enhancement to self-absorbing thin film thermal IR detectors,” Infrared Physics, vol. 34, no. 4, pp. 379–387, Aug. 1993.

[2] P. A. Silberg, “Infrared Absorption of Three-Layer Films,” J. Opt. Soc. Am., vol. 47, no. 7, pp. 575–578, Jul. 1957.

[3] L. N. Hadley and D. M. Dennison, “Reflection and Transmission Interference Filters,” J. Opt. Soc. Am., vol. 37, no. 6, pp. 451–453, Jun. 1947.

[4] N. Oda, “Uncooled bolometer-type Terahertz focal plane array and camera for real-time imaging,” Comptes Rendus Physique, vol. 11, no. 7–8, pp. 496–509, Aug. 2010.

[5] B. A. Munk, Frequency Selective Surfaces: Theory and Design, 1st ed. Wiley-Interscience, 2000.

[6] P. D. Mauskopf, J. J. Bock, H. Del Castillo, W. L. Holzapfel, and A. E. Lange, “Composite infrared bolometers with Si3N4 micromesh absorbers,” Appl. Opt., vol. 36, no. 4, pp. 765–771, Feb. 1997.

[7] E. D. Palik, Handbook of Optical Constants of Solids. Academic Press, 1985.

[8] R. Kitamura, L. Pilon, and M. Jonasz, “Optical constants of silica glass from extreme ultraviolet to far infrared at near room temperature,” Appl. Opt., vol. 46, no. 33, pp. 8118–8133, Nov. 2007.

Chapter 5 THz bolometer modeling

This chapter presents the design and modelling of several bolometers. On the basis of the mature CEA-Leti technology of infrared bolometers, the design of a specific bolometer stack, optimized for THz detection, was initiated. An innovative THz antenna-coupled bolometer design, named "THEDEX", emerged from this study and prototypes have been fabricated and characterized.

In the frame of this thesis, the THEDEX bolometer structure has been carefully studied, and in particular its optical coupling mechanism. We have employed a 3D electromagnetic receiving mode simulation in which the structure is excited by a plane wave. This kind of simulation is commonly applied for periodic structures including frequency selective surface (FSS) filters [1-2] and arrays of bolometer [3-4]. For antenna-coupled detectors, this approach is not sufficient to estimate all the parameters of the structure. Thus, in addition to the receiving mode, transmitting mode simulations have been carried out. This approach makes possible the calculation of the major antenna characteristics such as its impedance. Not only this method gives a deeper understanding on the detector physics but also it facilitates the impedance matching optimization. The optical coupling of the antenna equipped with a resistive load is formulated in terms of matching impedance, which is proven to be consistent with the absorption in the receiving mode simulation. The combination of the two methods, i.e. transmitting and receiving modes, helps for a better understanding of the THz bolometer operation and thus and for an improved modelling of the design.

By applying these two electromagnetic simulation approaches, several THz bolometer designs have been examined. The study focused on the optical coupling of these detectors in relation to other important features, such as heat capacity and thermal isolation. Clearly, the bolometer design is a trade-off between mechanical, optical, thermal and electric properties. Therefore, the optical coupling study has been considered carefully as part of a larger set of properties.

We first present the absorbing film bolometer (AFB) design. This design is a "THz version" of the traditional uncooled infrared bolometer. The design uses the same approach as uncooled infrared bolometer. However the detector is made bigger to be adjusted to the long THz wavelengths. Then, the antenna-coupled bolometer THEDEX is presented. The use of antennas in the bolometer architecture results in many additional characteristics compared to the AFB design, which should be examined carefully. Since this design has been prototyped, its theoretical study can be compared with experimental measurements that will be presented in the next chapter. The knowledge provided by this work allowed us to propose an improved design (Bambolo design) for THEDEX.

Last but not least, the optical coupling mechanism has been studied for low frequency range. New architectures at 850 GHz have been designed that employ frequency selective surfaces. This new design is very prospective for the development of low THz frequency bolometers. However, it should be noted that since fabrication of THz bolometers requires time and dedicated budget, only the THEDEX design was fabricated during this thesis.

5.1 Absorbing film bolometer (AFB design)

5.1.1 Structure

The perspective view of the bolometer is shown in the figure below. The design is derived from the THz bolometer stack that has been presented in chapter 4. This design makes

use of a large absorbing film as in usual infrared bolometers. The suspended membrane is above the substrate with an air gap of 2 µm.

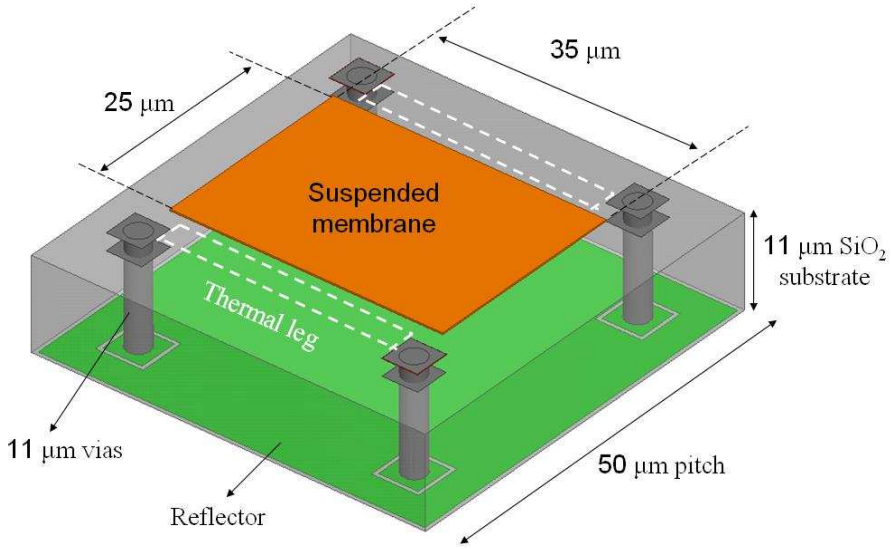

Fig. 5.1: Structure of the AFB design

The central membrane consists of the absorber and the thermometer layers, separated electrically by an insulator film. Its surface of approximately 25 µm × 35 µm results in a geometrical fill factor of 35 % in relation to the 50 µm square pixel pitch.

The suspended membrane and the thermal-insulation legs consist of stacks similar to the classical infrared bolometer case. Fig. 5.2 shows a cut of these layers. Their typical thicknesses have been mentioned elsewhere [5-6], and are synthesized in Table 5.1.

	Material	**Thickness**
Absorber layer	TiN	8 nm
Insulator layer	Si-N	20 nm
Thermometer	amorphous silicon	200 nm

Table 5.1: Thickness of different layers in AFB design

This upper stack is built above an 11-µm height SiO_2 cavity and four metallic vias are made though this substrate in order to electrically connect the thermometer to the read-out circuit. These vias have diameters of 3 µm and are separated from the reflector by a margin of 0.5 µm. The reflector is made of a 300 nm thick layer of aluminum with dimensions 49.5 µm × 49.5 µm. In this way, pixel reflectors are separated from each other by a margin of 1 µm. As explained in chapter 4, this patterning is applied to prevent short circuits.

As we can see, the main difference between this design and the standard infrared bolometer is the introduction of a thick cavity to enhance the THz radiation absorption. The other design difference lies in the dimensions. The pixel occupies a 50 µm × 50 µm square surface while the central microbridge covers an area of 25 µm × 35 µm. As a consequence of this modification of size, the thermal characteristics of detector change.

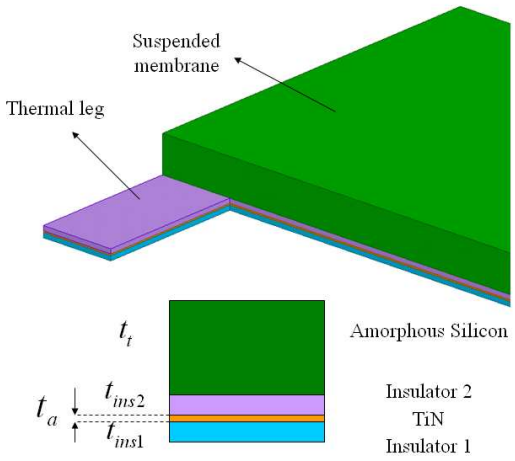

Fig. 5.2: Layered structure of the suspended membrane

5.1.2 Figures of merit

5.1.2.1 Absorption

THz absorption

The absorber is a rectangle, not a square; therefore the electromagnetic response of the bolometer differs from one polarization to the other polarization. In Fig. 5.3, the longer side of the absorber is parallel to the thermal leg direction. We name this direction "Leg-parallel polarization" or LP polarization. The orthogonal polarization is called "Leg-cross polarization" (LC polarization). This naming will applied to all bolometer designs thereafter.

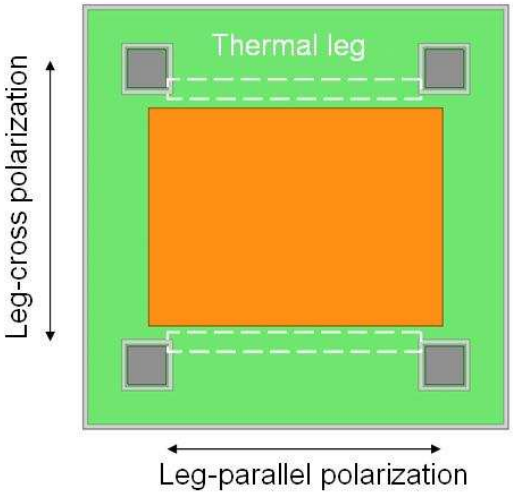

Fig. 5.3: Top view of the AFB design

Fig. 5.4 shows the simulated absorption of the AFB structure. It exhibits a broadband response over the range 1–5 THz. The absorption reaches a maximum near 3 THz and decreases slowly from the peak frequency. The polarization dependence is weak: the absorption in LP polarization is slightly higher than for the other polarization. This comes from the fact that the absorber length in this direction is longer.

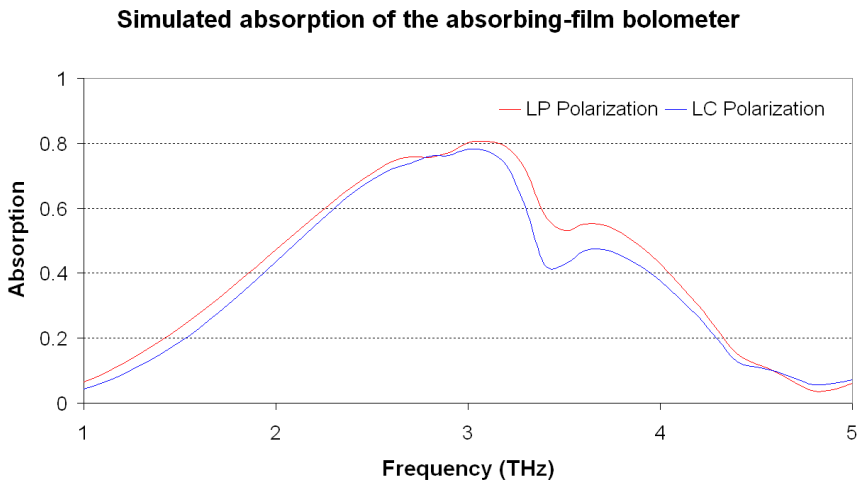

Fig. 5.4: Absorption in both polarization of the AFB design

One may note that the fill factor of this THz bolometer is lower than the one of infrared bolometers, which is usually in the range 50 – 70 %. In order to investigate the impact of the fill factor on absorption, we retrieve the simulation of artificial absorbing patch structures where the patch is freely standing above the SiO_2 substrate without any support leg and without metallic via. This structure has been studied in the last chapter to demonstrate the expected absorption of the proposed THz bolometer stack (refer to section 4.2.3).

We model two artificial structures as illustrated in Fig. 5.5. The first one has the same size of absorber as the actual bolometer. In the second structure, the absorbing patch size is increased to 41.8 µm × 41.8 µm to get a 70 % fill factor for the 50 µm-pitch pixel.

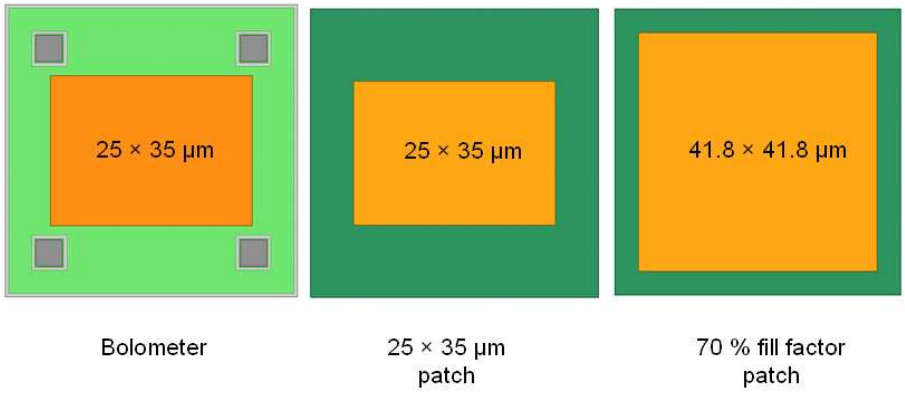

Fig. 5.5: Actual bolometer (left) and two artificial structures that employ the same absorbing film (center) or a bigger absorbing film (right)

In Fig. 5.6, simulations show that when metallic vias are omitted, the absorption of the 25 µm × 35 µm artificial structure is widened. However, the absorption maximum is still about 80 %, as in the case of the bolometer. For the 41.8 µm × 41.8 µm patch structure, the fill factor is increased up to 70%. Thus, the absorption is broader and higher, as expected.

From this simulation, one can say that the absorber size should be bigger to get a better absorption. However, two constraints limit this approach. First, a bigger absorber means an extended suspended membrane. This causes a problem of mechanical strength within the support legs. To maintain mechanical robustness, thermal legs have to be enlarged. This leads to a degradation of thermal insulation of the bolometer. Secondly, as we will show later, a small suspended membrane is necessary to obtain a small heat capacity and therefore a small time constant.

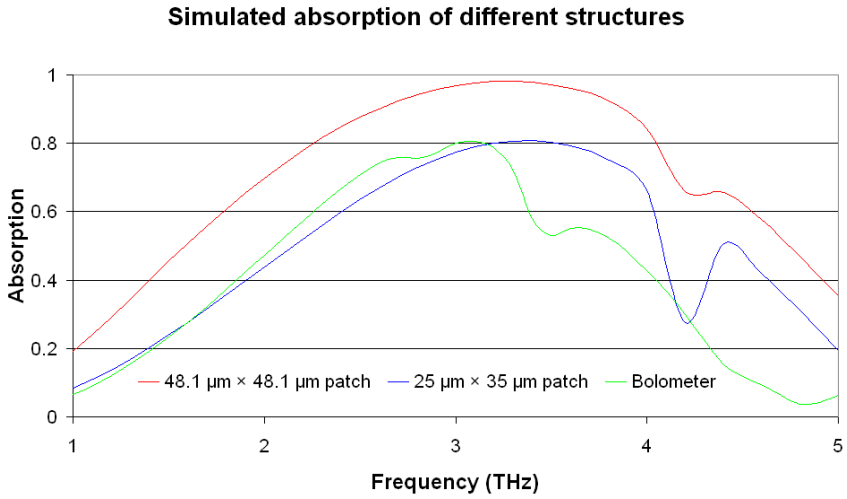

Fig. 5.6: Comparison of absorption between two absorbing-patch structures and bolometer

Infrared absorption

We have seen in chapter 4 that the absorption of a thin metallic film placed above a vacuum THz quarter-wavelength cavity exhibits interference fringes in the infrared range. The average absorption value within the band 8–14 µm is 66 %. The vacuum has constant unity refractive index and is lossless. Therefore, it does not absorb the radiation and the incident wave is dissipated only by the absorbing film.

The simulated absorption in the infrared range of the AFB design is shown in Fig. 5.7 over a very large band spreading from 5 to 25 µm. The cavity of the THz bolometer stack is made of SiO_2, a material that exhibits a strong variation in refractive index and also a high absorption in the range 5–25 µm [7]. This lossy cavity has an impact on the optical coupling efficiency of the detector as explained in the following.

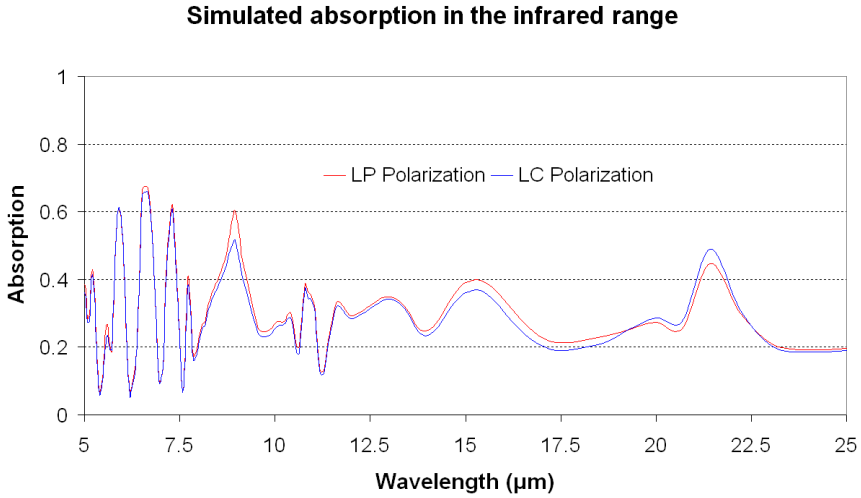

Fig. 5.7: Absorption in infrared range of the AFB design

Let us consider an infrared radiation that impinges on the AFB bolometer. After passing through the lossy 11-µm SiO_2 layer, the wave is reflected by the reflector and once again is attenuated by the SiO_2 layer. When the attenuated reflected wave recombines with the incident wave, the resulting standing wave does not have completely constructive or destructive interference. As a consequence, the absorption in the absorber does not attain to unity or null as in the case of vacuum cavity. The effective absorption of the detector in this

spectral range is 30 %. The definition of this quantity is given by the relation 5.2 in the next section.

5.1.2.2 Thermal characteristics & response time

Thermal conductance

As presented in chapter 3, the total thermal conductance is a combination of the thermal legs conductance and of radiation thermal conductance. The thermal legs have a width of 0.6 μm. By using the formula developed at chapter 3, we evaluate the thermal conductance of thermal legs to be 8.7 nW/K.

The radiation thermal conductance of the infrared bolometer has been presented in chapter 3. This heat exchange is due to radiation exchanges between the bolometer and the surrounding. However, radiation exchanges for THz bolometers have characteristics that differ from infrared bolometers. This heat exchange is inherent and inevitable for uncooled infrared bolometers. However, it is not necessarily true for THz bolometer. Indeed, the radiant spectrum of a blackbody at room temperature (300 K) delivers the greatest portion of energy (82 % of the total radiant power) in the band 5–25 μm. The infrared bolometer works at room temperature, consequently it radiates most of the radiant energy in this spectral range. The infrared radiation of the bolometer depends on the emissivity of the absorber, which is equal to its absorption rate (Kirchhoff's law). Since the infrared bolometer must absorb infrared radiation, it will radiate infrared radiation into the surrounding area. Therefore, the infrared radiation exchange is inherent to infrared bolometers due to the high absorption rate of the detector. Of course, the amount absorbed and radiated are not similar. Absorption is related to the thermal property of the scene and to the optics of camera. Radiation depends on the detector parameters: temperature, emissivity and area.

For THz bolometers, the absorption in the infrared range is strongly undesirable because the THz signal is most of the time weak in comparison to infrared radiation emitted by the ambient environment. In an ideal case, if the THz bolometer does not absorb any radiation in the band 5–25 μm, the infrared radiation exchange between the bolometer and its surroundings can be negligible. This means that the thermal conduction through the legs is the only mechanism of heat losses for the bolometer. In reality, depending on the design, the bolometer absorbs more or less infrared radiation, thus the radiation thermal conductance varies with the bolometer absorption in the infrared.

In order to evaluate more precisely the impact of the infrared absorption on each design, the radiation thermal conductance presented in chapter 3 should be modified as following:

$$g_{rad} = 4A\varepsilon_{eff}\sigma T^3 \text{ [W/K]}. \quad \textbf{(5.1)}$$

where ε_{eff} is the effective emissivity, equal to the effective absorption and defined as:

$$\varepsilon_{eff} = \eta_{eff} = \frac{\int_{\lambda_1}^{\lambda_2} \eta(\lambda) L(\lambda) d\lambda}{\int_{\lambda_1}^{\lambda_2} L(\lambda) d\lambda}. \quad \textbf{(5.2)}$$

Here, $L(\lambda)$ is the radiance of the blackbody at the temperature of interest. In the definition above, the interval λ_1–λ_2 should cover theoretically the whole spectrum. However,

as we have mentioned earlier, at room temperature, the band 5–25 μm gathers more than 80 % of the total radiant power of the blackbody. Therefore, we limit the calculation to this range in order to facilitate the electromagnetic simulations (in practice, it is excessively time consuming to numerically simulate the absorption on the whole spectrum).

A numerical application of equation 5.2 with the simulated spectral absorption of the AFB design (see Fig. 5.7) results in an effective emissivity value of 30 %. The radiation thermal conductance is then:

$$g_{rad} = 4 \times (2500 \times 10^{-12}) \times 0.3 \times (5.67 \times 10^{-8}) \times (298.15)^3 \approx 4.5 \text{ (nW/K)}. \quad \textbf{(5.3)}$$

The total thermal conductance is

$$g_{total} = g_{legs} + g_{rad} = 8.7 + 4.5 = 13.2 \text{ (nW/K)}. \quad \textbf{(5.4)}$$

We can see that the radiation contributes to 34 % of the total conductance in this case.

Heat capacity

The heat capacity of the bolometer is calculated using the formula established in chapter 3. The table below shows the parameters of each layer of the suspended membrane as well as its contribution to the heat capacity. By knowing the dimension and the specific heat capacity of the materials forming the suspended membrane, a simple calculation gives 355 pJ/K as the combined heat capacity. The thermometer contributes to 82 % of the total heat capacity, the same order as in classic infrared bolometers.

Element	**Material**	**Specific Heat Capacity**	**Surface** (μm^2)	**Volume** (μm^3)	Heat capacity (pJ/K)
Insulator 1+2	Si-N	1.12 pJ/(μm^3.K)	875	35.8	40.1
Absorber	TiN	3.26 pJ/(μm^3.K)	875	7.16	23.3
Thermometer	Amorphous Silicon	1.63 pJ/(μm^3.K)	875	179	291.8
Total heat capacity					355

Table 5.2: Detailed parameters and heat capacity for AFB design

In reference to previous electromagnetic simulations, if the size of the suspended membrane is increased to 41.8 μm × 41.8 μm (fill factor of 70 %) to achieve a higher absorption, this approach will be subjected to a penalty on the heat capacity. Actually, in this case, the heat capacity doubles to 700 pJ/K. Thus the time constant also doubles.

Response time

With a heat capacity of 355 pJ/K and a thermal conductance of 13.2 nW/K, the time constant of the AFB design is:

$$\tau_{th} = \frac{C_{th}}{g} = \frac{355\,pJ/K}{13.2\,nW/K} = 26.9\ ms \tag{5.5}$$

With this time constant, the optimum frame rate of detector is:

$$f_c = \frac{1}{3\tau_{th}} = \frac{1}{3\times 26.9\times 10^{-3}} = 12.4\,Hz \tag{5.6}$$

The useful range of frame rate depends on each application. For instance, standard real-time video rate is 25 Hz. Lower frequencies can be employed in stand-off imaging application, in which the object rests at its position during the imaging capture time. We can easily see that if the bolometer has a fill factor of 70 %, the time constant will be 54 ms. In this case, the frame rate decreases to 6 Hz.

It should be noted that thanks to microelectronic technology, the thermal conductance can be easily increased by processing larger thermal legs. Of course, this modification will degrade the sensitivity of the detector but also make it faster. If a 25 Hz frame rate is desired, the bolometer should have a thermal time constant equal or lower than 13.3 ms as mentioned previously in chapter 3. This can be accomplished by increasing the thermal conductance to

$$g_{th} = \frac{C_{th}}{\tau_{th}} = \frac{355\,pJ/K}{13.3\,ms} = 26.7\ nW/K. \tag{5.7}$$

The sensitivity will be roughly 2 times smaller than with a bolometer that has a thermal conductance of 13.2 nW/K.

5.2 Antenna-coupled bolometers (THEDEX design)

5.2.1 Structure

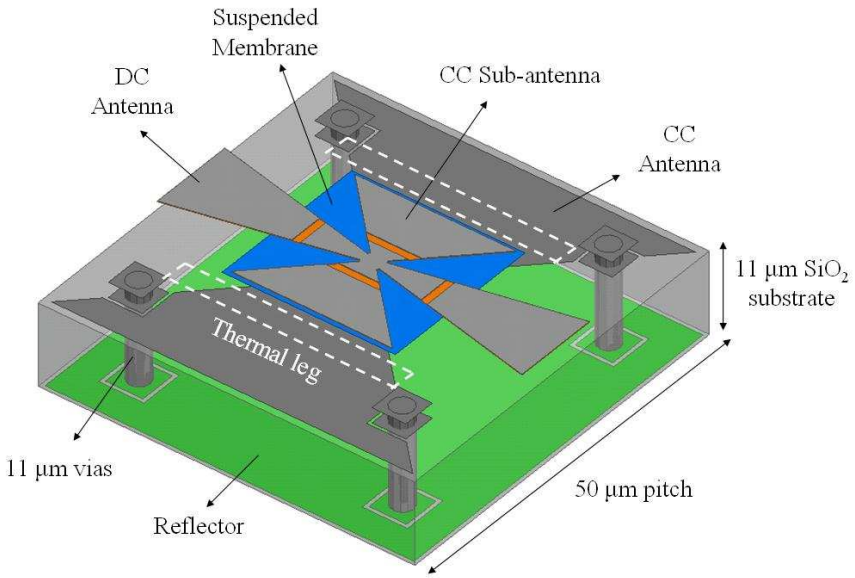

Fig. 5.8: Detailed structure of bolometer THEDEX

The antenna-coupled bolometer structure of a single 50-µm pitch pixel is shown in Fig. 5.8. The design associates quasi double-bowtie antennas to a thermometer microbridge

structure derived from the standard infrared bolometers. The function of these antennas is to couple the incident wave to the load resistances, located at the center of the bolometer suspended membrane. This membrane is mechanically suspended over the substrate by thermal legs and stud as the AFB design.

For one direction of THz radiation polarization, the longer bowtie antenna located on the microbridge, named "DC (direct coupling) Antenna", is directly excited by the incident wave. The induced THz current on the surface of this bow-tie is converted to heat at the resistive loads. Due to the limited distance between the two thermal arms, the antenna length in this direction is limited to 21 μm in comparison to 49 μm of the DC antenna. The limited length antenna (sub-antenna) is coupled via a capacitive coupling mechanism to a bigger antenna, "CC (capacitive coupling) Antenna," located below at the substrate level.

The loaded antennas and the bolometric element are represented together in Fig. 5.9. The DC antenna is 49 μm long and has a bow angle of 13^o. The CC antenna and sub-antenna have the same bow angle of 45^o, their lengths are 49 μm and 21 μm, respectively. For each antenna, the resistive load is a couple of two resistors. Resistors are made from a 300 Ohm/square resistive layer and have a value of 67 Ω for DC polarization and 47 Ω for CC polarization due to the different dimension between DC and CC resistors. Since these two resistors (for each antenna) are symmetric and the distance between them is small compared to the operating wavelength (100 μm), the antenna can be considered roughly as if it has a single resistive load at center with double resistance: 134 Ω and 94 Ω for DC and CC antennas, respectively. With this configuration, we can choose the value of the resistive load for each antenna independently to optimize the impedance matching for each antenna.

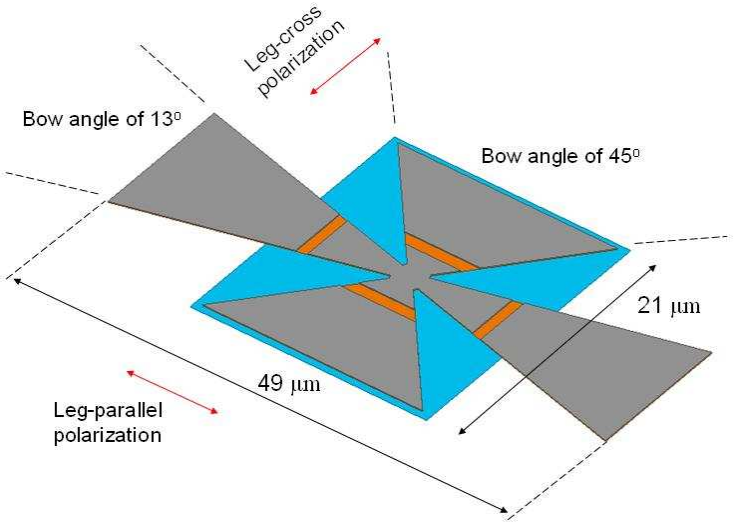

Fig. 5.9: General three layer structure for uncooled infrared bolometer

The amorphous silicon layer that serves as thermometer is isolated electrically from the loaded antennas by a thin insulator layer. In this way, we separate the energy collecting part (loaded antennas) from the sensing part (thermometric element) in order to easily optimize each function. In fact, the resistance of the amorphous-silicon bolometer is typically equal to several hundreds of kΩ, so it cannot be used as the resistive load of the antenna, as is usually the case of the superconducting antenna-coupled bolometer (for instance, the resistance of the superconducting bolometer of NIST/VTT [8] is 130 Ω). Fig. 5.10 represents the stack of layers that composes the suspended membrane. The layers are separated intentionally with an (artificial) large distance for clarity purpose.

We can see in Fig. 5.8 that the DC antenna has a part that overhangs the central membrane. This causes a risk of the mechanical weakness of the DC antenna. Thus, the thermometer has been extended out the central square part. These stubs mechanically strengthen the DC antenna tips. However, this extension increases the surface of the thermometer layer to 832 μm^2 when compared to the surface of the central part (598 μm^2).

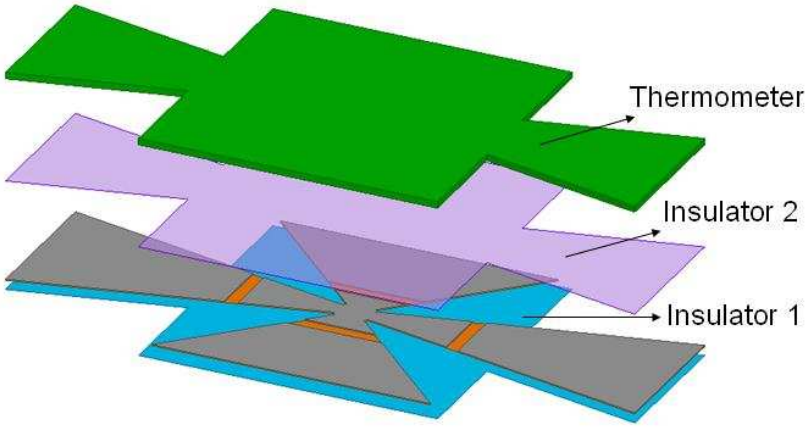

Fig. 5.10: Different layers of the suspended membrane showing the antenna is insulated from the thermometer

The stacks of the suspended membrane differ significantly between the absorbing film of the AFB design and this antenna-coupled bolometer (ACB) structure. The ACB design employs antennas to collect the incident wave. This type of absorber has different characteristics in term of optical coupling when compared to the large and thin rectangular absorbing film. Aside from the optical coupling, the presence of the aluminum chosen for the antenna layer of the suspended membrane will affect strongly the bolometer heat capacity and then the time constant. These aspects are considered in the following section.

5.2.2 Figures of merit

5.2.2.1 Absorption

THz absorption

The absorption of the antenna-coupled bolometer over 1–5 THz is presented in the figure below. We observe several absorption peaks that differ according to the polarization. At this point, it is clear that when loaded antennas are used as absorber instead of the absorbing thin film, the absorption depends strongly on the polarization. It is not surprising because, unlike AFB design that exhibits symmetric shape in each direction, antenna-coupled bolometer has different antenna structures for each polarization. This results in resonance frequencies specific to each antenna.

For the leg-parallel polarization, the DC bowtie antenna is excited. The bolometer exhibits an absorption peak of 86% at 1.35 THz. The absorption curve exhibits a dip at 1.8 THz with only 4 % of absorption. Beyond this frequency, the absorption increases with frequency in general. The absorption curve undergoes some oscillations at higher frequencies.

If a leg-cross polarized radiation is impinging, the CC bowtie antenna is excited. The absorption curve in this polarization shows a peak at 1.75 THz with absorption rate of 96 %. The bolometer has another 85% absorption peak at 4.2 THz. Between these two absorption peaks, the absorption curve exhibits a valley that shows a minimum of absorption of 40 % at 3 THz.

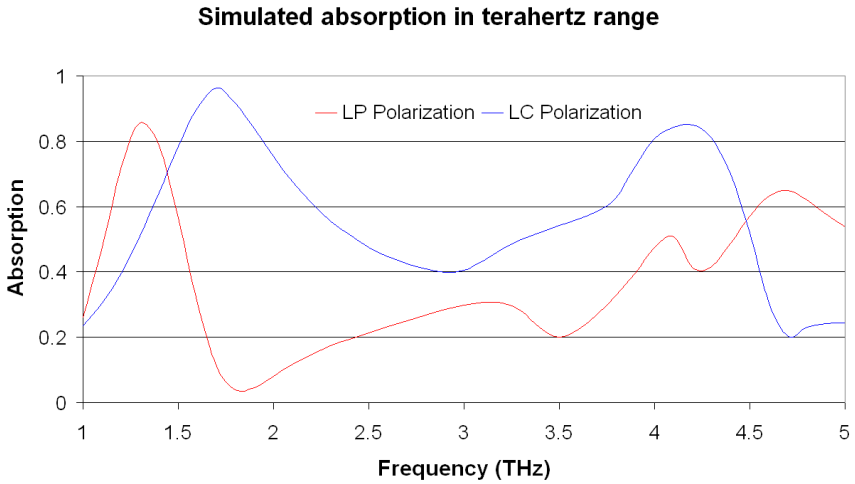

Fig. 5.11: Simulated THz range absorption of THEDEX design

The absorption in each polarization exhibits a rather large bandwidth in the range 1–5 THz although the bolometer does not show a flat response. The absorption rate between 2.5 THz and 3 THz is quite low, about 20 – 40 %. This can be improved by a proper design as we will see later. The most important characteristic of this design in terms of optical coupling is that, though the pixel pitch is kept small, the bolometer can absorb efficiently at low frequency (1.35 and 1.75 THz). This is not the case of the AFB design for which the absorption is optimized for frequency corresponding to the quarter wavelength, i.e. about 3 THz. The electromagnetic response of the antenna will be studied in detail in the section 5.2.3.

Infrared absorption

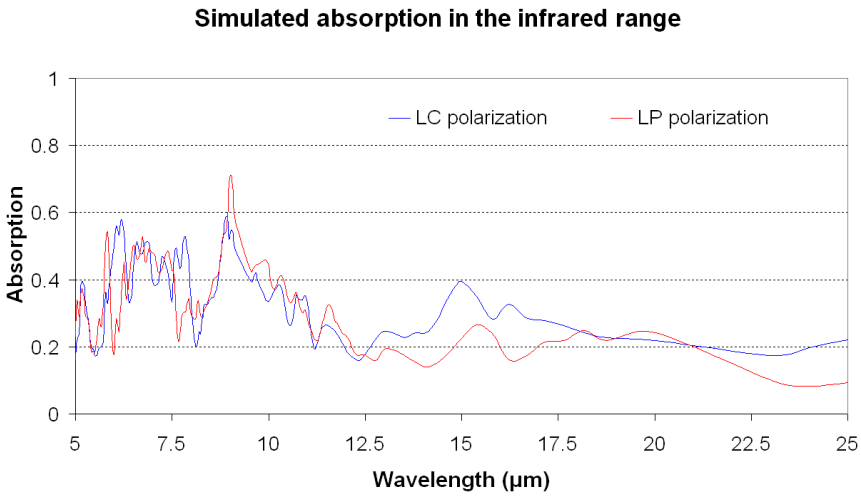

Fig. 5.12: Simulated infrared range absorption of THEDEX design

The absorption curves of the two polarizations are not as similar as found in the case of the AFB design. However, they are roughly in the same range. The effective absorption over the range 5–25 µm is 29 %, almost the same as the AFB design. This is quite surprising at a first glance. One would expect the AFB design to be more sensitive to infrared radiation since it has a large absorbing film. The THEDEX design does not integrate a large absorbing film but antennas loaded with a small resistor instead. Thus it should absorb much less the infrared radiation since the antennas do not function efficiently at this too high frequency (30 THz).

A close study of the different THEDEX design elements that contribute to the total absorption, reveals that the thermometer electrodes intervene greatly. As explained in chapter 4, the thermometer electrodes are made within the same layer as the absorber that has a 300 Ω/□ sheet resistance. The CC bowtie antenna is actually located 2 μm below this layer, thus it behaves as a reflector in the infrared range. The ACB electrodes absorb strongly infrared radiation because of this configuration. In the case of AFB design, although the absorber has a large area when compared to the electrodes area, the absorber does not absorb strongly infrared radiation because of the lossy SiO_2 cavity.

5.2.2.2 Thermal characteristics & response time

Thermal conductance

The thermal legs have a width of 0.6 μm, similarly to the AFB design. However, the shape of the thermal leg is modified in order to obtain a better mechanical strength. As we can see in Fig. 5.8, a portion of the DC antenna overhangs the rectangular membrane. The DC antenna is 49 μm long and is only at a 2 μm height above the SiO2 substrate. If it gets inclined because of mechanical stresses, it can easily touches the substrate and then thermally short-circuit the bolometer. In order to keep horizontal the DC antenna, the mechanical strength of the supporting legs has been increased by changing their shape, resulting in a slight decrease of the thermal isolation. Thermal conductance of legs is then 11.8 nW/K.

The simulated of infrared absorption of the antenna-coupled bolometer is employed in equation 5.2 and gives an effective emissivity value of 29 %. Hence the radiation thermal conductance is:

$$g_{rad} = 4 \times (2500 \times 10^{-12}) \times 0.29 \times (5.67 \times 10^{-8}) \times (298.15)^3 \approx 4.4 \text{ (nW/K)}. \quad \textbf{(5.8)}$$

We can see that the thermal conductance by radiation is almost the same as in the case of AFB design. The total thermal conductance is

$$g_{total} = g_{legs} + g_{rad} = 11.8 + 4.4 = 16.2 \text{ (nW/K)}. \quad \textbf{(5.9)}$$

In practice, the fabrication of the thermal legs may suffer of over-etching. For example, leg width may be reduced from 0.6 μm to 0.5 μm resulting in a higher thermal insulation. In such case, thermal conductance is reduced from 11.8 to 9.8 nW/K. If the over-etching is taken into account, the total conductance in this case is 14.2 nW/K.

Heat capacity

As seen previously, the calculation of the suspended membrane heat capacity requires the knowledge of the volume and of the specific heat capacity of each element. The presence of the antenna changes the size of each component in the suspended membrane. Also, the aluminum antenna layer adds a considerable portion to the total heat capacity of bolometers. The table below shows the calculation of the elementary and total heat capacities. The specific heat capacity of aluminum is its bulk value, which is reported in [9].

Element	**Material**	**Specific Heat Capacity** pJ/(μm^3.K)	**Surface** (μm^2)	**Volume** (μm^3)	Heat capacity (pJ/K)
Insulator 1+2	Si-N	1.12	832.1	33.3	37.3

Absorber	TiN	3.26	523.2	4.2	13.7
Thermometer	Amorphous Silicon	1.63	832.1	166.4/case 200 nm 249.6 /case 300 nm	271.3 406.8
Antenna	Aluminum	2.43	501.4	125.4 (250 nm thickness)	304.7
Total heat capacity					627/763

Table 5.3: Detailed calculated values of the heat capacities of the THEDEX design

Dimensions of each element are easily extracted from the computed aided design (CAD) models. However in practice, depending on the process employed to fabricate the bolometer, the dimension of each component may present some uncertainty, in particular the thickness. The greatest uncertainty comes from the thickness of aluminum layer (the antenna layer). It can vary from 300 nm by design to about 250 nm in reality. This layer is eroded during the process of removing the polyimide layer. So 250 nm Al thickness is considered in our calculation. Depending on the desired thermometer resistance, the amorphous silicon layer can be 200 nm or 300 nm thick. The later value decreases the thermometer resistance to match read-out circuit requirements at the expense of increased heat capacity.

As we can see in table 5.3, in the best case, the total heat capacity of the bolometer is 627 pJ/K for a 200 nm thickness thermometer. It may increase up to 763 pJ/K if the thermometer thickness is chosen to be 300 nm. The presence of the metal antenna imposes an extra heat capacity of about 305 pJ/K, which represents half the total bolometer heat capacity. The amorphous silicon thermometer contributes to 43–53 % of the total heat capacity. Compared to the 355 pJ/K value of the AFB design, the presence of this metallic antenna on the micro-bridge structure increases dramatically the heat capacity of the bolometer.

Response time

The smallest total heat capacity of the bolometer is 627 pJ/K (200-nm thermometer thickness). Combining this value to the thermal conductance presented above, it comes out that the time constant for the best case (lowest thermal conductance) is:

$$\tau_{\text{th}} = \frac{\text{C}_{\text{th}}}{\text{g}} = \frac{627\ \text{pJ/K}}{16.3\ \text{nW/K}} = 38.5\,(\text{ms}) \qquad \textbf{(5.10)}$$

With this time constant, the detector can reach the frame rate of:

$$\text{f}_{\text{frame}} = \frac{1}{3\tau_{\text{th}}} = \frac{1}{3\times 38.5\times 10^{-3}} = 8.7\,(\text{Hz}) \qquad \textbf{(5.11)}$$

In the envisaged case of over-etching, the thermal conductance is 14.2 nW/K so the time constant would be 44.2 ms. The frame rate would then be 7.5 Hz. We can see that such time constant becomes really disadvantageous for applications that require fast detection. It has motivated research of new designs that bring time constant reduction.

5.2.3 Impedance matching for antenna-coupled bolometer

From the optical coupling point of view, there is a significant difference in designing the absorbing film bolometer and the antenna-coupled bolometer. In AFB design, the absorber is a rectangular metallic film. The thickness of this film is made very small and the material is quite resistive so this layer is lossy. The incident wave induces THz currents in the film which in turn produce Joule heating in this layer. This conduction loss is distributed because the whole absorbing film is lossy.

In contrast, the resistively loaded antenna has two parts. The antenna itself is made of high conductive metal (aluminum) and is thick enough so that the conduction loss at the antenna is very small. This antenna is ended by a resistive load made from low conductive metal. The induced current is not dissipated at the antenna; it is dissipated essentially at the load by conduction loss mechanism. One can see that, in this case, the conduction loss is local.

We employ a simple calculation to demonstrate the above argument. The absorbing film of the CEA-LETI bolometer is made of titanium nitride (TiN), whose measured resistivity is 2.4×10^{-6} Ω.m. At 3 THz, the skin depth is:

$$\delta_{\text{skin}} = \sqrt{\frac{2\rho}{\omega\mu}} = \sqrt{\frac{2\times 2.4\times10^{-6}}{2\pi\times3\times10^{12}\times4\pi\times10^{-7}}} = 450\,\text{nm} \qquad \textbf{(5.12)}$$

Meanwhile, the skin depth in aluminum is 47 nm at 3 THz, and 149 nm at 300 GHz. This calculation uses the value of measured resistivity of 3×10^{-8} Ω.m that slightly differs from the value of 2.65×10^{-8} Ω.m given in literature [9]. The thickness of bolometer aluminum layer varies between 250 and 300 nm, and therefore is always greater than the skin depth. In contrast, the TiN layer thickness is 8 nm, much less than the skin depth in the THz range. This TiN layer is very lossy and has an impedance of 300 Ω/□.

In order to maximize the efficiency of the antenna loaded by resistors, antenna and load impedances must be matched. In the case of a resistor load, the load impedance is purely resistive. Supposing that the antenna impedance and the load resistance are respectively Z_A and R_L, the reflection coefficient at the feed point of the antenna is:

$$\Gamma = \frac{R_L - Z_A}{R_L + Z_A}. \qquad \textbf{(5.13)}$$

In receiving mode, the incident wave induces a THz current in the antenna; the antenna distributes the current to its load. Depending on the impedance matching, one part of the current is actually delivered to the load, the other part is reflected. The reflected part is then reradiated by the antenna into free space. In terms of power, the ratio between the power delivered to the load and the available power on the antenna is:

$$e_{\text{matching}} = 1 - |\Gamma|^2. \qquad \textbf{(5.14)}$$

This parameter defines the efficiency of antenna impedance matching in terms of power. If load resistances are not properly chosen, the wave is not entirely absorbed by the antenna-load structure. Therefore, impedance matching is important to get efficiently antenna-coupled bolometers. This problem does not occur in AFB design since, in this case, the induced

current in the absorber layer is dissipated in a wide spatially distributed manner. By contrast, in antenna-coupled structures, the current is dissipated locally in the resistive load.

The impedance matching is best performed when the antenna-impedance is known. In the next section, simulations are conducted in order to calculate this parameter.

5.2.3.1 Transmitting antenna oriented simulation

One possible way to model the antenna-coupled bolometer electromagnetic behavior is to use the Floquet port formalism with periodic boundary conditions. This simulation approach has long been used to simulate frequency selective surfaces (or FSS), thus we refer from now on as "FSS simulation".

Fig. 5.13 demonstrates the principle of this type of simulation. This simulation is usually applied to large periodic structures (large array of repetitive cells). The whole structure is usually very large in comparison to the wavelength; therefore the simulation with free space boundary is not efficient, and sometimes even impossible because of the enormous mesh numbers. The FSS simulation considers only one elementary cell and so one pixel in the case of array of detectors; it embeds the cell into an “air-box” that mimics the free space, and assumes periodic boundary conditions on the four lateral walls of the air box. In this way, the number of mesh is drastically reduced and the simulation is much more efficient than in the free space boundary case. An excitation is set at the upper Floquet port to mimic an incident planar wave propagating from free space into the simulated structure.

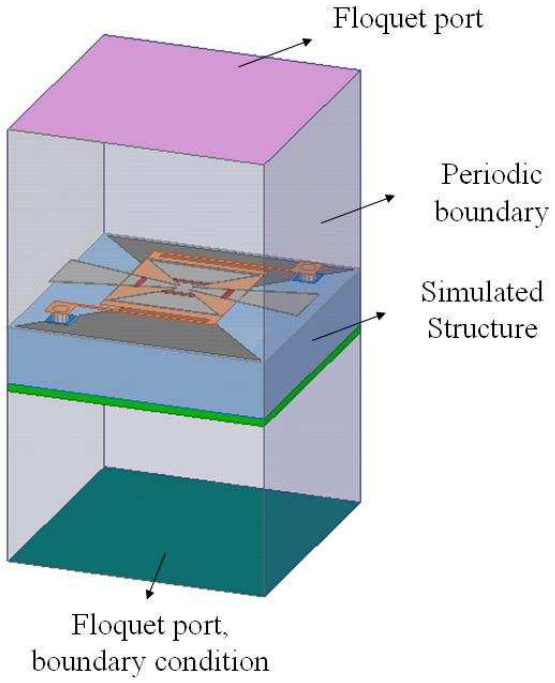

Fig. 5.13: Receiving mode simulation, the structure is excited by Floquet port that mimics plane wave

The FSS simulation can be applied to any periodic structure, whether it is lossy or lossless. Arrays of detectors have been successfully modeled with such an approach [3-4]. The great advantage is that this simulation can be very versatile: the structure can have any shape and any material. Therefore, the absorbing film or antenna-coupled bolometer design can benefit of this method.

By knowing the distribution of electric field in the sensor structure, the dielectric and conduction losses in any element may be retrieved. These loss mechanisms represent of

absorption of the whole sensor structure. The "useful" absorption, i.e. the one that contributes to the detection, here the Joule heating of the suspended membrane, is retrieved by properly selecting this component of the detector. Knowing this useful heat and the power of radiation incident at the Floquet port, one can deduce the spectral absorption $\eta(f)$ of the bolometer:

$$\eta(f) = \frac{\sum \text{Losses}_{\text{membrane}}}{P_{\text{Floquet\_port}}}. \quad \textbf{(5.15)}$$

The main drawback of FSS simulation, when applied to the antenna-coupled bolometer, is the impossibility to calculate the antenna impedance. In this context, in order to perform the impedance matching, the value of the resistive load is swept over the antenna impedance range that is typically from 50 to 150 Ω at resonance frequency. For each load value, the absorption is calculated and the optimum is identified. So impedance matching with FSS simulations can be achieved thanks to the computation of absorption. However, this method does not provide any information on the antenna behavior as a function of frequency that is ultimately important to design a good antenna with predefined bandwidth.

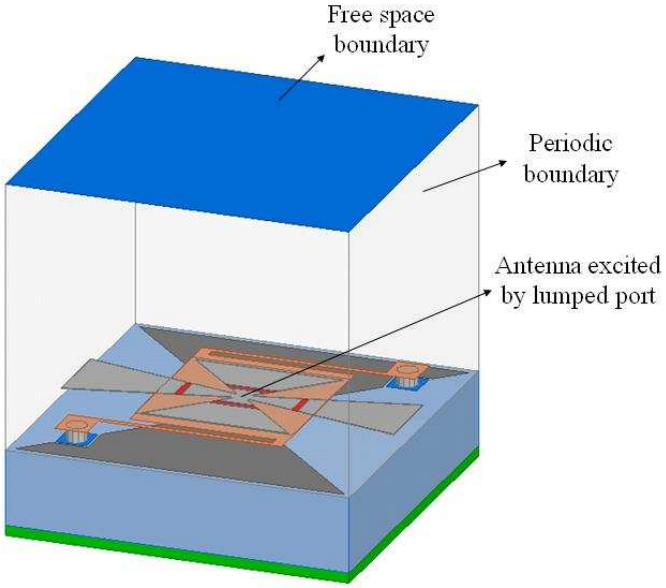

Fig. 5.14: Transmitting mode simulation, antenna is excited by lumped port.

We have tried to apply the transmitting simulation to the antenna-coupled bolometer structure in order to calculate the antenna-impedance. To work in the transmitting mode, we used a lumped-port to excite the antenna structure. The Floquet port is replaced by radiating boundary to mimic free space. The periodic boundary condition is still kept on the cell side to take into account the periodicity of the pixel array. Since, to the best of our knowledge, wafer probing techniques to measure the antenna impedance in the THz range are still limited to frequencies inferior to 1 THz, the simulated impedance is not experimentally verifiable. Thus, consistency between the transmitting simulation presented here and FSS simulation is very important to validate our study of antenna impedance. The consistency between the two types of simulation is given in this manuscript after presenting the antenna impedance.

The greatest difficulty in performing transmitting simulations is to define the antenna excitation. As presented in Fig. 5.15, the antenna layer contains both DC antenna and CC sub-antenna. Each antenna is equipped with a pair of resistors. The antennas and the four resistors are electrically connected. One can think about replacing the four resistors by four lumped-

ports. This can make the simulation very complex, especially when a portion of the current excited by one port will go towards another port instead of radiating into free space. Also, the antenna impedance cannot be obtained directly from the ports. To simplify the problem, we chose an approximated approach.

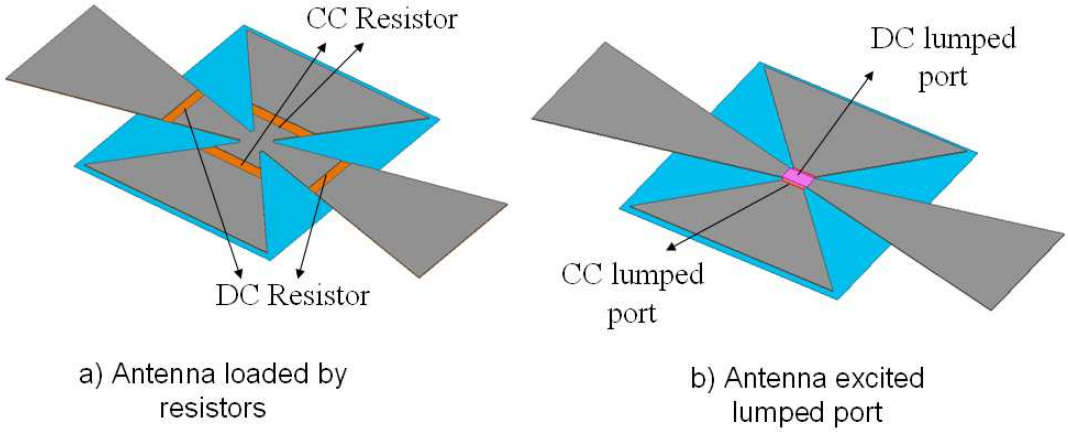

Fig. 5.15: Modeling of resistive load by lumped port

In this approach, we use a unique lumped-port to emulate antenna resistors; the port impedance value is set as the equivalent resistance of the pair of resistors (in series). Thus the DC lumped-port and the CC lumped-port are given impedance values of 94 and 134 Ω respectively. The DC antenna and its port are artificially transposed up (vertically) a distance of 0.2 µm referring to the CC antenna so that two ports are not superposed. With such modification, we have approximated the "monolayer" antenna to two distinct antennas, which are separated by a distance of 0.2 µm. Since this distance is very small when compared to the antenna size and wavelength, the functioning of both antennas is not affected greatly by the transposition.

5.2.3.2 Impedance matching

In antenna theory, the fundamental resonance of antennas is critical because it states the lowest frequency where the antenna can couple efficiently to electromagnetic waves. In the ACB structure, the antenna itself is a part of the suspended membrane. Previous calculations have shown that it contributes largely to the bolometer heat capacity. Thus one of the rules in designing such sensors is to use the smallest size antenna for a predefined frequency, meaning to operate at the fundamental resonance. This approach goes in the right direction since it helps the bolometer keeping a small heat capacity, and consequently a small time constant.

Using the transmitting simulation methods described previously, we examine the impedance of the antennas in the vicinity of their lowest absorption peaks (1.35 THz for DC antenna and 1.75 THz for CC antenna).

The DC antenna shows a resonance at 1.35 THz characterized by a local maximum of the resistance while the reactance curve exhibits an inflection point near this frequency. This "impedance resonance" coincides with the "absorption peak". The impedance of DC antenna at this resonance is $91 - j \times 99\,\Omega$. With a resistive load of 134 Ω, the efficiency (calculated with equation 5.11) of DC antenna at resonance is 81 %.

At resonance frequency, the reactance part is not null but is negative. It increases with frequency and attains zero at 1.9 THz. However, at this frequency, the resistance of antenna is very small meaning the radiation capability of antenna is low. At this point, we can see that the impedance of DC antenna in a dense array is different from antenna in free space. For the

latter, at resonance frequency, when the reactance is null, the resistance is high enough (73 Ω in the case of dipole) so that the antenna can radiate efficiently.

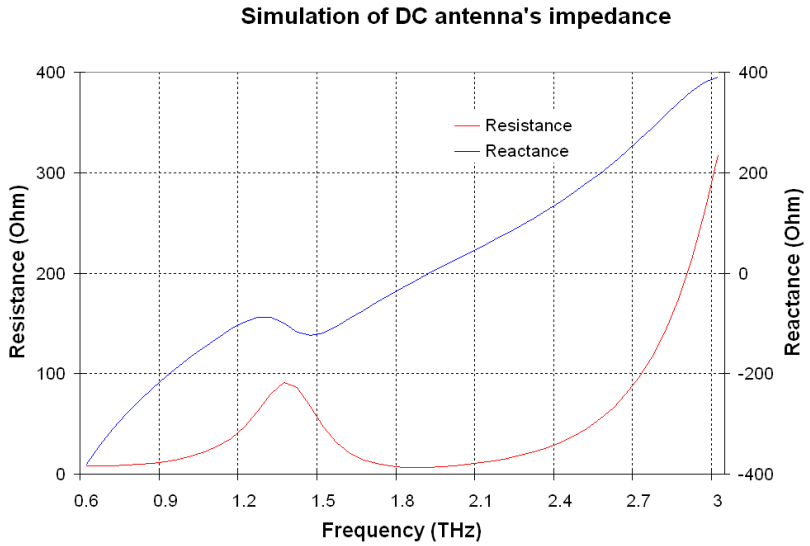

Fig. 5.16: Impedance of the DC antenna shows a resonance at 1.35 THz

The negative value of DC antenna reactance means that the antenna behavior is capacitive. There are several facts that may lead to this capacitive behavior. The first one is that the antenna length is too small in comparison with the wavelength. Let us consider the effective dielectric constant to be equal to 2.535 as the mean of dielectric constants of vacuum and SiO_2 ($\varepsilon = 3.869$ at 3 THz). A classic dipole antenna in such dielectric medium that exhibits the same resonance frequency at 1.35 THz would have a length of 70 µm. The DC antenna has a finite length of roughly 50 µm, thus smaller than this value.

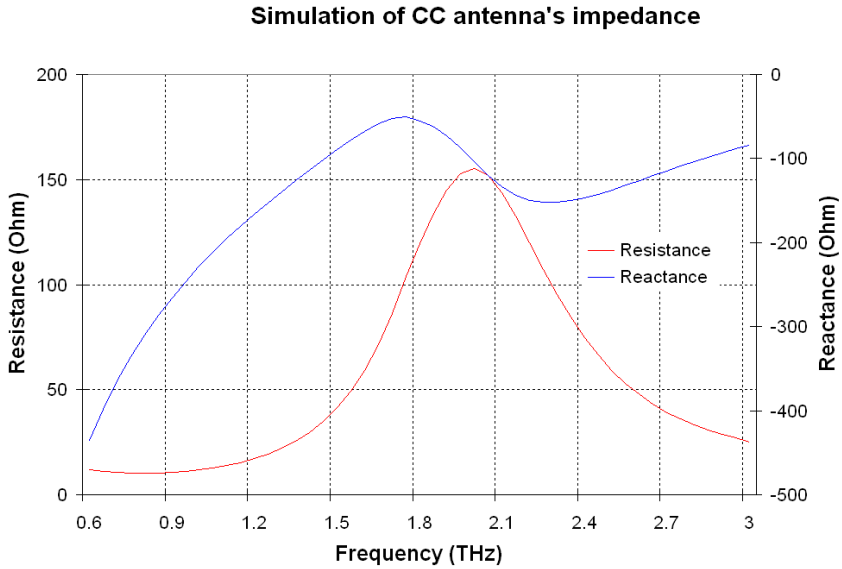

Fig. 5.17: Impedance of CC antenna shows a resonance at 2 THz.

Another phenomenon is that the antenna is set too close to the reflector if we consider the frequency of 1.35 THz. One should remember that the SiO_2 cavity height is optimized for nearly 3 THz. This height becomes too small when compared to quarter-wavelength at 1.35 THz. In such case, the coupling between antenna and reflector prevents antenna from radiating and adds a capacitive characteristic to the antenna behavior.

The last phenomenon is the capacitive coupling between metallic patches in a dense arrangement of metallic antennas. This is similar to the effect of the metallic reflector when the antenna is set too close to it.

Regarding the CC antenna, the simulated impedance shows a resonance at 2 THz. This "impedance resonance" is, however, slightly different from the "absorption peak" that occurs at 1.75 THz (see section 5.2.2). The absorption is affected strongly by the matching between the antenna impedance and the load–resistance. The CC antenna impedance has a value of $155 - j \times 104\ \Omega$ at 2 THz and $104 - j \times 50\ \Omega$ at 1.75 THz. With a load resistance of 94 Ω, the matching efficiency is 80 % at 2 THz, lower than 94% at 1.75 THz. However, if the load resistance were 250 Ω for example, the matching efficiency would be 66 % at 2 THz, higher than 57 % at 1.75 THz. Thus we can see that although the impedance of the antenna exhibits resonance at a frequency, the absorption peak frequency may be slightly different depending on the impedance matching.

The CC antenna–impedance also shows negative values at resonance similarly to DC antenna. Once again, we associate this behavior to the same phenomena as previously described.

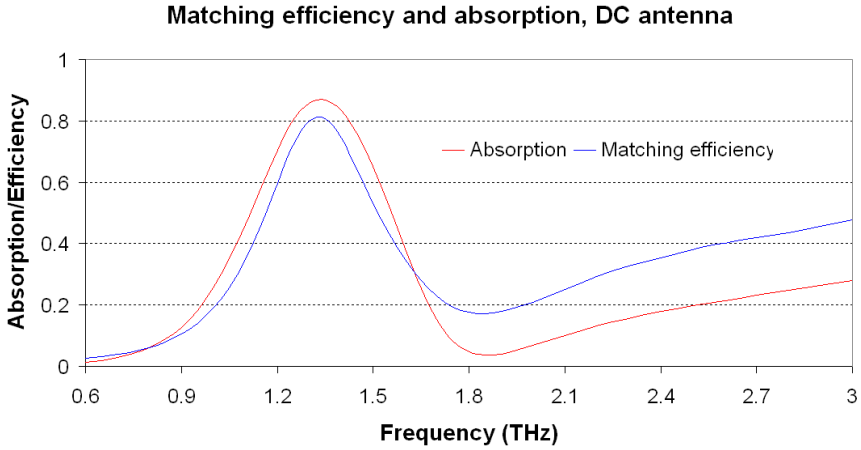

Fig. 5.18: Comparison between absorption (receiving mode simulation) and matching efficiency (transmitting mode simulation) for leg-parallel polarization.

These simulations show that the antenna impedances are not purely resistive at resonance frequency. Thus a perfect impedance matching between antenna and resistive load cannot be performed. However, the calculated antenna efficiency demonstrates that this issue is minor since the efficiency rate superior than 80 % corresponds to a high useful absorption. This is the range of absorption of uncooled IR bolometer. For THz detector, some other antenna-coupled bolometer designs, such as the superconducting bolometer at VTT/NIST [8], lead to an absorption in the same range (80 %) for the best case. In Figs. 5.18 and 5.19, the efficiency calculated from the transmitting mode simulation and the absorption of the FSS simulation is plotted on the same figure.

As shown by these plots, the results of the two simulation types (transmitting mode and receiving mode) are quite consistent. In general, the shape of the impedance matching efficiency and the absorption curves are similar, both curve predict the same absorption peak at 1.35 THz and 1.75 THz for DC and CC antennas, respectively. However absolute values differ. This discrepancy may come from the approximation that is applied in transmitting mode when the couple of resistors are modeled as-a lumped-port located at the antenna center.

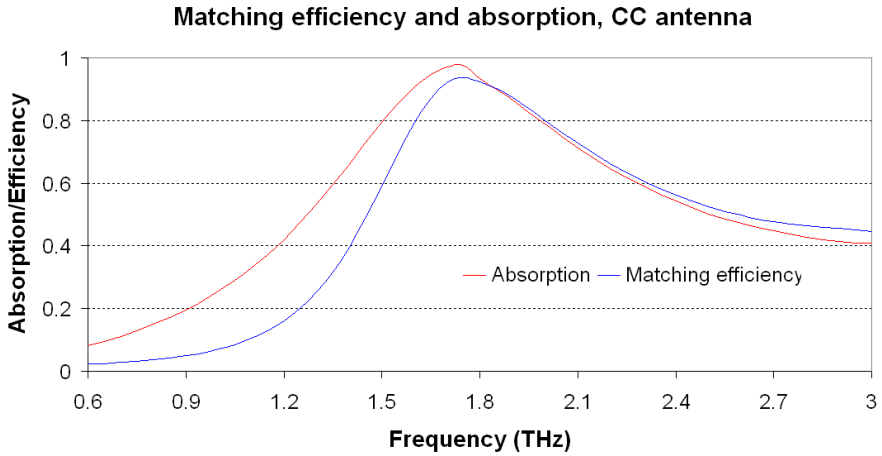

Fig. 5.19: Comparison between absorption (receiving mode simulation) and matching efficiency (transmitting mode simulation) for leg-cross polarization.

While designing antenna-coupled bolometers, simulations in transmitting mode are critical because they can reveal the electromagnetic behavior of antennas (capacitive, inductive or resonant). For instance, at 1.9 THz, the radiation capability of the CC antenna in transmitting mode is very weak (the real part of impedance is very small). It means that this antenna structure does not correctly couple the THz wave whatever the load resistance is. Therefore, it is meaningless to endeavor to sweep the load resistance in order to optimize absorption in this frequency range with receiving mode simulations.

5.3 Improved design (Bambolo)

In the frame of THz active imaging developments at CEA-Leti, the chosen sources are Quantum Cascade Lasers (QCL) that emit THz radiation in the range 2–3.5 THz. The first THEDEX bolometer design exhibits absorption peaks at 1.35 and 1.75 THz, thus is not optimized with respect to QCL operation spectrum. As presented in chapter 1, the QCL technology today suffers a dramatic drop in optical power at frequencies below 2 THz. Based on the knowledge acquired from the first THEDEX bolometer array prototypes, new developments aim at shifting the absorption of bolometers in the range 2.5–3 THz and simultaneously at decreasing the heat capacity of bolometer. This leads to the "Bambolo" design presented in this section.

5.3.1 Structure

The structure of the Bambolo bolometer in Fig. 5.20 inherits from some features of the THEDEX design, such as the pixel pitch, the SiO_2 cavity and the antennas loaded by resistors. The most important change comes from the novel antenna structures that provide at the same time a better optical coupling and a smaller heat capacity.

In this design, the antenna elements are located on a single level, i.e. the suspended membrane. The CC bowtie antenna has been suppressed. The antenna combines two long dipoles for the LP polarization with a 49-µm length like in THEDEX design. For LC polarization, the antenna also combines two short dipoles perpendicular to the LP dipoles. The length of these dipoles is limited by the distance between the two thermal legs. It is recalled that the thermal legs determine thermal isolation between the suspended membrane and the SiO_2 substrate. If the dipole antennas pass through thermal legs, thermal isolation would be dramatically degraded. Concretely, the length of the dipoles is restricted to 18 µm.

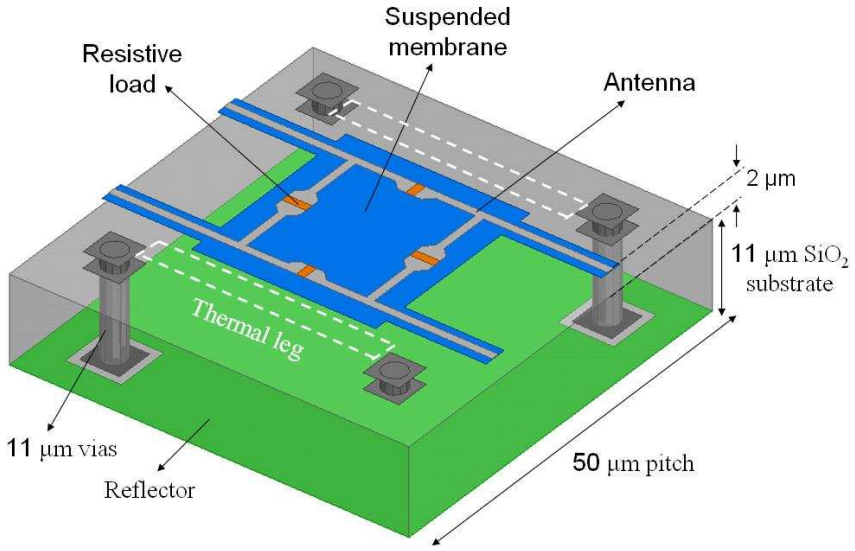

Fig. 5.20: Detailed structure of Bambolo design

Each dipole antenna has a width of 1 µm and is equipped with its own resistive load. Load resistances are 150 Ω and 100 Ω for the long and short dipoles, respectively. It should be noted that the four dipoles are connected directly, resulting in a close form. We will explain the reason in the next section.

Similarly to THEDEX design, the antenna layer is sandwiched between two insulating Si-N films. This structure ensures that the thermometer is not short-circuited by the antenna layer. The stack of the whole suspended membrane is presented in Fig. 5.21. One can see that the insulator and the thermometer extend beyond the rectangular bolometer membrane. This configuration helps to strengthen mechanically the long dipole.

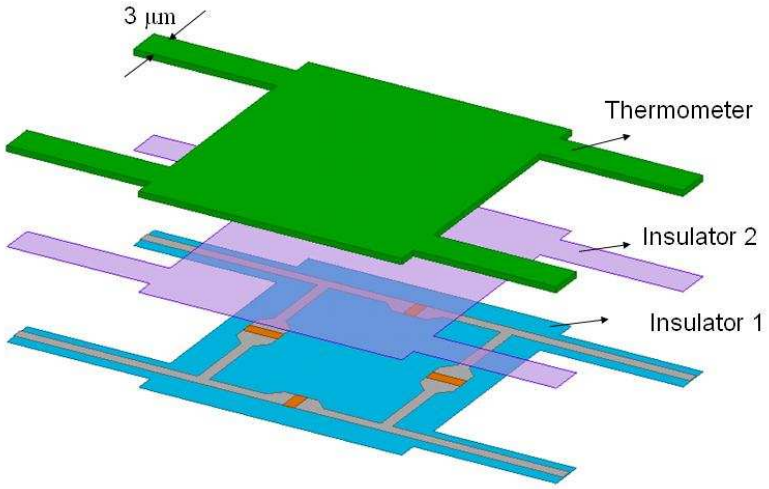

Fig. 5.21: Different layers of the suspended membrane in the case of Bambolo design.

The Bambolo fabrication challenge lies in the mechanical robustness of the part of the long dipole that extends beyond the central membrane. In THEDEX design, the DC antenna also overhangs the central rectangular microbridge. But the bow-tie antenna extensions have much larger width (5 - 11 µm) compared to the width of the Bambolo dipoles (1 µm). So Bambolo antenna tips should be supported by the insulator and thermometer layers. We envisage two versions. The first version (version A) uses rectangular extensions to support mechanically the metallic dipole antenna tips. In the second version (version B), a trapezoid shape is applied.

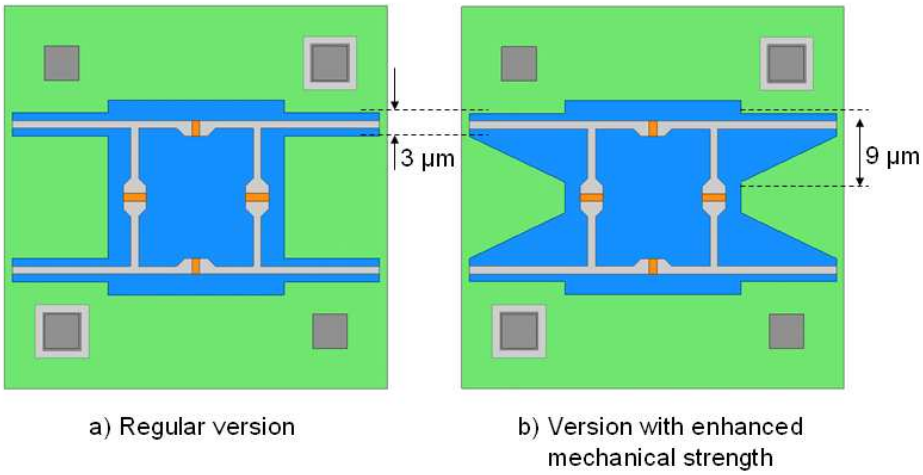

Fig. 5.22: Two versions of Bambolo design, two shapes of the thermometer (similar shape as insulator) are used to ensure a good mechanical strength for the dipole antenna overhanging tips.

The area of the thermometer in version B is slightly larger than in version A, meaning that the heat capacity is greater. The heat capacity of the bolometer will be calculated and compared with the THEDEX design.

5.3.2 Optimization of optical coupling

In the THEDEX design, bow-tie antennas have been chosen because of their broadband property, larger than for dipole antennas. This is true at least for a mono antenna standing in free space. In a dense array of antennas, due to the mutual coupling between elements, the impedance of bowtie antenna can vary quickly with frequency. Therefore, it is hard to state that the bowtie is better a dipole in terms of bandwidth.

The clear drawback of bowtie antennas when compared to the dipole antennas is its larger surface and consequently an expected greater heat capacity. As seen in previous calculations in section 5.2.2.2, the THEDEX bowtie antenna contributes to typically half the total heat capacity of the bolometer. Provided that optical coupling by the dipole antennas is acceptable, the replacement of bowtie antennas by such antennas allows the bolometer to decrease its heat capacity. In the next section, we elaborate the optical coupling of such dipole array.

5.3.2.1 Array of resistively loaded dipoles

Dipole antenna is the simplest type of antenna. A half wavelength λ/2 dipole in free space has impedance of 73 Ω at resonance frequency. In fact, both resistance and reactance increase quasi-linearly with frequency in the region around the resonance frequency. Because the antenna impedance changes quickly with frequency, this type of antenna is qualified as being narrow band.

In an array of antenna-coupled bolometer, each dipole (assuming dipole antenna) is equipped with its own resistive load. Each dipole is not connected to each other by feed line as in the case of the array antenna. However, if the dipole is set closely enough, the impedance of antenna can be strongly affected by mutual coupling. Due to this coupling, the whole array can have a broadband behavior different from the single dipole in free space.

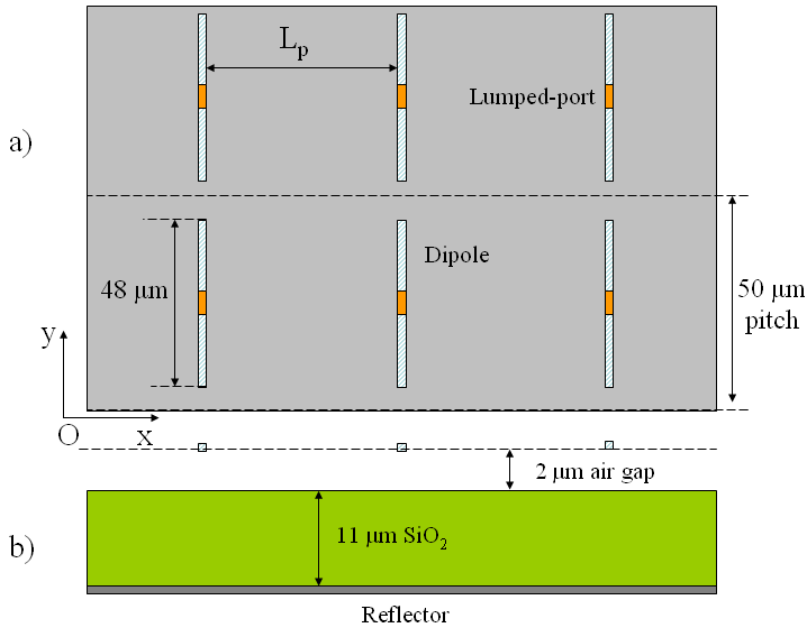

Fig. 5.23: Array of dipole equipped with resistive load, the distance between dipoles is swept to study the effect of mutual coupling

To calculate the dipole–impedance in an array, we apply the transmitting mode simulation mentioned previously with the configuration of Fig. 5.23. The dipole antenna has a size of 48 µm × 1 µm. The y-axis pitch is kept to be 50 µm, while the spacing between dipole L_p is swept to see the impedance evolution. Two values of L_p are considered. In the first case, L_p is set to 50 µm, resulting in 50 µm × 50 µm pixel that contains only a dipole antenna. In the second case, $L_p = 25$ µm, meaning that each pixel encompasses two dipoles.

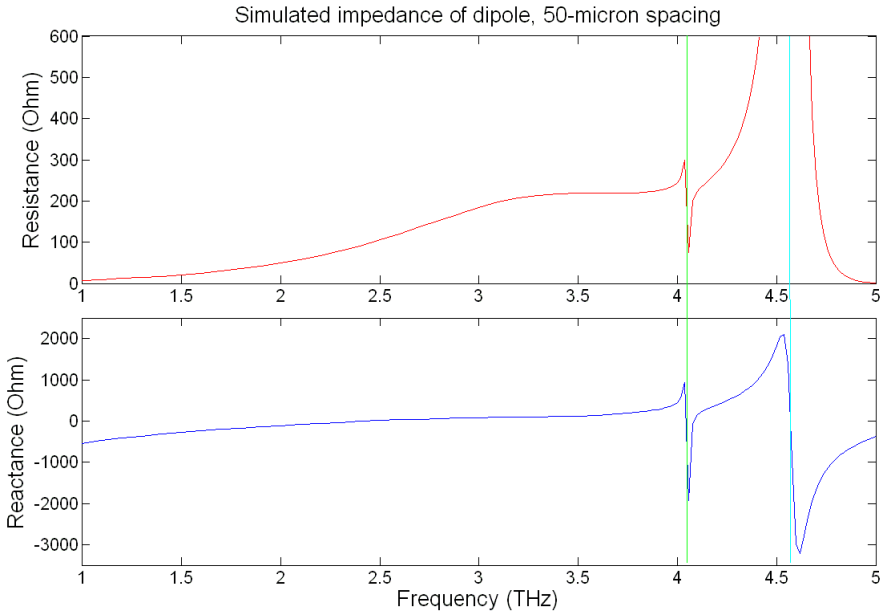

Fig. 5.24: Impedance of dipole over the range [1 – 5 THz], distance between dipole is 50 µm

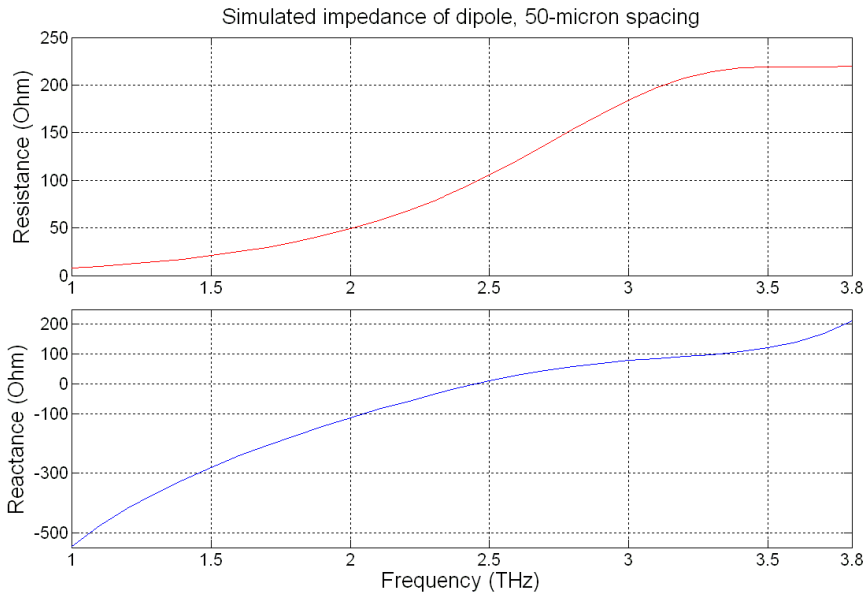

Fig. 5.25: Close-up of spectral range [1 – 3.8 THz]

The dipole impedance, when L_p is equal to 50 µm, is presented in Fig. 5.24. Some singularities are marked by the green and cyan lines. The first one occurs at 4.06 THz while the frequency of the second singularity is 4.62 THz. These singularities are related to higher modes of dipole antenna and have been presented in some antenna textbooks or discussed in publications [10]. For the fundamental mode, the current is maximum at the position of the reference plane, i.e. the central point of the dipole. For higher modes, the current at this central point may be very small, resulting in a very high impedance. Since these frequencies are beyond the spectral range of interest mentioned before (2.5–3 THz), these singularities are not considered in the detector design.

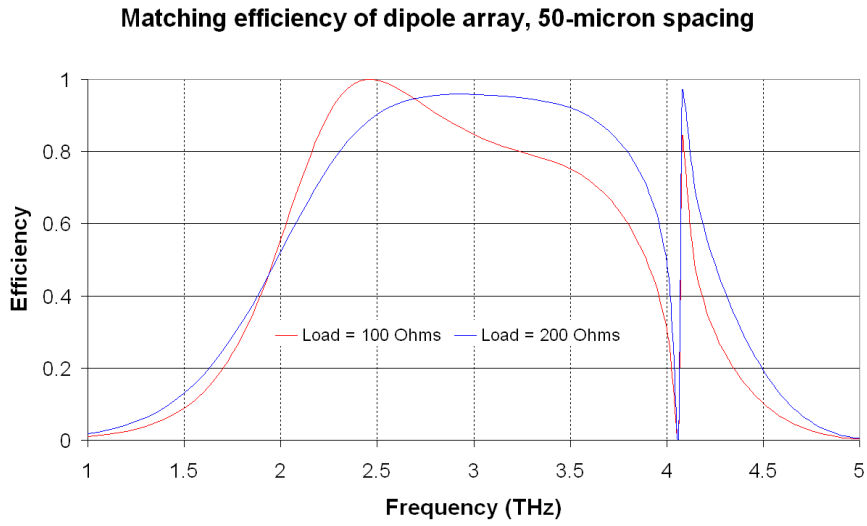

Fig. 5.26: Matching efficiency with different load resistances.

The Fig. 5.25 provides a close-up plot of the impedance from 1 to 3.8 THz. Both resistance and reactance increase monotonically with frequency. The resonance frequency that corresponds to null reactance is found to be close to 2.5 THz. At this frequency, the resistance equals 100 Ω. In order to evaluate the optical coupling of the dipole antenna, we calculate the impedance matching efficiency by using equation 5.13. Two load resistances (100 and 200 Ω) are considered by setting lumped-port impedance to the corresponding value. As seen in Fig. 5.26, the efficiency is higher than 80% over the 2.5–3 THz range in both cases. With a load

resistance of 100 Ω, the impedance matching efficiency peaks at the resonance frequency close to 2.5 THz. For a 200-Ω resistance, the efficiency becomes more "balanced", being better than 90 % from 2.5 to 3.5 THz.

When the spacing between dipoles L_p gets smaller, the mutual coupling between antennas is stronger. It is likely to change the dipole impedance presented above. We present here the case when L_p is equal to 25 µm, meaning each pixel of 50 µm × 50 µm size contains two parallel dipoles.

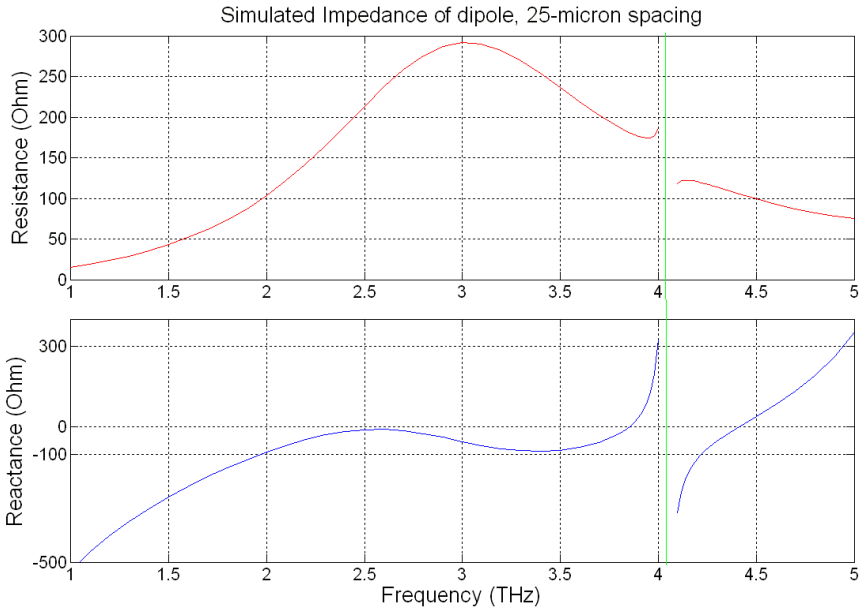

Fig. 5.27: Impedance of dipole over the range [1 – 5 THz], with dipole interspace of 25 µm

The resulting dipole impedance is shown in the figure above. As with 50 µm spacing, the impedance exhibits singularities at high frequency. The first singularity is observed at 4.06 THz as in the previous case. The second singularity has shifted to 5.6 THz and is not shown in the figure. Probably this singularity is related to the mutual coupling. However, once again, these singularities do not affect the design of bolometer in the spectral range below 3.5 THz.

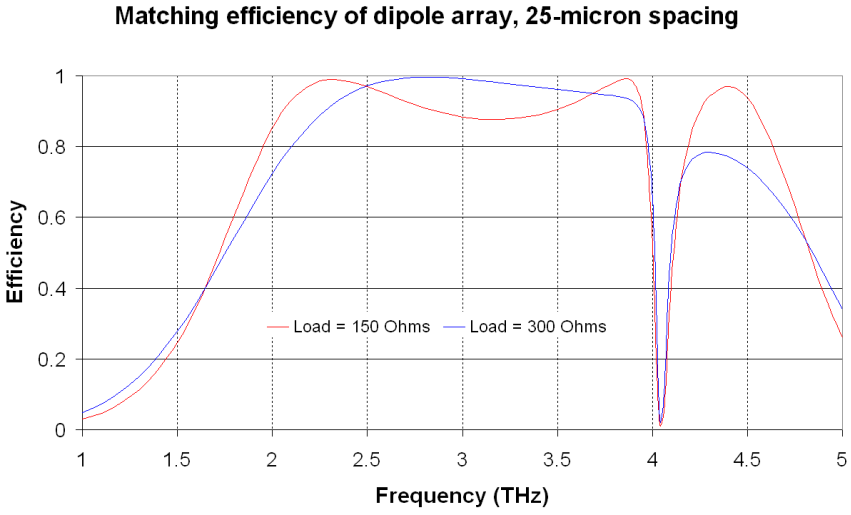

Fig. 5.28: Matching efficiency with different load's values

It is interesting to see that the shape of the impedance curve in this 25-µm spacing case differs from the 50-µm spacing case. The resistance curve has a local maximum (292 Ω) at 3

THz while the reactance curve exhibits an inflection point near this frequency. The reactance exhibits a negative value (-53 Ω) at 3 THz, which means a capacitive behavior of the antenna. At this point, we can point out that the impedances of the dipole and of the THEDEX bow-tie show similarities. This behavior reflects the strong mutual coupling between antennas in dense arrays.

The impedance matching efficiency is evaluated with two load resistances: 150 Ω and 300 Ω. The corresponding curve is shown in Fig. 5.28. The impedance matching efficiency is excellent for both cases, i.e. better than 80 % on a very large bandwidth. The 300 Ω load case shows a little better matching efficiency around 3 THz.

5.3.2.2 Application of dipole to bolometer structure

Dual polarization bolometer

The employment of dipole antennas in the detector requires some modifications to satisfy the constraints of the bolometer structure. Two constraints that should be solved before using dipole antenna are the load configuration and the dipole length

The load configuration concerns how to equip the dipole antenna a resistor so that the impedance matching efficiency remains high. In the case both polarizations are desired, the pixel must have at least two dipoles, one for each polarization. One can think of the cross dipoles sharing the same load. This configuration causes a problem for impedance matching since the load resistance for each antenna is not independent.

The resistive loads are made of TiN, which has a sheet resistance of 300 Ω/□. If the resistor dimension is $L \times W$, the resistance value for one direction is equal to $(L/W)^2$ times the resistance for other direction in respect to the resistance formula:

$$R = \rho_{sheet} \frac{L}{W}. \qquad \textbf{(5.16)}$$

For instance, if the resistance value for one direction is 100 Ω (thus $L = W/3$), then the resistance value is 900 Ω for other direction.

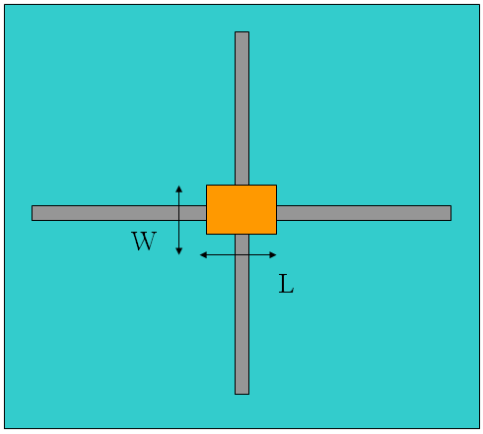

Fig. 5.29: Crossed dipoles sharing the same resistive load

If the two dipoles are symmetric, they will have the same impedance. In this case, the load shape should be chosen to be square, and it will have a value of 300 Ω. This can work in principle although the impedance matching is not optimized: the good value of the load should be in the range 100 – 200 Ω as suggested in Fig. 5.25. In an actual bolometer, the length of dipole for one polarization is in general different from the other polarization. Thus,

the impedance of each dipole is different. A configuration that permits independent impedance matching is preferred.

The feature of the bolometer microbridge structure that imposes the most important difficulty with respect to the optical coupling optimization is the limited distance between the thermometer electrodes and also the thermal legs (see Fig. 5.30). This distance is 22 µm in the 50 µm pitch THEDEX design. Due to the limited distance between thermometer electrodes, the dipole length in the LP polarization attains only 18 µm. In contrast, the dipole length in the other polarization can reach a maximum of c.a. 49 µm. Thus, the dipole antenna in one polarization is more than two times longer than the dipole in the other polarization. This causes a considerable hurdle for the optical coupling of leg-cross polarization because the resonance frequency of 18 µm dipole occurs at 6.7 THz and the efficiency in the range 2.5–3 THz is low.

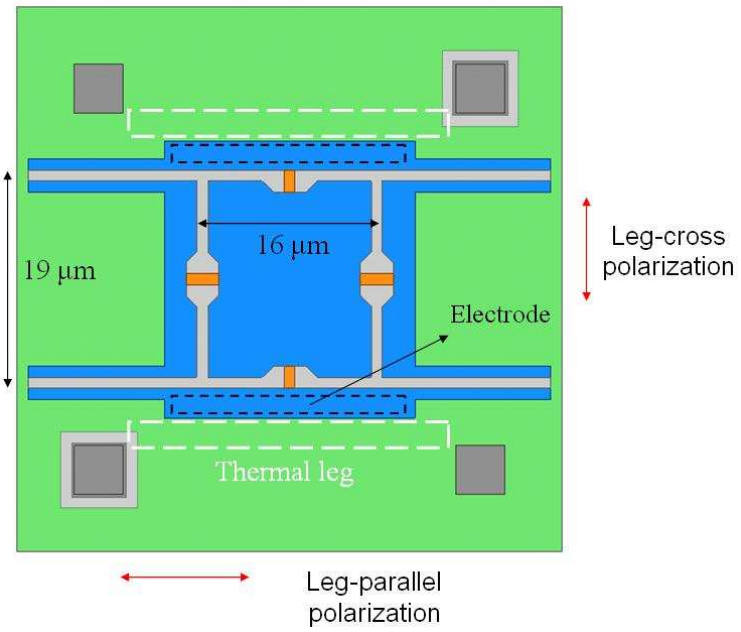

Fig. 5.30: Top view of Bambolo design showing the limited distance between electrodes.

In fact, this difficulty has already appeared in THEDEX design. One can think of applying the solution from THEDEX design, i.e. using of primary antenna and sub-antenna. In this design, the CC sub-antenna located on the suspended membrane has a length of 21 µm due to the limited distance between thermal legs. THEDEX design deals with this constraint by coupling this sub-antenna to the primary 49-µm long CC antenna placed beneath the suspended membrane. This requires a bowtie antenna to enhance the capacitive coupling between sub-antenna and primary antenna. But the use of such large antenna like in THEDEX design may affect strongly the optical coupling in the leg-parallel polarization. In the case of THEDEX bolometer, simulations show that if the CC antenna is suppressed, the optical coupling of the DC antenna is much better in the range 1.5–3.5 THz.

To overcome the limited dipole length hurdle, the short dipole has been connected to the long dipole to get the monolithic shape as illustrated in the Fig. 5.30. This configuration allows the leg-cross dipole to "use" a part of the leg-parallel antenna so that the induced (conduction) current does not get null abruptly at the end of the dipole. The dipole thus benefits of a capacitive loading at its extremities as illustrated in Fig. 5.31. This technique is extensively used in antenna designs to miniaturize the size of the dipoles. One can find a description of this technique in some antenna textbooks or its application in some publications [11].

Regarding the limited dipole length constraint, one can wonder why not designing a longer thermometer to increase electrodes interspacing. This can be fulfilled by displacing the thermal legs near the border of pixel. However, such modification leads to a larger suspended membrane. Apart the increase of heat capacity, it may cause a potential mechanical weakening of the micro-bridge structure.

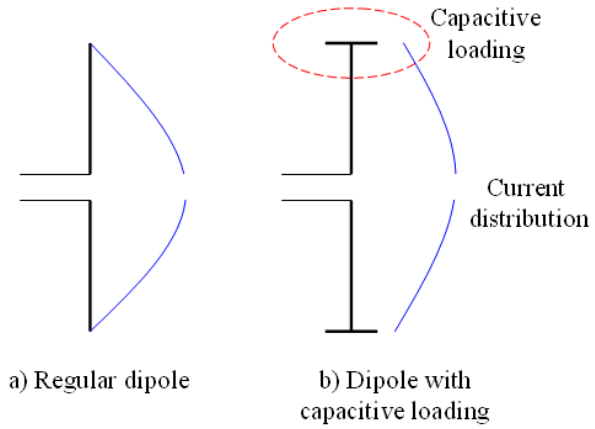

Fig. 5.31: Current distribution on regular dipole and on capacitive-loading dipole

Fig. 5.32 presents the absorption of the Bambolo design for leg-parallel polarization. This absorption results from the FSS simulation in which the structure is completely passive. One can see that the absorption of the real bolometer structure is a little lower than the ideal case of dipole arrays presented in Fig. 5.28. However, the general shape of absorption curve is not so different from the matching efficiency curve presented before. The optical coupling in the targeted range 2.5–3 THz is still very good, better than 80 %. In real bolometer structure, some components such as the 11 µm metallic vias or thermal legs and thermometer electrodes can interact with antennas. Some of them are made of lossy materials that can absorb incident wave. In general, these components degrade the absorption of the resistively loaded antenna.

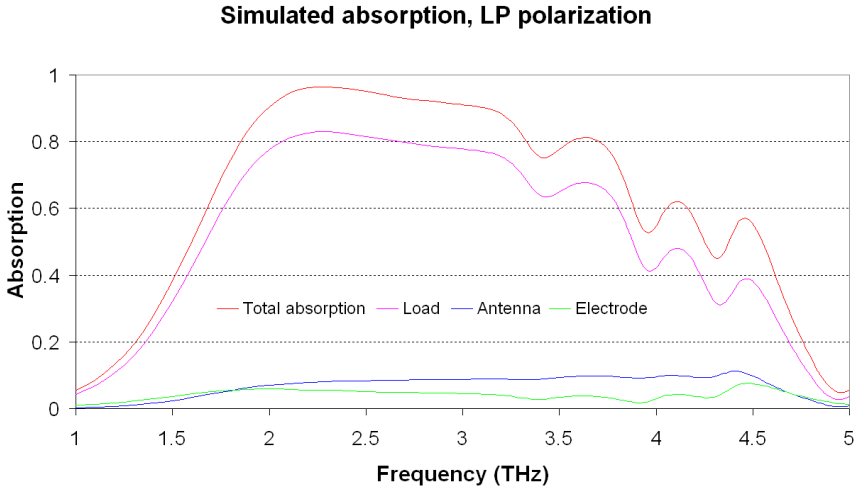

Fig. 5.32: Contribution of the suspended membrane elements to the bolometer absorption in leg-parallel polarization.

The overall radiation absorption of the suspended membrane includes contributions from all its elements: load, antenna, and electrode. The absorption of thermometer is negligible since thermometer material (amorphous silicon) does not exhibit absorption in the THz range.

As shown in Fig. 5.32, the load contributes mostly to the total absorption. The antenna, though made of highly conducting material, exhibits absorption of about 10 %. We can deduce that the induced current in the antenna is much stronger than the current in the electrodes. The loaded antenna is the main absorber of bolometers.

For the leg-cross polarization case, one can see in Fig. 5.33 that the spectral absorption is less broadband than the previous polarization. However, the optical coupling in the desired range 2.5–3 THz is still very good. In this spectral bandwidth, the bolometer can be considered as dual polarization sensitive since the absorption in each polarization is similar.

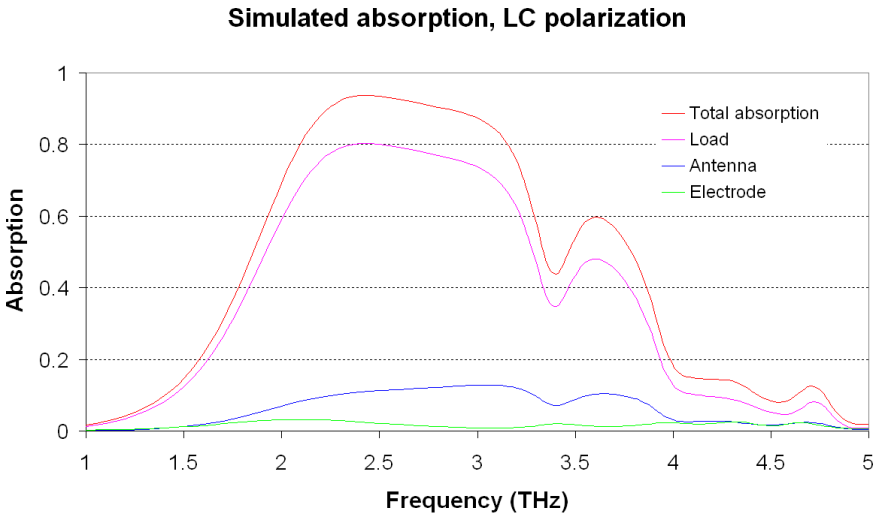

Fig. 5.33: Contribution of the suspended membrane elements to the bolometer absorption in leg-cross polarization

Mono-polarization bolometer

In the case of mono-polarization bolometer, as shown in the simulation of dipole array spaced by 50 µm, single dipole with 200-Ω resistive load would exhibit a good optical coupling in the range 2.5–3 THz. In such a case, the suspended membrane can be made much smaller, resulting in reduced heat capacity and so faster bolometer response.

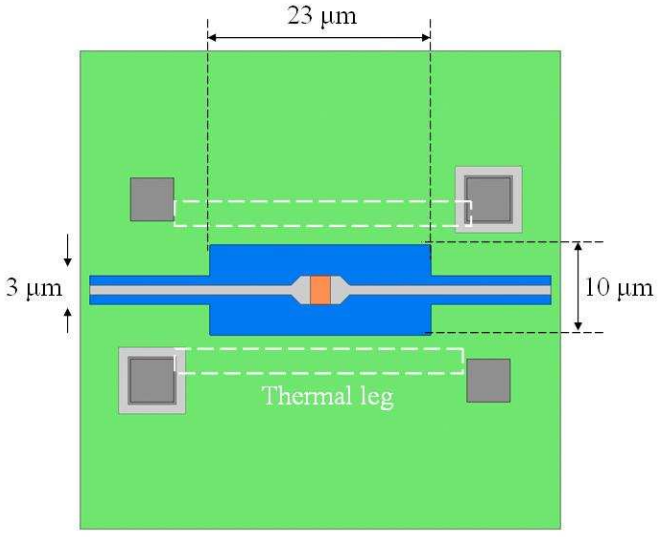

Fig. 5.34: Top-view of the mono-polarization bolometer.

Fig. 5.34 represents the structure of the mono-polarization pixel. It integrates only one dipole antenna, oriented in the leg-parallel direction. The antenna is loaded by a 200-Ω

resistor. The central part of the thermometer has a size of 23 µm × 10 µm. Two rectangular extensions of 3 µm × 12.5 µm dimensions are added to strengthen mechanically the dipole antenna tips. Unlike dual polarization antenna configuration, this single dipole design does not include any constraint in respect to the load configuration or the limited distance between thermometer electrodes. Also, the mechanical strength of the micro-bridge structure may be better since the suspended membrane width is very small (about 10 µm).

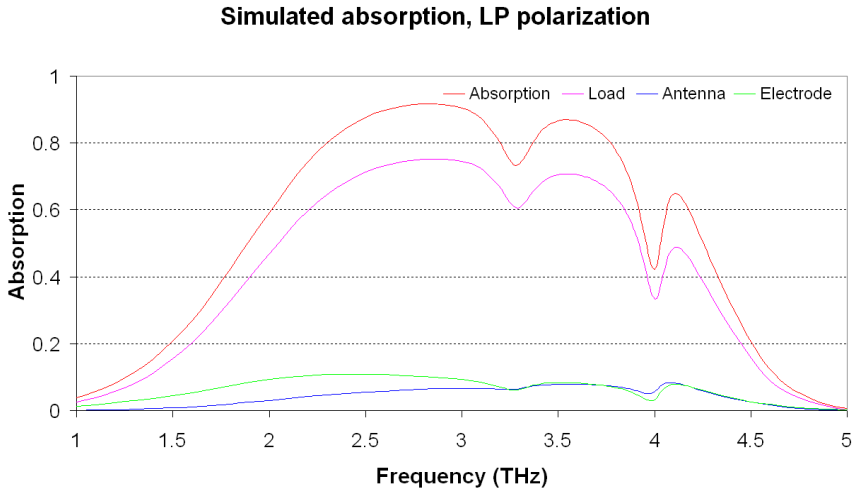

Fig. 5.35: Contribution of each element to absorption of mono-polarization bolometer.

The actual structure is simulated in receiving mode. The bolometer structure is completely passive, meaning that a resistive sheet models the dipole load instead of a lumped-port. The total absorption in the membrane and each contribution are presented in Fig. 5.35. One can see that the absorption curve is quite similar to the impedance matching efficiency of the simplified dipole array (Fig. 5.26) although the bolometer structure is more complex.

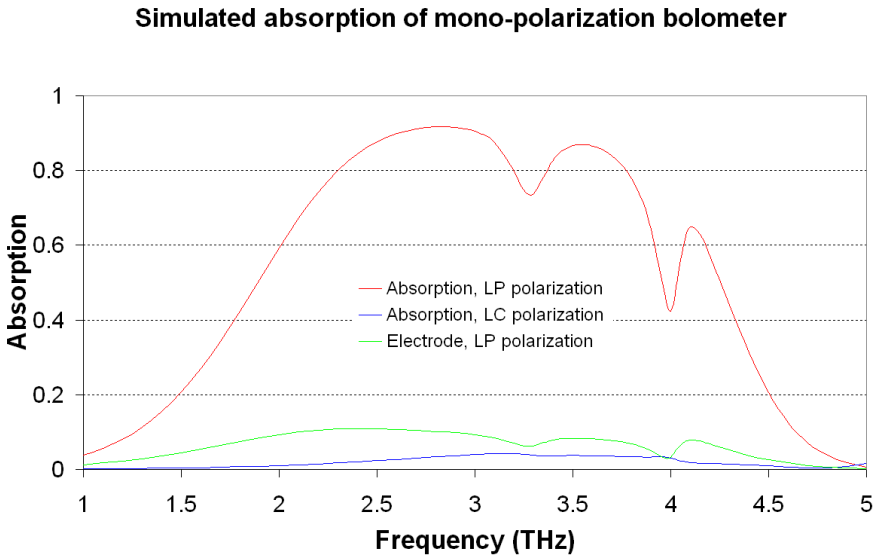

Fig. 5.36: Simulated absorption demonstrating the polarization-dependent response of the design.

The absorption in leg-parallel polarization is very good, higher than 80 % in the range 2.5–3 THz. The most significant contribution comes from the resistive load. The electrode sheet resistance is 300 Ω/□, thus it can also absorb the incident wave. It contributes to about 10 % of the total absorption. Antenna conductivity is very high (33×10^6 siemens/m), it exhibits a small absorption, a little lower than the electrodes.

Dipole antenna does not absorb THz radiation polarized in the leg-cross direction. However, the thermometer electrodes still show a little absorption (about 4 – 5 %) in this polarization and then contribute significantly to the total absorption of the bolometer. In Fig. 5.36, the absorption of electrodes in LP polarization is better in comparison to the LC polarization. This is predictable with respect to the shape of the electrodes, which is a long strip parallel to the LP direction.

5.3.3 Figures of merit

5.3.3.1 Absorption

THz absorption

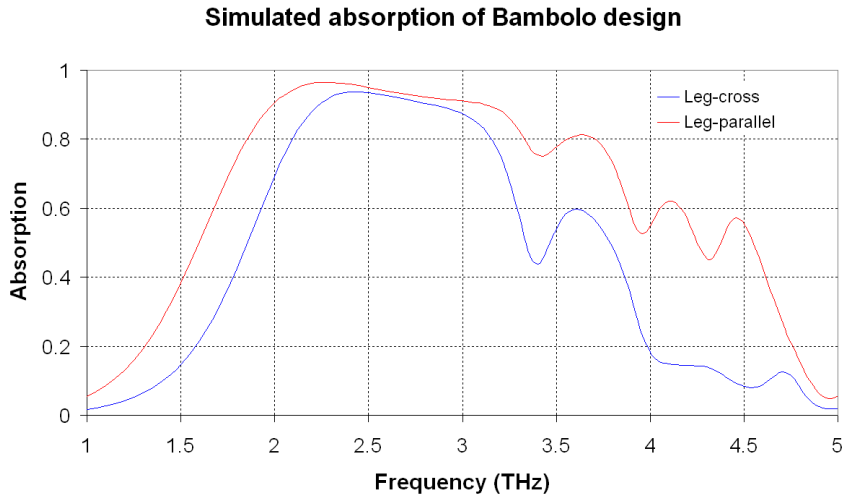

Fig. 5.37: Absorption in the THz range of the Bambolo design

The bolometer absorption in the THz range has been already examined in details in the previous section. Fig. 5.37 summarizes the absorption for both polarizations. The design ensures a high absorption in the desired spectral range 2.5–3 THz.

Infrared absorption

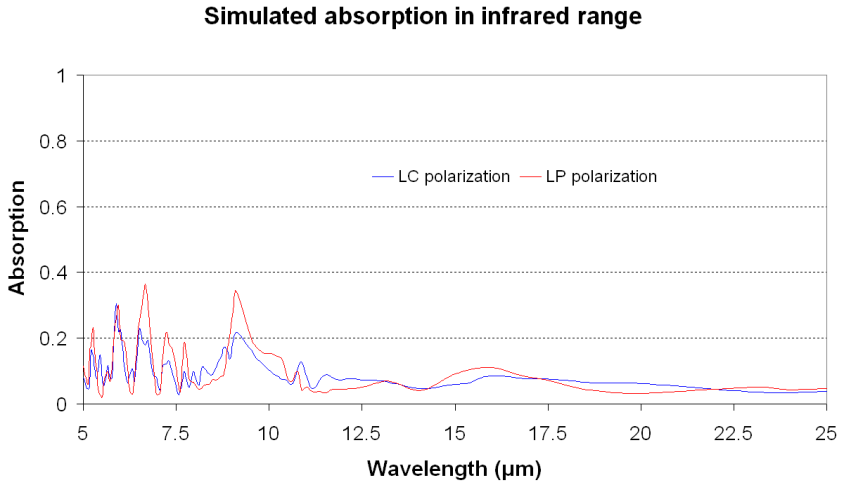

Fig. 5.38: Simulated absorption in infrared range of Bambolo design.

The simulation in the infrared range of the structure shows a small absorption for both polarizations (see Fig. 5.38). The absorption exhibits weak interference fringes at short wavelength as for AFB design. The main contribution comes from the electrodes (68 – 71 %).

The rest originates from the loaded antenna. The effective absorption over the range 5–25 μm is 8.8 %, significantly smaller than the 30 % of the AFB design and the 29 % of the THEDEX design. Unlike AFB, this design integrates no large absorbing film. It does not use a large CC antenna as in THEDEX either. Therefore, the infrared absorption is minimized in Bambolo design.

5.3.3.2 Thermal characteristics & response time

Thermal conductance

The Bambolo design has thermal legs structures similar to THEDEX pixel. Thus the thermal conductance of the legs is 11.8 nW/K for regular width (0.6 μm) leg and 9.8 nW/K in over-etched case (0.5 μm). Regarding the radiation exchange, the effective emissivity calculated according to equation 5.2 equals to 8.8 %. The radiation thermal conductance is then:

$$g_{rad} = 4 \times 50^2 \times 10^{-12} \times 0.088 \times 5.67 \times 10^{-8} \times 298.15^3 = 1.3 \text{ (nW/K)}. \quad \textbf{(5.17)}$$

This leads to a total thermal conductance of 13.1 nW/K for regular leg and 11.1 for the over-etched case.

Heat capacity

As mentioned before, the Bambolo design aims at reducing the heat capacity of the antenna (and hence the total heat capacity of the bolometer) by using dipole instead of bowtie designs. The Bambolo design features the same layer thickness (insulator, absorber, antenna, and thermometer) as in the THEDEX design. The difference originates from the shape of each component and thus from the area of each component. The total heat capacity, as well as the contribution of each Bambolo element, are presented in Table 5.4. Both version A (regular version) and version B (enhanced strength version) are reported so that we can look at the trade-off between them.

The Bambolo design exhibits a great improvement with respect to THEDEX in terms of heat capacity. As we can see in the table, the bolometer heat capacity is 365 pJ/K and 420 pJ/K for the versions A and B respectively, in comparison to 627 pJ/K for THEDEX. Thus, thanks to the Bambolo design, heat capacity is reduced by a factor 42 % and 33 %, respectively. This reduction originates from the dipole antenna smaller area (146 μm^2) when compared to the THEDEX bowtie (501.4 μm^2). Regarding the thermometer, its area is in the same range.

Comparing to the AFB design, the bolometer heat capacity of the Bambolo design is a little higher (365 or 420 pJ/K when compared to 355 pJ/K). This is not a surprise, since the AFB design does not have the antenna layer. A detailed comparison between designs will be presented in the summary of this chapter.

Element	**Area (THEDEX)** (μm^2)	**Area (version A)** (μm^2)	**Area (version B)** (μm^2)	**Heat capacity (version A)** (pJ/K)	**Heat capacity (version B)** (pJ/K)
Insulator 1+2	832.1	734.2	884.2	32.9	39.6
Absorber	523.2	156	156	3.9	3.9

Thermometer	832.1	734.2	884.2	239.4	288.2
Antenna	501.4	146	146	88.7	88.7
Total				365	420

Table 5.4: Heat capacity of the Bambolo and THEDEX designs.

The mono-polarization bolometer that integrates only one dipole antenna exhibits the smallest heat capacity. In this design, not only the area of the antenna is reduced but also the thermometer area is minimized. The antenna and the thermometer show a reduction of 64 % and 66 % respectively in comparison to the THEDEX design. The overall heat capacity is 146 pJ/K when compared to 365 pJ/K of the best case of THEDEX and 355 pJ/K of the AFB design. The table below gives the parameters and the heat capacity of the mono-polarization bolometer.

Element	**Material**	**Specific Heat Capacity** pJ/(μm^3.K)	**Surface** (μm^2)	**Volume** (μm^3)	Heat capacity (pJ/K)
Insulator 1+2	Si-N	1.12	305	12.2	13.7
Absorber	TiN	3.26	58	0.5	1.6
Thermometer	Amorphous Silicon	1.63	305	61/case 200 nm	99.4
Antenna	Aluminum	2.43	52	13 (250 nm thickness)	31.6
Total heat capacity					146

Table 5.5: Detailed calculation of heat capacity of mono-polarized bolometer

Response time

For dual polarization design, the heat capacity of the versions A and B, in respect to the 13.1–nW/K thermal conductance, results in a time constant of 27.9 ms and 32.1 ms, respectively. In the best case, the detector can reach the frame rate of:

$$f_{frame} = \frac{1}{3\tau_{th}} = \frac{1}{3 \times 27.9 \times 10^{-3}} = 11.9\,(\text{Hz}) \qquad \textbf{(5.18)}$$

For the mono-polarization design, the time constant is 11.1 ms and then the pixel could perform real-time imaging at a frame rate of 25 Hz.

5.4 Perspective design for low frequency

We have presented the THz bolometer stack optimized for detecting 3 THz signals. The simulated dipole antenna shows resonant frequency in the 2.5–3 THz range. For operation at lower frequencies, let say at 670 or 850 GHz, the height of the SiO_2 layer should be increased. In addition, the dipole should be longer, which implies a larger pixel pitch. The increase of these two dimensions is very challenging for microelectronic technology. And yet, the simulation of the THEDEX design shows a "resonant" frequency at 1.35 THz for the DC antenna. Although the reactance of the DC antenna is proven to be capacitive, the matching efficiency is quite high at this resonant frequency (about 80 %). The study of this low frequency resonant mode leads us to think about the use of frequency selective surface (FSS) in combination with the SiO_2 cavity. The FSS will be represented shortly below. The full presentation of these structures can be found in [12-13].

5.4.1 Frequency selective surface

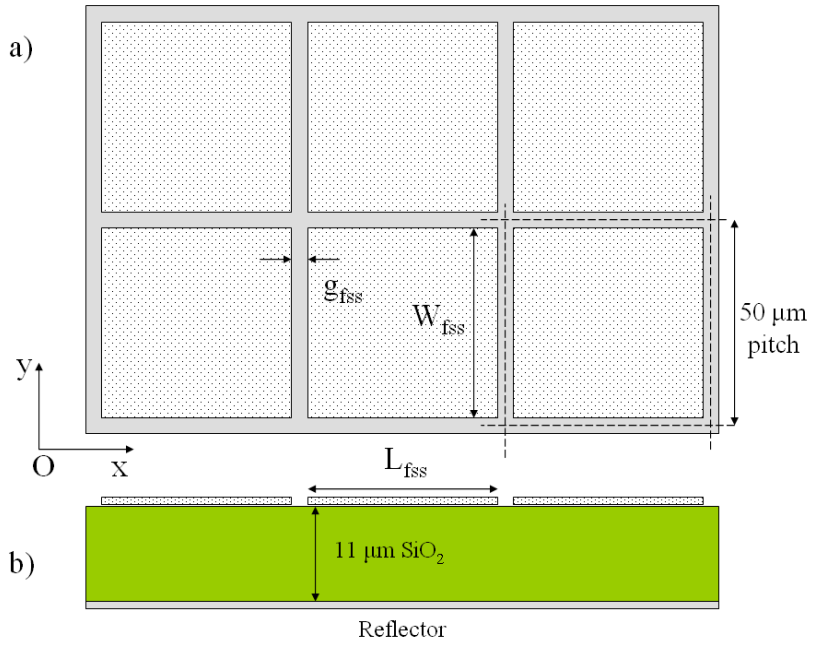

Fig. 5.39: Capacitive surface backed by a substrate layer over a continuous reflector.

In fact, FSSs of "capacitive" type have already been presented in chapter 4. It consists of rectangular metal patches separated by a small gap. The surface transmits low frequency wave while it reflects high frequency ones. However, transmission and reflection are partial. They evolve monotonically with frequency, showing no resonance. When the capacitive surface is backed by a conducting surface, the structure is completely reflective. The continuous conducting surface is inductive while the FSS surface is capacitive. The capacitance of the FSS surface comes from the fact that the electric field concentrates in the gap between metallic patches. The edge capacitance between patches is calculated as [14]:

$$C = \frac{W_{fss}(1+\varepsilon_{substrate})}{\pi}\cosh^{-1}\left(\frac{L_{fss}}{g_{fss}}\right). \qquad \textbf{(5.19)}$$

In the expression above, $\varepsilon_{substrate}$ is the (absolute) permittivity of the substrate below the FSS, in our case SiO_2. The quantities W_{fss}, L_{fss} and g_{fss} are the width, length and gap of the patch

respectively. The polarization in question is parallel with the Ox axis. One can see that regarding the geometry, the edge capacitance can be increased mostly by increasing the width of the metallic patch or decreasing the gap between them.

One interesting characteristic of this structure is that the phase of the reflected wave can be controlled by adjusting the FSS capacitance. There exists a resonant frequency at which the reflected wave and the incident wave are in phase. This frequency is lower than the regular frequency that corresponds to the quarter wavelength cavity, about 3 THz in the studied case. The FSS resonant frequency is inversely proportional to the root square of FSS capacitance. Thus to get the resonant at low frequency, one should increase the capacitance by using a larger patch or a smaller gap.

The FSS structure with rectangular patch in Fig. 5.39 has been simulated with receiving mode simulation mentioned previously. We aim to examine the phase shift between the reflected wave and incident wave. In this structure, the pixel pitch is kept to be 50 μm as in the THEDEX case. The width and length of the metallic patch is 48 μm. The gap between patches is 2 μm wide.

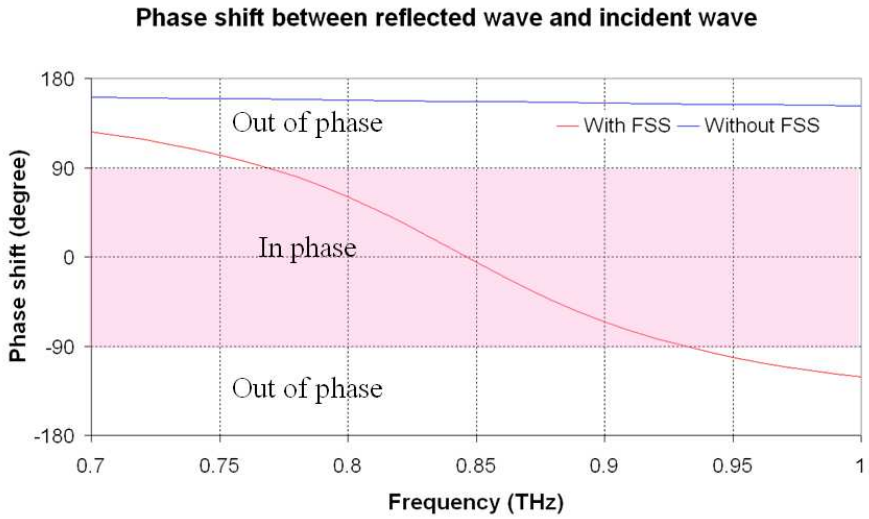

Fig. 5.40: Simulation showing a cavity equipped with FSS tuned for resonance at 850 GHz

The phase shift between the reflected wave and incident wave at the position of the metallic patch is plotted in Fig. 5.40 and compared to the case without capacitive surface. For the case without FSS, the structure in question is an 11-μm thick cavity of SiO_2 backed by a metallic reflector. The phase shift is zero at frequency corresponding to the quarter wavelength cavity, i.e. about 3 THz. At low frequency, 850 GHz for example (the wavelength is 353 μm), the 11 μm cavity is too small. The phase shift in this case is not far from the phase shift at the position just above the reflector, which is π (180^o). With this phase shift, the reflected wave and the incident wave are out of phase and cancel each other.

When the FSS is placed on the SiO_2 substrate, the phase shift varies from π at low frequency to -π at high frequency. It crosses zero near 850 GHz. At this resonant frequency, the reflected and incident waves are completely in phase; the electric field at the antenna location is enhanced. The spectral range, over which the phase shift varies from π/2 to -π/2, determines the bandwidth of the FSS structure. It corresponds to the spectral region where the reflected and incident waves are almost in phase and combine constructively.

5.4.2 Implementation in bolometer structure

5.4.2.1 Antenna equipped with FSS

Simulations were performed to investigate the optical coupling of the antenna deposited over the SiO_2 cavity integrating a FSS sheet. A bowtie antenna is placed on the FSS sheet at a distance of 2 µm. The antenna has a length of 48 µm and bow angle is about 13°. The pixel pitch is kept to be 50 µm. The antenna is excited by a lumped-port and its impedance is retrieved to evaluate the optical coupling at low frequency.

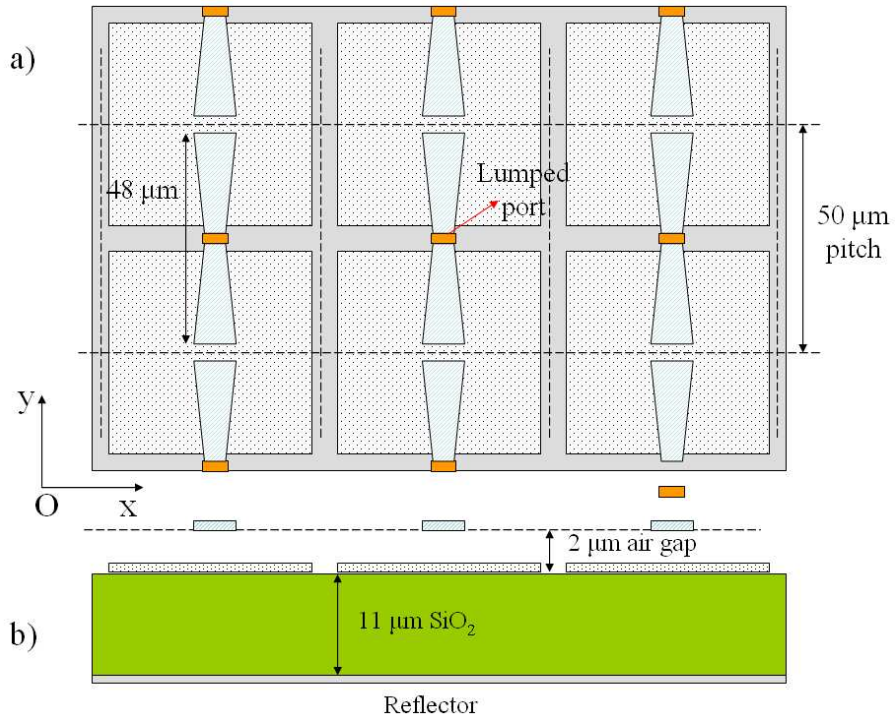

Fig. 5.41: Array of antennas located 2-µm above a capacitive surface

The simulated impedance of the bowtie antenna in Fig. 5.41 is presented in Fig. 5.42. One can see that this antenna has a resonant frequency near 900 GHz. The resistance at this frequency is about 300 Ω. However, the reactance is negative and has a value of -200 Ω. At 850 GHz, although the resistance decreases to 200 Ω, the reactance part is small, about -75 Ω. If a resistance of 300 Ω (for 900 GHz) or 200 Ω (for 850 GHz) is used, the impedance matching efficiency at these two frequencies can attain more than 90 %.

The dipole antenna equipped with FSS structure has also been simulated. In this case, the arrangement of the array is similar, except that the dipole is placed at the bowtie antenna location. In Fig. 5.42, simulation shows that the dipole resistance is slightly lower than in the bowtie case. However both resistance curves have a similar shape.

Regarding the reactance, although the shape of the reactance curve is also similar (refer to Fig. 5.42), the reactance value of the dipole is much smaller than the bowtie. This reduction is related to the ratio of dipole length with respect to the wavelength in question. The wavelength corresponding to 850 GHz frequency is 353 µm. The half-wave dipole requires a length of 177 µm. And yet, the length of dipole antenna in this case is only 48 µm. The SiO_2 has a dielectric constant of 3.83 at 1.2 THz. Taking into account the effect of the substrate; the electric length of the dipole is just:

$$l_{electric} = \sqrt{\frac{1+3.83}{2}} l_{physical} = 1.55 \times 48 = 74 \ \mu m. \quad \textbf{(5.20)}$$

The dipole is then too short for the 850 GHz frequency to ensure an efficient optical coupling. The bowtie in this case, in spite of its bigger area and thus higher heat capacity, should be used to provide a good optical coupling.

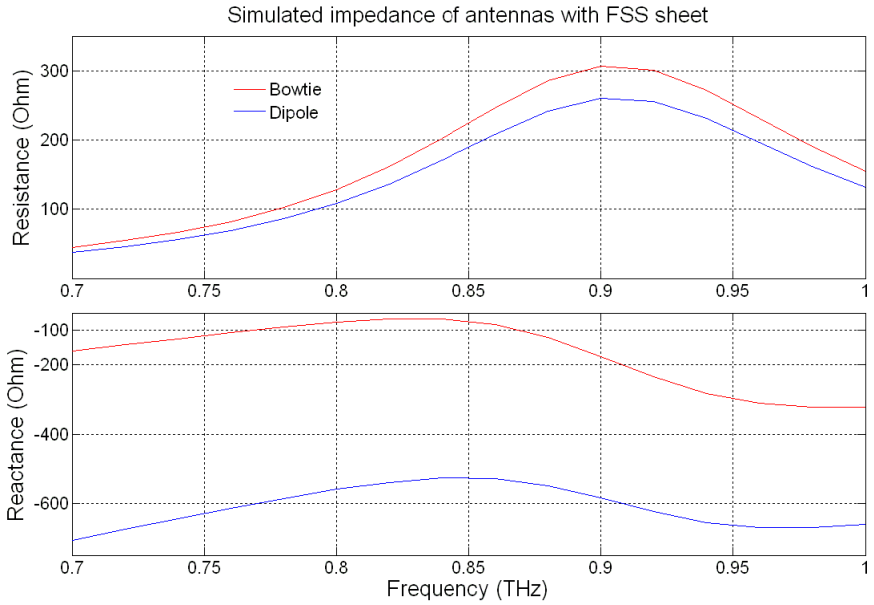

Fig. 5.42: Impedance of the bowtie and dipole when equipped with FSS

Fig. 5.43 shows simulated impedance matching efficiency of the bowtie antenna for two load values: 200 and 300 Ω. The 200-Ω curve is shifted a little to the low frequency range when compared to the 300-Ω curve. In both case, the matching efficiency is very good at 850 GHz, better than 90 %.

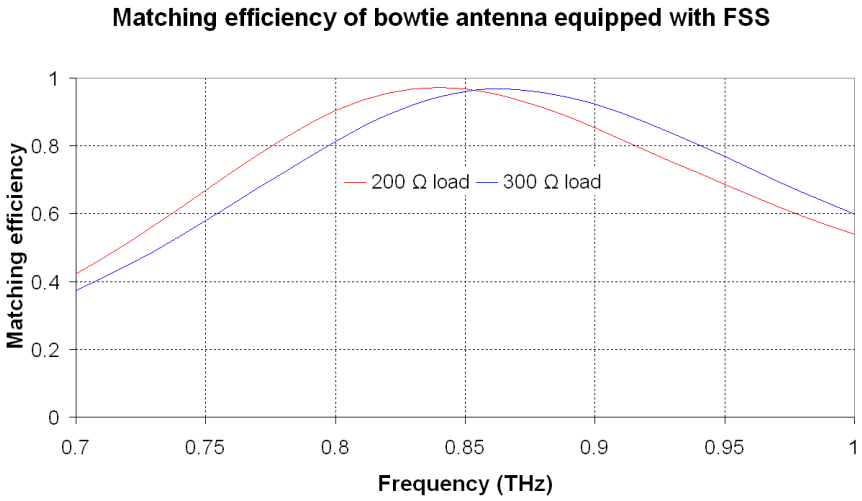

Fig. 5.43: Matching efficiency of bowtie antenna array with different load values

5.4.2.2 Bolometer equipped with FSS

Structure

The CEA-Leti THz bolometer stack includes an aluminum layer below the suspended membrane. This layer is deposited on the 11 µm thick SiO_2 substrate to make the CC antenna in the THEDEX design. This metallic layer can be employed to constitute the FSS patch.

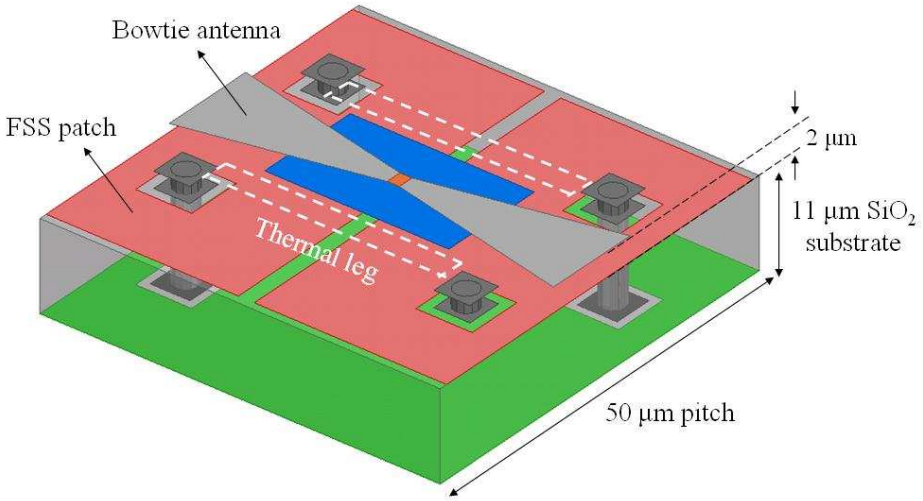

Fig. 5.44: Detailed structure of the 850 GHz bolometer.

The bolometer design below is issued directly from the structure of the array of bowtie antenna equipped with FSS discussed in the last section. The dimension of FSS patch is 48 µm × 48 µm. In Fig. 5.44, the FSS patch appears as a form of two partial parts separated by a gap of 2 µm. It should be noted that this patch arrangement is totally equivalent to the patch arrangement described in Fig. 5.40. With the periodic boundary, the patch structure in Fig. 5.44 is repeated, resulting in the arrangement in Fig. 5.40.

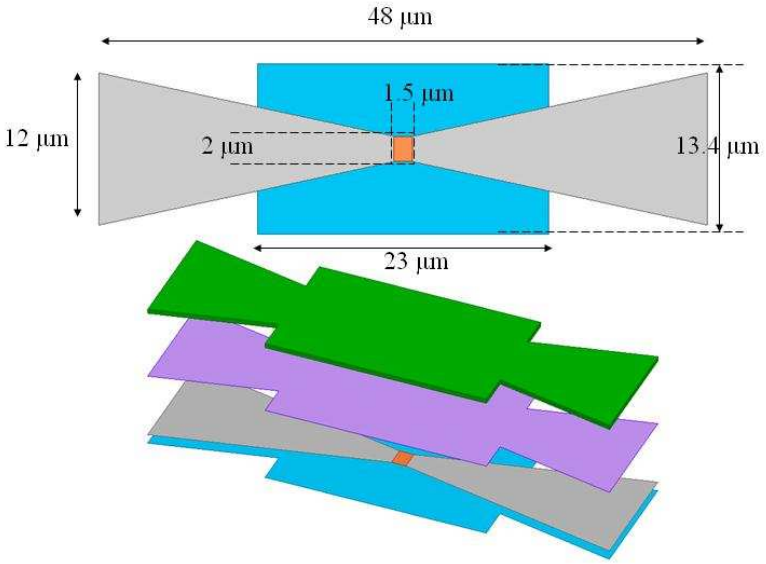

Fig. 5.45: Dimension and arrangement of the membrane

The patch in the bolometer structure has four holes to avoid contacts with the electrical metallic vias, and then avoid short-circuits. In fact, in one pixel, only two 11-µm long vias are required in order to provide the electrical contact function. For the two other vias, only the studs (the part outside the substrate) are kept for mechanical support.

The detailed dimension of the antenna with the suspended membrane is presented in Fig. 5.45. It should be noted that the load with 2 µm × 1.5 µm size results in a resistance of 225 Ω. The arrangement of two Si-N insulating layers and the thermometer layer is the same

as the previous designs. With this dimension, the antenna and the thermometer areas are 325.5 μm^2 and 541 μm^2 respectively.

Performances

This design includes only one bowtie antenna and thus is mono-polarized. The bolometer is sensitive to the leg-parallel polarization. In this direction, the detector ensures an absorption rate higher than 80 % at 850 GHz. The absorption in the perpendicular direction is very low as expected.

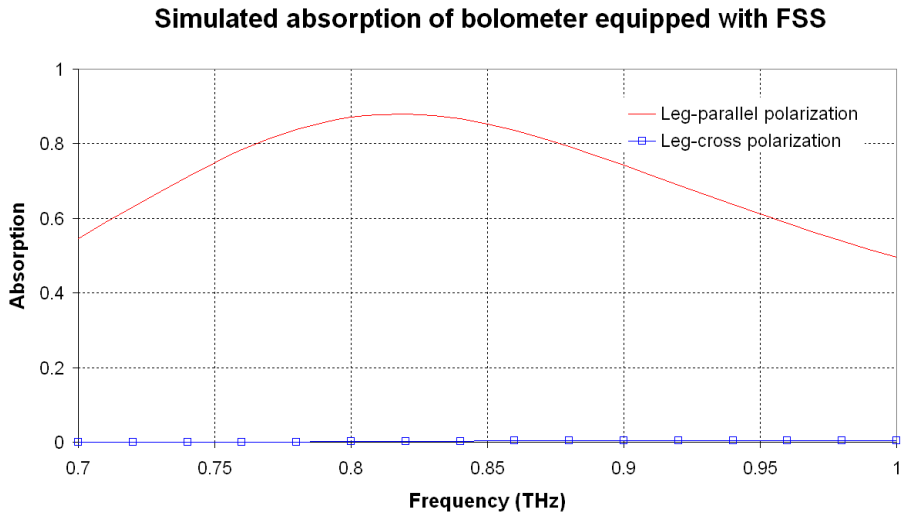

Fig. 5.46: Absorption of the 850 GHz bolometer showing a single polarization response.

Although this bolometer operates at 850 GHz, the design has the same pitch of 50 µm as the designs at 3 THz (THEDEX or Bambolo). This is a great advantage in term of heat capacity because the total heat capacity will be in the same range. The detailed calculation of heat capacity of each component in the suspended membrane is presented in the table below.

Element	**Material**	**Specific Heat Capacity** pJ/(μm^3.K)	**Surface** (μm^2)	**Volume** (μm^3)	Heat capacity (pJ/K)
Insulator 1+2	Si-N	1.12	541	21.6	24.2
Absorber	TiN	3.26	328.5	2.6	8.5
Thermometer	Amorphous Silicon	1.63	541	108 (200 nm thickness)	176
Antenna	Aluminum	2.43	325.5	81.4 (250 nm thickness)	197.8
Total heat capacity					407

Table 5.6: Detailed calculation of heat capacity of the 850 GHz bolometer.

The total heat capacity of the bolometer is 407 pJ/K. This is in the same range as the case of Bambolo design (dual polarizations). Assuming that the total thermal conductance is

14.2 nW/K, as in the case of THEDEX design, the thermal time constant will be 28.7 ms. With this time constant, the detector can perform a frame rate of:

$$f_{frame} = \frac{1}{3\tau_{th}} = \frac{1}{3 \times 28.7 \times 10^{-3}} = 11.6\,(\text{Hz}). \quad \textbf{(5.21)}$$

In order to perform real-time (25 Hz) video, the time constant should be at least 13.3 ms. This can be fulfilled by increasing the thermal conductance to:

$$g_{total} = \frac{C_{th}}{\tau_{th}} = \frac{407}{13.3} = 30.6\,(\text{nW/K}). \quad \textbf{(5.22)}$$

This thermal conductance is approximately twice the value 14.2 nW/K. Since the sensitivity is inversely proportional to thermal conductance, one can deduce that the bolometer sensitivity will be half of the one provided by the THEDEX design.

5.5 Summary

Several THz bolometer designs have been studied in this work. It should be noted that bolometer performances result from a trade-off between many features. The most important aspects could be stated as: mechanical strength, thermal isolation, optical coupling and electric function. The compromise between these parameters has to be considered in accordance to the application. The commercial infrared bolometer design is optimized for performing real-time passive thermal imaging. The THz bolometer design, which originates from this design, also should be optimized for a specific application. For instance, if an application prefers real-time 25 Hz video than dual polarization, the mono-polarization design should be used.

In terms of optical coupling, the CEA-Leti THz bolometer shows a very high absorption rate, better than 80 % at absorption peak. The bolometer response is broadband and its central frequency can be tuned. The studied stack is optimized for the spectral range around 3 THz. With this stack, the AFB and Bambolo designs show good optical coupling in both polarizations. However, the Bambolo has an advantage over the AFB as it exhibits smaller absorption of infrared radiation (8.8 % as compared to 30 %).

The THEDEX bolometer is the first THz bolometer successfully prototyped at CEA-Leti. Many technical challenges have been overcome during the fabrication of this design, like the fabrication of 11-µm thick SiO_2 layers and of metallic vias through these very thick layers. Also, the deposition of a long antenna directly on the suspended membrane was challenging in terms of mechanical stability. The detector shows an absorption peak at 1.35 THz for one polarization and 1.75 THz for other polarization. The absorption in the infrared range is about 29 %, the same order of magnitude as in the AFB design. THEDEX bolometers show a large (by a factor of 1.7) heat capacity when compared to other designs (AFB and Bambolo).

The bolometer exhibits lower resonance frequency when it includes FSSs. We have demonstrated that such pixel can absorb more than 80 % at 850 GHz even with a 50-µm pitch. The combination of FSS opens the way to many interesting perspectives. One can think about prototyping low frequency bolometers (850 GHz or 670 GHz) where atmospheric absorption is more favourable to THz imaging. Another perspective is to miniaturize the actual bolometer at 3 THz to get a smaller heat capacity.

In terms of thermal characteristics, with a heat capacity of ~ 670 pJ/K and a thermal conductance of ~15 nW/K, THEDEX exhibits the "sensitivity optimized" frame rate of ~8 Hz. Imaging faster than 8 Hz is possible at the expense of degrading the bolometer sensitivity.

Several designs, such as AFB or Bambolo, can decrease the heat capacity to the range 350 – 360 pJ/K. In such a case, the thermal conductance should be ~30 nW/K to ensure the 25 Hz frame rate. This of course degrades the sensitivity of the detector by a factor of two when compared to the THEDEX thermal conductance. In fact, the actual thermal insulation is quite high, knowing that the thermal conductance of infrared bolometer is 9 nW/K and 18 nW/K for 17-µm and 25-µm pitch pixel (see chapter 3). THz bolometers developed at other institutes, such as at NEC, Japan, are reported to have a thermal conductance of 30 nW/K [15].

The mono-polarization bolometer gets a small heat capacity (146 pJ/K) at the expense of being sensitive to only one polarization. In this case, the thermal conductance can be kept as ~15 nW/K. Thus the sensitivity of the detector is not degraded.

Last but not least, in this chapter, we have implemented successfully the transmitting mode simulation. Not only the impedance matching method is clearer but also the physical behavior of the structure is revealed. This method when combined with the traditional receiving mode simulation helps us in understanding the actually prototyped bolometer, i.e. THEDEX design. It also helps us in modeling efficiently many novel designs, such as Bambolo or the 850 GHz bolometer.

References

[1] R. Mittra, C. H. Chan, and T. Cwik, "Techniques for analyzing frequency selective surfaces-a review," Proceedings of the IEEE, vol. 76, no. 12, pp. 1593 –1615, Dec. 1988.

[2] R. Dickie, R. Cahill, H. S. Gamble, V. F. Fusco, P. G. Huggard, B. P. Moyna, M. L. Oldfield, N. Grant, and P. de Maagt, "Polarisation independent bandpass FSS," Electronics Letters, vol. 43, no. 19, pp. 1013 –1015, 2007.

[3] G. W. Wilson, T. C. Chen, E. S. Cheng, D. A. Cottingham, T. M. Crawford, T. Downes, F. M. Finkbeiner, D. J. Fixsen, D. W. Logan, S. Meyer, T. Perera, E. H. Sharp, and R. F. Silverberg, "Frequency Selective Bolometers - Progress and Projections," in Fifteenth International Symposium on Space Terahertz Technology, 2004, vol. -1, p. 106.

[4] G. Chattopadhyay, J. Glenn, J. J. Bock, B. K. Rownd, M. Caldwell, and M. J. Griffin, "Feed horn coupled bolometer arrays for SPIRE - design, simulations, and measurements," Microwave Theory and Techniques, IEEE Transactions on, vol. 51, no. 10, pp. 2139 – 2146, Oct. 2003.

[5] E. Mottin, "Uncooled amorphous silicon technology enhancement for 25-μm pixel pitch achievement," 2003, vol. 4820, pp. 200–207.

[6] J. J. Yon, A. Astier, S. Bisotto, G. Chamingis, A. Durand, J. L. Martin, E. Mottin, J. L. Ouvrier-Buffet, and J. L. Tissot, "First demonstration of 25 μm pitch uncooled amorphous silicon microbolometer IRFPA at LETI-LIR," Proceedings of SPIE, vol. 5783, no. 1, pp. 432–440, May 2005.

[7] R. Kitamura, L. Pilon, and M. Jonasz, "Optical constants of silica glass from extreme ultraviolet to far infrared at near room temperature," Appl. Opt., vol. 46, no. 33, pp. 8118–8133, Nov. 2007.

[8] A. Luukanen and J. P. Pekola, "A superconducting antenna-coupled hot-spot microbolometer," Applied Physics Letters, vol. 82, no. 22, pp. 3970–3972, Jun. 2003.

[9] J. F. Shackelford and W. Alexander, Eds., CRC Materials Science and Engineering Handbook, Third Edition, 3rd ed. CRC Press, 2000.

[10] W. Geyi, "Reply to 'Comments on "The Foster Reactance Theorem for Antennas and Radiation ,"'" IEEE Transactions on Antennas and Propagation, vol. 55, no. 3, pp. 1014 –1016, Mar. 2007.

[11] T. G. Spence and D. H. Werner, "A Novel Miniature Broadband/Multiband Antenna Based on an End-Loaded Planar Open-Sleeve Dipole," IEEE Transactions on Antennas and Propagation, vol. 54, no. 12, pp. 3614 –3620, Dec. 2006.

[12] B. A. Munk, Frequency Selective Surfaces: Theory and Design, 1st ed. Wiley-Interscience, 2000.

[13] D. Sievenpiper, L. Zhang, R. F. J. Broas, N. G. Alexopolous, and E. Yablonovitch, "High-impedance electromagnetic surfaces with a forbidden frequency band," IEEE Transactions on Microwave Theory and Techniques, vol. 47, no. 11, pp. 2059 –2074, Nov. 1999.

[14] D. Sievenpiper, "High-Impedance Electromagnetic Surfaces," University of California, Los Angeles, 1999.

[15] N. Oda, “Uncooled bolometer-type Terahertz focal plane array and camera for real-time imaging,” Comptes Rendus Physique, vol. 11, no. 7–8, pp. 496–509, Aug. 2010.

Chapter 6 Detector characterization results

In this chapter, we present the characterization results of the THz bolometer prototypes. The measurements were mostly dedicated to the optical coupling property of the detector. Two approaches are available, i.e. the measurements of the spectral reflectivity of the focal plane array (FPA) surface and of the spectral response at the bolometer electrical output. Bolometers that have been characterized correspond to the THEDEX design presented in chapter 5. Two array formats have been fabricated: a 320×240 pixels array monolithically processed above a CMOS ROIC and a second 160×120 pixels array that is electrically read-out by a simple circuit scheme. An important objective of these measurements was to validate the simulations described in chapter 5. These characterizations have also highlighted some phenomena, such as the coupling between the pixel array and the ROIC structure.

In this chapter, the developed measurement set-up is examined first. Then, the experimental results are compared to the simulated ones. Some other figures of merit, such as the thermal characteristic or the sensibility, are reported to give a global vision of the detector performance. Finally, some imaging demonstrations are presented to illustrate the application perspectives.

6.1 Optical coupling measurement

6.1.1 Characterization with a Fourier-transform spectrometer

6.1.1.1 Introduction of Fourier-transform spectroscopy

The measurement of the optical coupling of the detector in this PhD work employs a Fourier transform spectrometer. We give here a short presentation about Fourier transform infrared spectroscopy (FTIR). Infrared spectroscopy has been a popular technique for materials analysis in laboratory and industry for many decades. An infrared spectrum represents a fingerprint of a sample response with absorption peaks corresponding to the frequencies of vibrations between the bonds of the atoms making up the material (Fig. 6.1).

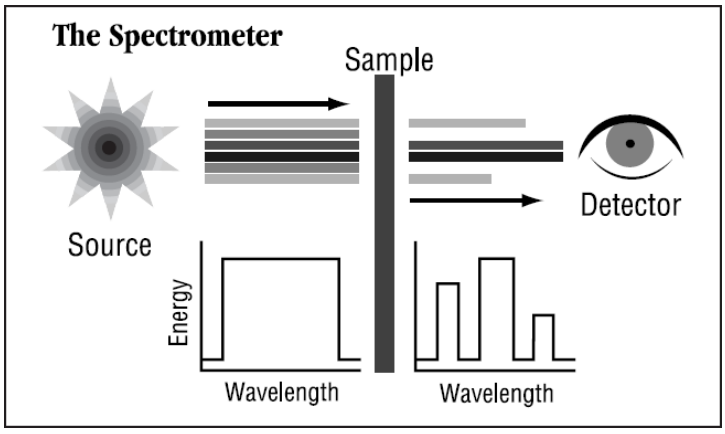

Fig. 6.1: FTIR technique principle.

Because each material is a unique combination of atoms, two different compounds do not exhibit exactly the same infrared spectrum. Therefore, infrared spectroscopy can be used to identify qualitatively materials and substances. In addition, the peak magnitudes in the spectrum provide direct indication of the amount of present material. Combined with advanced software algorithms, infrared spectroscopy is thus an excellent tool for quantitative

analysis. The original infrared spectrometers were based on dispersion. These instruments separate the individual frequencies of the optical beam into different positions. This was accomplished by the use of a prism or a grating. The detector is scanned in order to measure the amount of energy at each position. This results in a spectrum that corresponds to a plot of intensity vs. frequency.

Fourier Transform Infrared (FTIR) spectrometry was developed in order to overcome the limitations encountered with dispersive instruments, which is a slow scanning process due to the lack of powerful infrared sources at that time. Measuring all of the infrared frequencies simultaneously, rather than individually, makes the detecting signal stronger. The solution proposed and developed employs a simple optical device called an interferometer. The interferometer produces a unique type of signal, the so-called waveform, which contains all of the infrared spectral components "encoded" into it. Nowadays, in modern instruments, the signal can be measured very quickly, usually in the order of one second.

6.1.1.2 Principle of Fourier-transform spectroscopy

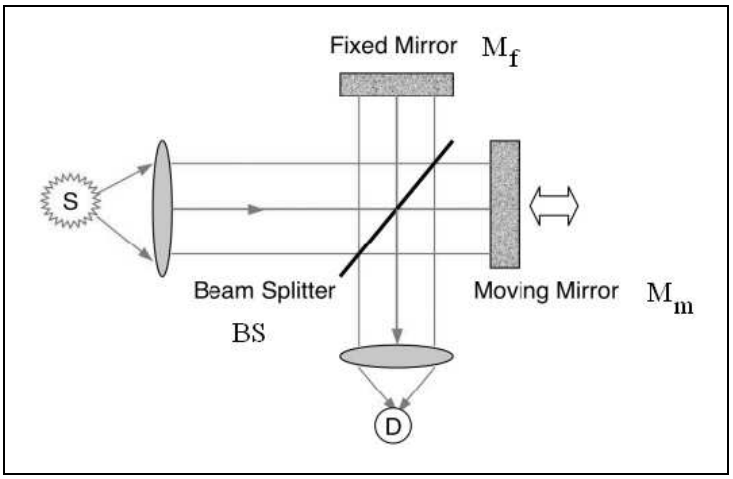

Fig. 6.2: Michelson interferometer.

Most of the FTIR instruments are based on Michelson interferometers (Fig. 6.2). The incoming beam is split in two beams propagating perpendicularly along what is called the arms of the interferometer. Each beam strikes a mirror at normal incidence and is reflected backwards. The two beams recombine at the beam splitter BS that directs the sum of the two beams onto a detector D. One of the mirrors, M_m, can be moved along the direction of the impinging beam, while the second one, M_f, is fixed. The interference pattern recorded by the detector depends on the difference of optical path x between the two arms, and it can be varied by moving the mirror M_m. Let us assume that the beam incoming into the interferometer is a monochromatic radiation of intensity I_o and of angular frequency $\omega = 2\pi\frac{c}{\lambda}$. At the detector, the recorded intensity of the sum of the two beams reflected respectively by the mirrors M_f and M_m is:

$$I(x) = \overline{\left(E_o \cos\left(\frac{\omega}{c}(X+x) - \omega t\right) + E_o \cos\left(\frac{\omega}{c}X - \omega t\right)\right)^2} = \frac{I_o}{4}\left(1 + \cos\left(\frac{\omega}{c}x\right)\right). \quad \textbf{(6.1)}$$

Here, we have supposed that the beam splitter is ideal (lossless and 50% splitting efficiency). The intensity varies as a cosine function with x. It is represented in the following figure.

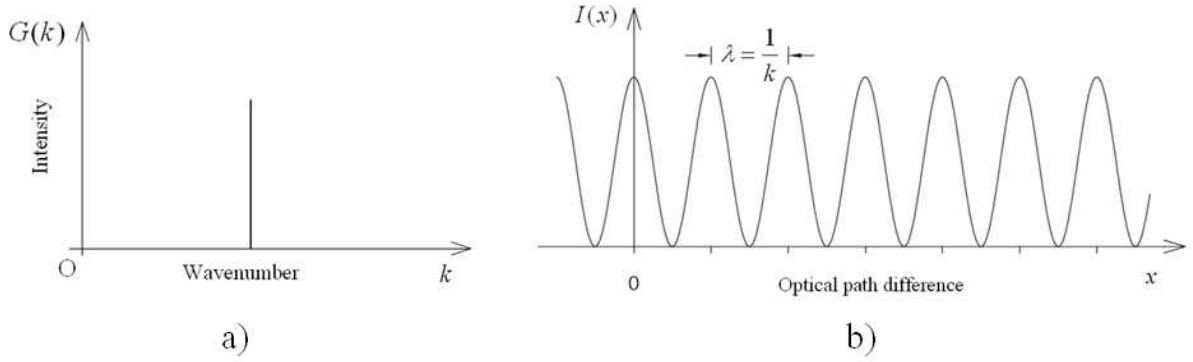

Fig. 6.3: Spectrum (a) and interferogram (b) of monochromatic wave

If a non-monochromatic light is used, the intensity is the sum of the preceding cosine functions obtained for all the wavelengths that compose the radiation.

$$I(x) = \int_0^{\infty} \frac{I_o(\omega)}{4}\left(1 + \cos\left(\frac{\omega}{c}x\right)\right)d\omega = \int_0^{\infty} \frac{I_o(\omega)}{4}d\omega + \int_0^{\infty} \frac{I_o(\omega)}{4}\cos\left(\frac{\omega}{c}x\right)d\omega. \qquad \textbf{(6.2)}$$

$I_o(\omega)$ corresponds to the spectrum of the incident beam, while the recorded signal $I(x)$ is called an interferogram. Then we can use a complex notation to write expression (6.2) in which we select only the term varying with x and suppressing the constant amplification factor 1/4 to simplify the representation:

$$I_v(x) = \int_{-\infty}^{+\infty} I_o(\omega) e^{j\frac{\omega}{c}x} d\omega. \qquad \textbf{(6.3)}$$

In (6.3), $I_o(-\omega) = I_o(\omega)$. This expression is nothing but the Fourier transform of $I_o(\omega)$. Thus the spectrum $I_o(\omega)$ is obtained by taking the inverse Fourier transform of $I_v(x)$. We get:

$$I_o(\omega) = \int_{-\infty}^{+\infty} I_v(x) e^{-j\frac{\omega}{c}x} dx. \qquad \textbf{(6.4)}$$

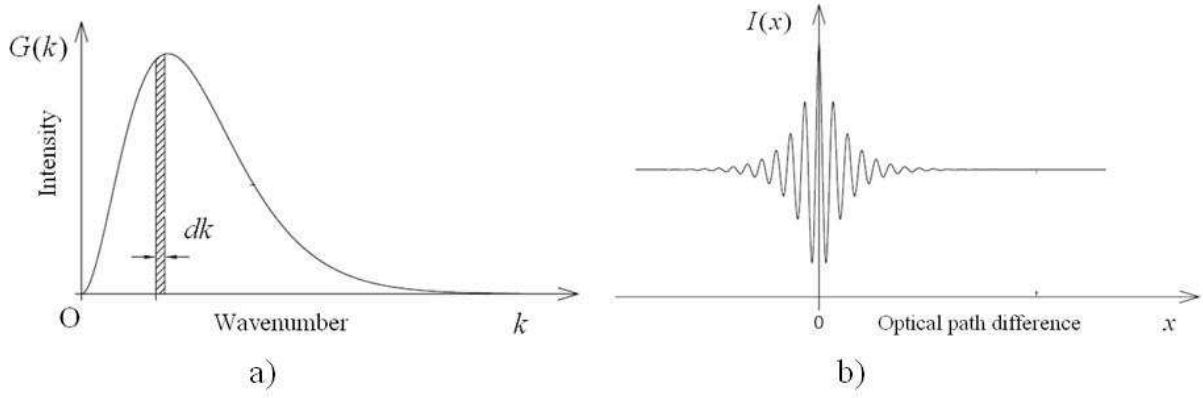

Fig. 6.4: Spectrum (a) and interferogram (b) of non-monochromatic light

Therefore, the spectrum $I_o(\omega)$ of the incoming radiation is obtained by recording the interferogram versus the mobile mirror displacement x and then by calculating the Fourier transform of the interferogram.

Practically, this interferogram depends also on the characteristics of transmission of the spectrometer and on the detector spectral response. In addition, as the distance x_{max} over which the interferogram is recorded cannot be infinite, expression (6.4) is limited in integration. It becomes that the achieved spectrum $I_{exp}(\omega)$ is:

$$I_{exp}(\omega) = \int_{-x_{max}/2}^{+x_{max}/2} I_v(x) e^{-j\frac{\omega}{c}x} dx = \int_{-\infty}^{+\infty} W_{x_{max}}(x) I_v(x) e^{-j\frac{\omega}{c}x} dx = I_o(\omega) \otimes W_{x_{max}}(\omega) \quad \textbf{(6.5)}$$

.

where $W_{x_{max}}(x)$ is a rectangle function equal to 1 in between $-x_{max}/2$ and $+ x_{max}/2$, and $W_{x_{max}}(\omega)$ is its Fourier transform:

$$W_{x_{max}}(\omega) = \int_{-\infty}^{+\infty} W_{x_{max}}(x) e^{-j\frac{\omega}{c}x} dx = \int_{-x_{max}/2}^{+x_{max}/2} e^{-j\frac{\omega}{c}x} dx = x_{max} \sin c\left(\frac{\omega}{c}\frac{x_{max}}{2}\right). \quad \textbf{(6.6)}$$

It follows that the spectral resolution of the FTS spectrometer is given by the spectral width of the sinc function, i.e. corresponding to $\frac{\Delta\omega}{c}\frac{x_{max}}{2} \approx \pi$ or $\Delta f = \frac{c}{x_{max}}$. The longer the displacement of the mirror, the better is the frequency resolution.

The characterization of a sample by Fourier transform spectroscopy is based on two measurements, with and without the sample under test in front of the spectrometer. By comparing these two measurements, one can extract the spectral information of the sample itself.

6.1.2 Reflectivity

6.1.2.1 Measurement set-up

The reflectivity measurement set-up makes use of the spectrometer Vertex 80v from Bruker Optics (scheme in Fig. 6.5). For our experiments, the THz source is a Hg arc lamp, located at the position In 2 of the figure, which behaves as a blackbody whose temperature is of the order of 1000°C. Its corresponding spectrum is quite flat over the wavelength range 25–1000 μm which is equivalent to the 0.3–12 THz frequency band. This THz radiation undergoes strong attenuation in the beam splitter whose spectral transmission presents a narrow bandwidth. Up to date, there is not a beam-splitter that can cover the whole THz range, so two beam-splitters are successively used to cover the 0.6–3 THz targeted range: one multilayer beam-splitter in the range 1.5–3 THz, a second in the lower range.

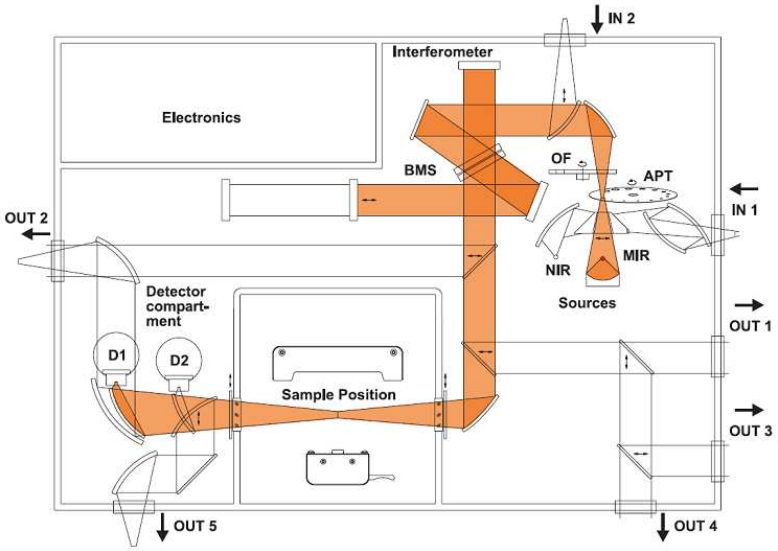

Fig. 6.5: Scheme of the spectrometer Vertex 80v.

One can see that the optical path plotted in Fig. 6.5 corresponds to the transmission configuration. To provide reflectivity measurement, the spectrometer is then equipped with a reflection module presented in Fig. 6.6.

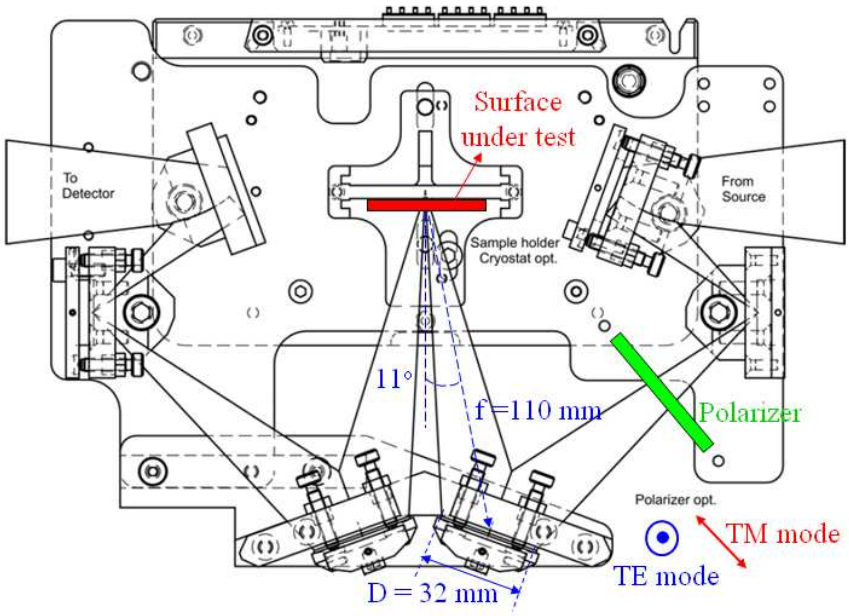

Fig. 6.6: Top view of the reflection module.

The reflection module consists of 3 input mirrors and 3 output mirrors. This module steers the beam onto the sample with an incident angle of 11 degrees. The last input mirror is an elliptical one that has focal length of 110 mm and a diameter of 32 mm, and so exhibits a 3.4 f-number.

A THz polarizer set before the last mirror makes possible the choice either of TE (the electric field is normal to the reflection plan) or TM (the electric field in the reflection plan) modes. Consequently, the polarization of the incident wave impinging on the surface under test is properly controlled.

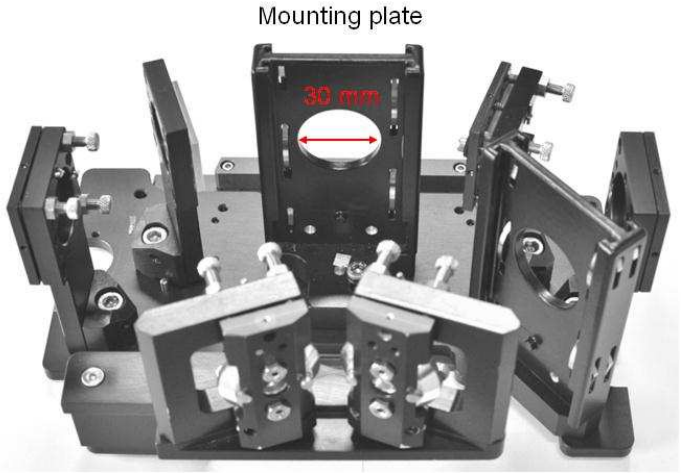

Fig. 6.7: Photo of the reflection module.

The photography of the reflection module is shown in Fig. 6.7. The (vertical) mounting plate has a 30-mm diameter hole. The beam spot is smaller than this hole size. Therefore, if the sample under test is not placed in the mounting plate, the THz beam will go through the hole and be scattered in the sample compartment. The signal sensed by the FTIR detectors will then be null. As presented in the next paragraph, by using a metallic plate with a hole etched at its center, the spot size of the THz beam can be determined.

6.1.2.2 Spot-size and area of surface under test

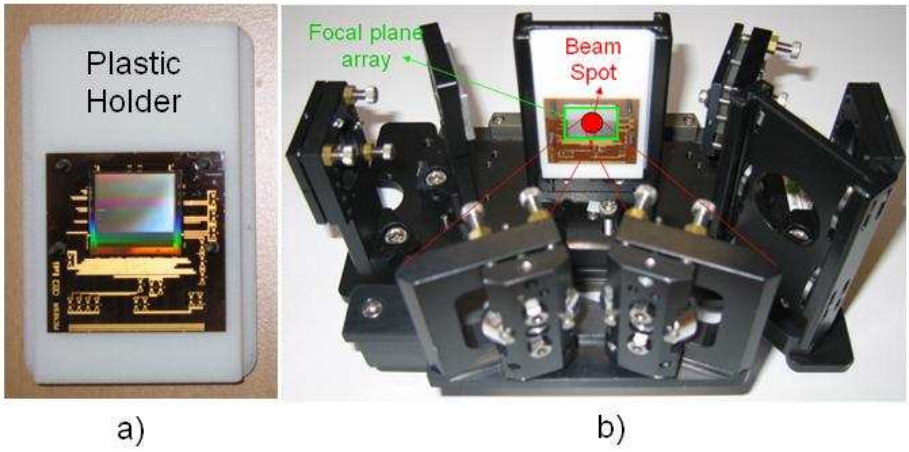

Fig. 6.8: a) Photo of the detector chip mounted on a plastic holder and b) Setup of the sample in the reflection module.

The detector chip presents an overall size of 20×18 mm^2 that encompasses the 320×240 bolometer focal plane array (FPA) and its read-out electronics. Since the pixel pitch is 50 µm, the FPA area is 16×12 mm^2. This surface corresponds to the effective sensitive surface whose reflectivity needs to be characterized. The detector chip is mounted on a ceramic card that connects the FPA output pads to the external front-end electronics. This card is in turn mounted on a plastic sheet to facilitate its holding in the reflection module.

In an ideal case, the spot of THz incident beam should be smaller than the FPA and centered in the optical sensitive area. This is necessary in order to characterize only the array of pixels with no contribution of its surrounding electronics. Moreover in this case, the diffraction at the edge of the FPA can be neglected. This scenario requires that the spot size and position are precisely controlled.

In reality, some constraints related to the equipment make difficult the achievement of this ideal set-up. First, in order to reduce the atmospheric attenuation, the spectrometer operates under vacuum condition. Due to this constraint, it is very challenging to use an XYZ displacement stage to control dynamically the position of the plastic holder (thus the position of the sensitive area). We have chosen to mount the detector chip symmetrically on the plastic holder and to align the beam spot at its center. This method of course cannot provide a precise alignment as good as with a XYZ displacement stage, however it can ensure a misalignment lower than 1–2 mm.

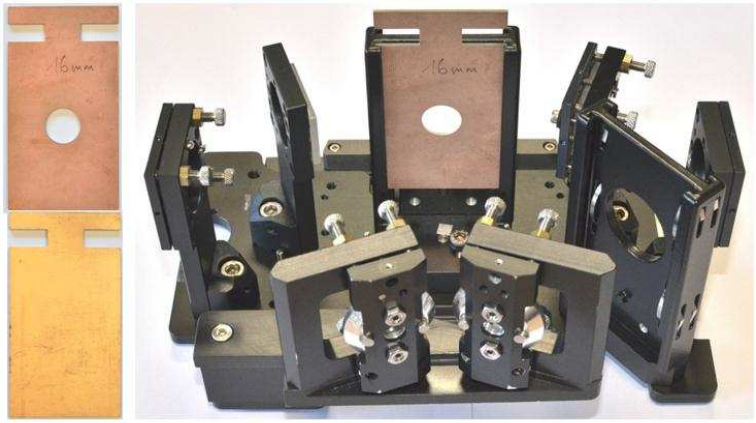

Fig. 6.9: a) Metallic plates, and b) mounting of plate in the reflection module.

To measure the spot size, we used several cooper plates with a hole in the center. When the THz radiation arrives on the metallic plate, depending on the beam spot and hole sizes, it can be reflected partially or completely go through the plate. By varying the diameter of the hole, the size of the THz beam-spot can be retrieved.

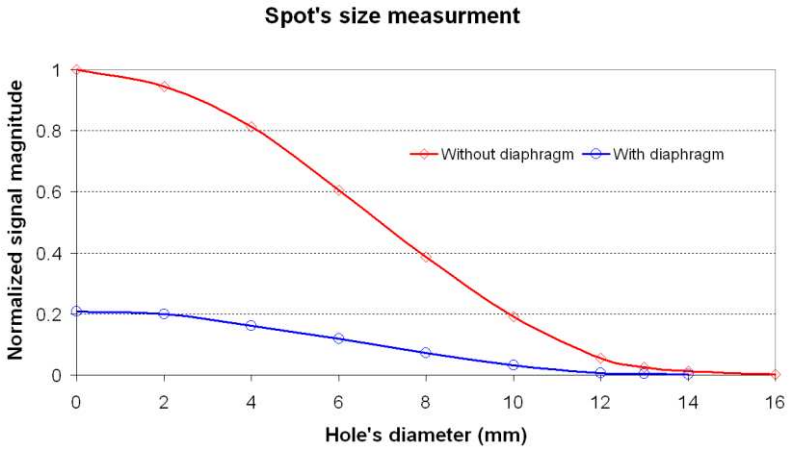

Fig. 6.10: Measurement of spot size by using different hole diameters.

If the metallic plate has no hole, the incident beam is completely reflected by the continuous metallic surface, resulting in a maximum detected signal. As the hole diameter increases, the portion of the incident beam that is reflected gets smaller and the signal at the detector decreases. Experiments show that for 16-mm diameter, the signal reaches the noise level. This means that the THz beam is completely lost through the hole, being scattered in the sample compartment and not reaching the FTIR detector.

Fig. 6.10 shows the (normalized) detected signal magnitude as a function of the hole diameter. The tested diameters were 0, 2, 4, 6, 8, 10, 12, 13, 14, and 16 mm. When the hole diameter is 10 mm, the normalized detected signal magnitude is 20 %. This means that 80 %

of the energy is lost through the hole of 10 mm diameter. Thus, we can conclude the area corresponding to 10 mm diameter contains 80 % the whole energy of the THz spot. In fact, for a Gaussian beam, the beam waist spot contains 86 % ($1-e^{-2}$) of the total optical power. This value corresponds to ~11-mm diameter in Fig. 6.10. Thus, the spot size can be considered roughly 11-mm diameter. This dimension is slightly smaller than the dimension of the sensitive area of the detector chip (16×12 mm^2).

One can think about using a diaphragm to reduce the spot size so that the illuminating beam is clearly smaller than the FPA area. This is not easy since the sample compartment is small and when the reflection module is placed inside, room is missing for a diaphragm. The most favorable position is at the polarizer location (see Fig. 6.6). Some trials were carried out with such a diaphragm at this position. It turns out that whereas the detector signal is reduced roughly by a factor 5 in comparison to the case without diaphragm, the spot size is not clearly decreased because of diffraction. Measurements show that the area of 10-mm diameter still contains 84.4 % the total energy when compared to 80 % the case without diaphragm.

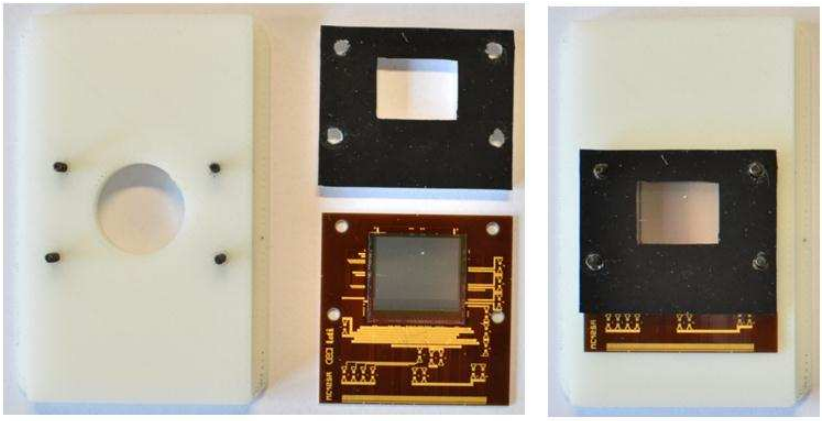

Fig. 6.11: Image of reflection module.

In order to solve the spot size problem, a THz absorbing diaphragm has been fixed onto the ceramic plate. This diaphragm has a rectangular hole with dimensions similar to the FPA area, i.e. 12×16 mm^2. Since spot size is roughly 12 mm, a portion of the beam-spot does not go through the rectangular hole but is reflected by the surface of the absorbing diaphragm due to the misalignment. However, tests where the diaphragm is used as a sample (without the detector chip below) have shown that the residual reflectivity is negligible.

6.1.2.3 Incident angle and polarization

From the top view of the reflection module (Fig. 6.6), we have seen that the incident THz beam can have two polarizations. TE mode is characterized by an electric field perpendicular to the plane of reflection while for TM polarization electric field is parallel to this plane. Let us precise that the reflection plane is the horizontal plane.

The electromagnetic response of the bolometer under test depends on polarization. For leg-parallel polarization, the DC antenna is excited while the CC antenna is excited by the other polarization (leg-cross polarization). One can see that since the incident angle with respect to the FPA surface is not null; each antenna can be excited by a TE or TM beam, depending on the arrangement of the FPA surface as explained following.

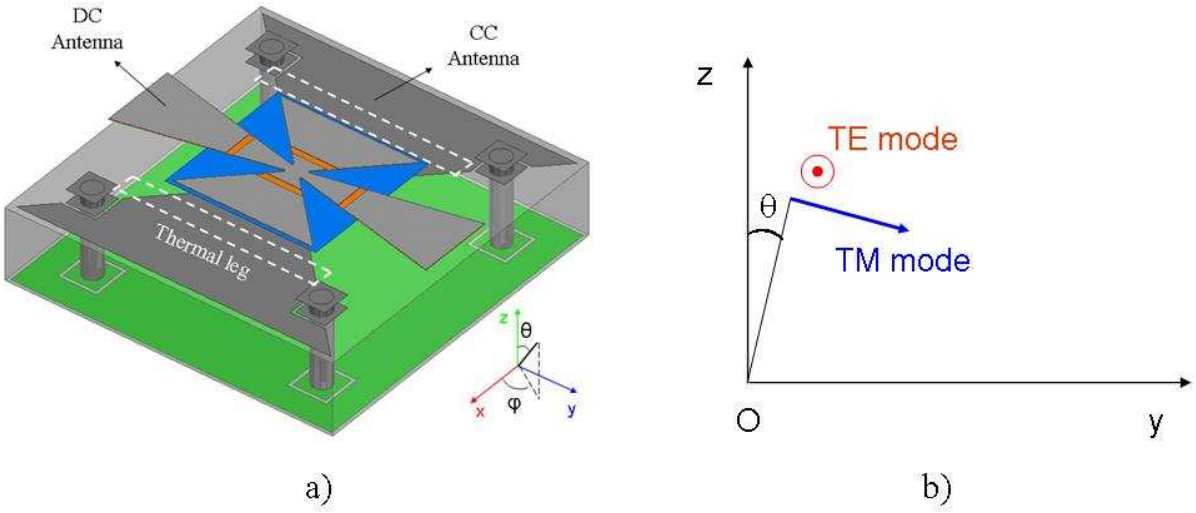

Fig. 6.12: Arrangement of the detector regarding the coordinate system.

Regarding Fig. 6.12, let us suppose that the FPA surface is set so that yOz is the plane of reflection. In this case, the TE mode is equivalent to a plane wave that has its electric field parallel with Ox and arrives on the array of pixel above from the direction (θ, φ) = (11^o, 90^o). The CC antenna is excited because it is parallel to the electric field.

The TM mode corresponds to a plane wave with E field parallel to the plane yOz and arrives from the direction (θ, φ) = (11^o, 90^o). Although the electric field of the TM mode is in the same plane as the DC antenna, it is not parallel with the DC antenna. In fact, it is inclined with the DC antenna by an angle equal to the θ angle, i.e. 11^o.

Now, let us suppose that the FPA surface is set so that the xOz is the plane of reflection. With a similar reasoning, we can deduce that the DC antenna is excited by TE mode while the CC antenna is excited by TM mode. Table below summarizes both cases of plane of reflection.

Plane of reflection	**TE mode**	**TM mode**
yOz	E-field is parallel with Ox CC antenna is excited	E-field is 11^o inclined with Oy DC antenna is excited
xOz	E-field is parallel with Oy DC antenna is excited	E-field is 11^o inclined with Ox CC antenna is excited

Table 6.1: 4 combinations between antenna direction and polarization of incident wave.

In summary, if the antenna is excited by the TE mode, the electric field is parallel with the antenna. In TM mode, the electric field is inclined with respect to the antenna by an angle θ. In such a case, the magnitude of the electric field reduces to its projected component by a factor of $\cos(\theta)$. One can see that if the incident angle is large, says 60^o, the projected component would be a half of the incident electric field. The electromagnetic response of the array of bolometer would differ between TE and TM modes.

Since, in our experiment θ is fixed at 11^o, $\cos(\theta)$ is very close to unity and hence the difference between TE and TM mode is very small. Thus, the incident beam can be considered approximately as normal to the FPA surface. In fact, simulations show that the bolometer response exhibits negligible variation between normal and 11^o incident angles.

Figures below show the measured reflectivity of the bolometer over 0.6–3 THz range. Antennas are excited by TE and TM beams as explained previously. We observe very similar results for TE and TM polarizations.

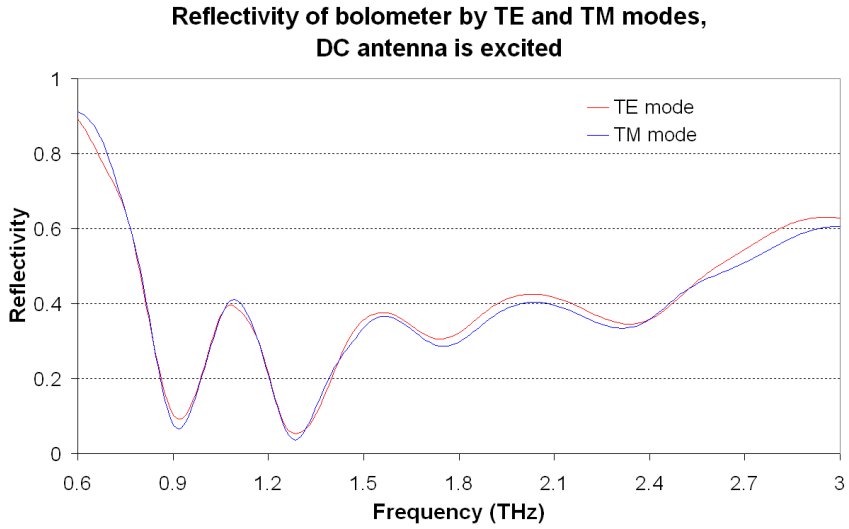

Fig. 6.13: Reflectivity of FPA when DC antenna is excited by TE and TM modes.

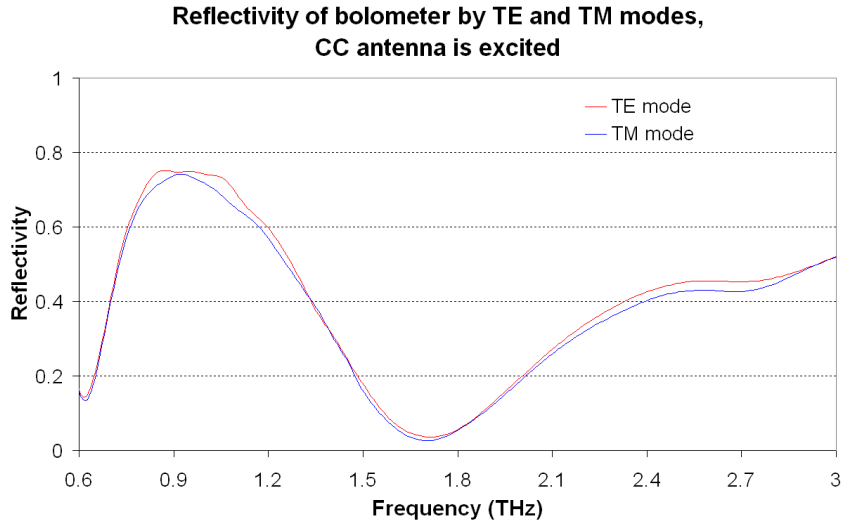

Fig. 6.14: Reflectivity of FPA when CC antenna is excited by TE and TM modes.

Since the difference between TE and TM cases is small, in order to simplify the presentation of the following results, we will refer to the bolometer polarization simply by naming the geometry of the detector (DC and CC antenna) afterward.

6.1.2.4 Measurement procedure and accuracy

Measurement procedure

The reflectivity of the FPA surface is deduced from two measurements: first a metallic mirror is placed in the sample holder plane and then a second measurement is made whereas the FPA replaces the mirror. The ratio of the sample to reference signals issues the reflectivity independently of the spectral characteristics of the setup. The mirror is a 3-µm thick aluminum layer deposited on a silicon wafer, exhibiting almost 100% reflectivity in the far infrared, so the measured value of sample reflectivity can be considered as the absolute reflectivity.

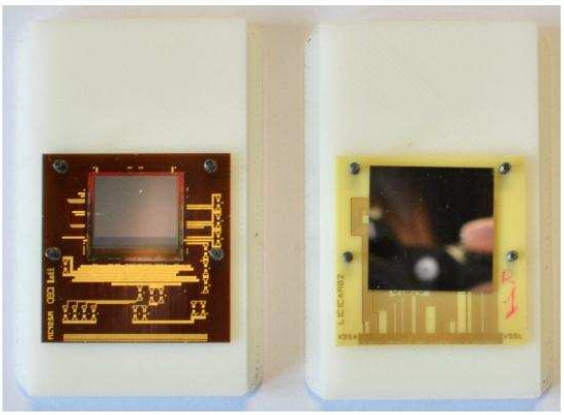

Fig. 6.15: a) Photo of the detector chip and b) photo of the mirror. Both are mounted with similar ceramic card and plastic holder.

Accuracy of measurement

The measurement was performed using the Bruker Vertex 80v FTS spectrometer. This research-dedicated spectrometer provides a very high resolution (0.2 cm^{-1}), with a very good wavenumber accuracy. To estimate the wavenumber accuracy, water vapor is used. Water vapor has the advantage of having extremely narrow bands, and the position of these bands is known with a very high degree of accuracy. Experimental tests show deviation of 0.041 cm^{-1} for the absorption peak at 1554.353 cm^{-1} of water vapor as compared to the published tables. So the relative deviation of our equipment is smaller than 0.003%. Although the wavenumber of this peak is not in the range 20–100 cm^{-1} (i.e. 0.6–3 THz in frequency), the test still gives credit to the wavenumber accuracy of our measurement. The reason is that the wavenumber accuracy depends mainly on the accuracy of interferogram, which is ensured by the capability of alignment of the interferometer (a spatial precision of 340 nm since the interferometer uses the 680-nm wavelength laser for alignment of the mobile mirror) regardless the spectral range in question. With this high wavenumber accuracy, to simplify the evaluation of measurement accuracy, we neglect the wavenumber position error (X-axis error) and discuss only on the amplitude error (Y-axis error). This error relates to the signal-to-noise ratio (SNR) of the measurement.

The total reflectivity spectrum results from merging two spectrally overlapping measurements: one in the spectral range 0.6–1.5 THz and the other for the range 1.05–3 THz. We remind that this procedure is compulsory because beam splitters show a limited bandwidth and do not cover the whole spectrum from 0.6 to 3 THz. To evaluate the accuracy of the resulting measured reflectivity, two consecutive measurements with complimentary beam splitters have been carried out and compared. It should be noted that each measure is already the result of averaging 64 scans. Performing many scans to get a better signal to noise ratio is one of the most important advantage of the FTIR technique.

In the following figure, we plot 2 measurements realized in the 0.6–1.5 THz and 1.05–3 THz ranges denoted as “low band” and “high band”. The low band curve exhibits a peak-to-peak error of 0.007 and an average error of 0.003. In the [1.05 – 3 THz] range, these values are 0.02 and 0.004, respectively. This very good accuracy is partly due to the fact that each measurement is an average result of 64 scans, so the signal to noise ratio is enhanced.

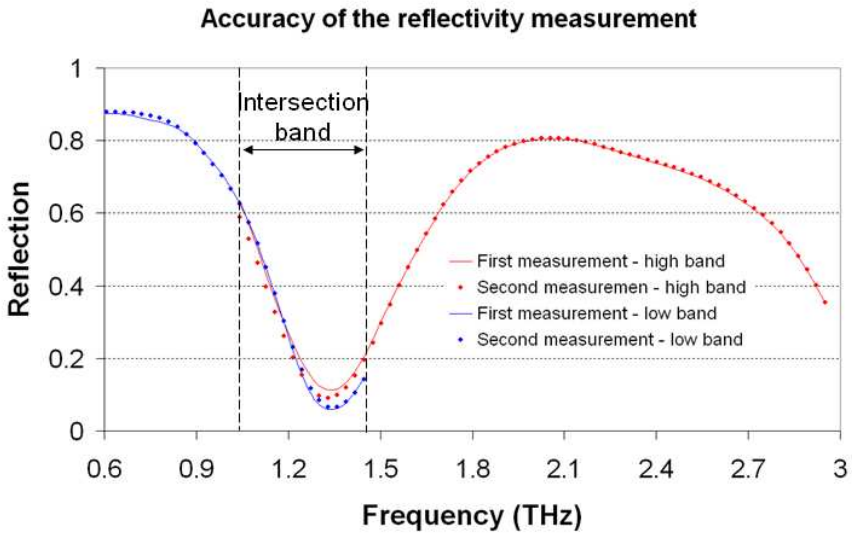

Fig. 6.16: Accuracy of the reflectivity measurement.

In the overlapping band 1.05-1.5 THz, the two curves show a little mismatch. The peak-to-peak value and the average value of mismatch over the intersection band are 0.027 and 0.016, respectively. This small discrepancy comes perhaps from the fact that changing the beam splitter may slightly alter the optical path in the interferometer. The final result is computed as the average of the two curves measured in this intersection band.

6.1.3 Spectral response

6.1.3.1 Measurement set-up

Optical setup

The direct measurement of the spectral response of the bolometer requires a second specific optical configuration. After passing through the FTS spectrometer (see Fig. 6.17), the parallel THz beam is deflected by a mirror toward a side window. The beam is then focused onto the bolometer under test with a Tsurupica lens, which has an f-number equal to 4. The bolometer is located in a vacuum vessel equipped with a HDPE window. The beam undergoes atmospheric attenuation only along a 15-cm path from the spectrometer window to the vessel window. The electrical current flowing through the resistance of a single bolometric pixel is read by using a low noise voltage/current (V/A) amplifier.

A mechanical chopper and a lock-in amplifier are used to perform a synchronous detection. The electric signal at the output of the lock-in amplifier is recorded versus the displacement of the mobile mirror of the interferometer leading to an interferogram that is subsequently Fourier transformed to get the spectral signal. This spectrum corresponds to the convolution of the spectral emission of the source, of the spectral transmission of the optical chain and of the spectral absorption of the bolometer. A reference spectrum is recorded by using the calibrated pyroelectric detector of the spectrometer instead of the studied bolometer, while maintaining all other components of the optical set up (the measure is performed under vacuum condition). By taking the ratio of the signal and reference spectra, we obtain the relative spectral response of the bolometer.

Although the focal plane array prototype had 160×120 pixels for this series of test, only 16 pixels were possibly addressed electrically since these chips were not processed over a CMOS ROIC. So only individual bolometer outputs were electrically read-out by an external

circuit. The spectral response measurement is therefore performed by measuring the signal of a single pixel selected in the prototype chip array.

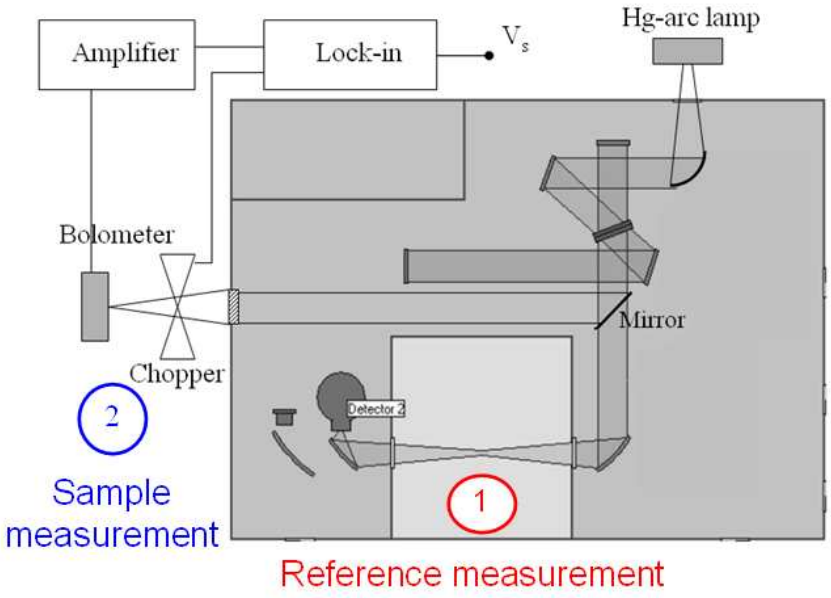

Fig. 6.17: Setup of the spectral response measurement.

Step-scan and synchronous detection

One of the difficulties of this measurement comes from the slow response of the bolometer. To perform an interferogram measurement, the mobile mirror moves and the signal of detector is acquired during this time. Thus the detector should be fast enough regarding the displacement velocity of the mobile mirror. When the mirror moves, the optical path difference (OPD) changes and the beam light in the interferometer will go in and out of phase depending on the OPD: we say that the beam light is modulated. In fact, if v_{mirror} is the velocity of the mobile mirror thus the OPD is equal to:

$$x = 2v_{mirror}t\,. \tag{6.7}$$

The factor 2 is due that the beam propagates over an additional distance of 2d when the mirror is shifted by d, because of the back and forth propagation of the light. As the intensity at the detector varies as $\cos\left(\frac{\omega}{c}x\right)$, it varies with time as $\cos\left(2\frac{\omega v_{mirror}}{c}t\right)$, i.e. with a modulation frequency equal to:

$$f_{modulation} = \frac{2\frac{\omega v_{mirror}}{c}}{2\pi} = 2\frac{v_{mirror}}{c}\ f = 2\frac{v_{mirror}}{\lambda}\,. \tag{6.8}$$

The cut-off frequency of the detector should be higher than this modulation frequency so that the modulation can be efficiently detected. For the Vertex 80v spectrometer, the lowest velocity of the mobile mirror is 0.05 cm/s. Therefore, the modulation frequency that corresponds to a beam light at 100 cm^{-1} (f = 3 THz) is:

$$f_{modulation} = 2\frac{v_{mirror}}{c} f = 2\frac{5\times10^{-4}}{3\times10^{8}} 3\times10^{12} = 10\,\text{Hz}. \quad \textbf{(6.9)}$$

The measured thermal time constant of the bolometer under test is ~ 50 ms. As explained in chapter 2, the 3 dB cut-off frequency of the detector is then:

$$f_c = \frac{1}{2\pi\tau_{th}} = \frac{1}{2\pi\times0.05} \approx 3.2 \text{ (Hz)}. \quad \textbf{(6.10)}$$

Since the bolometer cut-off frequency is lower than the modulation frequency, any signal delivered by the bolometer is very slow. To overcome this problem, we must implement the step-scan mode of the spectrometer. In this mode, the mobile mirror does not move continuously but with discrete increments. This means that the mirror moves to a position, waits a time there (this time can be chosen), during which performs the signal acquisition, and moves to the next position. The waiting time can be selected in such a way that the bolometer has enough time to reach its steady state. It should be at least:

$$T_{step} = 3\tau_{th}. \quad \textbf{(6.11)}$$

This time is 150 ms for a bolometer with 50-ms thermal time constant. However, in practice, the waiting time is several times higher than this value because of the lock-in measurement as explained in the following.

In FTIR technique, as already explained, the spectral resolution of the measurement is inversely proportional to the displacement distance of the mobile mirror, thus to the length of the interferogram. In step-scan mode, if a 4-cm^{-1} resolution is desired, the length of the interferogram should be at least 8886 steps. A 8-cm^{-1} resolution requires 4442 steps. Since each step takes at least 150 ms, the measurement time is 22 minutes (for 4 cm^{-1} resolution) and 11 minutes (for 8 cm^{-1} resolution). During this time, the temperatures of the ambient surroundings of the bolometer (the vacuum vessel and its HDPE window) may vary. Such variations cause a change in the far infrared flux emitted by these elements towards the bolometer, changing its resistance. Since the bolometer under test is polarized by a constant voltage source, this causes a varying current that may affect the interferogram measurement.

The measurement without lock-in technique shows that the variation magnitude is very serious when compared to the peak amplitude of the interferogram. In order to suppress this signal derivation of the bolometer signal, synchronous detection is applied. The chopper (shutter) modulates the beam light that comes out from the interferometer. Thus the signal sensed by the bolometer is also modulated at the same frequency. Performing the demodulation with a lock-in detection suppresses the unwanted signal coming from the surrounding elements since it filters only the beam light of the interferometer. Theoretically, the chopper should be as close as possible to the Hg-arc lamp source in order to ensure that the detector "sees" only the optical flux coming out from the source. However, this is practically difficult to implement because the Hg-arc lamp is integrated inside the spectrometer to ensure vacuum condition of the measurement. We have found that the position of the chopper as shown by Fig. 6.14 though is not optimal but can still give a reasonable result.

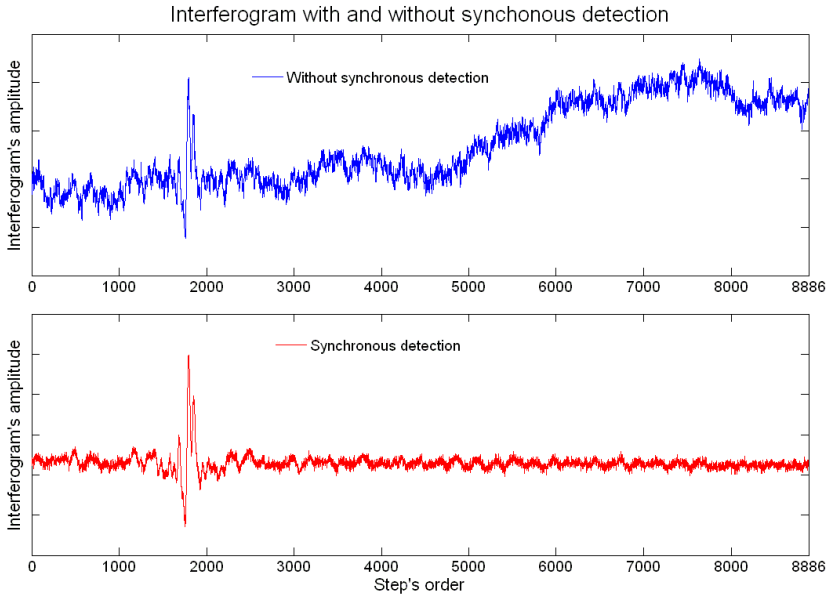

Fig. 6.18: Interferogram with (bottom) and without (top) synchronous detection.

In Fig. 6.18, both inteferograms obtained with and without synchronous detection are plotted. Without synchronous detection, the chosen waiting time is 200 ms, resulting in a total measurement duration of 30 minutes. When synchronous detection has been applied with a waiting time of 1 s, the whole data acquisition has taken 148 minutes. The figure shows that in the latter case, the signal of the bolometer is much more stable even though measurement duration is much longer.

Measurement duration

With the synchronous detection scheme, the period of the chopper is:

$$T_{chopper} = 2 \times 3\tau_{th} = 2 \times 3 \times 50 = 300 \text{ ms.} \quad \textbf{(6.12)}$$

The waiting time at each step position should be at least 3 times of the chopper period so that there is enough time to demodulate properly the chopped signal.

$$T_{step} = 3T_{chopper} = 3 \times 300 = 900 \text{ ms.} \quad \textbf{(6.13)}$$

We selected 1000 ms as waiting time. It comes out that the 4 cm^{-1} resolution measurement takes 148 minutes while the 8 cm^{-1} resolution measurement requires 74 minutes for each scan.

6.1.3.2 Measurement procedure and validation of measurement

Calibration and normalization of the spectral response

In direct response spectral measurement, the bolometer plays the role of the detector instead of the DTGAS detector of the spectrometer. The resulting spectrum is in fact a convolution of spectral characteristics of source, beam-splitter, optics (lens, filter), and bolometer. This spectrum needs to be calibrated so that we can extract only the spectral response of the bolometer under test while suppressing all spectral features related to optical chain.

The calibration requires a reference measurement in which an “ideal” detector is used, while maintaining all other components of the optical set up as during the measurement with bolometer under test. The ideal detector is the one that has a flat spectral response over the

targeted bandwidth. In such a case, after calibrating the sample measurement (measurement with bolometer under test) to the reference measurement, we obtain the spectral response of the bolometer.

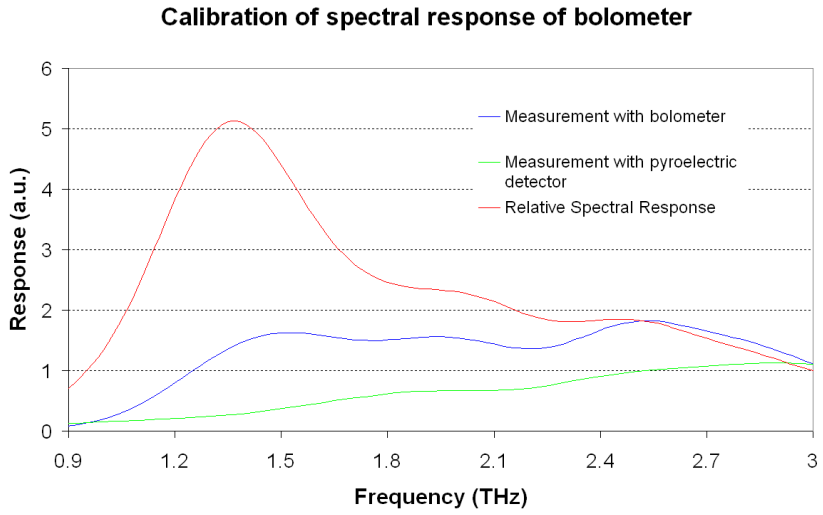

Fig. 6.19: Calibration of the measured spectrum.

In our experiment, to perform the reference measurement, we have used the pyroelectric detector supplied with the spectrometer. All other components of the optical set up are maintained. However, this measurement is performed under vacuum condition. Thus it does not undergo the atmospheric attenuation along 15-cm path as the measurement with the bolometer under test. We will discuss later the impact of this attenuation when presenting the measurement results.

The ratio of the signal over the reference spectra gives the relative spectral response of the bolometer (refer to Fig. 6.19). This is the spectral response of the bolometer compared to the spectral response of the FTS pyroelectric detector. In the ideal case, the pyroelectric detector response should be flat so that the bolometer response is independent of reference detector. This will be discussed later in the "Validation of Measurement" section.

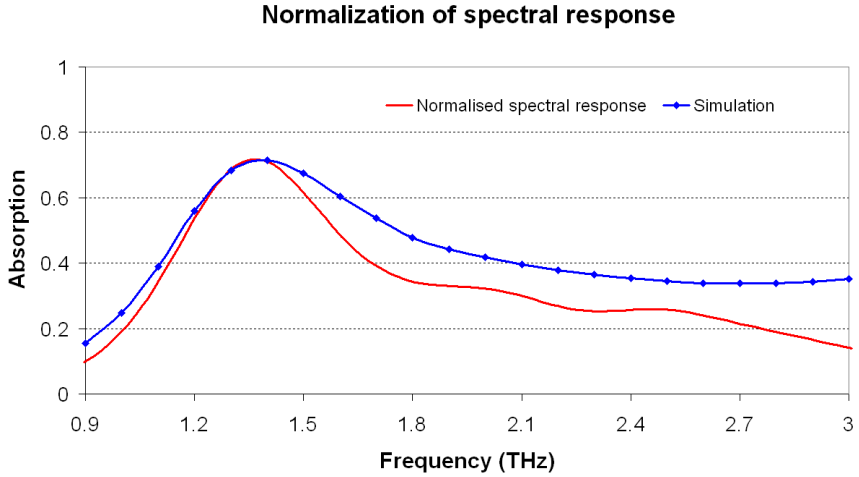

Fig. 6.20: Spectral response normalized with respect to the simulated absorption maximum.

The relative spectral response is then normalized so that its absorption peak has the same value as the simulation result. Such normalization makes possible qualitative comparison of the shape of the measured and simulated spectral response. One can point out that if quantitative matching is the main goal, normalization should be applied following the

least mean square method rather than this simple normalization procedure. However, in our opinion, the qualitative comparison is more meaningful since measurements make use of many hypotheses presented in the next paragraph.

Validation of Measurement:

The relative spectral response of the bolometer under test can be normalized and compared to its spectral absorption if the following conditions are satisfied:

- response (voltage or current) of the reference detector evolves linearly with the optical intensity;
- spectral response of the reference detector is flat;
- response of the bolometer under test is linear with respect to the optical intensity.

In general, the response of a pyroelectric detector is linear with respect to the optical intensity. One should point out that, in a FTS, the transmissivity (or the reflectivity) is calculated directly as the ratio between the sample-included measurement spectrum and the background spectrum. If the response of pyroelectric detector is not linear, the transmissivity will be distorted depending on optical intensity. Thus, the first condition is satisfied.

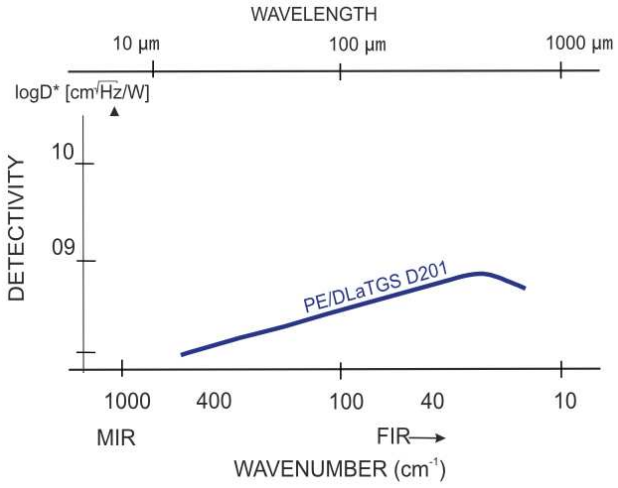

Fig. 6.21: Detectivity of the pyroelectric detector supplied with Vertex 80v FTS. Data reproduced from Bruker Optics [1]

The flatness of the spectral response of the pyroelectric detector is not perfectly assured. However, its pyroelectric nature presumes that it has a wider bandwidth than the antenna-coupled bolometer. Fig. 6.21 presents the spectral detectivity of the pyroelectric detector given by manufacturer (Bruker Optics) [1]. In the experimental band 0.9-3 THz (equivalent to 30-100 cm^{-1}), the detector response decreases monotonically with frequency. On the contrary, as we will see later, the bolometer response exhibits distinctive absorption peaks in this spectral range. Thus the calibration process, though not perfect, can be used to characterize qualitatively these absorption peaks.

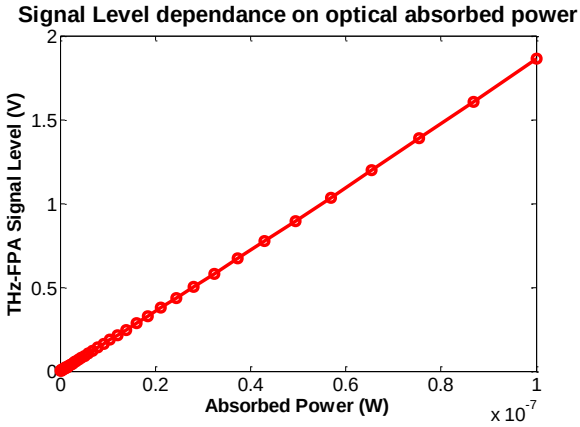

Fig. 6.22: Simulated responsivity R of the bolometer.

For a bolometer, when the beam intensity is low enough (which is the case for common blackbody THz sources), its response signal varies linearly with the incident radiation intensity. Fig. 6.22 shows the simulated responsivity of the bolometer for optical power below 100 nW. The model solves nonlinear thermal differential equation of the thermometer to simulate the bolometer analog bridge circuit.

6.1.3.3 Accuracy of measurement

We have seen that the reflectivity measurement presents very good accuracy and reproducibility. Reflectivity measurement is applied with the continuous scan mode and averaging of 64 acquisitions: the measurement is completed within about 10 minutes.

The spectral response is measured in the step-scan mode to match the slow response of the bolometer under test. As presented previously, each scan takes quite a long time: 74 minutes for 8-cm^{-1} resolution and 148 minutes for 4-cm^{-1} resolution. With this constraint, it is not practical to perform such a high number of scans as for reflectivity measurement. So typically, 3 or 4 scans were acquired in step-scan mode and then averaged.

4 cm^{-1} resolution measurement

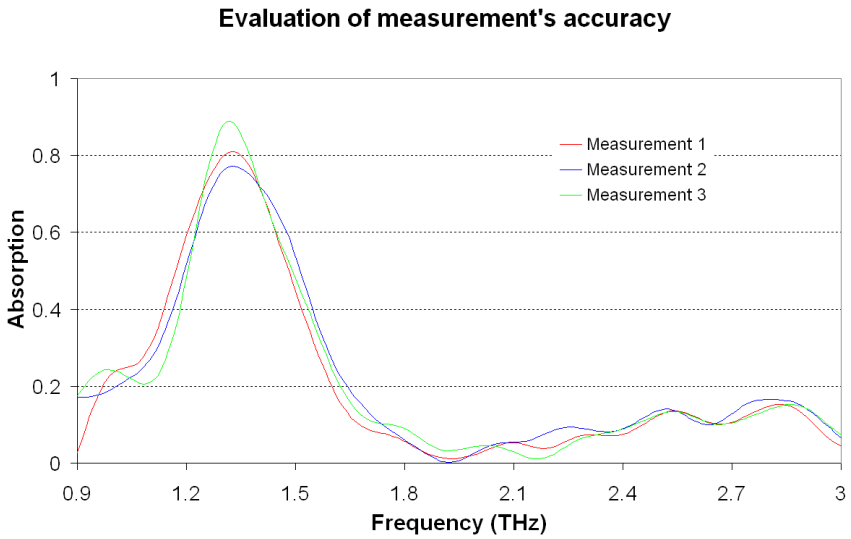

Fig. 6.23: Reproducibility of the spectral response measurement in the case of 4-cm^{-1} resolution.

To evaluate the reproducibility of the measurement, we performed 3 consecutive scans of the measurement at 4-cm^{-1} resolution, each scan taking 148 minutes. Let us recall that 4-

cm^{-1} around 1.5 THz, i.e. around 50 cm^{-1}, corresponds to a relative precision of 8%. In terms of frequency, the resolution is 120 GHz. Fig. 6.23 shows normalized and calibrated spectrum of three scans. The peak-to-peak and the average standard deviation over 0.9–3 THz are 0.07 and 0.02 respectively. At the absorption peak frequency, the relative deviation is 6 %. It gets degraded at minimum absorption frequency (for example, 58% at 0.9 THz). With this order of error magnitude, this measurement is relevant to characterize the position of the absorption peak. It is not adequate to use this measurement to characterize quantitatively the absorption rate at the valleys of absorption or at frequencies below 1 THz.

8 cm^{-1} resolution measurement

The 8-cm^{-1} resolution measurement provides better accuracy because of two reasons. First, the signal to noise ratio increases when the resolution decreases. Secondly, applying this resolution, the measurement duration is reduced by a factor 2 as compared to the 4-cm^{-1} case. In spite of the use of synchronous detection that compensates the variation of temperature in the detector vessel, the temperature of the source itself may vary during the acquisition time. Therefore, a faster measurement will give a better accuracy.

3 consecutive scans are also averaged. The peak-to-peak and the average standard deviation over 0.9–3 THz are 0.05 and 0.01 respectively. At the absorption peak frequency, the relative deviation is 2 % which represents an enhancement of 3 as compared to the 4-cm^{-1} resolution case.

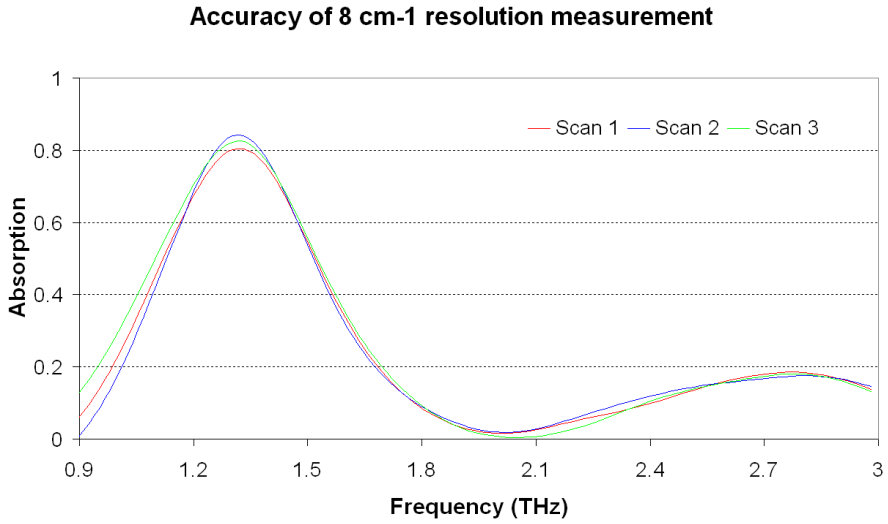

Fig. 6.24: Reproducibility of the spectral response measurement in the case of 8-cm^{-1} resolution.

Apart from reproducibility, the comparison of absorption curves obtained with these 2 resolutions reveals different characteristics. The 4-cm^{-1}↔120 GHz resolution measurement exhibits oscillations whereas the 8-cm^{-1}↔240 GHz curve is smoother. Moreover, the main absorption peak is narrower when the finer resolution is applied. This is not simply caused by the fact that higher resolution gives more details. As we will see later, it is in fact related to the atmospheric attenuation along the 15-cm path that is not taken into account during the calibration procedure.

6.2 Result of optical coupling measurement

6.2.1 Reflectivity

We have presented the simulated absorption of the THEDEX bolometer in chapter 5. There is no direct method of measuring the absorption of the bolometer since the bolometer itself converts the optical energy into heat in its suspended membrane. In contrast, the reflectivity $R(f)$ of the FPA surface can be measured directly by using the FTIR technique described previously. The bolometer absorption $\eta(f)$ (defined by equation 5.15 in chapter 5) is not necessary equal to the quantity $1-R(f)$. Actually the absorption $\eta(f)$ refers to the useful optical absorption that is converted into heat deposited onto the suspended membrane. There are of course other mechanisms of dissipation of the energy of the incident THz beam, for example, the dielectric loss in the SiO_2 cavity.

$\eta(f)$ is however consistent with $R(f)$ in the sense that absorption peak corresponds a dip in reflection. Since the reflectivity can be measured directly with a high precision, it contributes significantly to the characterization of the electromagnetic response of the detector.

6.2.1.1 Intrinsic response of the bolometer

The bolometer under test is a THEDEX one. For these experiments, the chip prototype encompasses a bolometer array directly processed above the silicon wafer, so without CMOS ROIC. The reflector plane is not continuous but is patterned as an array of 49×49 μm^2 metallic patches as presented in the chapter 5. The result of receiving mode simulation is reported here to allow us an easy comparison with the measurement.

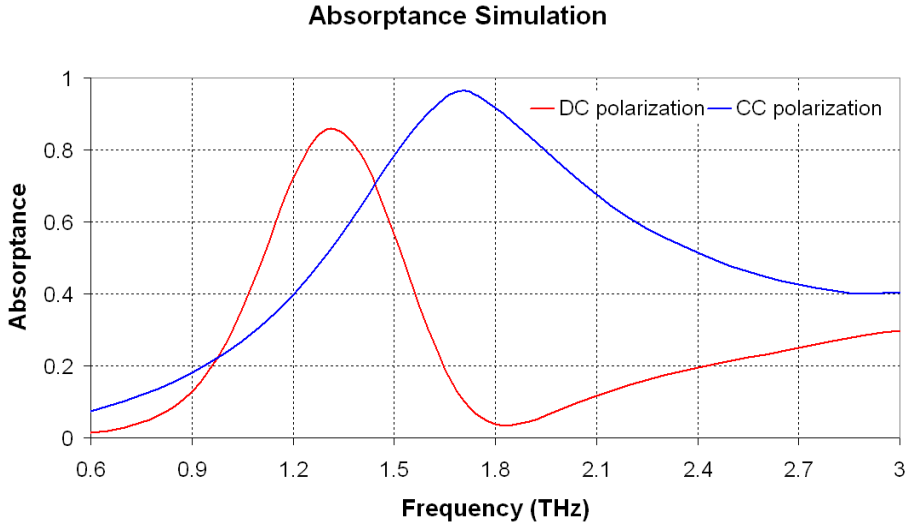

Fig. 6.25: Simulated absorption of the THEDEX bolometer.

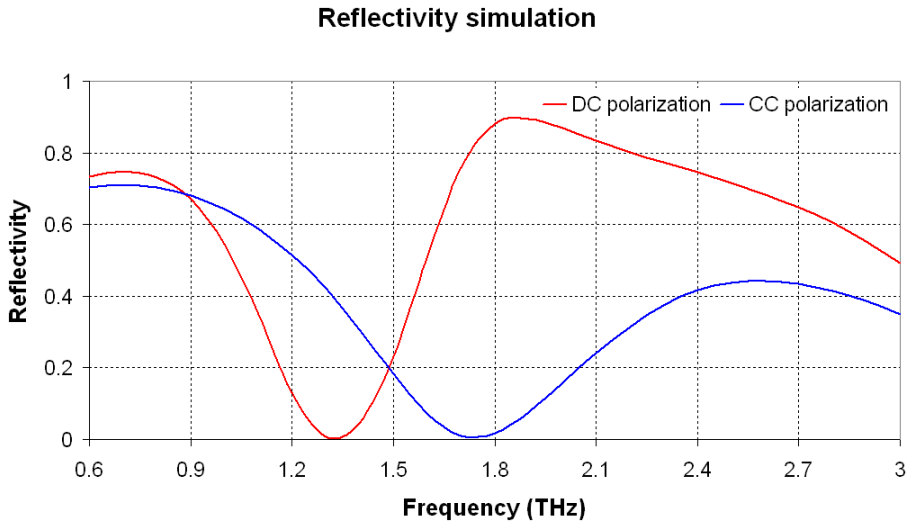

Fig. 6.26: Simulated reflectivity of the THEDEX FPA surface.

The receiving mode simulation can supply us with the bolometer absorption $\eta(f)$ and also the reflectivity $R(f)$ of the FPA surface. We have presented the calculation of $\eta(f)$ in chapter 5. $R(f)$ is simply the parameter $|S_{11}|^2$ of the Floquet port. These quantities are presented in Figs. 6.25 and 6.26. We observe a good consistency between the absorption and the reflectivity. The peak in absorption curve corresponds very well with the dip in reflection. As mentioned earlier, whereas the absorption cannot be directly measured, the reflectivity can be characterized directly by the FT-IR spectroscopic technique.

Figs. 6.27 and 6.28 show the simulated and measured reflectivity spectra. For both polarizations (aligned with the DC or CC antennas) the simulated reflectivity matches very well the measurement without any use of adjustable parameter. Frequencies of the dips coincide and the shapes of the curves are similar. This result validates the model and the 3D simulations we performed.

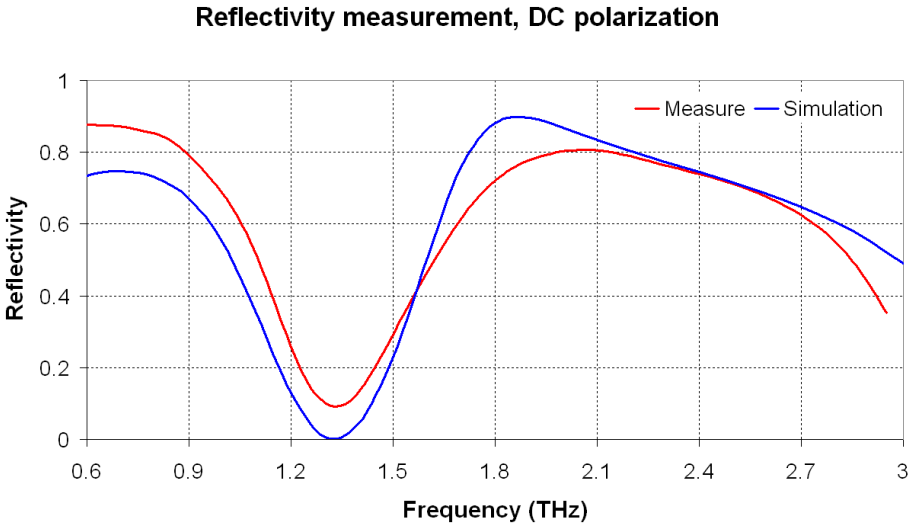

Fig. 6.27: Comparison between simulated and measured reflectivity for DC polarization.

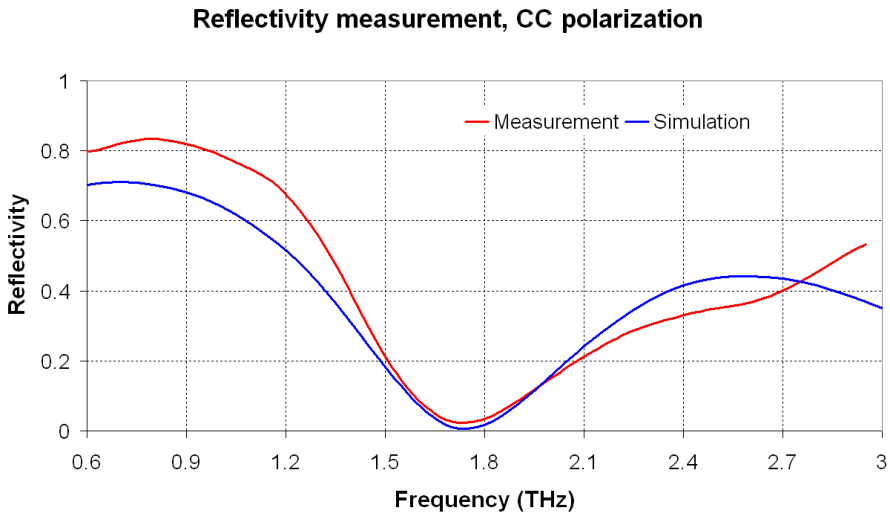

Fig. 6.28: Comparison between simulated and measured reflectivity for CC polarization.

6.2.1.2 Electromagnetic coupling between ROIC and FPA

Prototypes of 320×240 microbolometer arrays processed over a CMOS ROIC have also been characterized with reflectivity measurements. The CMOS ROIC structure has been described in chapter 4. We remind here that the ROIC upper stack includes a very complex structure with 6 metal strip layers. In an ideal case, the ROIC structure should not have an affect on the electromagnetic response of the array of detector as explained in chapter 4. We will see in this section, through tests of the THEDEX chip, that the ROIC does have an affect on the response of the FPA due to the patterned reflector level.

'Historically', the 320x240 FPA equipped with a CMOS ROIC has been measured before the 160x120 pixel array processed above a Si wafer with no integrated circuit. This choice was motivated by the fact that the area of the FPA in the former case is 16×12 mm^2 whereas the latter surface is 8×6 mm^2. A large area facilitates reflectivity measurements, especially at frequencies below 1 THz since the signal to noise ratio is enhanced.

The measured reflectivity of the FPA processed above a CMOS ROIC -presented in Figs. 6.29 and 6.30 - is quite different from the simulated curve. It comes out that the read-out circuit below the reflector has an effect on the FPA structure absorption.

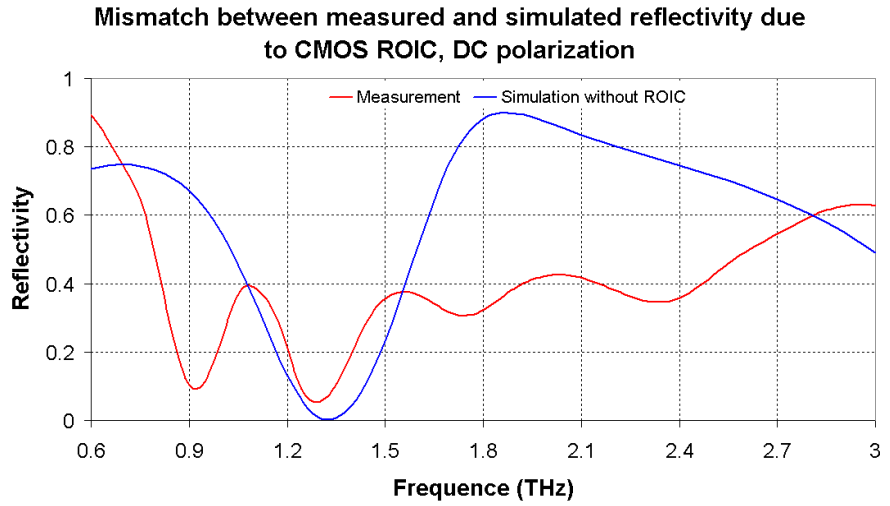

Fig. 6.29: Mismatch between measured and simulated reflectivities, DC polarization.

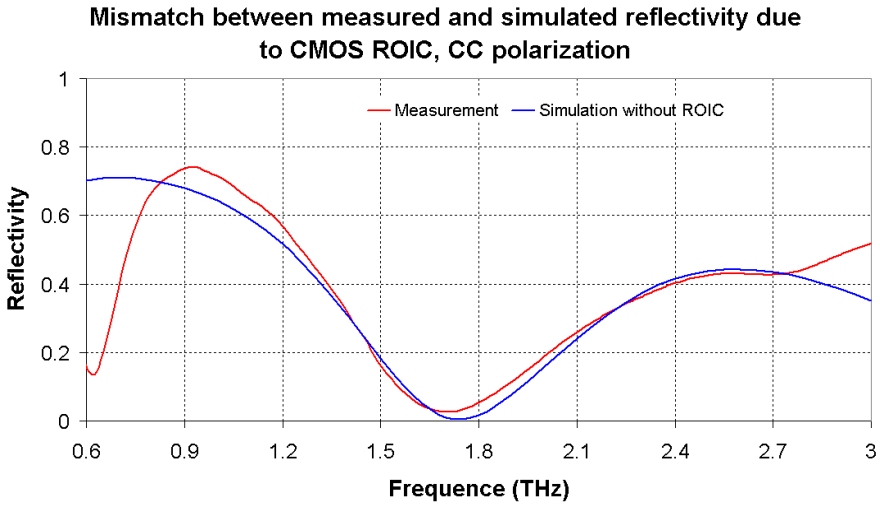

Fig. 6.30: Mismatch between measured and simulated reflectivities, CC polarization.

For the DC polarization, the reflectivity is very different from the expected value. The high reflecting region in the range 1.8–2 THz has disappeared. Also, the reflectivity curve exhibits some oscillations and not just a reflection dip at 1.35 THz as in the case of simulation. For CC polarization, reflectivity curves are similar, with the exception of a dip of reflection at 0.6 THz.

The effect on the FPA response of the ROIC structure located below the metallic reflector is revealed when we measure a simplified structure: the FPA with its bolometer structure taken away (see Fig. 6.31). This structure is obtained by simply "peeling away" the suspended membranes of the bolometers with a scotch-tape. The CC antenna that are directly deposited on the SiO_2 substrate remain as well as the SiO_2 cavity, metallic reflector and ROIC The study of this simplified structure has helped us in understanding some characteristics of the measured reflectivity of the complete structure.

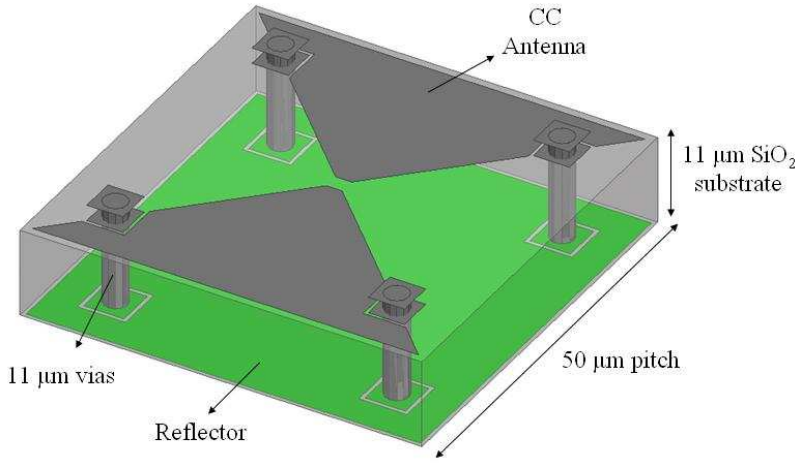

Fig. 6.31: Simplified structure: the suspended membrane is taken away by a scotch-tape.

As illustrated in Figs. 6.32 and 6.33, for the DC polarization, the spectral reflectivity of two structures, with and without bolometer, is quite unchanged. For the CC polarization, reflectivity with no bolometer exhibits the same dip of reflection at 0.6 THz. This observation makes questionable the fact that the 0.6 THz reflection dip does come or not from absorption by the bolometer suspended membrane. Actually the cavity cannot be responsible of this absorption because the absorption index of its SiO_2 material is low in the THz range as mentioned in chapter 4 and 5. One possible explanation is that the 49×49 μm^2 metallic patch

reflector reflects poorly the low frequency radiation as mentioned in chapter 4, and thus the THz wave can interact with the CMOS ROIC placed below the reflector.

From the above analysis, we have simulated the structure including the CMOS ROIC. We remind that the ROIC upper structure is really complex with 6 metal layers. This configuration makes 3D electromagnetic simulations difficult and results in limited precision.

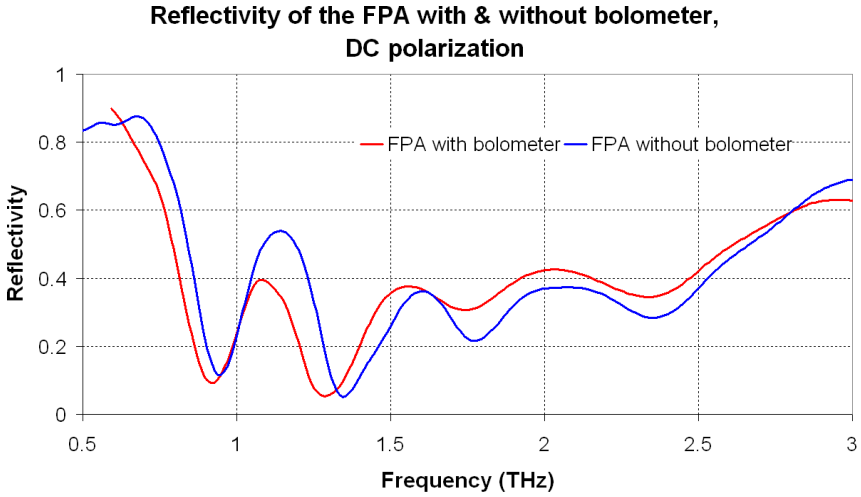

Fig. 6.32: Comparison between the reflectivity of the FPA with and without bolometer, DC polarization.

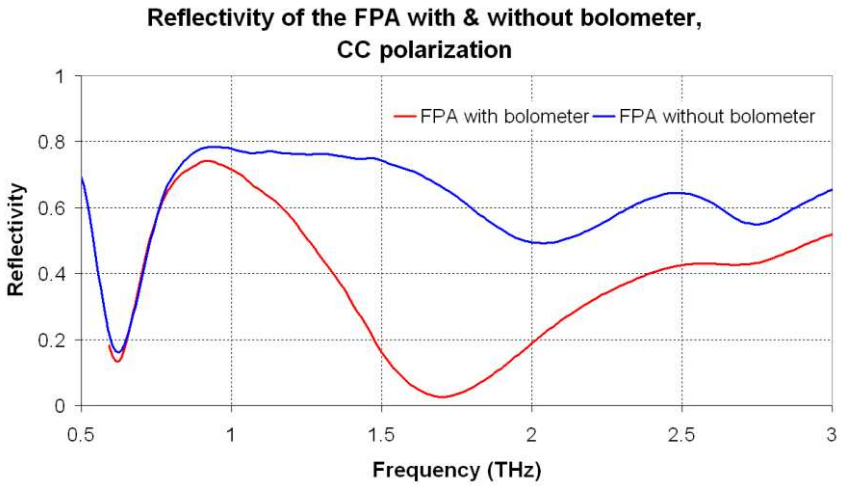

Fig. 6.33: Comparison between the reflectivity of the FPA with and without bolometer, CC polarization.

In Figs. 6.34 and 6.35, measured and simulated reflectivity curves of the surface of the FPA processed above CMOS ROIC are plotted together. For the "simulation with ROIC", 6 metal layers of the ROIC structure below the reflector have been meshed. We also plot the simulation without ROIC, which has been already drawn in Figs. 6.29 and 6.30, in order to demonstrate the effect of ROIC structure to the FPA reflectivity.

It is observed that the simulation with ROIC matches well the measurement. Regarding the DC polarization, dips of reflection at 0.9 and 1.3 THz are quite precisely matching. Although in the range 1.5–3 THz, measurement and simulation are not perfectly similar, they share the same behavior of weak oscillations. In contrast, the simulation without ROIC does not exhibit the reflection dip at 0.9 THz. Moreover in the range 1.5–3 THz, its reflectivity curve does not show an oscillating behavior.

For the CC polarization, both simulations predict well the reflection dip at 1.75 THz observed experimentally. At 0.6 THz, simulation with ROIC and measurement reveal correctly a dip, the small mismatch being due to the complexity of the CMOS structure. On the contrary, simulation without ROIC does not exhibit this reflection dip close to 0.6 THz.

From the results of simulation and the reflectivity measurements of the FPA with and without ROIC, we conclude that there exists an electromagnetic coupling of the incident THz radiation with the CMOS ASIC that influences the FPA response. This means that the "intrinsic response" of the detector structure presented in the last section is modified by the ROIC located under the reflector. This phenomenon is not desirable because it is almost uncontrollable or unpredictable by design. Moreover, in some case the ROIC is a commercial product, and consequently its structure is completely uncontrolled or even unknown.

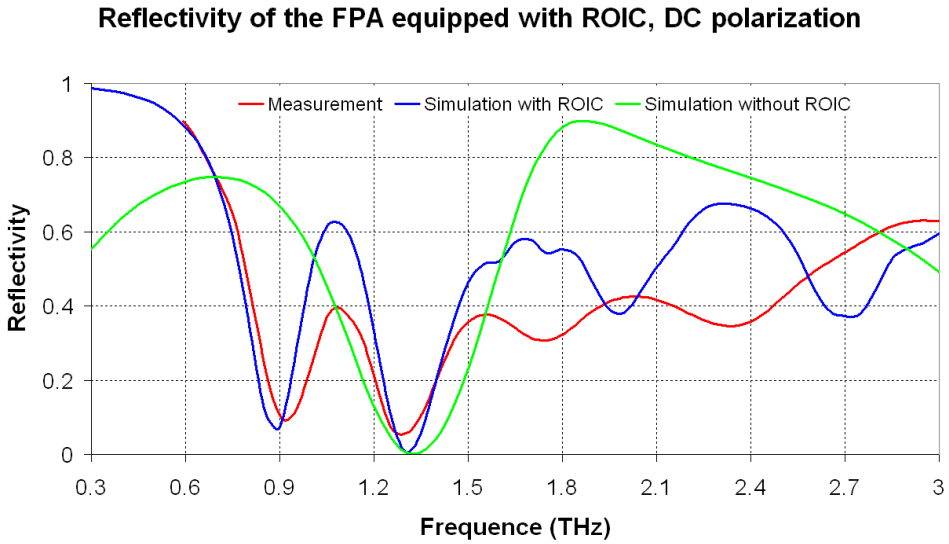

Fig. 6.34: Comparison between the reflectivity of the FPA processed above CMOS ROIC with and without bolometer, DC polarization.

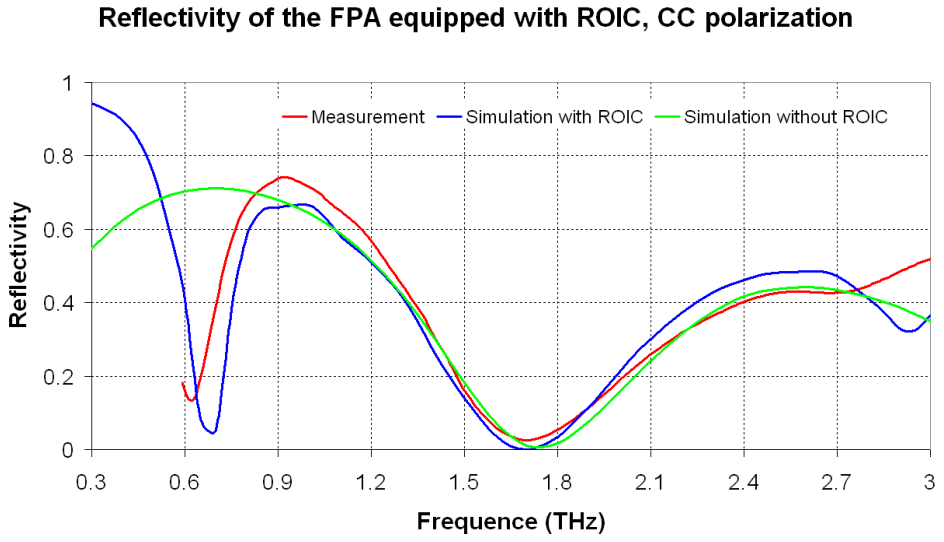

Fig. 6.35: Comparison between the reflectivity of the FPA processed above CMOS ROIC with and without bolometer, CC polarization.

After observing the perturbation of the bolometer array reflectivity induced by the underneath ROIC structure, let us examine its impact on absorption. In Figs. 6.36 and 6.37, simulated absorptions of the FPA bolometer with and without ROIC are compared for DC and CC polarization, respectively. We should remind that the absorption of the bolometer in the

FPA without ROIC is considered as the "intrinsic response" of the original bolometer design and has been studied in the last section.

For the DC polarization, one can see that the ROIC presence results in a narrower absorption peak at 1.35 THz. One interesting feature is that a small absorption peak at 0.85 THz appears. These two absorption peaks are well consistent with the dip in reflection observed in Fig. 6.34. One can see that the magnitude of the absorption peak at 0.85 THz is roughly half the quantity $1 - R(f)$.

For the CC polarization, the absorption of the original design is not impacted significantly by the presence of the ROIC. One interesting feature is that even if the reflection dip at 0.6 THz is very strong, the absorption curve exhibits just a minor bump. Apparently, the energy of the incident wave has been dissipated by other mechanisms than the absorption by the suspended membrane. By calculating the dielectric and conduction losses in each structure element (detector integrating a CMOS ROIC), we easily determine that the reflection dip close to 0.6 THz is due to the absorption by the metallic strips in the upper layers of the ROIC.

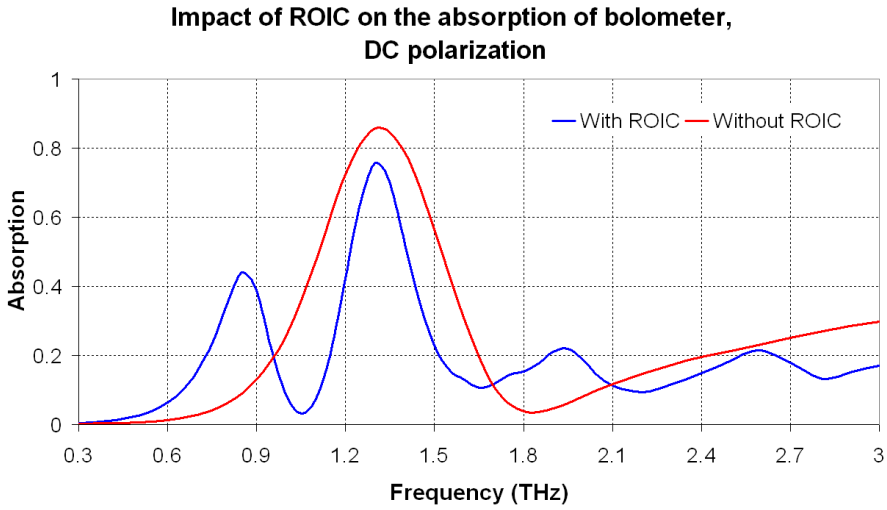

Fig. 6.36: Simulated spectral absorption of the THEDEX bolometer with and without the ROIC structure, DC polarization.

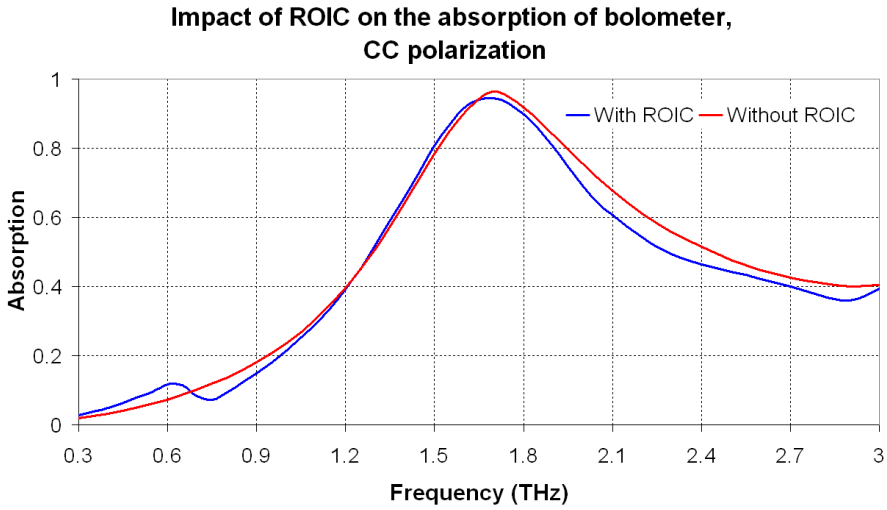

Fig. 6.37: Simulated spectral absorption of the THEDEX bolometer with and without the ROIC structure, CC polarization.

The electromagnetic coupling of the incident radiation downwards to the ROIC can be effectively minimized or even suppressed by employing a large or monolithic continuous metallic reflector, with the same size as the total FPA. In the former case, several bolometers (3×3 pixels for example) may share the same reflector. In the later, the whole array of pixels share the same reflector. As mentioned in chapter 4 the counterpart of this reflector configuration is that short-circuits may happen between bolometers. One remedy with respect to this risk is to increase the gap between the electrical vias and the reflector from 0.5 µm as in the actual design up to 1 µm or even more.

6.2.1.3 Reflectivity in infrared range

The reflectivity measurement and simulation of the bolometer over the 5–25 µm range are presented in Fig. 6.38. The measurement shows that the FPA reflectivity with and without ROIC exhibits the same behavior over this infrared range. This means that the ROIC structure below reflector level does not interfere with the bolometer electromagnetic response. This result is not surprising because the 49×49 μm^2 pattern reflector is significantly larger than the wavelength in the infrared range, so that the IR incident wave is correctly reflected by the reflector. The evanescent wave (if any) that can pass through the array of reflector patches is very weak so that its interaction with the ROIC is negligible. Another phenomenon that minimizes the effect of the ROIC on the detector IR absorption is the strong attenuation of infrared flux when passing the 11-µm thick SiO_2 cavity.

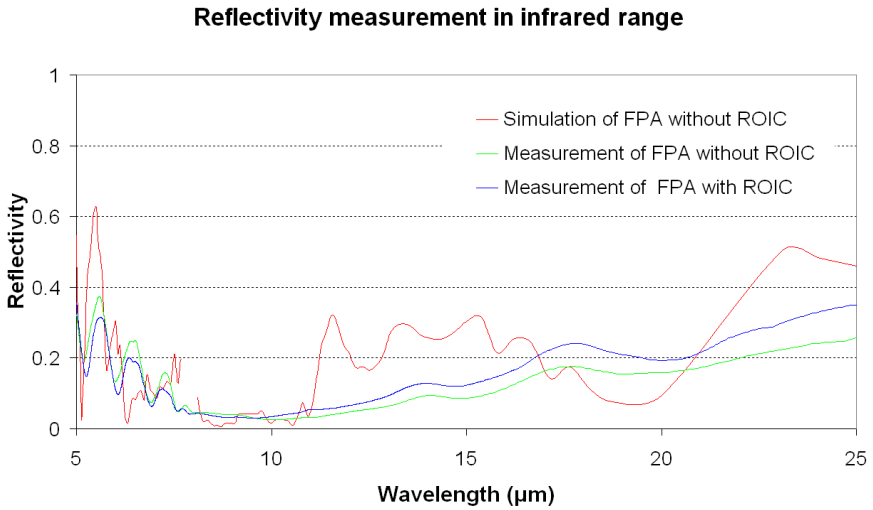

Fig. 6.38: Comparison between measured and simulated reflectivity curves in the infrared range, unpolarized light.

The measured reflectivity of the bolometer is quite low in the infrared range, mostly due to the absorption of the SiO_2 material as presented in chapter 5.

The simulation of the bolometer in the infrared range is quite challenging. In contrast to simulations in THz, the structure dimensions are much larger than the infrared wavelengths. This implies that the mesh nodes must be more numerous that for THz modeling in order to ensure a precise result. Simulations of the complete 3D structure with the ROIC layers cannot be performed due to the limited computer power. Only the simulation without ROIC has been performed. This is not a big issue because as seen earlier, the ROIC influence in the IR range is negligible.

The simulated reflectivity in Fig. 6.37 is in rough agreement with the measurement. The simulation shows similar oscillating fringes at short wavelength. It also low reflectivity near 10 µm as measurement. From 12 to 25 µm, the magnitude of simulated reflectivity is in the

order of the one of the experimental data. These results validate the calculation of the bolometer absorption in the infrared range presented in chapter 5.

6.2.2 Spectral response

The spectral absorption is a very important figure-of-merit of the imaging detector; however the measurement of this parameter is still not well established in the THz range. Reference [2] presents the measurement of spectral response of a horn-coupled bolometer, in combination with the optical chain characteristics. In this case, the result mixes up the spectral absorption of the detector with the characteristics of the optics, which is undesired. In our work, we aim at extracting the spectral response of the detector itself.

6.2.2.1 Measurements at different spectral resolutions

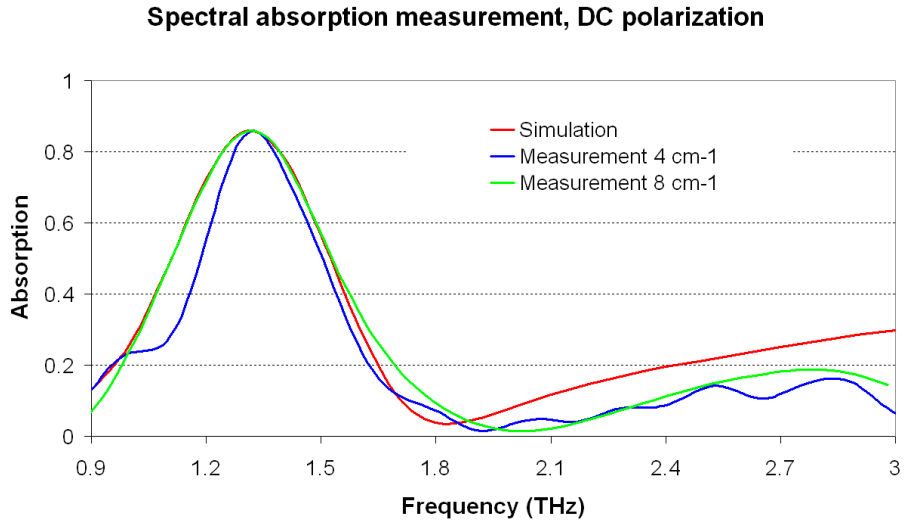

Fig. 6.39: Measured spectral responses with different resolutions, DC polarization.

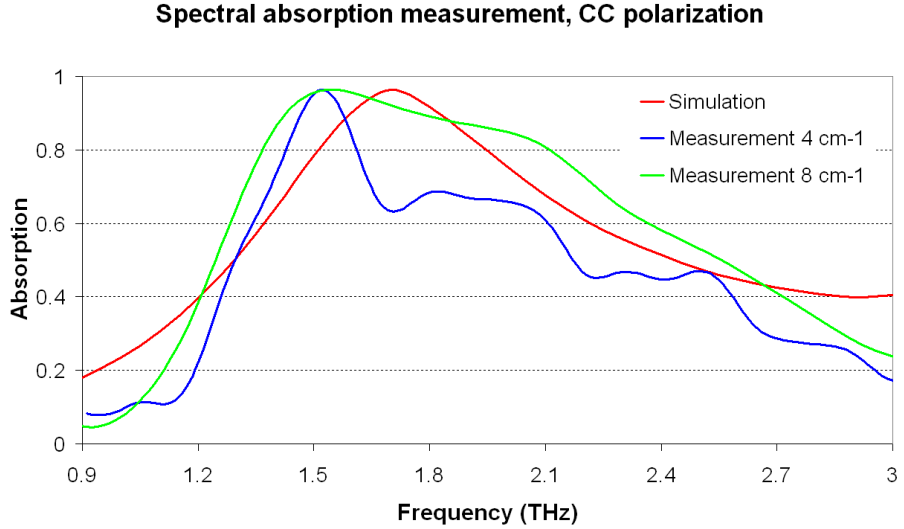

Fig. 6.40: Measured spectral responses with different resolutions, CC polarization.

The measured spectral absorptions of the bolometer for 4 cm^{-1} and 8 cm^{-1} resolutions are compared with the simulation in Figs. 6.39 and 6.40 for DC and CC polarizations, respectively. The resolutions 4 cm^{-1} and 8 cm^{-1} are equivalent to 120 and 240 GHz resolutions in frequency.

For the DC polarization, measurements show the same absorption peak as the simulated one at 1.35 THz (see Fig. 6.39). The absorption peak recorded with 4 cm^{-1} is narrower. The shapes of the absorption curve match well, showing an absorption dip in the 1.8~2 THz region. Weak oscillations observed in the 2–3 THz range are smoothed when the record is performed with a 8 cm^{-1} resolution.

For the CC polarization, both measurements exhibit an absorption peak at 1.5 THz, whereas simulated curve peaks rather at 1.75 THz. The 4 cm^{-1} resolution measurement also exhibits some oscillations as seen for DC polarization.

6.2.2.2 Impact of the atmospheric attenuation

The optical setup implemented for spectral response measurement exhibits propagation in atmosphere along a 15-cm path. In spite of this short length, the corresponding attenuation of the THz wave radiation is considerable due to the high absorption of water vapor.

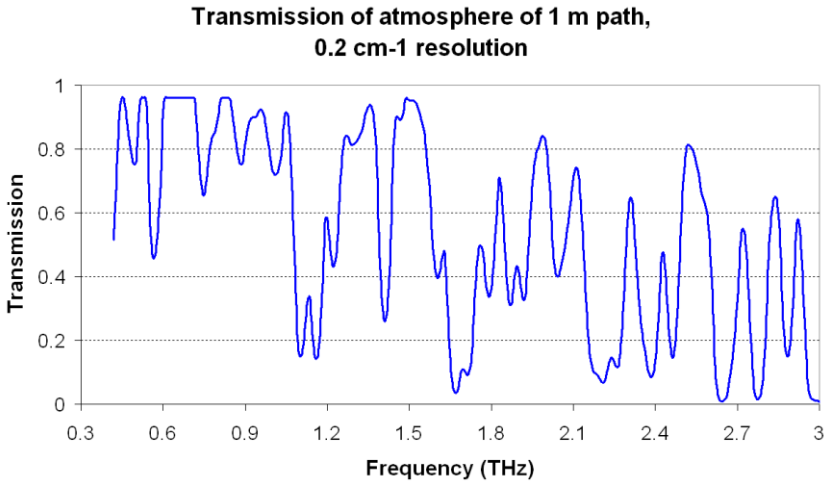

Fig. 6.41: Transmission of atmosphere measured with 0.2 cm^{-1} resolution.

The atmospheric transmission in the THz region shows transmission windows and many strong absorption lines. The figure above shows an atmospheric transmission spectrum measured with the FTS. The measurement is actually performed in laboratory environment, at a temperature of 23~25^{o} C and a relative humidity of 50~60%. For the reference measurement, the 26-cm long sample compartment is under vacuum. By performing measurement after filling atmosphere into this compartment, we obtain the atmospheric transmission for 26-cm path. The result is then calculated for 1 m distance by using the Beer-Lambert law. The applied 0.2 cm^{-1} resolution is equivalent to 6 GHz in frequency.

For frequencies below 1 THz, the transmission is still good in windows centered at 670 GHz or 850 GHz. For the 1–3 THz range, the atmospheric attenuation becomes severe and tends to increase with frequency. One can see that, at 3 THz, the transmission is only ~1% in comparison to ~98 % at 670 GHz.

Figures 6.42 and 6.43 show the measured absorption of the bolometer as well as the transmission of a 15-cm path in air. The atmospheric transmission was measured with a 4 cm^{-1} resolution, the same as the one applied for bolometer absorption measurement. Once again, the 15-cm path atmospheric attenuation data are extracted from FTS measurement with propagation through 26 cm path in the sample compartment thanks to the Beer-Lambert formula.

A very good coherence is observed between several features of the atmospheric transmission curve and the measured bolometer absorption. We can easily see that

atmospheric attenuation creates oscillations in experimental absorption curves. Especially for CC polarization, at 1.75 THz, the measured absorption undergoes a dip because of atmospheric attenuation. This makes the measured absorption of the bolometer seems to have a peak at 1.5 THz instead of 1.75 THz as the simulation.

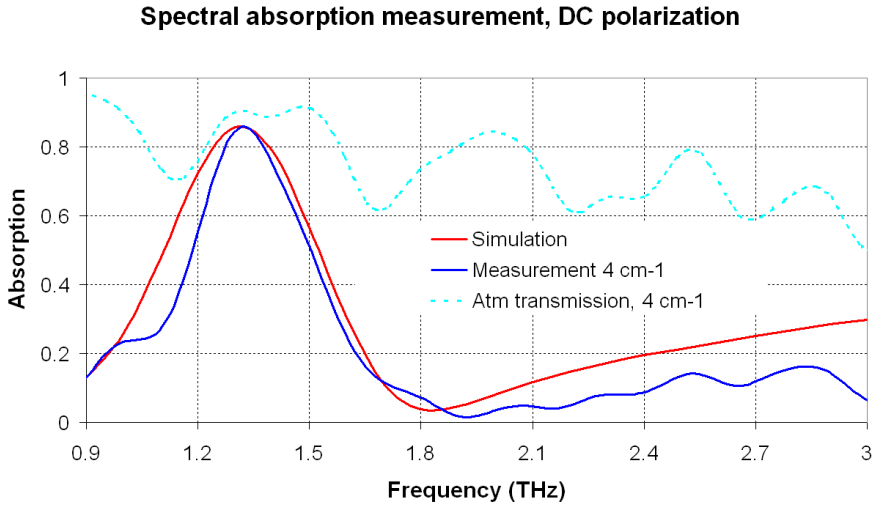

Fig. 6.42: Impact of atmospheric attenuation on spectral response measurement, DC polarization.

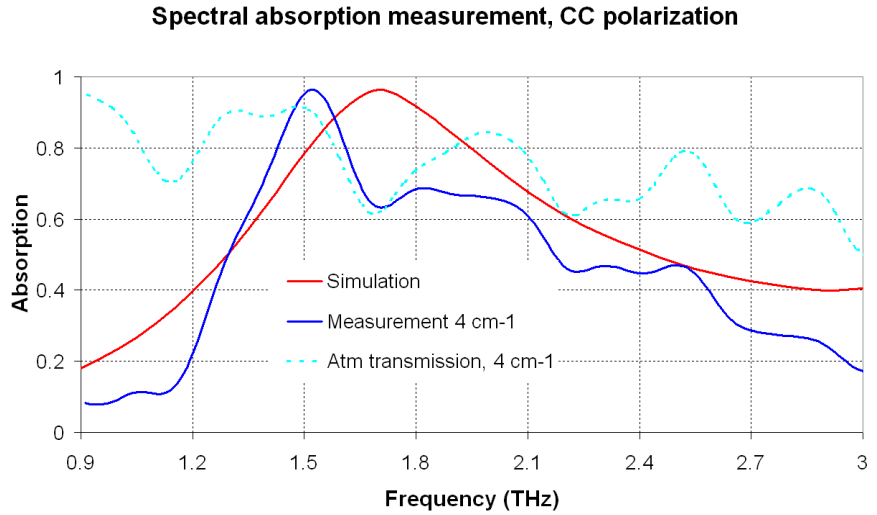

Fig. 6.43: Impact of atmospheric attenuation on spectral response measurement, CC polarization.

A simple way of getting rid of the effect of air absorption is to divide the (initial) absorption measurement by the atmospheric transmission. Both measurements are necessarily performed with the same resolution. The results are presented in Figs. 6.42 and 6.43 for the case of a 4 cm^{-1} resolution for the DC and CC polarizations, respectively. The case of 8 cm^{-1} resolution is not shown here. However, the corrected spectra will be reported together with the 4 cm^{-1} resolution at the end of this section to summarize the measurements.

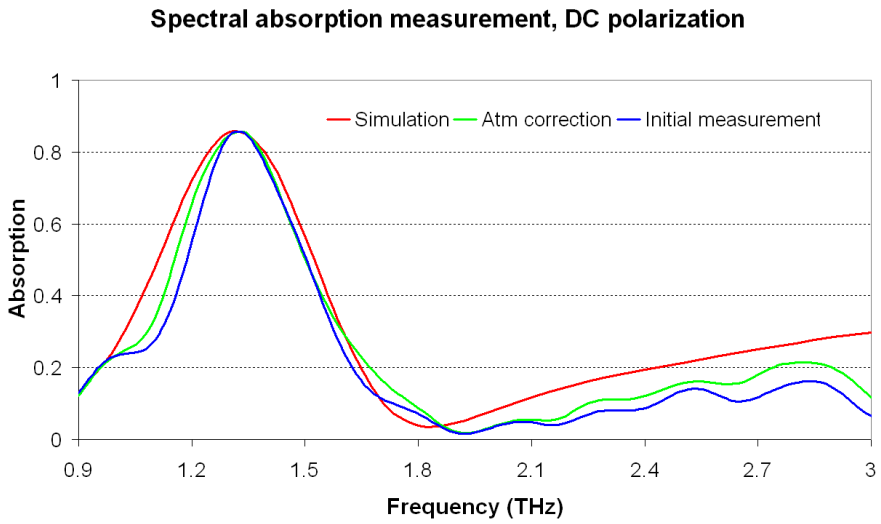

Fig. 6.44: Correction of atmospheric attenuation for DC polarization.

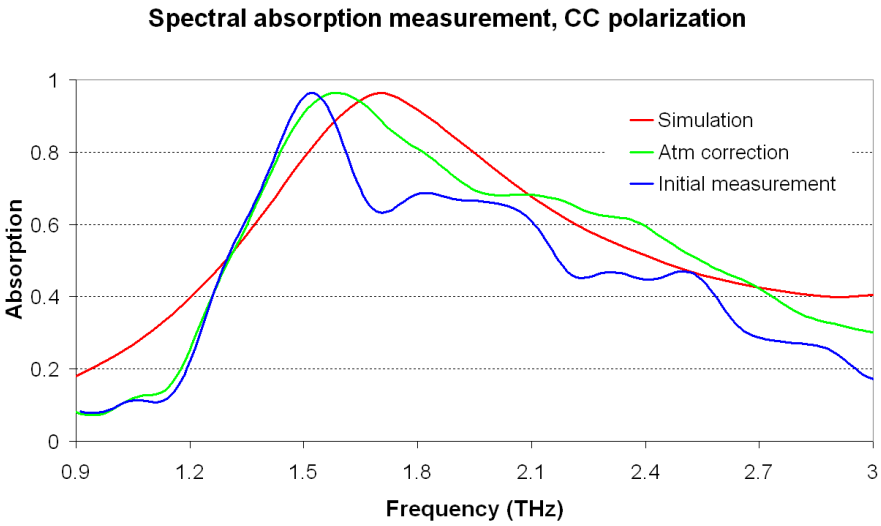

Fig. 6.45: Correction of atmospheric attenuation for CC polarization.

The correction of the curves, by removing the effect of the air absorption in the set up, leads to a good agreement between modeling and measures. Most of the weak oscillating features in the recorded data have been eliminated or strongly reduced. For the CC polarization case, the absorption peak recorded at 1.5 THz was in fact narrowed by neighbor water vapor absorption lines. Nevertheless, the experimental and calculated spectra do not overlap perfectly. This is certainly due to some parameters that are not completely introduced in the calculation: dimensions of the details of the structure, actual values of the material parameters that, in situ, can be different from their bulk values, etc.

Figs. 6.44 and 6.45 summarize the measured spectral responses when corrected from atmospheric absorption, together with the simulated absorptions for DC and CC polarizations, respectively. The good matching observed between these curves consolidates the reflectivity measurement presented in the last section.

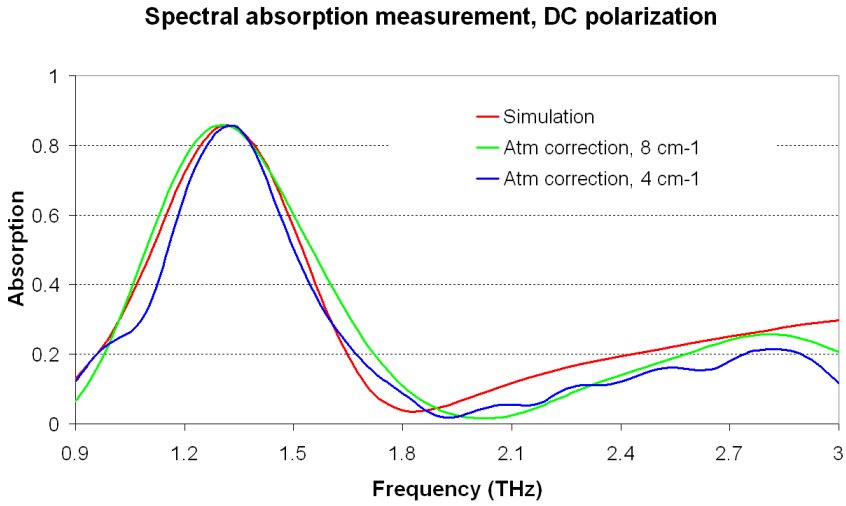

Fig. 6.46: Simulated and measured spectral response for DC polarization with different resolutions.

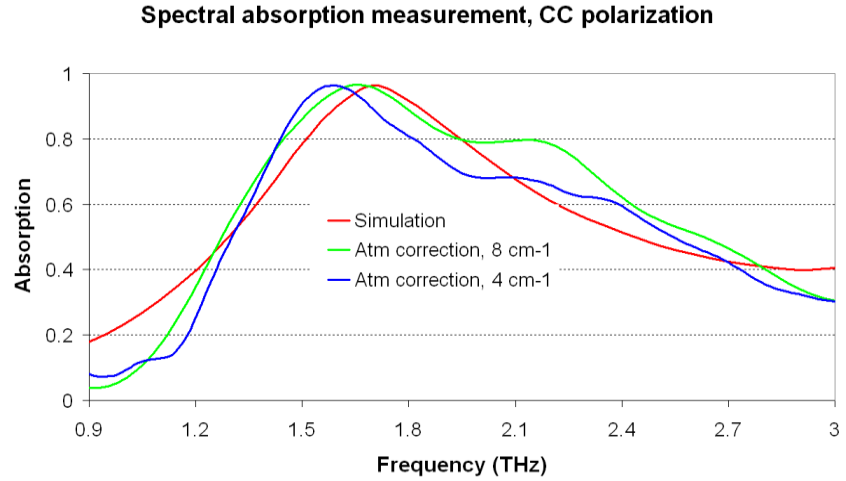

Fig. 6.47: Simulated and measured spectral response for CC polarization with different resolutions.

6.3 Other figures of merit

6.3.1 Thermal conductance and response time

Thermal conductance g_{th} and response time τ_{th} have been measured by the CEA-Leti team. Here we report the results of these characterizations to complete the presentation of THz bolometer performances.

Thermal conductances g_{th} of bolometers having the same design can lightly vary from one batch to another. For example, actual thermal leg width and thickness can vary because of the limited precision of photo-lithographic etching. So the measured thermal conductance is generally expressed within a range instead of giving a single value.

The measured total thermal conductance of the THEDEX bolometer is in the range 12.3–13.9 nW/K at room temperature (25°C), which shows a deviation of ~14% in comparison to computed value (14.2–16.2 nW/K, cf. chapter 5). As mentioned earlier in chap 3, specific thermal conductivity of thin film is different from bulk value and quite sensitive to the deposition processes. The thermal conductance modeling employs thermal conductivity

data from literature, not measured data of each bolometer. Thus, it is difficult to calculate precisely the bolometer thermal conductance. The modeling can ensure a precision of about 10-20 %. This does not cause a significant problem for bolometer designing since its thermal conductance can be adjusted during manufacturing.

Regarding the thermal time constant, experimental characterizations give τ_{th} in the range 47–50 ms also depending on each detector batch. This value range is higher than the computed one, 38.5–44.2 ms. It is reminded that:

$$\tau_{th} = C_{th} / g_{total}. \quad \textbf{(6.14)}$$

Because the time constant and the thermal conductance are related through equation 6.14, an over-estimation in thermal conductance will lead to an under-estimation of the time constant. However, this does not change the trade-off between the thermal isolation and response time of the bolometer, which depends only on the heat capacity.

This relation (6.14) makes possible the determination of the bolometer heat capacity C_{th} that is less sensitive to technological manufacturing drifts than the thermal conductance. It should recall that specific heat capacity does not vary considerably between thin-film and bulk value. For a bolometer with τ_{th} = 47.3 ms and g_{total} = 13.3 nW/K (measured values), the corresponding heat capacity is C_{th} = 629 pJ/K, a value very close to the calculated 627 pJ/K.

With a thermal time constant close to 50 ms, the bolometer THEDEX can perform video at the frame rate:

$$f_{frame} = \frac{1}{3\tau_{th}} = \frac{1}{3 \times 50 \times 10^{-3}} = 6.7 \text{ Hz}. \quad \textbf{(6.15)}$$

6.3.2 Responsivity and sensitivity measurement

This section describes briefly the responsivity and sensitivity characterizations. More details can be found in [3].

6.3.2.1 Experiment setup

One of the experimental arrangements used during this study is shown in Fig. 6.46. It includes a THz-Quantum Cascade Laser source housed in a helium circulation cryostat. The QCL beam is first collimated by a 3'' f/1 off-axis parabolic mirror (OAPM), and a second OAPM focuses the beam onto the THz focal plane array (FPA). This array is integrated in a vacuum vessel dynamically pumped by a turbo-molecular pump. This vessel encompasses electrical interfaces from the FPA to the external electronics (bias, clocks, AD converter).

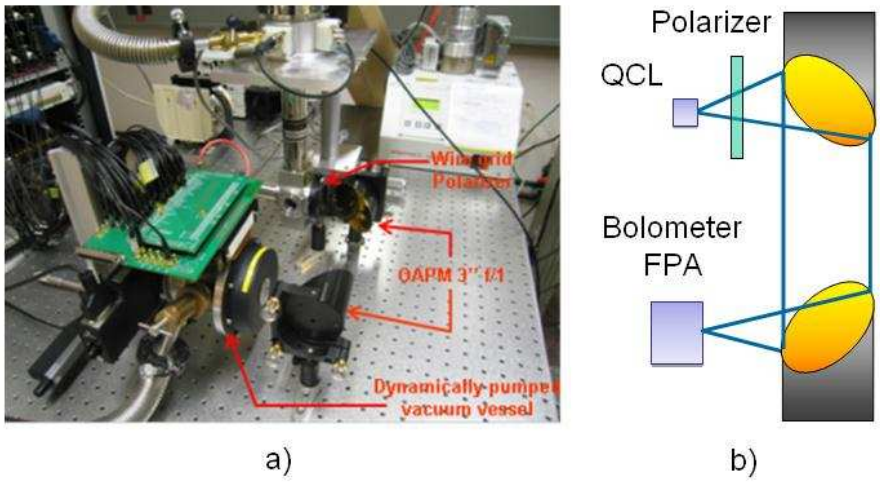

Fig. 6.48: a) Photo of the experiment setup and b) optical scheme of the experiment.

The QCL design is based on a bound-to-continuum active region [4]. It delivers a 15-mW peak power beam at 2.4 THz. When the laser chip is mounted in the cryostat, some mounting imperfections can make the laser chip slightly inclined in regards to the horizontal plane (the plane of reflection). Hence we used a wire grid polarizer to ensure that the linear polarized QCL beam is properly oriented with respect to the bolometer antennas. For this measurement, the TM polarization (the electric field is in the plane of reflection) is chosen: it corresponds to the CC polarization.

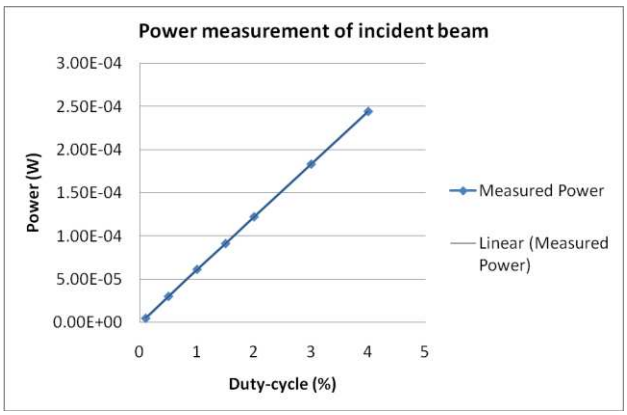

Fig. 6.49: Measured power of the QCL laser versus the QCL duty-cycle.

The THz power P_{THz} is measured with a Golay cell power-meter for different QCL duty cycles. As expected, P_{THz} increases linearly with the duty cycle (Fig. 6.49). By varying the duty cycle, we can control the power of the THz beam to match it with the dynamic range of the THz-FPA under test.

6.3.2.2 Responsivity & sensitivity of detector

An image of the QCL beam, shown in Fig. 6.50, was acquired for a measured total THz power of 24.3 µW impinging on the FPA.

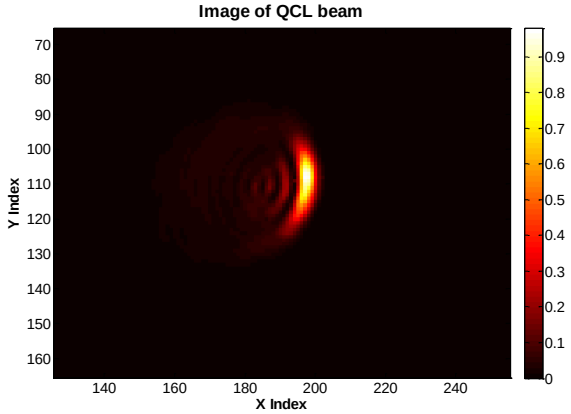

Fig. 6.50: 2.4 THz QCL beam imaged by the Thedex array.

The integrated value of the signal, induced by the QCL beam and delivered by the FPA, equals 143.5 V which leads to a mean experimental responsivity R_{exp}.

$$R_{exp} = \frac{143.5V}{24.3\mu W} \approx 5.9 \text{ MV/W.} \quad \textbf{(6.16)}$$

The measured total RMS voltage noise that includes contributions of the ROIC and digitizing chain is $V_{noise} = 400$ µV rms. This voltage corresponds to the one delivered by a single pixel when illuminated with a 67.8-pW THz beam. From these values, the NEP is evaluated as 1 pW/√Hz (see [3] for more details of the calculation). The FPA dynamic range is close to 74 dB.

This NEP is in fact limited by the not-optimized CMOS ROIC with respect to the thermometer resistance values. Originally, the targeted THEDEX bolometer resistance was 500 kΩ and the read-out circuit has been optimized for this value. However, due to some technological issues, a value of 2.5 MΩ has been obtained. Considering that the same voltage is applied by the ROIC at the resistance outputs, the current going through 2.5 MΩ is of course 5 times lower than through 500 kΩ. Since the sensitivity is inversely proportional to the current (see chapter 2), the sensitivity is degraded considerably by this resistance mismatch.

The resistance mismatch between bolometer and ROIC is not a considerable problem. A simple solution is grouping an array of 2×2 pixels in a parallel electric scheme so that the resistance equivalent is reduced to 600 kΩ, instead of the single pixel value of 2.5 MΩ.

6.4 Examples of THz active imaging with the antenna-coupled bolometer FPA

6.4.1 Raster scanning imaging

Fig. 6.51 shows a raster scanning optical set-up and the THz image of a plant leaf obtained with the bolometer FPA. The beam of a 2.4 THz-QCL was focused on a limited spot of the leaf and the amplitude of the total transmitted signal was recorded whereas the leaf was translated along the normal plane to the incident radiation. This THz image of the leaf reveals the spatial distribution of water inside the leaf.

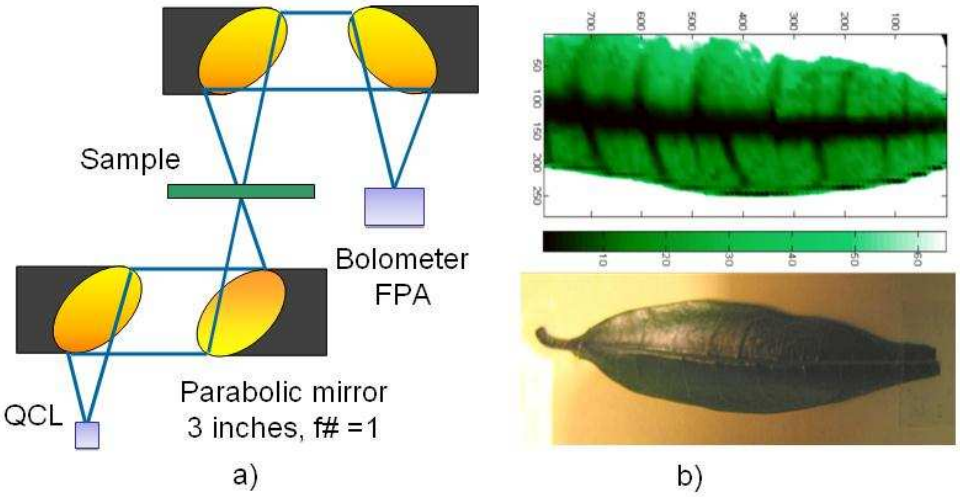

Fig. 6.51: a) Optical setup of raster scanning imaging and b) THz image of leaf at 2.4 THz.

THz images of a plant leaf in transmission scheme have been already published by several teams (for example [5] or [6]). These demonstrations are usually performed in the lower spectral part of the THz domain, i.e. below 1 THz, to exploit the high THz transmission of the leaf in this range. Also, the optical beam is modulated by a chopper and thus a synchronous detection is performed in order to get a better signal to noise ratio. In our case, the image is at 2.4 THz and is retrieved without the synchronous detection. The quality of the image recorded with the THEDEX array is found to be comparable with published results.

6.4.2 Real-time imaging with 320×240 pixel array

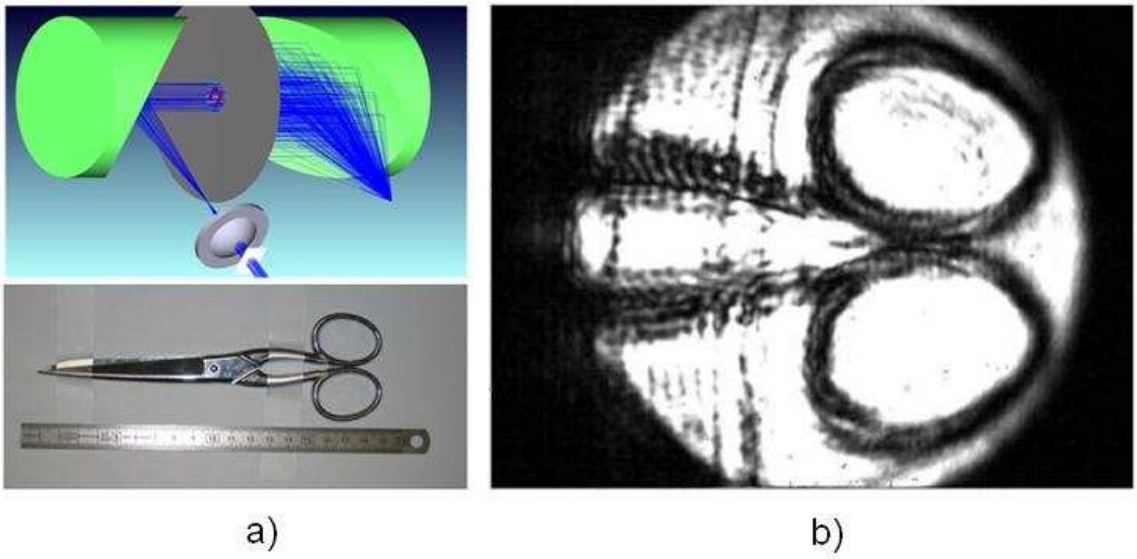

Fig. 6.52: a) Optical setup and b) THz image taken from a video sequence.

A video sequence has been acquired with the use of a very simple optical setup, shown in Fig. 6.52. The sample is a couple of scissors hidden in a postal envelop. With this optical setup, the image of 5×5 cm^2 field of view can be acquired without raster scanning. This illustrates the application potentiality of the focal plane micro-bolometers array, especially the capability of imaging a large field of view.

6.5 Summary

In this chapter, we have presented the techniques developed for the characterization of the optical coupling. Up to our knowledge, measurement of optical coupling (reflectivity and spectral response) of THz sensors is still not well established, probably due to the limited available instruments for THz characterization and to the difficulty of getting absolute values. In this PhD thesis, both reflectivity and spectral absorption were characterized. The experimental results are found to be in good agreement with the simulations. This validates our bolometer model and makes us confident in our ability to optimize the design of detector.

The reflectivity measurement ensures a very good accuracy and can give the absolute value without normalization. Moreover, the measurement is performed under vacuum and consequently is not disturbed by any varying atmospheric condition. However, this measurement approach requires a large area of sensitive pixels. In our case, the smallest array is composed of 160×120 pixels, which occupies an area of 8×6 mm^2. With this area, the measurement can still ensure a good signal to noise ratio.

The spectral absorption is a very important figure-of-merit of the detector. However, it is also very difficult to characterize. This information is contained in the spectral response measurement, which usually mixes up the absorption of the detector with the optics (source, filter, lens, etc.) characteristics. To extract only the spectral absorption of the detector itself, the (total) spectral response must be calibrated. The result of our measurement matches well with the simulation, which validates the precision of the calibration process.

It should be noted that some other works in literature, such as [6] and [7], also have reported spectral response measurements. The spectra were obtained by simply sweeping the frequency of the source (dispersive spectroscopic technique). The results are however poorly detailed: calibration and simulation are not mentioned. Reference [2] has used the FTIR technique to measure the spectral response of a horn-coupled bolometer. The result, however, is not calibrated. Thus it is difficult to know precisely the absorption of the detector itself.

We also presented other important measured figures of merit. The measured heat capacity of the bolometer is found to be in good agreement with the calculation. This parameter is very meaningful because it figures out the trade-off between the response time and the thermal isolation (thus, sensitivity) of the bolometer. This trade-off has been discussed for each bolometer design in chapter 5. The measured thermal conductance is in the range 12.3–13.9 nW/K, which is at the level of the state-of-the-art of uncooled infrared bolometers. The thermal time constant lies in the range 47–50 ms. This value constitutes a performance degradation when compared to ~10 ms of infrared bolometers. This is due to the large size of the membrane of the THz bolometer, leading to a large heat capacity. Some designs presented in chapter 5 should remedy to this slower response.

Regarding the sensitivity, the measured NEP of the THEDEX bolometer is ~ 68 pW at 2.4 THz and the NEP per bandwidth unit is 1 pW/√Hz. Some recent improvements [8] have increased the sensitivity of the THz bolometer to a NEP of 30 pW. This result is comparable with the THz bolometer of NEC-Japan, which reports a measured NEP of 41 pW at 3.1 THz [9]. However, it should be noted that the NEC bolometer is issued directly from the infrared bolometer with very small modification. Thus the spectral absorption decreases dramatically when the frequency decreases. Consequently, the sensitivity of this detector is very poor at lower frequencies. For instance, at 1.1 THz, the NEC bolometer has a measured NEP of 2 nW, larger by a factor of ~50 when compared to the sensitivity at 3.1 THz. Our THEDEX bolometer exhibits a 47 % absorption at 1.1 THz, in the same order as at 2.4 THz. Therefore, the NEP of our detector is kept to be the same as at 2.4 THz, i.e. around 68 pW.

Finally, some demonstrations of imaging and video records have been performed with the 320×40 bolometer array.

References

[1] Bruker Optics, “Product Note M25-01/07,” Product specification.

[2] G. Chattopadhyay, J. Glenn, J. J. Bock, B. K. Rownd, M. Caldwell, and M. J. Griffin, “Feed horn coupled bolometer arrays for SPIRE - design, simulations, and measurements,” IEEE Transactions on Microwave Theory and Techniques, vol. 51, no. 10, pp. 2139 – 2146, Oct. 2003.

[3] J. Meilhan, B. Dupont, V. Goudon, G. Lasfargues, J. Lalanne Dera, D. T. Nguyen, J. L. Ouvrier-Buffet, S. Pocas, T. Maillou, O. Cathabard, S. Barbieri, and F. Simoens, “Active THz imaging and explosive detection with uncooled antenna-coupled microbolometer arrays,” 2011, p. 80230E–80230E–13.

[4] S. Barbieri, J. Alton, H. E. Beere, J. Fowler, E. H. Linfield, and D. A. Ritchie, “2.9 THz quantum cascade lasers operating up to 70 K in continuous wave,” Applied Physics Letters, vol. 85, no. 10, pp. 1674–1676, Sep. 2004.

[5] A. Dobroiu, M. Yamashita, Y. N. Ohshima, Y. Morita, C. Otani, and K. Kawase, “Terahertz Imaging System Based on a Backward-Wave Oscillator,” Appl. Opt., vol. 43, no. 30, pp. 5637–5646, Oct. 2004.

[6] F. Schuster, D. Coquillat, H. Videlier, M. Sakowicz, F. Teppe, L. Dussopt, B. Giffard, T. Skotnicki, and W. Knap, “Broadband terahertz imaging with highly sensitive silicon CMOS detectors,” Opt. Express, vol. 19, no. 8, pp. 7827–7832, Apr. 2011.

[7] E. N. Grossman, C. R. Dietlein, M. Leivo, A. Rautiainen, and A. Luukanen, “A passive, real-time, terahertz camera for security screening, using superconducting microbolometers,” in *Microwave Symposium Digest, 2009. MTT ’09. IEEE MTT*-S International, 2009, pp. 1453 –1456.

[8] F. Simoens, J. Lalanne-Dera, J. Meilhan, S. Pocas, D. T. Nguyen, J.-L. Ouvrier-Buffet, O. Cathabard, P. Gellie, and S. Barbieri, “Active imaging with THz fully-customized uncooled amorphous-silicon microbolometer focal plane arrays,” presented at the 2011 36th International Conference on Infrared, Millimeter and Terahertz Waves (IRMMW-THz), 2011, pp. 1 –2.

[9] N. Oda, “Uncooled bolometer-type Terahertz focal plane array and camera for real-time imaging,” Comptes Rendus Physique, vol. 11, no. 7–8, pp. 496–509, Aug. 2010.

Chapter 7 General conclusion

7.1 General summary

The main objective of this PhD thesis is to establish electromagnetic models of bolometer-based terahertz imagers that bring better understanding of the electromagnetic behavior of these sensors and can be used for forthcoming new designs of focal plane arrays.

To fulfill this aim, the thesis work was first particularly focused on the study of the optical coupling of an existing bolometer design, named THEDEX, which consists in THz antenna-coupled bolometer operating at room temperature. Two types of 3D electromagnetic simulation have been performed. The modeled spectral absorptions are well matched and the combination of these two simulation approaches leads to a powerful toolset to design terahertz bolometer. Regarding experimental work, measurement procedures have been developed and performed with the use of a Fourier-Transform spectrometer. Thanks to these procedures, the reflectivity of the focal plane array and its spectral response can be characterized. Experimental results were found to be in good agreement with simulated data. These achievements have given better understanding of the behavior of the actual detector THEDEX design. On the basis of these results, some ways of sensitivity enhancements have been identified and designs of bolometer operating at different frequencies (for example at the lower frequency 850 GHz) have been proposed. This latter design opens the perspective of using bolometer for terahertz imaging in atmospheric transmission windows below 1THs that are more favorable for stand-off distance imaging.

In a more detailed description, the first study was dedicated to THz optical coupling of the existing infrared bolometer structure. The theoretical model based on thin film absorbing multilayer model has been examined. In particular, the role of the quarter-wavelength cavity in the optical coupling has been carefully examined with 3D electromagnetic simulation. We have demonstrated that the infrared bolometer stack cannot provide a high absorption rate in the low frequency terahertz range, especially for $f < 3$ THz. For the high frequency part of the range [5 – 10 THz] the infrared stack can be moderately efficiently used. Especially the sensitivity can be enhanced by the adjustment of the absorber layer sheet resistance from 300 Ω/□ to 50 Ω/□: optical absorption close to ~ 50 % can be reached, a result that is consistent with NEC results (Japan). The main feature that degrades the absorption of this infrared bolometer stack in the terahertz range comes from the mismatch of the quarter-wavelength cavity thickness (i.e. 2 μm) with respect to the THz wavelengths. CEA-Leti has proposed an innovative terahertz bolometer design where in particular an 11-μm thick substrate of SiO_2 combined with an air gap of 2 μm quarter-wavelength plays the role of quarter-wavelength cavity. This stack improves significantly the optical coupling efficiency especially for $f < 3$ THz.

Another specific feature of the CEA-Leti THz bolometer THEDEX design stands in the use of resistively loaded antennas to collect the terahertz radiation. This approach differs clearly from the large absorbing film deposited on the bolometer suspended membrane of standard infrared bolometers. This film consists in a TiN resistive sheet that absorbs radiation by conduction loss mechanism. This Joule loss is spatially distributed on the whole absorbing film surface. In contrast, the resistively loaded antennas of the THEDEX design encompass two parts, conductive antennas and resistive loads. The antenna itself is made from high conductive metal and is thick enough so that the conduction loss at the antenna is very small.

The following performances parameters have been studied in details either experimentally and with modeling: absorption efficiencies in the terahertz and infrared ranges, polarization.

The absorbing film has been modeled is in receiving mode. In this mode, the whole detector is passive. The pixel is modeled according to a Floquet-port formalism where the upper plane integrates the excitation plane. The optical characteristic of the detector such as the absorption or reflectivity is calculated by solving the electromagnetic field distribution in the structure.

For the resistively loaded antenna approach, the receiving mode can also be used. The parameters calculated by the means of this approach, especially the absorption, contain only the amplitude information, not the phase. However, for antenna design study, the phase information is very important because it determines precisely the frequency range over which the antenna operates efficiently. In particular, the knowledge of the antenna impedance facilitates the impedance matching study.

Hence, for the antenna-coupled design, in addition to the receiving mode, we have used the transmitting mode simulation. This simulation implies that the resistive film layer is replaced by a lumped-port where a uniform current distribution is applied. When the load is small enough in comparison to the wavelength, the current is modeled as exhibiting uniform distribution. Periodic boundary conditions are applied to take into account the 2D array distribution of the pixels.

The results of simulations obtained from receiving and transmitting modes show a good consistency. The THEDEX design bolometer exhibits an absorption peak at 1.35 THz for DC polarization and 1.75 THz for CC polarization. A good absorption rate is found, better than 80 % at the resonant frequencies. The thermal characteristics of the bolometer have also been calculated to compare antenna-coupled design with traditional absorbing film design. We have found that the heat capacity is significantly by the addition of metallic antenna layers on the suspended membrane.

An innovative design named Bambolo has been proposed to ensure a good absorption in the range [2.5 – 3 THz] while having a reduced heat capacity (365 pJ/K when compared to the value 627 pJ/K for THEDEX), by a factor of 42 %. Another important characteristic of the Bambolo design is that it ensures a very low absorption in infrared range (9 % to compare to 30 % for THEDEX).

At frequency below 1 THz, the THEDEX bolometer design would require a thicker cavity than 11µm. Such thickness increase is very challenging due to the technological keylocks. The use of frequency selective surface (FSS) in the bolometer structure has been proposed to keep cavity thickness unchanged and efficient absorption at frequencies smaller than 1THz. For example, such implementation in a 50µm pitch bolometer design at 850 GHz shows good results. The maintenance of 50µm pixel pitch and SiO_2 cavity thickness is ensured so that mechanical robustness but also small thermal constant needs are ensured.

Regarding the experimental thesis work, two measurement methods have been developed and applied to THEDEX focal plane array prototypes (320 × 240 pixels or 160 × 120 pixels). In the first method, the spectral reflectivity of the FPA surface is characterized. Measurements have been performed for each polarization in the range [0.6 – 3 THz]. Experimental results are in good agreement with simulations. Dips in reflection at 1.35 THz for DC polarization and 1.75 THz are well confirmed. The absolute value of this measurement helps us in determining the reflection value without any parameter adjustment.

The second method consists in the measurement of the detector spectral response. We should emphasize that the result has been calibrated and normalized so that the absorption information of the detector itself is extracted. Spectral responses have been measured for each polarization in the range [0.9 – 3 THz]: the absorption peaks are matching the values found with reflectivity measurements.

Some other figures of merit, such as the thermal characteristic or the sensibility are reported to give a global vision of the detector performance. At 2.4 THz the measured NEP of one THEDEX design bolometer is 68 pW and the NEP per bandwidth unit is 1 pW/√Hz. It should be noted that although the measurement is performed at 2.4 THz, the result can be deduced for other frequency provided that the absorption is known precisely. Some other modified version of THEDEX bolometer has attained a NEP of 30 pW because the absorption at 2.4 THz had been improved to ~80 % instead of ~50 % initially. Finally, some imaging demonstrations have been presented to show the real-time imaging the detector in the application phase.

7.2 Perspectives

The electromagnetic models established by this PhD work will facilitate the design of future innovative bolometers. The developed measurement methods, especially the spectral response, will provide an important experimental tool to validate the simulations. Therefore, this PhD work has generated important tool to study the optical coupling of the bolometer. However, the development of the terahertz bolometer still requires more research to improve the performance and applicability to real-life use. Here we state some of those.

Enhanced sensitivity in the 1-3.5THz

Some additional studies should be carried out to keep on enhancing the detector sensitivity. For example binning of pixels read out by a unique electronic chain is envisaged. The use of thermometer materials better than amorphous silicon is under study.

Theses future work will aim at proposing improved uncooled FPAs for spectro-imaging where applications need to image objects though obstacles (like paper, clothes…) and to identify its chemical compositions (drugs, biological agents…).

Bolometer at low frequency (670 & 850 GHz)

Design of 850 GHz bolometer structure is to be manufactured. The simulated absorption is about 80 % thus the bolometer should ensure a NEP of ~ 30 pW as with the THEDEX design. This range of NEP is far better than other kind of uncooled detector, such as transistor-based detector or Schottky diode, which has the NEP per bandwidth in the range of ~nW/√Hz.

The absorption frequency of the bolometer may be further decreased by the use of **high impedance surface** (HIS). The high impedance surface concept goes further the FSS by the fact that at the range of frequency of interest, not only the incident and reflected wave are in phase but also the structure suppresses the surface current. This is fulfilled by presenting a conductive via between the FSS and the back surface. When two surfaces are linked together, the combined structure has impedance of the parallel resonant circuit of the elementary cell.

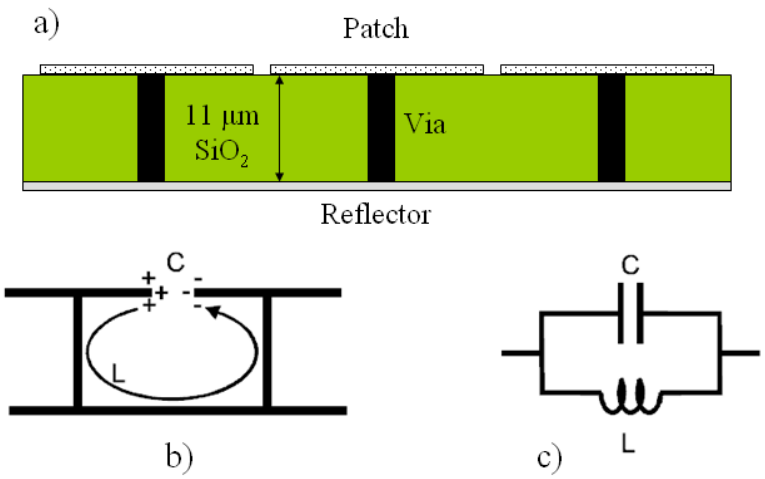

Fig. 7.1: FSS transformed to HIS structure by connecting the via to patch and reflector

Hence, the resonnant frequency of the HIS structure can be even lower than for FSS structure. Thus, with this combination, 670 GHz bolometer design with the 50-µm pitch and 11-µm SiO_2 cavity is achievable.

These bolometer designs operating at frequency below 1THz are very promising for stand-off imaging where low-cost system is needed. Indeed in this frequency range, the atmospheric and cloths or other dielectric material attenuations are lower than above 1 THz. So uncooled reduced cost sources can be combined with the uncooled THz bolometer sensors to fulfill large volume market.

Vita

Duy Thong NGUYEN received his Engineer diploma in electronics from Hanoi University of Science and Technology, Hanoi, Vietnam, in 2008, the M.S. and Ph.D. degrees in optics from the University of Grenoble, France, in 2009 and 2012 respectively.

During three years working at the laboratory CEA-Leti, France as Ph.D. student, he has three pending patents for development of uncooled microbolometer. His current research interests include bolometer design, electromagnetic simulation, infrared antennas, and terahertz sensing technologies.

Email: duythong.ng@gmail.com

Publications of the author

International journals

[J1] D.-T. Nguyen, F. Simoens, J. Ouvrier-Buffet, J. Meilhan, and J. Coutaz, "Broadband THz Uncooled Antenna-Coupled Microbolometer Array - Electromagnetic Design, Simulations and Measurements," IEEE Transactions on Terahertz Science and Technology, vol. 2, no. 3, pp. 299 –305, May 2012.

Pending patents

[P1] D.-T. Nguyen, F. Simoens, J. Ouvrier-Buffet, J. Meilhan, "Détecteur bolométrique d'un rayonnement électromagnétique dans le domaine du térahertz," FR1161425, submitted on 09 december 2011.

[P2] J. Ouvrier-Buffet, J. Meilhan, D.-T. Nguyen, F. Simoens, "Détecteur bolométrique d'un rayonnement électromagnétique dans le domaine de térahertz et dispositif de détection matriciel comportant de tels détecteurs," FR1161426, submitted on 09 december 2011.

International conferences

[IC1] D.-T. Nguyen, F. Simoens, J.-L. Ouvrier-Buffet, J. Meilhan, and J.-L. Coutaz, "Simulations and measurements of the electromagnetic response of broadband THz uncooled antenna-coupled microbolometer array," in 2012 19th International Conference on Microwave Radar and Wireless Communications (MIKON), 2012, vol. 1, pp. 116 – 121.

[IC2] D. –T. Nguyen, F. Simoens, J.-L. Coutaz, "Measurement of Spectral Response of Terahertz Uncooled Antenna-coupled Microbolometer", Workshop of the international GDR project "Semiconductor sources and detectors of THz radiation," Tignes, April 2012.

[IC3] F. Simoens, J. Lalanne-Dera, J. Meilhan, S. Pocas, D. T. Nguyen, J.-L. Ouvrier-Buffet, O. Cathabard, P. Gellie, and S. Barbieri, "Active imaging with THz fully-customized uncooled amorphous-silicon microbolometer focal plane arrays," in 2011 36th International Conference on Infrared, Millimeter and Terahertz Waves (IRMMW-THz), 2011, pp. 1 –2.

[IC4] F. Simoens, J. Meilhan, B. Delplanque, S. Gidon, G. Lasfargues, J. Lalanne Dera, D. T. Nguyen, J. L. Ouvrier-Buffet, S. Pocas, T. Maillou, O. Cathabard, and S. Barbieri, "Real-time imaging with THz fully-customized uncooled amorphous-silicon microbolometer focal plane arrays," 2012, p. 83630D–83630D–12.

[IC5] J. Meilhan, B. Dupont, V. Goudon, G. Lasfargues, J. Lalanne Dera, D. T. Nguyen, J. L. Ouvrier-Buffet, S. Pocas, T. Maillou, O. Cathabard, S. Barbieri, and F. Simoens, "Active THz imaging and explosive detection with uncooled antenna-coupled microbolometer arrays," 2011, p. 80230E–80230E–13.

National conferences

[NC1] D.-T. Nguyen, F. Simoens, "Electromagnetic study of uncooled 2D microbolometer sensors specifically designed for THz imaging," 6e Journées THz, La Grande Motte, May 2011.

[NC2] D. –T. Nguyen, F. Simoens, J. Coutaz, "Conception, modélisation et caractérisation de détecteurs THz innovants," Journée thématique CEA-DGA, Saclay, September 2010.

[NC3] D. –T. Nguyen, F. Simoens, J. Coutaz, "Conception, modélisation et caractérisation de détecteurs THz innovants," Journée thématique CEA-DGA, Saclay, March 2012.

National magazines

[NM1] D. T. Nguyen, F. Simoens, J. L. Ouvrier-Buffet, J. Meilhan, S. Pocas, "Modeling of THz uncooled antenna-coupled bolometer at CEA-Leti," Leti annual research report 2011 Optics & Photonics, 2011.

[NM2] J. Meilhan, B. Dupont, V. Goudon, G. Lasfargues, D.T. Nguyen, S. Pocas, F. Simoens, "THz micro-bolometers applied to explosives detection," Leti annual research report 2011 Optics & Photonics, 2011.

List of figures

Fig. 1.1: Terahertz region is between infrared and microwave domains 1
Fig. 1.2: Simple scheme of imaging system 7
Fig. 1.3: Angle of view is determined by optics and size of array of detectors 9
Fig. 1.4: Atmospheric attenuation from millimeter to visible range [5] 10
Fig. 1.5: Atmospheric attenuation (dB/km) from 10 GHz to 10 THz 11
Fig. 1.6: Atmospheric attenuation (dB/km) at different weather conditions from 0.1 to 1 THz 11
Fig. 1.7: Transmission through some common clothing materials [25]. 12
Fig. 1.8: Passive imaging at 94 GHz from QinetiQ [13] 15
Fig. 1.9: Passive imaging with superconducting bolometer at NIST & VTT 15
Fig. 1.10: 2D image and 3D image obtained by heterodyne detection at JPL [31] 16
Fig. 1.11: a): Threat need to be detected; b) and c): Detection by terahertz active imaging ... 17
Fig. 1.12: Demonstration of terahertz imaging with uncooled bolometer [33] 18
Fig. 2.1: Bolometer principle 23
Fig. 2.2: Example of bolometer 24
Fig. 2.3: I-V characteristic of bolometer under constant voltage bias 27
Fig. 2.4: Typical spectral response of uncooled mid-infrared bolometer 32
Fig. 3.1: Structure of a superconducting antenna-coupled bolometer 36
Fig. 3.2: Spider-web design 37
Fig. 3.3: Horn antenna coupled bolometer 38
Fig. 3.4: Schematic view of bolometer 39
Fig. 3.5: Schematic view of the bolometer 40
Fig. 3.6: Schematic view of bolometer 40
Fig. 3.7: Spectral range of bolometer for several cavity heights (Ref [9]). 41
Fig. 3.8: SEM image of 17-μm pitch bolometer shows contact and thermal leg [10]. 42
Fig. 3.9: Composition of an elementary leg 43
Fig. 3.10: Stack of IR bolometer at Leti 46
Fig. 3.11: THz bolometer (NEC, Japan) with “eaves”-like absorber to enhance coupling. 49
Fig. 3.12: Absorber structure with parameters 49
Fig. 3.13: Absorption as function of absorber sheet resistance at several wavelengths. 50
Fig. 3.14: IR bolometer structure associated with antenna to enhance optical coupling. 51
Fig. 4.1: General three-layers structure for uncooled infrared bolometers. 55
Fig. 4.2: Absorption of the three-layer structure with different values of absorber resistance R_s 56
Fig. 4.3: Absorption of the three-layers structure with different values of reflector resistance R_r 57
Fig. 4.4: Absorption of infinite size thin film absorber at THz range, air gap is 2μm 58
Fig. 4.5: Absorption of infinite size thin film absorber, air gap is 25μm, $R_s = 300\ \Omega/\square$ 59
Fig. 4.6: Periodic metallic square patch with infinite reflector underneath: 60
Fig. 4.7: Absorption of a patch standing 2 μm above an infinite reflector. 61
Fig. 4.8: Absorption at infrared range of a patch standing 2 μm over infinite reflector. 61
Fig. 4.9: Periodic metallic square patch with reflector underneath. 62
Fig. 4.10: Absorption of a patch standing 2 μm above a finite reflector. 63
Fig. 4.11: Transmission through a patch standing 2 μm above a finite reflector. 63

Fig. 4.12: Absorption in the infrared range of absorbing patches standing 2 μm above a finite reflector. 64
Fig. 4.13: CEA-LETI bolometer stack with 2 μm air gap. 64
Fig. 4.14: Metallic reflector patterning. 65
Fig. 4.15: Structure of CMOS read-out circuit at CEA-LETI contains 6 metallic layers. 65
Fig. 4.16: Geometry of two different metallic layers 66
Fig. 4.17: Simulated reflection of the CMOS ROIC structure with many conductor strips 66
Fig. 4.18: Distribution of electric field on a conducting surface 68
Fig. 4.19: Bolometer stack with 11 μm SiO_2 substrate 69
Fig. 4.20: Periodic metallic square patch with 11 μm SiO_2 substrate and reflector underneath 70
Fig. 4.21: Simulated absorption of the THz bolometer stack 71
Fig. 5.1: Structure of the AFB design 74
Fig. 5.2: Layered structure of the suspended membrane 75
Fig. 5.3: Top view of the AFB design 75
Fig. 5.4: Absorption in both polarization of the AFB design 76
Fig. 5.5: Actual bolometer (left) and two artificial structures that employ the same absorbing film (center) or a bigger absorbing film (right) 76
Fig. 5.6: Comparison of absorption between two absorbing-patch structures and bolometer. 77
Fig. 5.7: Absorption in infrared range of the AFB design 77
Fig. 5.8: Detailed structure of bolometer THEDEX 80
Fig. 5.9: General three layer structure for uncooled infrared bolometer 81
Fig. 5.10: Different layers of the suspended membrane showing the antenna is insulated from the thermometer 82
Fig. 5.11: Simulated THz range absorption of THEDEX design 83
Fig. 5.12: Simulated infrared range absorption of THEDEX design 83
Fig. 5.13: Receiving mode simulation, the structure is excited by Floquet port that mimics plane wave 87
Fig. 5.14: Transmitting mode simulation, antenna is excited by lumped port. 88
Fig. 5.15: Modeling of resistive load by lumped port 89
Fig. 5.16: Impedance of the DC antenna shows a resonance at 1.35 THz 90
Fig. 5.17: Impedance of CC antenna shows a resonance at 2 THz. 90
Fig. 5.18: Comparison between absorption (receiving mode simulation) and matching efficiency (transmitting mode simulation) for leg-parallel polarization. 91
Fig. 5.19: Comparison between absorption (receiving mode simulation) and matching efficiency (transmitting mode simulation) for leg-cross polarization. 92
Fig. 5.20: Detailed structure of Bambolo design 93
Fig. 5.21: Different layers of the suspended membrane in the case of Bambolo design. 93
Fig. 5.22: Two versions of Bambolo design, two shapes of the thermometer (similar shape as insulator) are used to ensure a good mechanical strength for the dipole antenna overhanging tips. 94
Fig. 5.23: Array of dipole equipped with resistive load, the distance between dipoles is swept to study the effect of mutual coupling 95
Fig. 5.24: Impedance of dipole over the range [1 – 5 THz], distance between dipole is 50 μm 95
Fig. 5.25: Close-up of spectral range [1 – 3.8 THz] 96
Fig. 5.26: Matching efficiency with different load resistances. 96
Fig. 5.27: Impedance of dipole over the range [1 – 5 THz], with dipole interspace of 25 μm 97
Fig. 5.28: Matching efficiency with different load's values 97
Fig. 5.29: Crossed dipoles sharing the same resistive load 98

Fig. 5.30: Top view of Bambolo design showing the limited distance between electrodes. ... 99
Fig. 5.31: Current distribution on regular dipole and on capacitive-loading dipole 100
Fig. 5.32: Contribution of the suspended membrane elements to the bolometer absorption in leg-parallel polarization. 100
Fig. 5.33: Contribution of the suspended membrane elements to the bolometer absorption in leg-cross polarization 101
Fig. 5.34: Top-view of the mono-polarization bolometer. 101
Fig. 5.35: Contribution of each element to absorption of mono-polarization bolometer. 102
Fig. 5.36: Simulated absorption demonstrating the polarization-dependent response of the design. 102
Fig. 5.37: Absorption in the THz range of the Bambolo design 103
Fig. 5.38: Simulated absorption in infrared range of Bambolo design. 103
Fig. 5.39: Capacitive surface backed by a substrate layer over a continuous reflector. 106
Fig. 5.40: Simulation showing a cavity equipped with FSS tuned for resonance at 850 GHz 107
Fig. 5.41: Array of antennas located 2-μm above a capacitive surface 108
Fig. 5.42: Impedance of the bowtie and dipole when equipped with FSS 109
Fig. 5.43: Matching efficiency of bowtie antenna array with different load values 109
Fig. 5.44: Detailed structure of the 850 GHz bolometer. 110
Fig. 5.45: Dimension and arrangement of the membrane 110
Fig. 5.46: Absorption of the 850 GHz bolometer showing a single polarization response. .. 111
Fig. 6.1: FTIR technique principle. 116
Fig. 6.2: Michelson interferometer. 117
Fig. 6.3: Spectrum (a) and interferogram (b) of monochromatic wave 118
Fig. 6.4: Spectrum (a) and interferogram (b) of non-monochromatic light 118
Fig. 6.5: Scheme of the spectrometer Vertex 80v. 120
Fig. 6.6: Top view of the reflection module. 120
Fig. 6.7: Photo of the reflection module. 121
Fig. 6.8: a) Photo of the detector chip mounted on a plastic holder and b) Setup of the sample in the reflection module. 121
Fig. 6.9: a) Metallic plates, and b) mounting of plate in the reflection module. 122
Fig. 6.10: Measurement of spot size by using different hole diameters. 122
Fig. 6.11: Image of reflection module. 123
Fig. 6.12: Arrangement of the detector regarding the coordinate system. 124
Fig. 6.13: Reflectivity of FPA when DC antenna is excited by TE and TM modes. 125
Fig. 6.14: Reflectivity of FPA when CC antenna is excited by TE and TM modes. 125
Fig. 6.15: a) Photo of the detector chip and b) photo of the mirror. Both are mounted with similar ceramic card and plastic holder. 126
Fig. 6.16: Accuracy of the reflectivity measurement. 127
Fig. 6.17: Setup of the spectral response measurement. 128
Fig. 6.18: Interferogram with (bottom) and without (top) synchronous detection. 130
Fig. 6.19: Calibration of the measured spectrum. 131
Fig. 6.20: Spectral response normalized with respect to the simulated absorption maximum. 131
Fig. 6.21: Detectivity of the pyroelectric detector supplied with Vertex 80v FTS. Data reproduced from Bruker Optics [1] 132
Fig. 6.22: Simulated responsivity R of the bolometer. 133
Fig. 6.23: Reproducibility of the spectral response measurement in the case of 4-cm^{-1} resolution. 133

Fig. 6.24: Reproducibility of the spectral response measurement in the case of 8-cm^{-1} resolution. 134
Fig. 6.25: Simulated absorption of the THEDEX bolometer..... 135
Fig. 6.26: Simulated reflectivity of the THEDEX FPA surface. 136
Fig. 6.27: Comparison between simulated and measured reflectivity for DC polarization... 136
Fig. 6.28: Comparison between simulated and measured reflectivity for CC polarization... 137
Fig. 6.29: Mismatch between measured and simulated reflectivities, DC polarization. 137
Fig. 6.30: Mismatch between measured and simulated reflectivities, CC polarization..... 138
Fig. 6.31: Simplified structure: the suspended membrane is taken away by a scotch-tape... 138
Fig. 6.32: Comparison between the reflectivity of the FPA with and without bolometer, DC polarization. 139
Fig. 6.33: Comparison between the reflectivity of the FPA with and without bolometer, CC polarization. 139
Fig. 6.34: Comparison between the reflectivity of the FPA processed above CMOS ROIC with and without bolometer, DC polarization. 140
Fig. 6.35: Comparison between the reflectivity of the FPA processed above CMOS ROIC with and without bolometer, CC polarization. 140
Fig. 6.36: Simulated spectral absorption of the THEDEX bolometer with and without the ROIC structure, DC polarization. 141
Fig. 6.37: Simulated spectral absorption of the THEDEX bolometer with and without the ROIC structure, CC polarization. 141
Fig. 6.38: Comparison between measured and simulated reflectivity curves in the infrared range, unpolarized light. 142
Fig. 6.39: Measured spectral responses with different resolutions, DC polarization. 143
Fig. 6.40: Measured spectral responses with different resolutions, CC polarization. 143
Fig. 6.41: Transmission of atmosphere measured with 0.2 cm^{-1} resolution. 144
Fig. 6.42: Impact of atmospheric attenuation on spectral response measurement, DC polarization. 145
Fig. 6.43: Impact of atmospheric attenuation on spectral response measurement, CC polarization. 145
Fig. 6.44: Correction of atmospheric attenuation for DC polarization. 146
Fig. 6.45: Correction of atmospheric attenuation for CC polarization. 146
Fig. 6.46: Simulated and measured spectral response for DC polarization with different resolutions. 147
Fig. 6.47: Simulated and measured spectral response for CC polarization with different resolutions. 147
Fig. 6.48: a) Photo of the experiment setup and b) optical scheme of the experiment..... 149
Fig. 6.49: Measured power of the QCL laser versus the QCL duty-cycle. 149
Fig. 6.50: 2.4 THz QCL beam imaged by the Thedex array. 150
Fig. 6.51: a) Optical setup of raster scanning imaging and b) THz image of leaf at 2.4 THz. 151
Fig. 6.52: a) Optical setup and b) THz image taken from a video sequence. 151
Fig. 7.1: FSS transformed to HIS structure by connecting the via to patch and reflector 158